EFFECTS OF CHARGE TRANSPORT AND HETEROGENEOUS CHARGE TRANSFER ON THE OPERATION OF INORGANIC SEMICONDUCTOR LIGHT-HARVESTING SYSTEMS

by

Michelle Janiece Chitambar

A dissertation submitted in partial fulfillment
of the requirements for the degree of
Doctor of Philosophy
(Applied Physics)
in The University of Michigan
2012

Doctoral Committee:

Assistant Professor Stephen Maldonado, Chair
Professor Jasprit Singh
Associate Professor Max Shtein
Assistant Professor Vanessa Sih
Assistant Professor Zhaohui Zhong

DEDICATION

To my parents, who have given me the courage, strength and perseverance to rise to this challenge; and to my husband, who gave me the love, faith and friendship that made every struggle worthwhile.

ACKNOWLEDGEMENTS

Many thanks to the classmates who made coursework engaging (and occasionally entertaining!), the labmates who were always ready to help with experiments, feedback or just by listening with empathy, the professors who made science an adventure, the staff who made experiments and simulations possible and kept morale high, and all my committee members, including my advisor Professor Stephen Maldonado, for their invaluable time and feedback. No endeavor can be separated from the community that supports us, and I would like to extend gratitude to my wonderful husband Eric, our many friends and family members in Ann Arbor and elsewhere, St. Thomas the Apostle Catholic Church, the Mounties and border crossing guards at the Blue Water Bridge, and the massive crew of mechanics, tow truck drivers and AAA agents who resuscitated the Jimmy time and time again. Particular acknowledgement goes to Mr. Justin Foley and Dr. Zhijie Wang, collaborations with whom resulted in co-first author publications from which Chapters III and VI, respectively, were based. Thanks also to Ms. Sabrina Peczonczyk, who graciously volunteered so much of her time to help me make samples, characterize their surface content and keep me sane. I am heavily indebted to the Applied Physics Program for their help, fraternity and assistance through every step of the PhD process. Many thanks also for the financial and academic support provided by a Regents' Fellowship from the University of Michigan, a Rackham Merit Fellowship from the Rackham Graduate School at The University of Michigan, a Graham Doctoral Fellowship from the Graham Environmental Sustainability Institute at the University of Michigan, and an Office of Science Graduate Fellowship from the Office of Science at the U.S. Department of Energy.

My doctoral studies would not have been possible without the education I received from my professors and classmates at Gustavus Adolphus College. I would particularly like to thank my undergraduate physics advisor Prof. Paul Saulnier for not losing in a flurry of equations the beauty and mystery of our field; the world truly didn't

have to work this way. Thanks also to Prof. Dennis Henry, who always pushed me further than I imagined I could go. I will continue trying to “walk on heavy water!” I would also like to thank Prof. Charles Niederriter for making physics fun and constantly illustrating that people and faith will always be the most important gifts in life. Thank you also to Prof. Tom Huber, who volunteered his time to help me study for the physics GRE, and to Jim Miller, who showed me that the ability to solve a physics problem doesn’t always have much to do with getting an experiment to work. Particular thanks go to Prof. Alisa Rosenthal and Prof. Richard Lietch, who helped me to understand that people on both sides of a contentious issue are mostly just trying to do the right thing.

TABLE OF CONTENTS

LIST OF FIGURES

FIGURE

LIST OF TABLES

LIST OF APPENDICES

APPENDIX

LIST OF SYMBOLS

[A]	Concentration of acceptors in electrolyte
[A-]	Concentration of donors in electrolyte
A^{**}	Reduced effective Richardson constant
A_s	Surface area
B_m	Bessel function of order m
c	Speed of light
C	Capacitance
D_n	Electron diffusion constant
D_p	Hole diffusion constant
E	Potential applied to photoelectrode
$\vec{E}$	Electric field
$\left\|\vec{E}\right\|$	Electric field magnitude
E_{CB}	Energy of conduction band edge
E_g	Energy of band gap
E_{int}	Interfacial electric field
E_T	Energy of trap states
E_{VB}	Energy of valence band edge
FF	Fill factor
h	Distance from the top of a nanowire
J_0	Dark exchange current density
J_{sc}	Short-circuit current density
k_B	Boltzmann's constant
k_{et}	Electron charge transfer rate
k_{ht}	Hole charge transfer rate
k_{opt}	Imaginary part of complex refractive index

L	Carrier diffusion length
L_{n}	Electron diffusion length
L_{p}	Hole diffusion length
n	Electron density
n_{d}	Effective density of donor-like defect states
n_{i}	Intrinsic carrier density
n_{opt}	Real part of complex refractive index
n_{s}	Surface density of electrons
n_{s0}	Surface density of electrons in the dark at equilibrium
N	Dopant density
N_{A}	Acceptor density
N_{CB}	Effective density of states in conduction band
N_{D}	Donor density
N_{t}	Defect density in bulk
$N_{\mathrm{t,surface}}$	Surface defect density
N_{VB}	Effective density of states in valence band
p	Hole density
p_0	Hole density in the dark at equilibrium
p_{d}	Effective density of acceptor-like defect states
p_{s}	Hole surface density
p_{s0}	Hole surface density in the dark at equilibrium
q	Unsigned charge of an electron
r	Radial coordinate (cylindrical)
r_0	Radius of non-tapered nanowire
$r_{0,\mathrm{base}}$	Radius of nanowire base
$r_{0,\mathrm{top}}$	Radius of nanowire top
R_{opt}	Optical reflectance
S	Surface recombination velocity
S_{n}	Electron surface recombination velocity
S_{p}	Hole surface recombination velocity
t	Thickness of semiconductor surface layer

T	Temperature
T_{opt}	Optical transmission
v_d	Drift velocity
v_n	Velocity at which electrons cross the semiconductor interface
V_{bi}	Built-in potential
V_{oc}	Open circuit voltage
W_D	Semiconductor depletion width
v_p	Velocity at which holes cross the semiconductor interface
z	Length coordinate (cylindrical)

α	Material absorptivity
ε_s	Semiconductor permittivity
ε_0	Permittivity of free space
ε_r	Relative permittivity
η	Ideality factor
λ	Wavelength
μ	Carrier mobility
μ_n	Electron mobility
μ_p	Hole mobility
ρ_{trap}	Charge density associated with traps
σ_n	Electron interaction cross section
σ_p	Hole interaction cross section
τ_B	Bulk time constant
τ_n	Electron lifetime
τ_p	Hole lifetime
ϕ	Electric potential
Φ	Quantum yield
Φ_B	Equilibrium interfacial barrier height
Φ_{ph}	Solar irradiance
Φ_{sc}	Short-circuit internal quantum yield

ABSTRACT

This dissertation quantitatively details the operational features of five separate light-harvesting systems based on crystalline inorganic semiconductors. Specifically, charge transport and heterogeneous charge transfer are characterized in silicon (Si) and gallium phosphide (GaP) light-harvesting systems via both experiments and simulations. The goal of this work is to provide a quantitative framework to facilitate the design of efficient, scalable solar energy conversion systems.

Nanostructured, high-aspect-ratio semiconductors are attractive materials for light-harvesting systems due in part to their ability to decouple light absorption and carrier collection to minimize bulk recombination in low-purity materials. For n-type GaP photoelectrodes featuring short minority carrier diffusion lengths, high-aspect-ratio structuring leads to an order of magnitude increase in energy conversion efficiency for sufficiently thick macroporous films as compared to planar photoelectrodes. The design of most high-performance nanostructured devices has been elusive due to a lack of detailed information on their design and operation. Chapter III provides quantitative guidelines for the design of such systems via a finite-element simulation analysis that focuses on how charge transport and recombination affect the performance of nanowire photoelectrodes featuring various radii, dopant densities, defect densities, surface recombination velocities, nanowire tapering, and doping uniformity. Notably, a novel discrete-contact nanowire scheme featuring high open-circuit potentials is shown to significantly outperform analogous devices featuring conformal Schottky contacts over a broad range of these parameters. Charge transfer/transport is also investigated in two systems featuring inorganic semiconductors in contact with an organic polymer or chromophore. Specifically, the low electron collection velocity at n-Si/PEDOT:PSS interfaces is shown to mitigate carrier loss at heterojunctions, leading to increased open-circuit potentials and short-wavelength internal quantum yields as compared to n-Si/Au

devices. Charge injection and collection are also characterized in planar dye-sensitized p-GaP photoelectrodes featuring strong electric fields within the depletion regions of the semiconductors. These fields effectively sweep holes away from interfacial recombination centers and facilitate large internal quantum yields even in systems with relatively poor kinetics for carrier collection. Taken together, the results in this dissertation provide clear design requirements for high-performance light-harvesting systems and highlight the importance of understanding and controlling charge transport/transfer in semiconductor devices.

CHAPTER I

Introduction

A. Context and Importance

Energy plays a critical role in the structure, interaction and prosperity of societies today, with access to energy serving as a strong, positive determinant of the economic development of a state.[1] The relationship between access to energy and wealth is particularly strong in developing nations,[2] where access to modern energy sources can have profound impacts on the health,[3] opportunities for education,[4] gender equality[5] and other basic metrics of well-being[6] for billions of individuals. Access to energy can also strongly impact individuals' decisions and behaviors. For instance, energy powers transportation and communication systems that can connect distant family and friends (facilitating relocation for college/employment), air conditioning systems that can transform harsh climates into homes,[7] and electric lights that allow procrastinators and night owls to work or play late into the night. Clearly, meeting global energy demand is an endeavor with consequences that can affect nearly every dimension of the human experience.

Energy demand (the amount of energy that consumers wish to purchase) is expected to increase dramatically in the near future, from over 16 TW of average, continuous global demand in 2008 to more than 25 TW by 2035.[8] This growth in demand is projected to come primarily from developing nations and is likely to be met with low-cost energy sources such as coal-fired power plants, natural gas turbines and other fossil fuel sources.[8] One consequence of the burning of fossil fuels is the emission of large amounts of greenhouse gases into the atmosphere, with more than 35 billion metric tons of carbon dioxide (CO_2) produced globally each year.[9] The resulting increase in the concentration of CO_2 in the Earth's atmosphere can have staggering environmental

consequences that range from global warming[10] to ocean acidification[11-13] and climate change.[14,15] Human health has also been shown to suffer as exposure to fossil fuel emissions increases.[16] In fact, emissions-correlated health concerns such as carbon monoxide poisoning, damage to the immune system, asthma and other respiratory disorders are anticipated to set back human development if current trends in energy use continue unchecked.[17] Additional geopolitical concerns associated with access to fossil fuel reserves further complicate the continued use of conventional energy sources.[18] Taken together, the environmental, human health and geopolitical concerns surrounding the access and use of fossil fuel energy have led many to conclude that the development and implementation of alternative, sustainable energy technologies are the greatest challenges facing the world in our lifetime.[19]

Despite the magnitude and gravity of the issue of sustainable energy access, relatively little progress has been made toward increasing the sustainability of today's energy profile. As of February 2012, for instance, only 12.2% of the electricity generated in the United States was derived from renewable sources.[20] There are several renewable energy sources that are mature enough from a technical standpoint to contend viably in the commercial sector, including hydroelectric, geothermal, wind, tidal, biomass and solar power. A quantitative analysis of the maximum energy that could feasibly be generated from the first five sources, however, shows that even optimistic projections fall well short of the 16 – 25 TW range needed to meet current and projected demand.[8] Solar power, on the other hand, represents an unequaled energy source with nearly 120,000 TW continually incident on Earth.[19,21] The development of one or more efficient, widely accessible systems to harvest solar energy could, in principle, satisfy human energy demand for the foreseeable future.[19] The following section addresses the required functional and design features of such a system.

B. Technical Background

i. Light-Harvesting System Requirements

Every solar cell must satisfy the same three functional requirements in order to achieve high energy conversion efficiency, regardless of its structure or operating principles. The cell must[22]

(1) absorb light to generate photoexcited electron/hole pairs,

(2) separate charge carriers, and

(3) collect the carriers to do useful work.

Given the relatively low market penetration of solar energy today (0.038% of electricity generated in the US[20]), it is perhaps surprising to learn that these technical challenges have already been met in efficient solar-to-electrical energy conversion devices. The maximum confirmed efficiency for a GaInP/GaAs/GaInNAs multijunction concentrator solar cell, for instance, is 43.5%, three times higher than the efficiency of typical commercial silicon solar modules.[23] There are many reasons why a particular high-efficiency light-harvesting device may not be suitable for large-scale implementation. Relatively low earth abundance of component materials[24] may make it difficult to produce more than a handful of devices, while extensive environmental damage and greenhouse gas emissions[25] could result from attempting to mine particularly difficult-to-extract materials. Complex or energy-intensive material purification processes can also detract from an otherwise attractive system,[26] while issues with device stability may undermine long-term operation[26,27] and the use of particularly toxic materials may make the production or end-of-life disposal of a device prohibitive. While none of these individual factors necessarily preclude the adoption of a given device, these and other considerations can all contribute to an increase in environmental, energy and monetary cost per unit of energy produced which the end user may not be willing to absorb.[19] Thus, while the three requirements listed above define the operational principles necessary for an efficient cell, they are not sufficient guidelines for the design of a disruptive light-harvesting technology that can be implemented on a massive scale.

A viable light-harvesting technology for large-scale implementation must also

(4) possess a sustainable life-cycle footprint.

Although it is often taken for granted that solar cells are an ‘environmentally friendly’ alternative energy option, life-cycle analyses of the environmental impacts of a solar cell suggest that there is still much room for improvement.[26] In addition to the significant emissions and other environmental damage caused by large mining operations (particularly for cells that utilize non-earth-abundant materials),[25] the high processing temperatures necessary to produce and purify inorganic semiconductors add significantly

to the energy inputs needed to produce a cell.[26] Material losses due to wafer sawing can then reduce by up to 50% the amount of material obtained for a given energy input.[26] When all inputs are accounted for, the energy payback time for a typical silicon panel is about three to five years, meaning that an average panel has to produce electricity for three to five years just to generate the amount of energy that it took to make the panel in the first place.[26] Thus, solar cell designs that require a smaller volume of materials, utilize materials with fewer processing inputs or increase the efficiency of a solar device all translate directly to a smaller environmental footprint for solar energy. Nanowire array solar cells are a prime example of a design that may achieve all of these objectives, since they can be fabricated using only a small fraction of the semiconductor material required for traditional solar cells, but typically exhibit light absorption properties far superior to planar materials without the need for additional processing to reduce reflectance losses.[27-29] Much progress has also been made on growing semiconductor nanowires at far lower temperatures than traditional single-crystalline boules,[29-32] which could significantly reduce the processing inputs and corresponding greenhouse gas emissions associated with solar cell manufacturing.[26]

ii. Energy Storage

The intermittency of sunlight is a significant drawback to the large-scale adoption of solar-to-electrical energy conversion systems. In addition to the obvious issues that arise after sunset, the output of a solar field also drops by up to 80% on overcast days or whenever a cloud passes overhead.[33] Today's solar cells are almost exclusively grid-tied photovoltaics which produce electricity that must be used immediately. Since electricity demand is much more stable than the output of a typical field, solar energy cannot provide a reliable base load and must be accompanied either by expensive, often carbon-intensive backup energy sources that can be continuously idled or quickly ramped up to cover demand, or by viable energy storage technologies.[34] Without such backup sources, the electrical grid cannot handle the level of fluctuations inherent in solar energy systems.[33-35]

Photoelectrochemical cells represent attractive systems for the efficient generation and *storage* of energy-rich chemical fuels.[36-39] Although a number of external energy storage options (battery arrays with a variety of chemistries, flywheels, pumped water

storage, etc.) are being developed and refined for grid-scale applications today, efficiency losses and cost barriers have impeded the large-scale adoption of such technologies thus far.[40] An alternative to external energy storage is the direct conversion and storage of solar energy in the form of chemical bonds,[21] a pervasive natural example of which is photosynthesis. With further development, photoelectrochemical cells may offer an intrinsic solution to the problem of energy storage while vastly improving on the typical 0.5% solar-to-chemical energy conversion efficiency achieved by most plants.[21]

C. Concepts and Expressions of Merit

i. Semiconductor Band Gap

The band gap of a semiconductor, given by the energetic difference between its valence band maximum and conduction band minimum, has important implications for both the semiconductor's light absorption properties and the maximum photovoltage that can be expected from a corresponding device. In order to absorb a photon, an electron generally must be excited from the valence band of the semiconductor to the conduction band. Thus, a photon must possess energy greater than or equal to that of the semiconductor band gap in order to be absorbed and create an excited electron-hole pair. As a rule of thumb, the cutoff wavelength for optical absorption can be estimated by the relation in Equation I.1,

$$E_g \lambda_g = 1240 \quad \text{eV·nm} \qquad \text{(I.1)}$$

where E_g is the semiconductor band gap energy in eV and λ_g is the cutoff wavelength in nm. Figure I.1 shows the absorption range of silicon (Si), gallium phosphide (GaP) and titanium dioxide (TiO_2) superimposed on the AM1.5 solar spectrum. Si, which has a band gap of ~1.1 eV, absorbs light with wavelengths ≤ 1127 nm, while GaP can absorbs light with wavelengths ≤ 549 nm due to its larger band gap of 2.26 eV and TiO_2 can only absorb light with wavelengths ≤ 588 nm due to its band gap of ~3.2 eV.

To first order, it may appear as if Si or semiconductors with an even smaller band gap are superior materials for solar energy conversion since they can absorb a greater amount of solar irradiation. Although Si devices *are*, in fact, capable of achieving large energy conversion efficiencies,[41] this conclusion may be premature for two reasons. First, even materials with a large band gap can form the basis for highly absorptive devices if

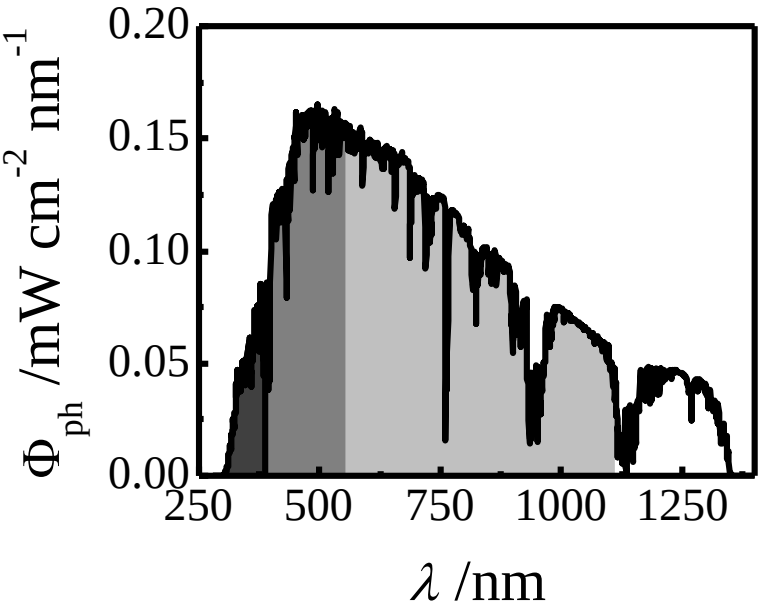

Figure I.1: AM1.5 solar irradiance as a function of wavelength. The light gray shaded region represents the portion of the solar spectrum that can be absorbed by only Si, the medium gray shaded region represents the portion of the solar spectrum that can be absorbed by only Si and GaP, and the dark gray shaded region represents the portion of the solar spectrum that can be absorbed by Si, GaP and TiO_2.

they are sensitized with quantum dots or chromophores featuring optimized HOMO/LUMO gaps. A prolific example of this technique is found in conventional dye-sensitized solar cells, which utilize TiO_2 coated with a broad-spectrum dye to yield efficiencies of more than 12%.[42] Second, the net energy produced by a solar cell depends not only on the amount of light that can be absorbed (related to photocurrent density), but is also directly proportional to the operating potential of the device. For most light-harvesting devices, the band gap (divided by the elementary charge) represents a fundamental limit for the open-circuit potential (V_{oc}) of the device, and the voltage corresponding to the maximum energy conversion efficiency of a device will generally not exceed E_g/q. The optimal band gap for a light-harvesting material is thus not typically extremely low (corresponding to panchromatic light absorption but a low V_{oc}) or extremely high (corresponding to poor optical absorption and a potentially larger V_{oc})[41] and often varies depending on the device design and applications.

Solar-to-*chemical* energy conversion systems typically have more stringent requirements for operating potential than solar-to-*electrical* energy conversion systems due to the fixed standard potentials for reduction and oxidation of various species in a fuel-forming electrochemical system. Generally, larger operating cell voltages than those obtained with single-junction commercial silicon photovoltaics under AM1.5 illumination are needed to drive the kinetically slow, multi-electron charge-transfer reactions involved in fuel production.[38] Due to fundamental limitations imposed by their band gap energies and bulk recombination processes,[22,43] even ideal semiconductor heterojunctions employing common small- to mid-bandgap semiconductors such as Si, gallium arsenide or germanium cannot individually generate open-circuit photovoltages larger than ~ 0.8 V under typical solar insolation. Gallium phosphide, on the other hand, has a sufficiently large band gap energy to support an open-circuit photovoltage $\geq$ 1 V,[44-46] is also capable of absorbing a meaningful fraction of the solar spectrum (Figure I.1), and can achieve efficiencies of 20% for single optimized heterojunctions under AM1.5 irradiation.[47] GaP has long been recognized as a potentially useful semiconductor electrode material for photoelectrochemical energy conversion/storage,[48-52] and methods for doping, contacting, and depositing are also well known.[53] Thus, GaP is well-suited for

the detailed quantitative photoelectrochemical studies pursued in this dissertation and is used extensively in Chapters II, III and VI.

ii. Carrier Transport/Transfer at Inorganic Semiconductor Heterojunctions

In order to do useful work, photoexcited electrons and holes in a light-harvesting system must be transported to an electrical contact or reaction center to drive a photoelectrochemical reaction or power an external load. Carrier *drift* and *diffusion* are the primary transport mechanisms used to characterize and model the light-harvesting systems studied in this dissertation.

Carrier *drift* refers to the motion of a carrier in response to an electric field. Electric fields within depletion regions at semiconductor interfaces are a defining feature of most solar cell homojunction and heterojunction devices, which are typically comprised of two materials with different Fermi levels that form a built-in potential on the order of 1 V when in contact with one another. Electric fields in these devices effectively 'sweep' electrons to n-type contacts and holes to p-type contacts, preferably before they recombine in the semiconductor. The sensitivity of a charge carrier to a field within a semiconductor can be quantified by defining the carrier mobility, μ, via Equation I.2,

$$\vec{v}_d = \mu\vec{E} \qquad \text{(I.2)}$$

where $\vec{v}_d$ is the drift velocity and $\vec{E}$ is a small applied electric field. Figure I.2 shows a schematic of a generic heterojunction solar cell featuring carrier drift.[54] Large carrier mobilities are generally preferred in light-harvesting systems, as carriers with higher drift velocity can typically more easily be collected before they are lost to deleterious processes. Carrier mobility can range by many orders of magnitude depending on the semiconductor type, purity, doping characteristics and temperature. The effective mobility of doped amorphous Si,[55] for example, may be << 1 $cm^2\ V^{-1}\ s^{-1}$, while the mobility of pristine GaAs[56] may exceed 7000 $cm^2\ V^{-1}\ s^{-1}$.

Typical light-harvesting devices feature strong internal electric fields in the depletion regions that form within the semiconductor adjacent to a contact or junction (Figure I.2). The width of the depletion region within at an abrupt inorganic semiconductor heterojunction is given by Equation I.3,

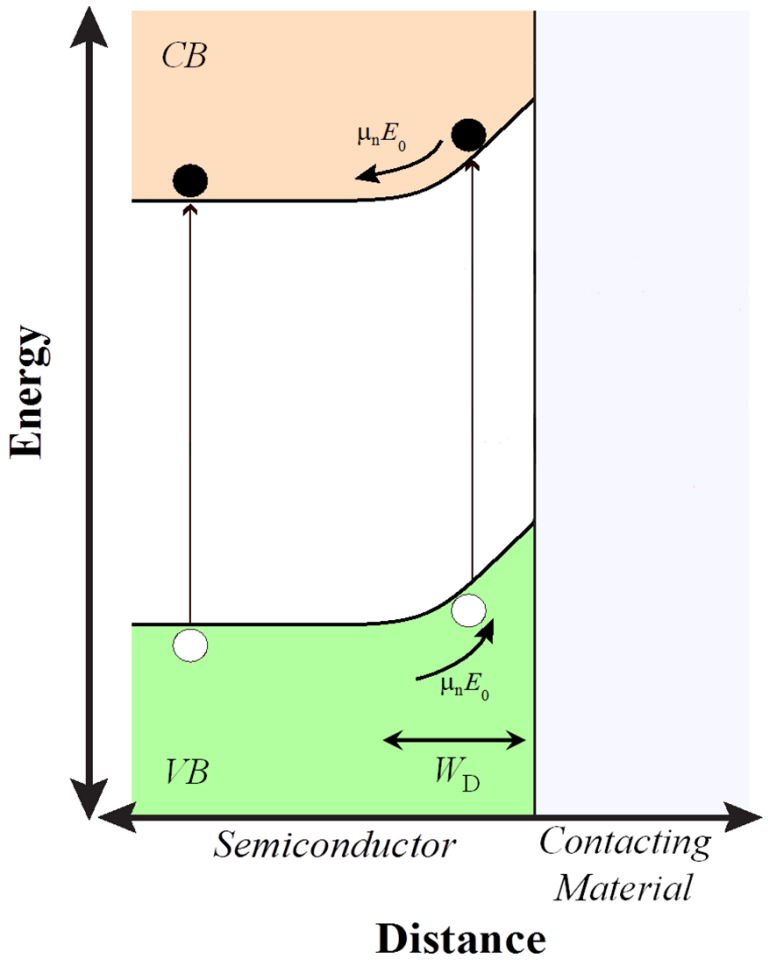

Figure I.2: Band bending diagram for an n-type semiconductor heterojunction device under illumination. Open (closed) circles indicate photoexcited holes (electrons), and *VB* (*CB*) indicates the valence (conduction) band, and W_D indicates the depletion width.

$$W_D = \sqrt{\frac{2\varepsilon_s}{qN}\left(V_{bi} - V - \frac{k_b T}{q}\right)} \qquad \text{(I.3)}$$

where ε_s is the semiconductor permittivity, N is the dopant density, V_{bi} is the built-in voltage and V is the applied potential. The depletion width is a particularly important metric for many nanostructured devices, which typically cannot support efficient carrier collection when their dimensions fall below ~W_D.[57]

Carrier *diffusion* describes the motion of a charge carrier in response to a carrier concentration gradient. Diffusion current densities for electrons and holes are derived from Fick's law,[56]

$$\vec{J}_{n,Diff} = qD_n \nabla n \qquad \text{(I.4a)}$$

$$\vec{J}_{p,Diff} = -qD_p \nabla p \qquad \text{(I.4b)}$$

where D_n and D_p are the diffusion constants for electrons and holes, respectively, n and p are the respective densities of electrons and holes, and positive current densities correspond to holes traveling along the direction of increasing spatial coordinate. The sign of Equations I.4a and I.4b indicate that carriers tend to diffuse away from regions with a higher density of carriers and toward those with a lower carrier density.

A rigorous solution of net carrier transport due to drift and diffusion processes within a semiconductor is achieved by solving the coupled set of Equations I.5 and I.6,

$$\nabla \cdot \varepsilon_s \nabla \phi = -q\left(p - n + N_D - N_A\right) - \rho_{trap} \qquad \text{(I.5)}$$

$$\nabla \cdot \vec{J}_n = qR_{net} + q\frac{\partial n}{\partial t} \qquad \text{(I.6a)}$$

$$-\nabla \cdot \vec{J}_p = qR_{net} + q\frac{\partial p}{\partial t} \qquad \text{(I.6b)}$$

where ϕ is the local electric potential, ε_s is the semiconductor permittivity, q is the unsigned charge of an electron, N_D and N_A are the donor and accepter concentrations, respectively, ρ_{trap} is the charge density associated with traps and fixed charges and R_{net} is the net carrier recombination rate. The current densities $\vec{J}_n$ and $\vec{J}_p$ are given by Equation I.7,[22]

$$\vec{J}_n = q\mu_n n\vec{E} + qD_n \nabla n \qquad \text{(I.7a)}$$

$$\vec{J}_p = q\mu_p p\vec{E} - qD_p \nabla p \qquad \text{(I.7b)}$$

where $\vec{E}$ is the local electric field. The first term in Equation I.7 corresponds to carrier drift, while the second corresponds to carrier diffusion. Equation I.5 represents the Poisson equation, while Equations I.6a and I.6b represent the carrier continuity equations for electrons and holes, respectively. It is possible to solve Equations I.5 and I.6 analytically for simple geometries and boundary conditions, and Chapter III of this dissertation describes the dark exchange current density within a cylindrical semiconductor nanowire device for select limiting scenarios. Chapters III, IV and VI of this dissertation, however, primarily utilize numerical techniques to rigorously solve for carrier transport utilizing the expressions in Equations I.5- I.7.

iii. Carrier Recombination

There are numerous types of deleterious carrier recombination processes that can reduce the energy conversion efficiency of a light-harvesting semiconductor device. The experimental and modeling results presented in this dissertation primarily address or incorporate radiative, Shockley-Read-Hall, and Auger recombination processes, which represent the three most significant loss pathways for the systems reported herein.

Radiative recombination is a process by which an electron in the conduction band recombines with a hole in the valence band to emit a photon. Since each radiative recombination event involves one electron and one hole, the rate density of radiative recombination is proportional to both the electron density and the hole density according to Equation I.8,

$$R_{radiative} = \Gamma_{rad} np \qquad \text{(I.8)}$$

where Γ_{rad} is the radiative recombination constant, equal to 4.73 x 10^{-15} cm^3 s^{-1} for Si[58] and 10^{-13} cm^3 s^{-1} for GaP.[59] Notably, Equation I.8 does not contain any dependencies on defects or non-ionized impurities within the semiconductor. Rather, radiative recombination is inherent to every semiconductor device and cannot be removed by extensive material processing or purification. For this reason, radiative recombination represents a fundamental limitation to the performance of an optimized semiconductor device under low-level injection conditions and forms the basis for Shockley and Queisser's detailed balance limit assessment of the maximum efficiency projected for optimized single-junction devices under one-sun illumination.[41]

Shockley-Read-Hall (SRH) recombination processes occur when carriers recombine at a defect or trap site in a semiconductor. Unlike for the case of radiative recombination, SRH recombination can be mitigated by purifying the semiconductor to minimize the number of traps and increase its SRH lifetime. Because extensive purification of semiconductors can require large additional energy inputs that can translate to higher production costs and an increase in fossil fuel emissions,[26] it is critical that the operational effects of SRH recombination in light-harvesting devices are well-characterized so that materials are only purified to levels required for efficient operation.

The rate for SRH recombination is given by Equation I.9,[60]

$$R_{SRH} = \sigma \, v_{th} N_t \frac{np - n_i^2}{p + n + 2n_i \cosh\left(\frac{E_i - E_t}{k_B T}\right)} \qquad \text{(I.9)}$$

where N_t is the bulk trap density, n_i is the intrinsic carrier density within the semiconductor, E_i is the intrinsic Fermi level, E_t is the trap state energy, and the cosh(x) function is at its minimum for $x = 0$. Equation I.9 assumes that the capture cross section, σ, is equal for both carrier types. The cosh(x) term in Equation I.9 indicates that R_{SRH} reaches a maximum when $E_i = E_t$, i.e. when the trap energy level is equal to the intrinsic Fermi level of the material. Thus, deep-level defects—those that are energetically located near the middle of the band gap—have a much stronger effect on the SRH time constant than shallow defects, which are located just a few times $k_B T/q$ or so from the semiconductor valence or conduction band. For most treatments, therefore, it is sufficient to model SRH recombination as occurring at a single trap energy in the middle of the semiconductor band gap. This approach is adopted in the device simulations featured in Chapters III, IV and VI in this dissertation. Under low-level injection conditions, the characteristic carrier lifetime assuming a single defect located at E_i is given by Equation I.10,[56]

$$\tau_{SRH,n} = \frac{1}{\sigma_n v_{th} N_t} \qquad \text{(I.10a)}$$

$$\tau_{SRH,p} = \frac{1}{\sigma_p v_{th} N_t} \qquad \text{(I.10b)}$$

where σ_n and σ_p are the capture cross-sections for electrons and holes, respectively and v_{th} is the thermal carrier velocity. For a device operated under high-level injection conditions (Chapter IV simulations), the SRH time constant is given by Equation I.11,

$$\tau_{SRH} = \frac{\sigma_n + \sigma_p}{\sigma_n \sigma_p v_{th} N_t} \tag{I.11}$$

If we approximate $\sigma_n \approx \sigma_p = \sigma$, Equation I.11 simplifies to Equation I.12,

$$\tau_{SRH} = \frac{2}{\sigma\, v_{th} N_t} \tag{I.12}$$

indicating that the SRH carrier lifetime for a device operating under high-level injection conditions is double the carrier lifetime for devices operating under low-level injection conditions. SRH recombination has been shown experimentally to depend on dopant density in a manner empirically described[61] by the Scharfetter relation,

$$\tau_{SRH,Eff} = \frac{\tau_{\max}}{\left(\frac{N_A + N_D}{N_{ref}}\right)^{\gamma}} \tag{I.13}$$

where $\tau_{SRH,Eff}$ is the effective SRH time constant, τ_{max} is generally approximated as τ_{SRH} and for Si $N_{ref} = 10^{16}$ cm^{-3} and $\gamma = 1$. Equation I.13 indicates that the effective time constant in a material can decrease dramatically for semiconductors with large dopant densities, which in some cases can affect optimal benchmarks for material purity, etc. Inclusion of the Scharfetter relation was particularly important for the discrete contact nanowire devices simulated in Chapter IV, the operation of which showed marked sensitivity to SRH recombination processes.

Auger recombination describes a variety of three-carrier processes in which two carriers recombine and transfer energy to a third carrier, which may partially or wholly dissipate the energy via rapid thermalization. The Auger recombination rate is given by Equation I.14,

$$R_{Auger} = \left(C_n n + C_p p\right)\left(np - n_i^2\right) \tag{I.14}$$

where C_n and C_p are the temperature-dependent Auger coefficients[62]

$$C_n = \left(A_n + B_n \frac{T}{T_0} + M_n \left(\frac{T}{T_0}\right)^2\right)\left(1 + H_n e^{\frac{-n}{N_{0,n}}}\right) \tag{I.15a}$$

$$C_p = \left(A_p + B_p \frac{T}{T_0} + M_p \left(\frac{T}{T_0} \right)^2 \right) \left(1 + H_p e^{\frac{-p}{N_{0,p}}} \right) \qquad \text{(I.15b)}$$

Here A_x, B_x, M_x and H_x are fit parameters, T_0 is the baseline temperature, $N_{0,x}$ is the characteristic carrier density and Equation I.15 was applied explicitly to Si devices. As a three-carrier process, Auger recombination scales as the cube of the carrier density and typically outpaces radiative recombination as the limiting recombination process for devices operating under high-level injection conditions such as those simulated in Chapter IV. The exponential factor in Equations I.15a-b accounts for the sensitivity of Auger recombination to carrier injection levels and is required to accurately incorporate Auger effects under the concentrated illumination conditions simulated in Chapter IV.

In addition to the recombination processes listed above, which can occur throughout a semiconductor, another set of recombination processes occur specifically at semiconductor surfaces/interfaces. Deleterious loss of carriers at the semiconductor surface can occur through a variety of processes that include the recombination of a carrier in the semiconductor with a chromophore or other moiety adsorbed to the semiconductor surface, participation of a surface carrier with reduction or oxidation reactions in a photoelectrochemical system, tunneling of a carrier from the semiconductor into a contact or other interface, etc. Various combinations of these processes are considered throughout this dissertation, particularly in Chapter IV and Chapter VI, which detail modeling and experimental efforts in which such factors can play a sizeable role. For the most part, however, surface recombination is approximated throughout this work specifically as SRH recombination processes occurring within one lattice spacing of the semiconductor surface. In the modeling results contained in Chapters III, IV and VI, the lattice spacing is approximated as 5 Å and SRH time constants and/or defect densities can be set independently of bulk values within a thin surface layer which is otherwise identical to the semiconductor bulk. Surface recombination velocity is calculated according to Equation I.16,

$$S = \frac{t}{\tau_{SRH,s}} \qquad \text{(I.16)}$$

where t is the thickness of the semiconductor surface layer (5 Å) and $\tau_{SRH,s}$ is the SRH time constant at the surface.

The net carrier lifetime from all recombination processes can be coupled with the ability of a carrier to move within a semiconductor (mobility) to yield a powerful metric called the carrier diffusion length,

$$L_n = \sqrt{\frac{k_B T}{q} \mu_n \tau_{net,n}} \quad \text{(I.17a)}$$

$$L_p = \sqrt{\frac{k_B T}{q} \mu_p \tau_{net,p}} \quad \text{(I.17b)}$$

Equations I.17a-b represent the characteristic distance that an electron or hole travels in a semiconductor before recombining. In other words, the probability that a carrier will recombine after diffusing a distance *d* within a planar semiconductor operating under purely diffusive conditions is given by

$$P = 1 - e^{-\frac{d}{L}} \quad \text{(I.18)}$$

The likelihood of carrier loss due to recombination therefore becomes significant for carriers generated distances of ~*L* or greater from a collection or reaction site.

High semiconductor aspect ratios offer a key advantage in overcoming poor bulk optoelectronic properties (i.e. short carrier diffusion lengths) by decoupling processes of light absorption and carrier collection in a device.[57,63-66] Figure I.3 illustrates the potentially dramatic decrease in minority carrier collection length (the distance between where a minority carrier is photogenerated and the contact where it is collected) afforded by the lateral collection of minority carriers in an n-type device featuring a nanowire architecture. In practice, decreased carrier collection lengths can translate to improved performance of materials which would otherwise be unsuitable for light-harvesting applications.[28]

D. Content Description

The focus of this dissertation is to provide a quantitative framework for the further development of select solar energy conversion systems by describing fundamental

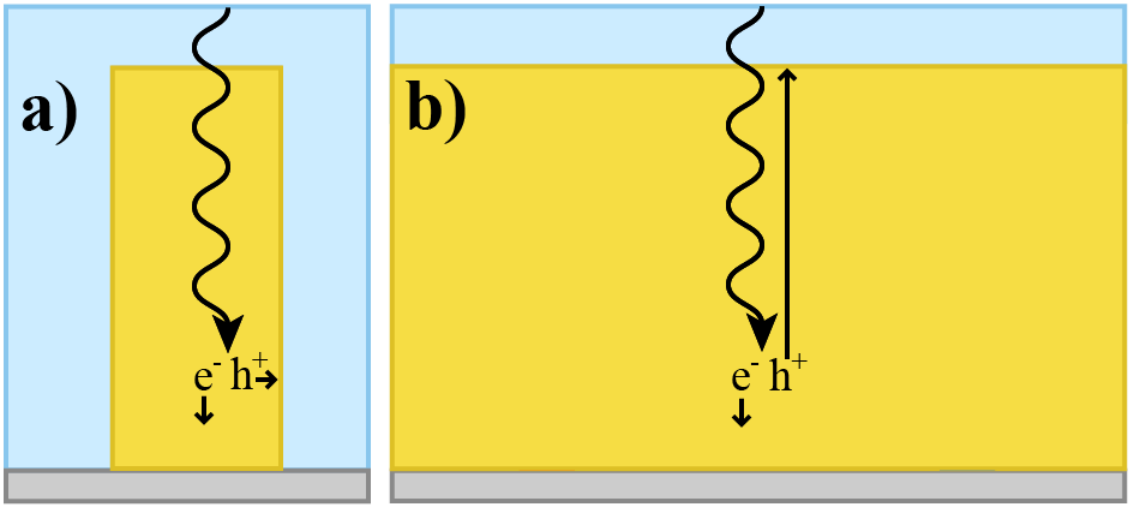

Figure I.3: Cross-section schematic of transport processes within an n-type (a) nanowire or (b) planar solar cell device. Majority carriers (electrons) are collected at the back contact (yellow/gray interface) and minority carriers (holes) are collected at the front contact (yellow/light blue interface). The minority carrier collection length can be dramatically decreased in nanowire devices. Not drawn to scale.

aspects and implications of charge transport/transfer within systems operating under steady-state conditions. Numerous reports detail the efficient operation of devices featuring high-aspect-ratio semiconductor surface morphologies,[67,68] polymer/inorganic semiconductor heterojunction devices,[69,70] or dye-sensitized solar cells.[42,71] However, the development of specific, quantitative design criteria for such systems has lagged behind and the successes realized by earlier devices has often been elusive in subsequent designs that feature updated materials, polarity (i.e. n-type versus p-type), and fabrication techniques. The five technical chapters in this dissertation (each of which resulted in a first-author publication) aim to provide useful guidelines for the design and optimization of various single-crystalline inorganic semiconductor systems arranged in single-junction configurations.

In the first technical chapter of this dissertation (Chapter II), n-type GaP photoelectrodes were anodically etched to create uniformly macroporous surface structures of varying depth. The performance of these electrodes under illumination was investigated experimentally in a nonaqueous, regenerative photoelectrochemical cell. Unetched (planar) electrodes featured low photocurrent densities and small energy conversion efficiencies, due primarily to the relatively poor optoelectronic properties of the GaP wafers used as a starting material. The minority carrier diffusion length in the electrode was shorter than the optical penetration depth in GaP for most of the solar spectrum, resulting in large bulk recombination losses that were modeled analytically using the so-called Gärtner equation. By utilizing high-aspect-ratio macroporous photoelectrodes, however, the processes of light absorption and carrier collection were effectively decoupled and carriers could be extracted from the material only a short distance from their photogeneration site. This resulted in a dramatic decrease in bulk recombination processes and a corresponding order of magnitude increase in photocurrent densities and energy conversion efficiency versus planar electrodes.[63]

Chapter III of this dissertation investigates the impacts on performance of commonly encountered experimental conditions for nanowire devices, including incomplete nanowire doping, tapering of nanowires, a broad range of both bulk time constant and mobility within the semiconductor, etc. The finite-element software package TCAD Sentaurus (Synopsys) was used to develop a detailed, quantitative understanding

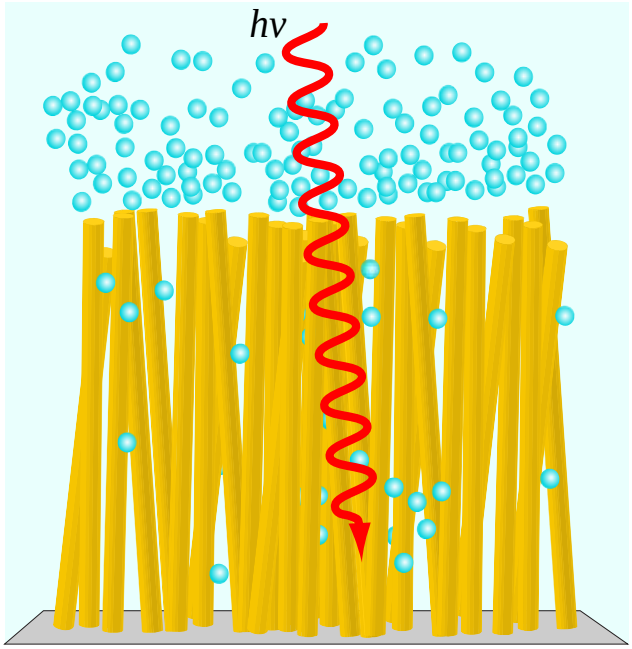

Figure I.4: Schematic of a nanowire film photoelectrode forming H_2 fuel via water splitting. Chapter III modeled a single-nanowire device with surface boundary conditions specified to replicate those of a photoelectrode in solution. The gray slab represents the back contact for majority carrier collection.

of charge transport and recombination properties subject to these features in single-nanowire Si or GaP photoelectrodes under illumination (Figure I.4). The coupled Poisson and hole and electron continuity equations (Equations I.5-I.7) were solved subject to specified physical processes and detailed optoelectronic parameters for both Si and GaP. Charge transport and recombination processes were then presented analytically in form of current densities for various limiting scenarios to explicitly describe how design features such as nanowire radius, dopant density, bulk time constant, surface recombination, nanowire tapering, and nonuniform doping affected device performance. Nanowire device operation was found to be sensitive to a variety of design features, but the primary constraint was that the radius of the nanowire had to exceed a particular 'cutoff' value determined by the width of material (W_D) necessary to support a full depletion region at the semiconductor dopant density. This chapter also introduced a novel discrete contact nanowire design, the operating principles of which did not require significant depletion regions within devices. Preliminary results indicated that this device scheme led to enhanced performance for nanowires with radii that fell short of the cutoff value identified above.[64]

Chapter IV includes a more rigorous investigation (also using the TCAD Sentaurus software suite) of the discrete contact nanowire devices introduced in Chapter III. Specifically, discrete contact nanowires were assessed for their capacity to (1) outperform analogous nanowire devices (Figure I.5a) featuring rectifying contacts and (2) relax the stringent material purity requirements typical for planar discrete contact devices (Figure I.5b). Planar solar cells featuring discrete, ohmic-selective contacts can achieve large energy conversion efficiencies but are particularly vulnerable to the short carrier lifetimes and diffusion lengths that accompany all but the most highly-processed semiconductors.[72] Nanowire architectures such as the one shown in Figure I.5a can decrease carrier collection lengths to more efficiently collect carriers, but generally only exhibit sizeable photocurrent densities and open-circuit photovoltages if the nanowire dopant density and radius (r) fall within a narrow window defined by the barrier height and dielectric properties of the semiconductor (Equation I.3).[57,64] This restriction is problematic for many semiconductors, as it is notoriously difficult to control both the n-type and p-type dopant density of a material.[73-79] Although planar discrete contact

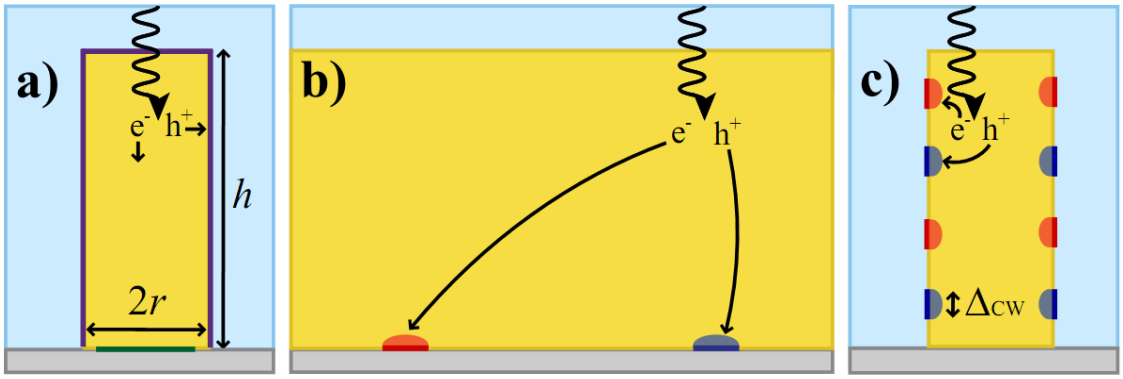

Figure I.5: Partial cross-section schematics for (a) a typical heterojunction nanowire solar cell, (b) a planar discrete contact solar cell, and (c) a nanowire discrete contact solar cell. N-type (p-type) contacts are shown in red (dark blue). Not drawn to scale.

devices could seemingly benefit from the shorter carrier collection lengths inherent to nanowire structures and nanowire devices could benefit from the minimal doping requirements of point-contact devices, an analysis of discrete contact devices featuring semiconductor nanowires as compared to planar structures had not been previously reported. The results presented in Chapter IV indicate that discrete contact nanowire designs (Figure I.5c) can relax material purity requirements by up to three orders of magnitude as compared to planar discrete-contact devices and exhibit ≥ 80% larger open-circuit potentials as compared to nanowire Schottky contact devices for a broad range of dopant densities and radii. Such large V_{oc} values are atypical for nanowire devices,[27,80-84] which generally feature large dark exchange current densities due to their high surface areas. The small contact areas, concentrated illumination conditions and low deleterious recombination rates in the discrete contact nanowire devices investigated in Chapter IV were all found to contribute to the substantial carrier population densities that sustained these large V_{oc} values.[85]

Chapter V reports on an experimental investigation of the magnitude and operational implications of the majority carrier collection velocity in heterojunctions between n-Si and the conductive polymer PEDOT:PSS. Carrier collection and recombination processes can be strongly impacted by the rate at which carriers in a semiconductor approach a device contact. In Chapter V, two sets of silicon heterojunctions with either Au or PEDOT:PSS contacts were prepared and values of interfacial majority carrier charge transfer were determined for both devices by fitting temperature-dependent current density-voltage curves and spectral response measurements to analytical models. Steady-state current density-voltage responses under illumination indicated that the open-circuit voltage of n-Si/PEDOT:PSS devices tracked bulk-recombination-limited values, while n-Si/Au devices featured significantly smaller open-circuit voltages. The cumulative data suggested that the velocity of majority carrier charge transfer, v_n, was several orders of magnitude smaller at n-Si/PEDOT:PSS contacts than at n-Si/Au junctions, resulting in superior photoresponse characteristics at short wavelengths for these inorganic semiconductor/polymer heterojunctions as compared to the n-Si/Au devices.[54]

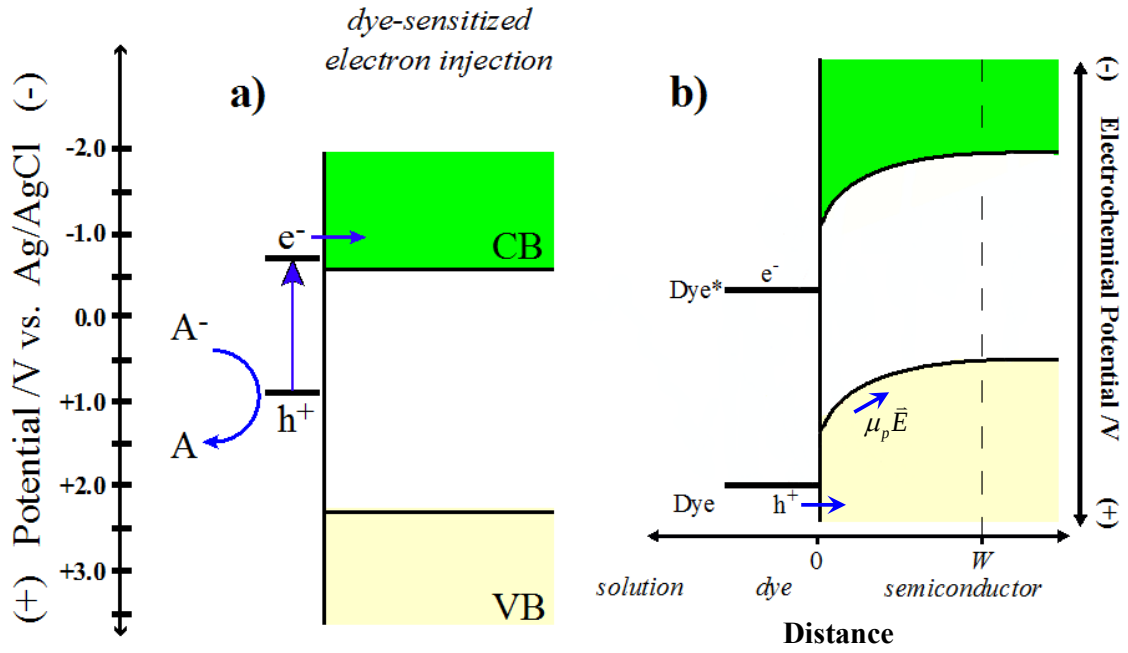

Figure I.6: Depiction of dye sensitization at semiconductor photoelectrodes. (a) Dye-sensitized electron injection from a photoexcited chromophore at the surface of a metal oxide semiconductor. (b) Dye-sensitized hole injection from a photoexcited chromophore at the surface of a phosphide semiconductor under depletion conditions. Holes are swept away from the interface at a velocity $\mu_p\vec{E}$.

Chapter VI investigates charge injection, transport and collection processes in planar dye-sensitized p-type GaP photoelectrodes. To date, an overwhelming majority of dye-sensitized solar cell (DSSC) research has focused on systems that utilize an inorganic semiconductor photoelectrode made from nanoparticles too small to support internal electric fields at the electrode/solution interface (Figures I.6a-b). Although the ubiquitous Grätzel DSSC features favorable charge-transfer kinetics that facilitate efficient carrier collection despite the absence of strong electric fields, the development of alternative systems – particularly dye-sensitized photocathodes – that operate in an analogous manner has been difficult. Chapter VI focuses on characterizing the effects of carrier drift in a p-GaP dye-sensitized system that had not been kinetically optimized. The electrochemical system investigated in this chapter featured a photoelectrode with a ~ 8.5 x 10^5 V cm^{-1} internal electric field immersed in an aqueous electrolyte containing one of six triphenylmethane dyes (rose bengal, rhodamine B, crystal violet, ethyl violet, fast green fcf, or brilliant green). At high concentrations of dissolved dye, the measured steady-state photocurrent-potential responses collected at sub-bandgap wavelengths suggested unexpectedly high (>0.1) net internal quantum yields for sensitized hole injection. Finite-difference simulations of the experimental system indicated that these high internal quantum yield values were most likely afforded by the internal electric field present within p-GaP, which effectively swept injected holes away from the interface and minimized their participation in deleterious pathways (Figure I.6c). The cumulative experimental and modeling data provide insight on design strategies for assembling new types of dye-sensitized photocathodes that operate under depletion conditions.[85]

E. References

1 Lee, C.-C. Energy Consumption and GDP in Developing Countries: A Cointegrated Panel Analysis. *Energy Economics* **27**, 415-427 (2005).

2 Martínez, D. M. & Ebenhack, B. W. Understanding the Role of Energy Consumption in Human Development Through the Use of Saturation Phenomena. *Energy Policy* **36**, 1430-1435 (2008).

3 Bailis, R., Ezzati, M. & Kammen, D. M. Mortality and Greenhouse Gas Impacts of Biomass and Petroleum Energy Futures in Africa. *Science* **308**, 98-103 (2005).

4 Legros, G., Havnet, I., Bruce, N. & Bonjour, S. The Energy Access Situation in Developing Countries: A Report Focusing on the Least Developed Countries and

Sub-Saharan Africa. (United Nations Development Programme, New York, NY, 2009).
5 Dinkelman, T. The Effects of Rural Electrification on Employment: New Evidence from South Africa. *American Economic Review* **101**, 3078-3108 (2011).
6 *Human Development Index (HDI)*, <http://hdr.undp.org/en/statistics/hdi/> (2011).
7 Arsenault, R. The End of the Long Hot Summer: The Air Conditioner and Southern Culture. *The Journal of Southern History* **50**, 597-628 (1984).
8 International Energy Outlook 2011. Report No. DOE-EIA-0484(2011), (United States Energy Information Administration, Washington, DC, 2011).
9 Boden, T. A., Marland, G. & Andres, R. J. Global, Regional, and National Fossil-Fuel CO_2 Emissions. (Carbon Dioxide Information Analysis Center, Oak Ridge National Laboratory, Oak Ridge, Tenn., U.S.A., 2010).
10 Jones, P. D., New, M., Parker, D. E., Martin, S. & Rigor, I. G. Surface Air Temperature and its Changes Over the Past 150 Years. *Reviews of Geophysics* **37**, 173-199 (1999).
11 Doney, S. C., Fabry, V. J., Feely, R. A. & Kleypas, J. A. in *Annual Review of Marine Science* Vol. 1 169-192 (2009).
12 Hoegh-Guldberg, O. *et al.* Coral Reefs Under Rapid Climate Change and Ocean Acidification. *Science* **318**, 1737-1742 (2007).
13 Orr, J. C. *et al.* Anthropogenic Ocean Acidification Over the Twenty-First Century and its Impact on Calcifying Organisms. *Nature* **437**, 681-686 (2005).
14 Forster, P. *et al.* in *Climate Change 2007: The Physical Science Basis* (eds S. Solomon *et al.*) Ch. 2, (Cambridge University Press, 2007).
15 Crowley, T. J. Causes of Climate Change Over the Past 1000 Years. *Science* **289**, 270-277 (2000).
16 Schwartz, J. Air Pollution and Daily Mortality: A Review and Meta Analysis. *Environmental Research* **64**, 36-52 (1994).
17 Sustainability and Equity: A Better Future for All. (United Nations Development Programme, New York, NY, 2011).
18 Rice, C. in *Goff Smith Lecture at the University of Michigan* (30 March 2011).
19 Lewis, N. S. Powering the Planet. *MRS Bulletin* **32**, 808-820 (2007).
20 Electric Power Monthly April 2012: With Data for February 2012. Report No. DOE/EIA-0226, (United States Energy Information Administration, Office of Electricity, Renewables & Uranium Statistics, Washington, DC, 2012).
21 Lewis, N. S. & Nocera, D. G. Powering the Planet: Chemical Challenges in Solar Energy Utilization. *Proceedings of the National Academy of Sciences of the United States of America* **103**, 15729-15735 (2006).
22 Fonash, S. *Solar Cell Device Physics*. (Academic Press, 1982).
23 Green, M. A., Emery, K., Hishikawa, Y., Warta, W. & Dunlop, E. D. Solar Cell Efficiency Tables (Version 39). *Progress in Photovoltaics* **20**, 12-20 (2012).
24 Winter, M. *Abundance in Earth's Crust: Periodicity*, <http://www.webelements.com/periodicity/abundance_crust/> (2012).
25 Fthenakis, V., Wang, W. & Kim, H. C. Life Cycle Inventory Analysis of the Production of Metals Used in Photovoltaics. *Renewable and Sustainable Energy Reviews* **13**, 493-517 (2009).

26 Jungbluth, N. Life Cycle Assessment of Crystalline Photovoltaics in the Swiss Ecoinvent Database. *Progress in Photovoltaics* **13**, 429-446 (2005).
27 Garnett, E. & Yang, P. D. Light Trapping in Silicon Nanowire Solar Cells. *Nano Letters* **10**, 1082-1087 (2010).
28 Hochbaum, A. I. & Yang, P. D. Semiconductor Nanowires for Energy Conversion. *Chemical Reviews* **110**, 527-546 (2010).
29 Zhu, J. *et al.* Optical Absorption Enhancement in Amorphous Silicon Nanowire and Nanocone Arrays. *Nano Letters* **9**, 279-282 (2009).
30 Carim, A. I., Collins, S. M., Foley, J. M. & Maldonado, S. Benchtop Electrochemical Liquid–Liquid–Solid Growth of Nanostructured Crystalline Germanium. *Journal of the American Chemical Society* **133**, 13292-13295 (2011).
31 Fan, H. J., Werner, P. & Zacharias, M. Semiconductor Nanowires: From Self-Organization to Patterned Growth. *Small* **2**, 700-717 (2006).
32 Mozetič, M., Cvelbar, U., Sunkara, M. K. & Vaddiraju, S. A Method for the Rapid Synthesis of Large Quantities of Metal Oxide Nanowires at Low Temperatures. *Advanced Materials* **17**, 2138-2142 (2005).
33 Stein, J. S., Hansen, C. W. & Reno, M. J. The Variability Index: A New and Novel Metric for Quantifying Irradiance and PV Output Variability. (Sandia National Laboratories, 2012).
34 Hund, T. D. G., S.; Barrett, K. Grid-Tied PV System Energy Smoothing. (Sandia National Laboratories, 2010).
35 Coddington, M. *et al.* Updating Interconnection Screens for PV System Integration. (National Renewable Energy Laboratory, Oak Ridge, TN, 2012).
36 Parkinson, B. A. On the Efficiency and Stability of Photoelectrochemical Devices. *Accounts of Chemical Research* **17**, 431-437 (1984).
37 Gerischer, H. Electrochemical Photo and Solar Cells: Principles and Some Experiments. *Journal of Electroanalytical Chemistry and Interfacial Chemistry* **58**, 263-274 (1975).
38 Bard, A. J. Photoelectrochemistry and Solar Energy: Progress, Promise and Problems. *Journal of Electroanalytical Chemistry* **168**, 5-20 (1984).
39 Archer, M. D. Electrochemical Aspects of Solar Energy Conversion. *Journal of Applied Electrochemistry* **5**, 17-38 (1975).
40 Barton, J. P. & Infield, D. G. Energy Storage and its Use with Intermittent Renewable Energy. *IEEE Transactions on Energy Conversion* **19**, 441-448 (2004).
41 Shockley, W. & Queisser, H. J. Detailed Balance Limit of Efficiency of p-n Junction Solar Cells. *Journal of Applied Physics* **32**, 510-519 (1961).
42 Yella, A. *et al.* Porphyrin-Sensitized Solar Cells with Cobalt (II/III)–Based Redox Electrolyte Exceed 12 Percent Efficiency. *Science* **334**, 629-634 (2011).
43 Rosenbluth, M. L., Lieber, C. M. & Lewis, N. S. 630 mV Open Circuit Voltage, 12-Percent Efficient n-Si Liquid Junctions. *Appl Phys Lett* **45**, 423-425 (1984).
44 Gronet, C. M. & Lewis, N. S. Design of a 13% Efficient n-$GaAs_{1-x}P_x$ Semiconductor-Liquid Junction Solar Cell. *Nature* **300**, 733-735 (1982).
45 Kohl, P. A. & Bard, A. J. Semiconductor Electrodes. 1 3. Characterization and Behavior of n-Type ZnO, CdS, and GaP Electrodes in Acetonitrile Solutions. *Journal of the American Chemical Society* **99**, 7531-7539 (1977).

46 Sulima, O. V. *et al.* in *3rd World Conference on Photovoltaic Energy Conversion.* 737-740 (IEEE).
47 Werner, J. H., Kolodinski, S. & Quiesser, H. J. Novel Optimization Principles and Efficiency Limits for Semiconductor Solar Cells. *Physical Review Letters* **72**, 3851-3854 (1994).
48 Dare-Edwards, M. P., Hammett, A. & Goodenough, J. B. The Efficiency of Photogeneration of Hydrogen at p-Type III/V Semiconductors. *Journal of Electroanalytical Chemistry* **119**, 109-123 (1981).
49 Finklea, H. O. *Semiconductor Electrodes*. (Elsevier, 1984).
50 Halmann, M. Photoelectrochemical Reduction of Aqueous Carbon Dioxide on p-Type Gallium Phosphide in Liquid Junction Solar Cells. *Nature* **275**, 115-116 (1978).
51 McCann, J. F. & Handley, L. J. The Photoelectrochemical Effect at a p-GaP Electrode. *Nature* **283**, 843-845 (1980).
52 Petit, J. P., Chartier, P., Beley, M. & Deville, J. P. Molecular Catalysis in Photoelectrochemical Cells: Study of an Efficient System for the Selective Photoelectroreduction of CO_2 : p-GaP of p-GaAs / $Ni(cyclam)^{2+}$, Aqueous Medium. *Journal of Electroanalytical Chemistry* **269**, 267-281 (1989).
53 White, T., Carter, M. A., Mottram, A., Peaker, A. R. & Sudlow, P. D. Monolithig Light Emitting Diode Arrays using Gallium Phosphide. *Nature* **232**, 469-470 (1971).
54 Price, M. J., Foley, J. M., May, R. A. & Maldonado, S. Comparison of Majority Carrier Charge Transfer Velocities at Si/polymer and Si/metal Photovoltaic Heterojunctions. *Appl Phys Lett* **97**, 083503-083503 (2010).
55 Mattheis, J., Werner, J. H. & Rau, U. Finite Mobility Effects on the Radiative Efficiency Limit of pn-Junction Solar Cells. *Physical Review B* **77** (2008).
56 Sze, S. M. & Ng, K. K. *Physics of Semiconductor Devices*. 3 edn, (Wiley-Interscience, 2007).
57 Hagedorn, K., Forgacs, C., Collins, S. & Maldonado, S. Design Considerations for Nanowire Heterojunctions in Solar Energy Conversion/Storage Applications. *Journal of Physical Chemistry C* **114**, 12010-12017 (2010).
58 Trupke, T. *et al.* Temperature Dependence of the Radiative Recombination Coefficient of Intrinsic Crystalline Silicon. *Journal of Applied Physics* **94**, 4930-4937 (2003).
59 Yunovich, A. E. in *Radiative Recombination in Semiconductors* (ed E. Ya) (Pokravskii, 1972).
60 Galup-Montoro, C. & Schneider, M. C. *MOSFET Modeling for Circuit Analysis and Design*. (World Scientific, 2007).
61 Palankovsky, V. Q., Rudiger. *Analysis and Simulation of Heterostructure Devices*. (Springer-Verlag/Wien, 2004).
62 TCAD Sentaurus (Synopsys Incorporated, 2010).
63 Price, M. J. & Maldonado, S. Macroporous n-GaP in Nonaqueous Regenerative Photoelectrochemical Cells. *The Journal of Physical Chemistry C* **113**, 11988-11994 (2009).

64 Foley, J. M., Price, M. J., Feldblyum, J. I. & Maldonado, S. Analysis of the Operation of Thin Nanowire Photoelectrodes for Solar Energy Conversion. *Energy & Environmental Science* **5**, 5203-5220 (2012).

65 Kayes, B. M., Atwater, H. A. & Lewis, N. S. Comparison of the Device Physics Principles of Planar and Radial p-n Junction Nanorod Solar Cells. *Journal of Applied Physics* **97** (2005).

66 Wen, W. *et al.* Structural and Photoelectrochemical Properties of GaP Nanowires Annealed in NH_3. *Journal of Physical Chemistry C* **115**, 22652-22661 (2011).

67 Kelzenberg, M. D. *et al.* High-Performance Si Microwire Photovoltaics. *Energy & Environmental Science* **4**, 866-871 (2011).

68 Peng, K. Q., Wang, X., Wu, X. L. & Lee, S. T. Platinum Nanoparticle Decorated Silicon Nanowires for Efficient Solar Energy Conversion. *Nano Letters* **9**, 3704-3709 (2009).

69 Zhang, F. T., Sun, B. Q., Song, T., Zhu, X. L. & Lee, S. Air Stable, Efficient Hybrid Photovoltaic Devices Based on Poly(3-hexylthiophene) and Silicon Nanostructures. *Chem. Mat.* **23**, 2084-2090 (2011).

70 Ackermann, J., Videlot, C., El Kassmi, A., Guglielmetti, R. & Fages, F. Highly Efficient Hybrid Solar Cells Based on an Octithiophene-GaAs Heterojunction. *Adv. Funct. Mater.* **15**, 810-817 (2005).

71 O'Regan, B. & Gratzel, M. A Low-Cost, High-Efficiency Solar Cell Based on Dye-Sensitized Colloidal TiO_2 Films. *Nature* **353**, 737-740 (1991).

72 Sinton, R. A. & Swanson, R. M. Design Criteria for Si Point-Contact Concentrator Solar Cells. *IEEE Transactions on Electron Devices* **34**, 2116-2123 (1987).

73 Erwin, S. C. *et al.* Doping Semiconductor Nanocrystals. *Nature* **436**, 91-94 (2005).

74 Norris, D. J., Efros, A. L. & Erwin, S. C. Doped Nanocrystals. *Science* **319**, 1776-1779 (2008).

75 Takenaka, K., Imanaka, Y., Tamasaku, K., Ito, T. & Uchida, S. Anisotropic Optical Spectrum of Untwinned $PrBa_2Cu_3O_7$ - Persistence of the Charte-Transfer Insulating State of the CuO_2 Plane Against Hole Doping. *Physical Review B* **46**, 5833-5836 (1992).

76 Laks, D. B., Vandewalle, C. G., Neumark, G. F., Blochl, P. E. & Pantelides, S. T. Native Defects and Self-Compensation in ZnSe. *Physical Review B* **45**, 10965-10978 (1992).

77 Di Paola, A. *et al.* Preparation of Polycrystalline TiO_2 Photocatalysts Impregnated with Various Transition Metal Ions: Characterization and Photocatalytic Activity for the Degradation of 4-Nitrophenol. *The Journal of Physical Chemistry B* **106**, 637-645 (2001).

78 Persson, C., Zhao, Y.-J., Lany, S. & Zunger, A. N-Type Doping of $CuInSe_2$ and $CuGaSe_2$. *Physical Review B* **72**, 035211 (2005).

79 Wei, S. H. Overcoming the Doping Bottleneck in Semiconductors. *Computational Materials Science* **30**, 337-348 (2004).

80 Tian, B., Kempa, T. J. & Lieber, C. M. Single Nanowire Photovoltaics. *Chemical Society Reviews* **38**, 16-24 (2009).

81 Garnett, E. C. & Yang, P. Silicon Nanowire Radial p-n Junction Solar Cells. *Journal of the American Chemical Society* **130**, 9224-9225 (2008).
82 Tsakalakos, L. *et al.* Silicon Nanowire Solar Cells. *Appl Phys Lett* **91**, 233117 (2007).
83 Kempa, T. J. *et al.* Single and Tandem Axial p-i-n Nanowire Photovoltaic Devices. *Nano Letters* **8**, 3456-3460 (2008).
84 Stelzner, T. *et al.* Silicon Nanowire-Based Solar Cells. *Nanotechnology* **19**, 295203 (2008).
85 Chitambar, M., Wang, Z., Liu, Y., Rockett, A. & Maldonado, S. Dye-Sensitized Photocathodes: Efficient Light-Stimulated Hole Injection into p-GaP Under Depletion Conditions. *Journal of the American Chemical Society*, 10670-10681 (2012).

CHAPTER II

Macroporous n-GaP in Nonaqueous, Regenerative Photoelectrochemical Cells

A. Introduction

This chapter reports the photoresponse characteristics of macroporous n-GaP electrodes in a nonaqueous, regenerative photoelectrochemical cell. Specifically, the effects of macroporous surface architectures in the efficient collection of carriers photogenerated in GaP electrodes featuring a short minority carrier diffusion length are investigated. These results thus provide insight on the design of high-performance photoelectrochemical energy conversion/storage systems.

Photoelectrochemical solar energy conversion systems are garnering increased consideration as a viable pathway for commercial light-harvesting systems, due not in a small part to the continued success of electrochemical dye-sensitized solar cells. The intrinsic suitability of electrochemical systems to be directly coupled to and drive fuel-forming redox reactions makes the characterization of relevant charge separation and transport in such systems of particular importance for furthering the prospects of renewable chemical fuel generation.[1-4] The macroporous n-GaP system reported here is highly germane to addressing these concerns for several reasons. First, as will be discussed in detail below, the carrier collection properties of this system couple strongly with semiconductor morphology to dramatically affect performance, making the system a suitable platform for elucidating the mechanisms relevant to the operation of such systems. Second, GaP possesses a sufficiently large band gap (2.26 eV) to support a cell emf greater than 1 V under solar illumination,[5-7] making it a suitable electrode material for driving the kinetically slow, multi-electron charge transfer reactions necessary for most chemical fuel generation.[3,8] Unlike larger band gap materials such as TiO_2, however, GaP is still capable of absorbing a meaningful fraction of the solar spectrum (λ < 550 nm). Third, the Schockley-Quiesser limit for solar energy conversion efficiency at

a single optimized GaP heterojunction under 1.5 AMU solar irradiation is 20%.[9] Additionally, GaP has long been recognized as a potentially useful electrode material for photoelectrochemical energy conversion due to its demonstrated photoactivity and ability to drive hydrogen and carbon dioxide reduction reactions.[10-14] From a practical perspective, GaP is also a technologically mature material commonly used in light emitting diodes and well-defined protocol exist for doping, contacting, and depositing processes.[15]

A key disadvantage to using GaP as a photoelectrode material in planar heterojunctions is its short carrier diffusion length relative to the depth of visible light absorption. The optical absorptivity, α, of light with energies near E_g is small due to the indirect band gap of GaP, with λ = 540 nm light having an average absorption depth of 28 μm (α^{-1}) as shown in Figure II.1.[16] The minority carrier diffusion lengths, L, however, are only[17] 1-10 μm in the highest quality epitaxial GaP films and 10-100 nm in single-crystalline wafers.[18,19] Thus, most carriers generated more than L from the GaP surface recombine before they can be collected as useful current, severely limiting the ability of GaP photoelectrodes to capture and convert visible light to usable energy (see Figure II.2).

One method of decoupling the path length of photogenerated minority carriers from the optical penetration depth of a material is to utilize high-aspect-ratio electrode morphologies.[18,20-26] Numerical models suggest that such techniques can result in sizeable efficiencies from crystalline semiconductors with poor light absorption and minority carrier collection properties (Figure II.2).[27] This principle has not been rigorously explored with GaP photoelectrodes, however, and few reports indicate the absolute performance enhancements in relevant GaP-based photovoltaic and photoelectrochemical systems. For example, Vanmaekelbergh et. al. previously demonstrated enhanced photocurrents using macroporous n-GaP, but large applied biases and strongly acidic and alkaline solutions were employed in those investigations.[18,28,29] Corrosion and interface instability are serious impediments to the analysis of GaP in aqueous photoelectrochemical systems under intense white light illumination[30] and thus prevent direct quantitative assessment of the solar energy conversion properties of n-GaP

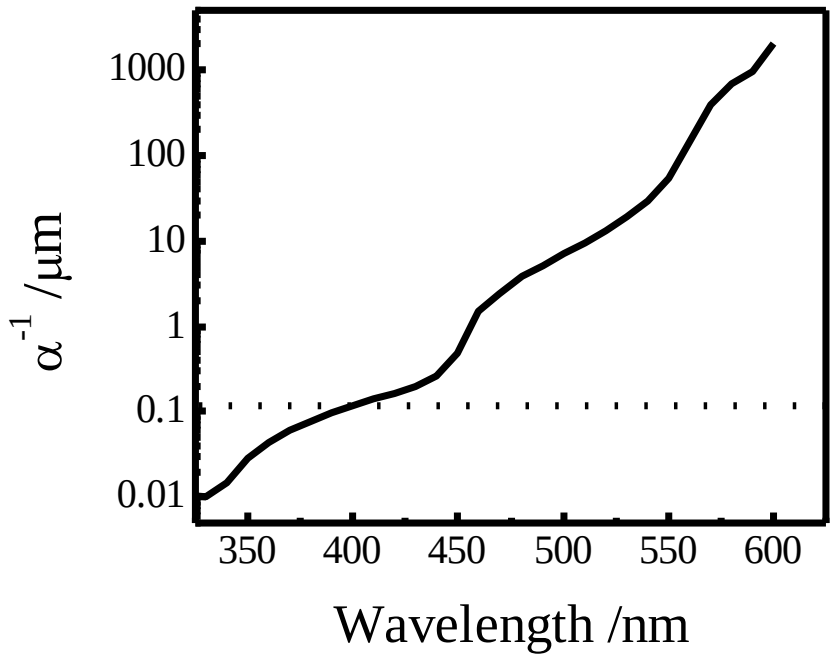

Figure II.1: Penetration depth of visible light in GaP. Dotted line indicates the typical minority carrier diffusion length for commercially available GaP wafers.

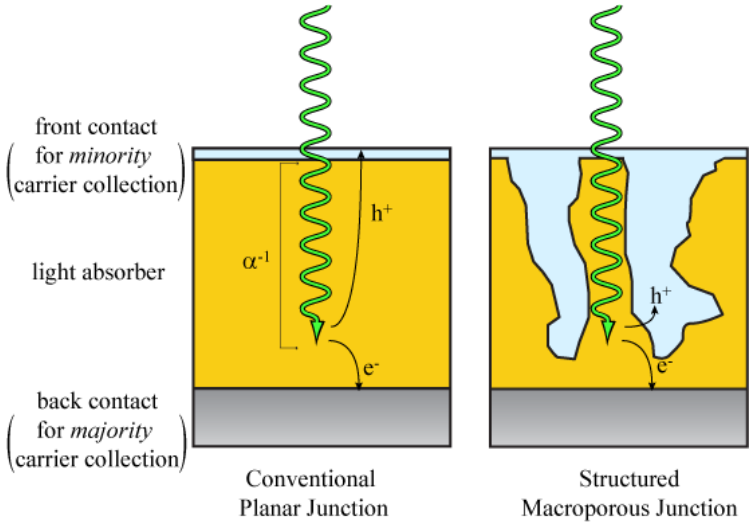

Figure II.2: Schematic of photoexcited charge carrier generation and collection for (left) planar and (right) macroporous electrodes.

photoanodes in water. Thus, several questions regarding the viability of high surface area GaP photoelectrodes remain, including what sort of material length scales are necessary to effect optimal photoresponse enhancements and whether deleterious recombination at high surface area GaP and/or mass transport through deep macropores would severely distort photoresponses.

In order to assess the operational features of GaP photoelectrodes with high-aspect-ratio surface morphologies without ambiguity from corrosion or other undefined chemical processes, the photoelectrochemical responses of planar and macroporous n-GaP electrodes were measured in dry acetonitrile solutions containing a ferrocene/ferrocenium (Fc/Fc^+) redox couple. Acetonitrile and similar non-aqueous electrolytes have proven useful in the study of charge-transfer processes at both planar[6,31-33] and high surface area semiconductor electrodes[22,34] and its use herein enabled the construction of a regenerative photoelectrochemical cell that did not require a sacrificial additive that could introduce contamination. The solid/liquid heterojunction additionally allowed for conformal physical contact to the electrode's 'front' contact, which in combination with the fast kinetics of the Fc/Fc^+ redox couple resulted in reliable electrical contact.

B. Methods

Single-crystal, 500 μm thick single-side polished n-type GaP(100) wafers doped with sulfur at N_D = 5 x 10^{17} cm^{-3} (MTI Inc) were diced into ~0.5 x 0.5 cm sections. Ohmic contact to the back side of the GaP sections was achieved by etching the back for 30 s with concentrated NH_4F(aq) (49% v/v, Transene), rinsing with deionized water (>18 Mohm cm, Barnstead Nanopure III purifier), soldering a thin, even film of pure indium onto the etched surface and then annealing in forming gas (5% H_2 and 95% N_2, Metro Welding) for 10 min at 400° C. Electrodes were prepared from the sections by attaching a copper wire coil to the In-coated back surface with silver print (GC Electronics), threading the wire through a glass tube and sealing with inert epoxy (Hysol C). Electrode areas were defined by the edge of the epoxy and were nominally 0.05 cm^2. A custom-built PTFE cell[35] was used instead of epoxy to define the electrode area for samples subjected to microscopic analysis. Macropores were etched into the planar electrode

surface by submerging the electrode in 1 M H_2SO_4 and applying a constant anodic current density of 100 mA cm^{-2} versus a platinum gauze counter electrode for 15 to 120 minutes.[36] Etching took place in the dark under ambient conditions and the H_2SO_4 solution was stirred vigorously during etching. The etched n-GaP electrodes turned a shade of yellow that became more vibrant as etching time increased, as shown in Figure II.3. Scanning electron micrographs were obtained with a Philips XL-ESEM instrument operated at 15 kV with a secondary electron detector.

Photoelectrochemical measurements were taken in a quartz cell with a uniform (flat) base serving as the optical window. The full electrochemical cell was assembled in an inert atmosphere glovebox purged to prevent O_2 contamination. Dry acetonitrile (Aldrich) was prepared with an MBraun purification system and used as the solvent, while battery-grade lithium perchlorate (99.99%, Aldrich) was purchased in an ampule, opened in the glovebox, and used as received as the electrolyte. Ferrocene (Sigma) was sublimed and dried before use and ferrocenium was generated electrolytically in the cell using a Vycor frit and platinum working electrode. Platinum gauze was used as the counter electrode and a Luggin capillary containing a platinum wire poised at the solution potential served as the reference electrode. After assembly, the cell was sealed to prevent O_2 contamination, removed from the glovebox, connected to a Schlenk line and kept under argon gas (Metro Welding) at a pressure > 1 ATM during use. A platinum working electrode was used to measure concentration overpotentials and solution resistances. Prior to use, n-GaP electrodes were briefly etched using a protocol modified from Aspnes et. al.[37] Electrodes were first immersed for 30 s in a CH_3OH (Aldrich) solution containing 0.5% Br_2 (Aldrich), then rinsed with deionized water and dried under a stream of N_2. Electrodes were then immersed in concentrated NH_4F(aq) (Transene) for 30 s, rinsed with deionized water, dried under a stream of N_2 and used immediately.

Photoelectrochemical analyses under white light illumination were conducted using an ELH light source (spectra shown in Figure II.4)[38] with output moderated by a quartz diffuser and a custom-designed filter comprised of a 1 cm thick water-filled quartz reservoir. Illumination power densities were calibrated with a thermopile (S302A, Thorlabs) and were set to 100 mW cm^{-2}. Quartz neutral density filters (Thorlabs) were used to uniformly decrease light intensities across the ELH spectrum. Current-potential

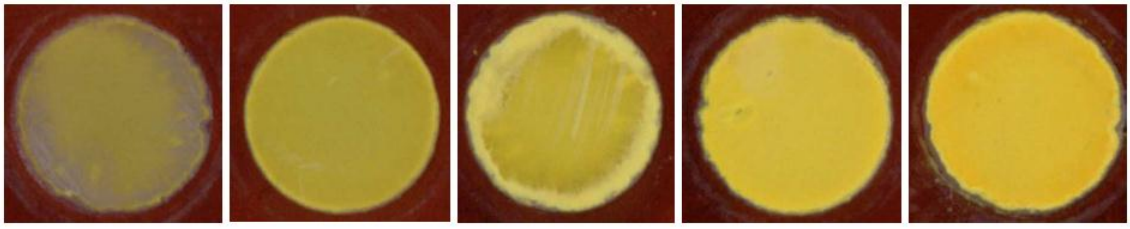

Figure II.3: Optical images of anodically etched n-GaP. Samples were etched in 1M H_2SO_4 at 100 mA cm^{-2} for (right to left) 15, 30, 60, 90 and 120 minutes. The reddish background is unetched n-GaP. The area of each spot is 0.128 cm^2.

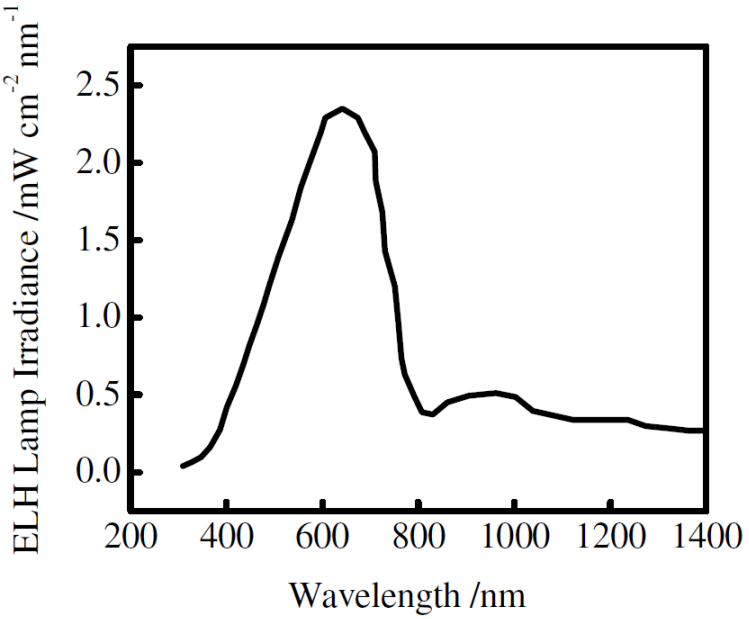

Figure II.4: Representative spectral irradiance from an ELH lamp with a dichroic mirror. Data adapted from Reference 40.

data was recorded using a CH Instruments 700 potentiostat. QE measurements were obtained with an Oriel 150 W Xe arc lamp (Newport) and a quarter-turn single-grating monochromator (Newport). Sample measurements were recorded with 15 Hz chopped illumination, and a quartz slide was used as a beam splitter to simultaneously record the light output intensity with a separate Si photodiode (Newport) in order to adjust for fluctuations in lamp intensity. The potential difference between the working and reference/counter electrodes was set to 0 V and absolute photocurrents were measured by a digital PAR 273 potentiostat. The output current signal was connected to a Stanford Instruments SR830 lock-in amplifier, and the output signals from the lock-in amplifier and the reference Si photo-diode were read by a computer controlled by custom-written LabVIEW software. Reported spectra are corrected to account for reflectivity losses at the quartz/air and quartz/acetonitrile interfaces.

C. Results

Figure II.5 shows scanning electron micrographs[37] of n-GaP(100) cross sections after various etching times. The macropores were uniformly sized and spaced throughout their entire depth and were oriented perpendicular to the surface plane. As observed previously with electrochemically etched crystalline GaP,[36,39] the pores were not completely separated but were instead slightly interconnected. These results are in contrast to GaP wafers etched under potentiostatic control (e.g. at +10 V),[29] which feature macroporous GaP films composed of a porous layer oriented in the <111> direction or are covered by a relatively smooth, less porous surface overlayer.[36] Modulation of anodic etching time appeared to only influence the average macropore depth (Figures II.5a-e) and did not alter pore shape, direction, or spacing (Figures II.5f and II.5g), consistent with 'current-line' etching in III-V semiconductors.[39] Unlike for previous reports,[28,29] no further bulk material etching procedures were necessary to expose the macroporous layers and the thicknesses of the macroporous films were directly correlated to the anodic etch times. The macroporous films in Figure II.5 exhibit approximately 35% void space.

Figure II.6b shows the spectral response of n-GaP electrodes of varying porosity immersed in a solution of 4.5 mM ferrocene and 0.5 mM ferrocenium in acetonitrile. Measurements were made at short circuit, i.e. with zero potential applied across the cell.

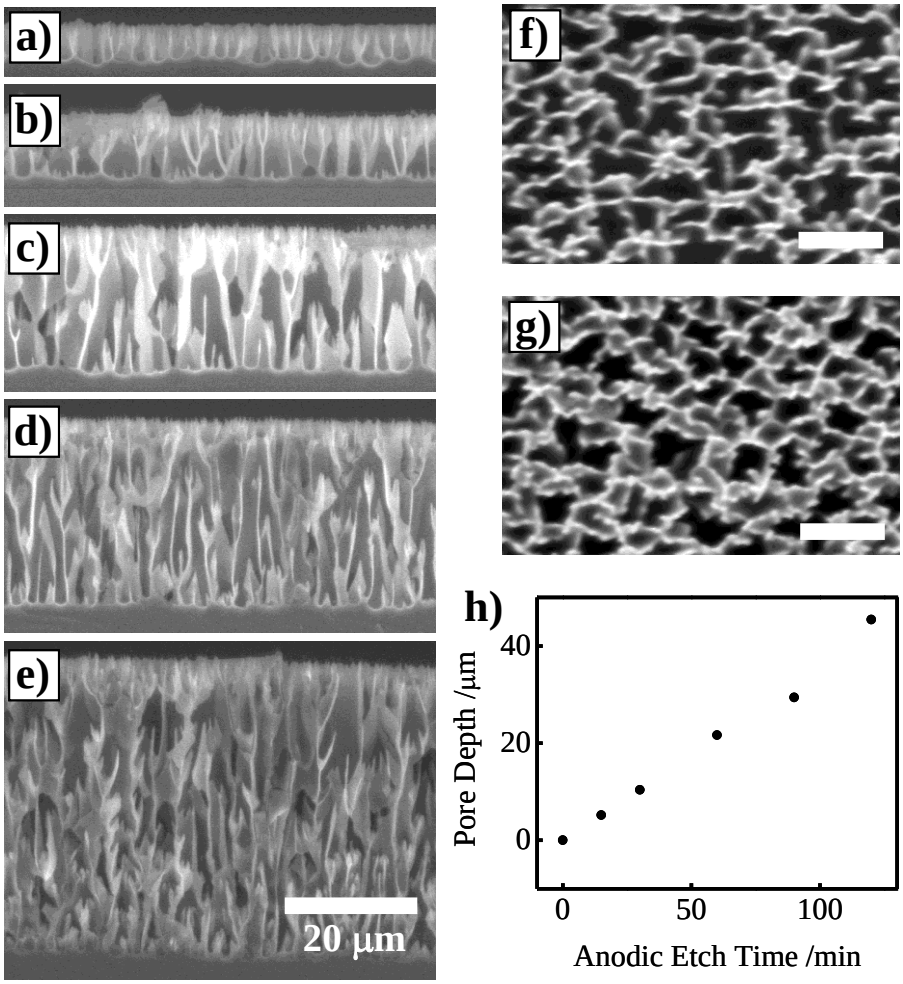

Figure II.5: Scanning electron micrographs of n-GaP electrode cross sections after (a) 15, (b) 30, (c) 60, (d) 90 and (e) 120 min of anodic galvanostatic etching at 100 mA cm^{-2}. (f) Top-down view of macroporous n-GaP after 15 min etch time. Scale bar = 10 μm (g) Top-down view of macroporous n-GaP after 120 min etch time. Scale bar = 10 μm (h) Measured pore depth as a function of anodic galvanostatic etching time.

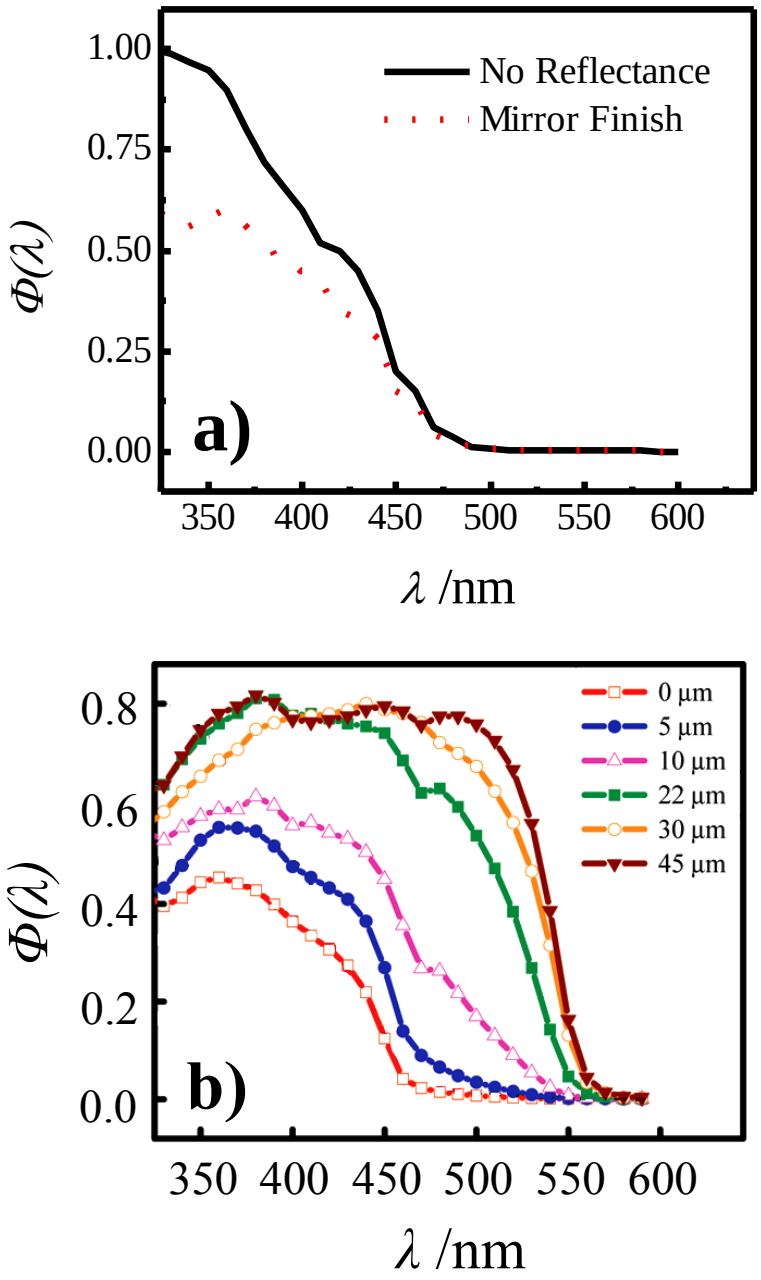

Figure II.6: (a) Theoretical spectral quantum yield for n-GaP photoelectrodes. Determined from Equation II.1 in the text for an electrode with L_p = 110 nm and (solid black line) a mirror finish or (red dotted line) no reflectivity losses. (b) Internal quantum yields as a function of wavelength for n-GaP photoelectrodes featuring macropores of varying depth. Electrodes were immersed in dry acetonitrile containing 1.0 M $LiClO_4$, 4.5 mM ferrocene and 0.5 mM ferrocenium. Measurements taken at 0 V applied bias.

The spectral quantum yield, $\Phi(\lambda)$, of a photosensitive semiconductor heterojunction can be approximated via the Gärtner model,

$$\Phi(\lambda) = \left(1 - \frac{e^{-\alpha(\lambda)W_D}}{1+\alpha(\lambda)L}\right)(1 - R(\lambda)) \qquad \text{(II.1)}$$

where W_D is the space charge layer thickness calculated from the dopant density and interfacial equilibrium barrier height, Φ_B (W_D = 33 nm for Φ_B =1.6 V at the specified N_D)[40] and R is the reflectance at the semiconductor/solution interface. Equation II.1 is a reasonable approximation for devices limited by bulk semiconductor properties, as it accounts for bulk recombination losses only and does not include 1) minority carrier recombination in the depletion region or at the surface[41] or 2) majority carrier recombination losses across the interface.[42,43] The predicted response for a polished, planar n-GaP photoelectrode with a hole diffusion length L_p = 110 nm immersed in an acetonitrile solution is given by the red dotted line in Figure II.6a. This result can be compared with the solid red line in Figure II.6b, which is the experimentally recorded data for the planar n-GaP electrodes used in this study. These data are in excellent qualitative agreement with Equation II.1 for L_p = 110 nm, which is the expected minority carrier diffusion length for the GaP wafers used in this investigation. The solid black line in Figure II.6a demonstrates the predicted spectral response for a hypothetical planar n-GaP electrode with the same bulk minority-carrier diffusion length but no reflection losses. This response indicates that even with a substantial built-in field, measures that solely reduce optical losses at such heterojunctions have a limited impact on photoresponses at wavelengths longer than approximately 470 nm. The purple line in Figure II.6b shows a representative spectral response of an n-GaP electrode with a 10 μm pore depth. These macroporous films acquired a yellow ochre hue after etching, as shown in Figure II.3. At all wavelengths, electrodes with these morphologies demonstrated improved photoresponses relative to the planar electrode. At wavelengths longer than 410 nm, these macroporous n-GaP photoelectrodes show enhancements that exceed those predicted purely from minimizing reflectance losses. These results strongly suggest that the macroporous surface architecture investigated herein facilitates the diffusion of photogenerated holes to the interface before they recombine in the bulk. Figure II.5a also shows photoresponses for macroporous electrodes with progressively deeper pores (up to

45 μm). Performance is considerably enhanced across all wavelengths, consistent with previous reports of macroporous n-GaP electrodes.[28,29] Note that the decrease in observed internal quantum yield for wavelengths less than $\lambda \sim 380$ nm in Figure II.6b is consistent with increased majority-carrier recombination at semiconductor heterojunctions at short wavelengths.[43] Even with these losses, however, the surface condition of the etched GaP photoelectrodes appears to be of sufficient quality to enable good charge injection into solution under the experimental conditions described herein. In fact, the electrodes with the highest surface areas consistently yielded the best collection efficiencies, indicating that the beneficial decrease in minority carrier (hole) collection lengths outweighed any likely increase in surface recombination losses.

Figure II.7 shows representative photocurrent density-potential responses[44] for n-GaP photoelectrodes immersed in acetonitrile with 20 mM ferrocene and 0.5 mM ferrocenium. Measurements were taken under white light illumination using an ELH lamp source with a 100 mW cm^{-2} flux.[38] In accord with Figure II.6b, these data show progressive enhancements of the photocurrent density for electrodes with increasing porosity at short circuit. Photocurrent densities for the highest porosity electrodes were more than an order of magnitude higher than for analogous planar electrodes. The upper bound on photocurrent density assuming 100% photon collection for wavelengths below 510 nm is nominally 2.2 mA cm^{-2}. Photocurrent densities for the highest porosity photoelectrode in Figure II.7a are approximately at this limit, indicating that the capture and conversion of incident light near E_g is significantly improved over that for planar electrodes. Significantly lower concentrations of ferrocene and ferrocenium resulted in reduced optical losses through solution but did not allow appreciable increases in the attainable photocurrent density, as mass transport limitations began to dominate system responses. Nevertheless, using the data in Figure II.7 as a conservative estimate, complete collection, capture, and conversion of photons with $\lambda \leq 510$ nm from sunlight at 1.5 AMU (i.e. eliminating optical losses) should result in a photocurrent density of 8.5 mA cm^{-2} using the most porous n-GaP electrodes. Assuming no change in V_{oc} or fill factor, *FF*, this translates to a photoelectrode efficiency of 6.1% under AM1.5 illumination.

The data in Figure II.7a are normalized to projected geometric area but are not corrected for concentration overpotential or solution absorbance losses. Previous photo-

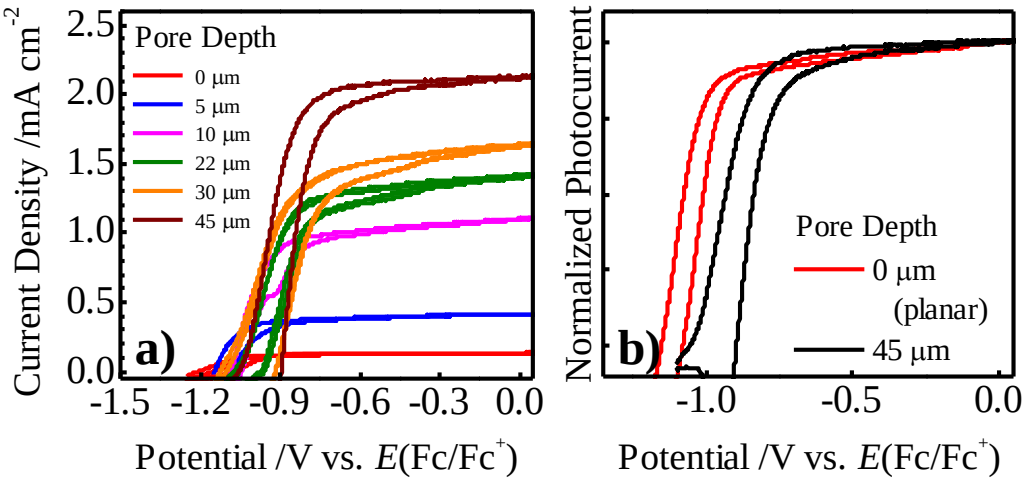

Figure II.7: (a) Current density-potential responses for n-GaP photoelectrodes with various pore depths. Electrodes were immersed in dry acetonitrile with 1 M $LiClO_4$, 0.02 M ferrocene and 0.0005 M ferrocenium and were under 100 mW cm^{-2} white light illumination from an ELH source. Scan rates were 0.01 V s^{-1}. (b) Normalized photoresponses of planar and macroporous n-GaP photoelectrodes.

electrochemical investigations of macroporous GaP showed that saturated photocurrent densities could only be obtained if a bias 3 V more positive than open circuit was applied (Figure 2B in Reference 29), indicating that mass transport through the macropores may have been limiting. The planar and macroporous photocurrent density-potential profiles shown in Figure II.7a, however, do not vary substantially and the photocurrent density plateau was only 0.3 V positive of the open-circuit photovoltage for even the highest surface area photoelectrodes. Hysteresis between the forward and back sweeps was observed for all photoelectrodes and was not exacerbated or systematically influenced by electrode porosity. Similar hysteresis has been noted in the photoelectrochemical responses of other semiconductor electrodes immersed in nonaqueous solvents containing fast outer-sphere redox couples,[33,44,45] indicating that the hysteresis is not attributable to problems specifically associated with the non-planar GaP/liquid interface. Rather, Figure II.6b indicates that mass transport through the macroporous electrodes is sufficient to avoid any distortion of the photocurrent density-voltage response. In fact, fill factors did not substantially deteriorate for any of the electrode types and GaP appeared to be fully capable of yielding good photocurrent density-voltage responses in this electrode morphology. The GaP electrode responses reported herein are consistent with the premise that mass transport need not be a limiting factor for interfaces that are stable and support fast interfacial charge transfer.

The potential intercepts of the current density-voltage curves shown in Figures II.7a-b are observed to shift to more positive values as macropore depths increase. This intercept shift can be interpreted by comparison with the approximation for the open-circuit potential of a solar device,[40]

$$V_{oc} \approx \frac{k_B T}{q} \ln\left(\frac{J_{ph}}{J_0}\right) \qquad \text{(II.2)}$$

where k_B is Boltzmann's constant, T is temperature, q is the unsigned charge of an electron, J_{ph} is the photocurrent density and J_0 is the exchange current density. Figure II.7b shows the normalized current density-voltage characteristics of representative planar (red line) and macroporous (black line, 45 μm pore depth) n-GaP photoelectrodes. Under nominally the same illumination conditions, higher surface area electrodes exhibit a ~150 mV decrease in open-circuit voltage. Similar trends have been noted among other

high surface area semiconductor photoelectrodes[22,46] and are consistent with an increase in J_0, which is typically proportional to the electrode surface area. For the 45 μm thick macroporous film with ~500 nm wall thicknesses featured in Figure II.7b, the actual surface area is approximately 280 times the geometric surface area. From Equation II.2, at room temperature this corresponds to a ~ 146 mV decrease in V_{oc}, close to the shift observed. This result suggests that the entire surface of the macroporous photoelectrodes is in excellent electrical contact to the electrolyte and that current passes through the entire surface area and not just the substrate underlying the macroporous layer. Thus, the macroporous layer does not appear to act only as a light trapping/directing medium.[47,48] Instead, the macroporous layer participates fully in light absorption, charge carrier separation and supporting heterogeneous charge transfer processes.

D. Discussion

The collective data presented here suggest that GaP with poor bulk carrier collection properties can function as a high-quality photoelectrode when macroporous surface architectures are adopted. This result is particularly encouraging given the large trap state densities and corresponding high surface recombination velocities ($> 10^5$ cm s^{-1} at T = 300 K) present at native planar III-V interfaces.[49-53] This type of interfacial recombination has been proposed to account for poor *FF* and V_{oc} responses in InP nanowire photoelectrodes in solid-state photovoltaic heterojunctions.[54] Surface states have also been proposed as a source of Fermi-level pinning in GaP and other III-V semiconductor/liquid contacts.[55] Although surface recombination processes were not quantitatively assessed here, the present data indicate that high surface area GaP photoelectrodes do not innately possess too many surface trap states to preclude good photoresponses. Specifically, deleterious surface recombination at these macroporous n-GaP photoelectrodes is not sufficient to distort[56] the shapes of the photoresponses of the macroporous n-GaP photoelectrodes relative to analogous planar photoelectrodes. Also, the overall photocurrent densities and photoelectrode energy conversion efficiencies are improved by more than a factor of 10 despite an increase in surface area of several orders of magnitude. Surface passivation strategies that minimize surface recombination and/or favorably shift the band edge energetics to push GaP into inversion

conditions should further improve the observed photoresponses but were not necessary to achieve the results reported herein.

Galvanostatic etching of n-GaP substrates is a simple, versatile means of tuning the surface architecture of GaP electrodes that can be used to obtain a wide range of n-type photoelectrode morphologies and porosities.[39,57] This method provides a promising avenue for optimizing the optical (e.g. light trapping) and physical (e.g. doping) properties of GaP electrodes while minimizing the total amount of material needed. Here we only highlight only one combination of macroporous morphology and GaP electrical properties, and it remains to be seen whether this particular form factor will prove to be the optimal design. In fact, bottom-up strategies for GaP electrode fabrication are likely to have more potential for impact than anodic etching of single-crystalline wafers for producing solar energy conversion systems to be implemented on a large scale. Alternative techniques have been used to produce semiconductor nanowires with minority carrier diffusion lengths as large as 1 μm and may be used to generate photoelectrode structures analogous to those utilized in this report.[58,59] Regardless of the manner in which a porous or high-aspect-ratio film is obtained, however, this work indicates that good photoelectrochemical performance can be achieved even with materials with poor bulk optoelectronic properties. The present work establishes an encouraging benchmark for such materials in photoelectrochemical applications.

E. Conclusion

Photoelectrochemical energy conversion efficiencies of n-GaP photoelectrodes in contact with dry acetonitrile solutions containing ferrocene and ferrocenium were improved by more than an order of magnitude by introducing a macroporous surface morphology. An n-type GaP photoelectrode with a 45 μm thick macroporous layer featuring ~500 nm wall thicknesses and 35% void space achieved a quantum yield exceeding 0.8 for light with wavelengths less than 510 nm. This was despite a hole diffusion length (110 nm) that was significantly less than the photogeneration depth within GaP at wavelengths greater than 420 nm. Observed fill factors did not decrease significantly as macropore depth increased, indicating that mass transport was not limiting through the depth of the macroporous region. Open-circuit photovoltages

decreased with increased interfacial area, consistent with the photocurrent being passed across the entire macroporous surface. The data thus indicate that the use of tailored electrode architectures is an effective strategy for overcoming the carrier-collection limitation of GaP in photoelectrochemical applications.

F. References

1 Parkinson, B. A. On the Efficiency and Stability of Photoelectrochemical Devices. *Accounts of Chemical Research* **17**, 431-437 (1984).

2 Gerischer, H. Electrochemical Photo and Solar Cells: Principles and Some Experiments. *Electroanalytical Chemistry* **58**, 263-274 (1975).

3 Bard, A. J. Photoelectrochemistry and Solar Energy: Progress, Promise and Problems. *Journal of Electroanalytical Chemistry* **168**, 5-20 (1984).

4 Archer, M. D. Electrochemical Aspects of Solar Energy Conversion. *Journal of Applied Electrochemistry* **5**, 17-38 (1975).

5 Gronet, C. M. & Lewis, N. S. Design of a 13% Efficient n-$GaAs_{1-x}P_x$ Semiconductor-Liquid Junction Solar Cell. *Nature* **300**, 733-735 (1982).

6 Kohl, P. A. & Bard, A. J. Semiconductor Electrodes. 1 3. Characterization and Behavior of n-Type ZnO, CdS, and GaP Electrodes in Acetonitrile Solutions. *Journal of the American Chemical Society* **99**, 7531-7539 (1977).

7 Sulima, O. V. *et al.* in *3rd World Conference on Photovoltaic Energy Conversion.* 737-740 (IEEE, 2003).

8 Turner, J. A. A Realizable Renewable Energy Future. *Science* **285**, 687-689 (1999).

9 Werner, J. H., Kolodinski, S. & Quiesser, H. J. Novel Optimization Principles and Efficiency Limits for Semiconductor Solar Cells. *Physical Review Letters* **72**, 3851-3854 (1994).

10 Dare-Edwards, M. P., Hammett, A. & Goodenough, J. B. The Efficiency of Photogeneration of Hydrogen at p-Type III/V Semiconductors. *Journal of Electroanalytical Chemisty* **119**, 109-123 (1981).

11 Finklea, H. O. *Semiconductor Electrodes*. (Elsevier, 1984).

12 Halmann, M. Photoelectrochemical Reduction of Aqueous Carbon Dioxide on p-Type Gallium Phosphide in Liquid Junction Solar Cells. *Nature* **275**, 115-116 (1978).

13 McCann, J. F. & Handley, L. J. The Photoelectrochemical Effect at a p-GaP Electrode. *Nature* **283**, 843-845 (1980).

14 Petit, J. P., Chartier, P., Beley, M. & Deville, J. P. Molecular Catalysis in Photoelectrochemical Cells: Study of an Efficient System for the Selective Photoelectroreduction of CO_2 : p-GaP of p-GaAs / $Ni(cyclam)^{2+}$, Aqueous Medium. *Journal of Electroanalytical Chemistry* **269**, 267-281 (1989).

15 White, T., Carter, M. A., Mottram, A., Peaker, A. R. & Sudlow, P. D. Monolithig Light Emitting Diode Arrays using Gallium Phosphide. *Nature* **232**, 469-470 (1971).

16 Aspnes, D. E. & Studna, A. A. Dielectric Functions and Optical Parameters of Si, Ge, GaP, GaAs, GaSb, InP, InAs, and InSb from 1.5 to 6.0 eV. *Physical Review B* **27**, 985-1009 (1983).

17 Hamilton, B., Wight, D. R., Blenkinsop, I. D. & Harding, W. Diffusion-Limited Lifetime in Semiconductors. *Physical Review B* **23**, 5495-5510 (1981).

18 Vanmaekelbergh, D., Erne, B. H., Cheung, C. W. & Tjerkstra, R. W. On the Increase of the Photocurrent Quantum Efficiency of GaP Photoanodes due to (Photo)anodic Pretreatments. *Electrochimica Acta* **40**, 689-698 (1995).

19 Li, J., Peat, R. & Peter, L. M. Surface Recombination at Semiconductor Electrodes Part II. Photoinduced "Near-Surface" Recombination Cetners in p-GaP. *Journal of Electroanalytical Chemistry* **165**, 41-59 (1984).

20 Maiolo, J. R. *et al.* High Aspect Ratio Silicon Wire Array Photoelectrochemical Cells. *Journal of the American Chemical Society* **129**, 12346-12347 (2007).

21 Yang, F. & Forrest, S. R. Photocurrent Generation in Nanostructured Organic Solar Cells. *ACS Nano* **2**, 1022-1032 (2008).

22 Maiolo, J. R., Atwater, H. A. & Lewis, N. S. Macroporous Silicon as a Model for Silicon Wire Array Solar Cells. *Journal of Physical Chemistry C* **112**, 6194-6201 (2008).

23 Kelly, J. J. & Vanmaekelbergh, D. Charge Carrier Dynamics in Nanoporous Photoelectrodes. *Electrochimica Acta* **43**, 2773-2780 (1998).

24 Shchetnin, A. A., Drozhzhin, A. I., Sedykh, N. K. & Novokreshchenova, E. P. Opticophysical Measurements: Photoconverters Based on Silicon-Crystal Whiskers. *Izmeritel'naya Tekhnika* **4**, 35-36 (1978).

25 Yang, C. Y. & Heeger, A. J. Morphology of Composites of Semiconducting Polymers Mixed with C-60. *Synthetic Metals* **83**, 85-88 (1996).

26 Park, J. H., Kim, S. & Bard, A. J. Novel Carbon-Doped TiO_2 Nanotube Arrays with High Aspect Ratios for Efficient Solar Water Splitting. *Nano Letters* **6**, 24-28 (2006).

27 Kayes, B. M., Atwater, H. A. & Lewis, N. S. Comparison of the Device Physics Principles of Planar and Radial p-n Junction Nanorod Solar Cells. *Journal of Applied Physics* **97** (2005).

28 Erne, B. H., Vanmaekelbergh, D. & Kelly, J. J. Porous Etching - A Means to Enhance the Photoresponse of Indirect Semiconductors. *Advanced Materials* **7**, 739-742 (1995).

29 Erne, B. H., Vanmaekelbergh, D. & Kelly, J. J. Morphology and Strongly Enhanced Photoresponse of GaP Electrodes Made Porous by Anodic Etching. *Journal of the Electrochemical Society* **143**, 305-314 (1996).

30 Ellis, A. B., Bolts, J. M., Kaiser, S. W. & Wrighton, M. S. Study of n-Type Gallium Arsenide- and Gallium Phosphide-Based Photoelectrochemical Cells. Stabilization by Kinetic Control and Conversion of Optical Energy to Electricity. *Journal of the American Chemical Society* **99**, 2848-2854 (1977).

31 Segar, P. R. & Koval, C. A. Interfacial Energetics of P-InP in Acetonitrile Solutions. *Journal of the Electrochemical Society* **135**, 2655-2656 (1988).

32 Koval, C. A. & Austermann, R. L. The Effects of Surface Energetics on the Cyclic Voltammetry of Metallocenes at Nonilluminated n-InP Electrodes. *Journal of the Electrochemical Society* **132**, 2656-2662 (1985).

33 Casagrande, L. G., Juang, A. & Lewis, N. S. Photoelectrochemical Behavior of n-GaAs and n-$Al_xGa_{1-x}As$ in CH_3CN. *Journal of Physical Chemistry B* **104**, 5436-5447 (2000).

34 Goodey, A. P., Eichfeld, S. M., Lew, K. K., Redwing, J. M. & Mallouk, T. E. Silicon Nanowire Array Photoelectrochemical Cells. *Journal of the American Chemical Society* **129**, 12344-12345 (2007).

35 Maldonado, S., Plass, K. E., Knapp, D. & Lewis, N. S. Electrical Properties of Junctions Between Hg and Si(111) Surfaces Functionalized with Short-Chain Alkyls. *Journal of Physical Chemistry C* **111**, 17690-17699 (2007).

36 Tiginyanu, I. M. *et al.* Cathodoluminescence Microanalysis of Porous GaP and InP. *The European Physical Journal - Applied Physics* **27**, 81-84 (2003).

37 Aspnes, D. E. & Studna, A. A. Chemical Etching and Cleaning Procedures for Si, Ge and some III-V Compound Semiconductors. *Applied Physics Letters* **39**, 316-318 (1981).

38 Emery, K., Myers, D. & Rummel, S. in *Photovoltaic Specialists Conference* 1087-1091 (IEEE, Las Vegas, NV, 1988).

39 Foll, H., Langa, S., Carstensen, J., Christophersen, M. & Tiginyanu, I. M. Pores in III-V Semiconductors. *Advanced Materials* **15**, 183-198 (2003).

40 Sze, S. M. N., Kwok K. *Physics of Semiconductor Devices*. 3rd Ed. edn, (John Wiley & Sons, 2007).

41 Fonash, S. *Solar Cell Device Physics*. (Academic Press, 1982).

42 Kumar, A. & Lewis, N. S. Short-Wavelength Spectral Response Properties of Semiconductor Liquid Junctions. *Journal of Physical Chemistry* **94**, 6002-6009 (1990).

43 Green, M. A. The Depletion Layer Collection Efficiency for pn Junction, Schottky Diode, and Surface Insulator Solar Cells. *Journal of Applied Physics* **47**, 547-554 (1976).

44 Gronet, C. M. & Lewis, N. S. N-Type GaAs Photo-Anodes in Acetonitrile - Design of a 10.0-Percent Efficient Photo-Electrode. *Applied Physics Letters* **43**, 115-117 (1983).

45 Lieber, C. M., Gronet, C. M. & Lewis, N. S. Evidence Against Surface-State Limitations on Efficiency of P-Si/CH_3CN Junctions. *Nature* **307**, 533-534 (1984).

46 Spurgeon, J. M., Atwater, H. A. & Lewis, N. S. A Comparison Between the Behavior of Nanorod Array and Planar Cd(Se, Te) Photoelectrodes. *Journal of Physical Chemistry C* **112**, 6186-6193 (2008).

47 Mel'nikov, V. A. *et al.* Optical Anisotropy of Strongly Photonic Porous Gallium Phosphide. *Laser Physics* **14**, 660-663 (2004).

48 Rivas, J. G., Lagendijk, A., Tjerkstra, R. W., Vanmaekelbergh, D. & Kelly, J. J. Tunable Photonic Strength in Porous GaP. *Applied Physics Letters* **80**, 4498-4500 (2002).

49 Yablonovitch, E. & Gmitter, T. J. A Contactless Minority Lifetime Probe of Heterostructures, Surfaces, Interfaces, and Bulk Wafers. *Solid State Electronics* **35**, 261-267 (1992).

50 Stringfellow, G. B. Effect of Surface Treatment on Surface Recombination Velocity and Diode Leakage Current in GaP. *Journal of Vacuum Science and Technology* **13**, 908-913 (1976).

51 Gershenzon, M. & Mikulyak, R. M. Radiative Pair Recombination and Surface Recombination in GaP Photoluminescence. *Applied Physics Letters* **8**, 245-247 (1966).

52 Heller, A. Chemical Control of Surface and Grain Boundary Recombination in Semiconductors. *ACS Symposium Series* **146**, 57-77 (1981).

53 Sturzenegger, M., Prokopuk, N., Kenyon, C. N., Royea, W. J. & Lewis, N. S. Reactions of Etched, Single Crystal (111)B-Oriented InP to Produce Functionalized Surfaces with Low Electrical Defect Densities. *Journal of Physical Chemistry B* **103**, 10838-10849 (1999).

54 Novotny, C. J., Yu, E. T. & Yu, P. K. L. InP Nanowire/Polymer Hybrid Photodiode. *Nano Letters* **8**, 775-779 (2008).

55 Bard, A. J., Bocarsly, A. B., Fan, F. R. F., Walton, E. G. & Wrighton, M. S. The Concept of Fermi Level Pinning at Semiconductor/Liquid Junctions. Consequences for Energy Conversion Efficiency and Selection of Useful Solution Redox Couples in Solar Devices. *Journal of the American Chemical Society* **102**, 3671-3677 (1980).

56 Anz, S. J. & Lewis, N. S. Simulations of the Steady-State Current Density vs Potential Characteristics of Semiconducting Electrodes. *Journal of Physical Chemistry B* **103**, 3908-3915 (1999).

57 Yoriya, S., Paulose, M., Varghese, O. K., Mor, G. K. & Grimes, C. A. Fabrication of Vertically Oriented TiO_2 Nanotube Arrays Using Dimethyl Sulfoxide Electrolytes. *Journal of Physical Chemistry C* **111**, 13770-13776 (2007).

58 Allen, J. E. *et al.* High-Resolution Detection of Au Catalyst Atoms in Si Nanowires. *Nature Nanotechnology* **3**, 168-173 (2008).

59 Kelzenberg, M. D. *et al.* Photovoltaic Measurements in Single-Nanowire Silicon Solar Cells. *Nano Letters* **8**, 710-714 (2008).

CHAPTER III

Design Considerations for Nanowire Photoelectrodes

A. Introduction

This chapter develops a detailed, quantitative understanding of how charge transport and recombination properties are affected by various design features in single-nanowire Si or GaP photoelectrodes under illumination. Specifically, the operational implications of features such as nanowire radius, dopant density, bulk time constant, surface recombination, nanowire tapering, and nonuniform doping are addressed. A particular emphasis is placed on developing useful characterizations and guidelines for the construction of high-performance nanowire photoelectrodes.

The field of photoelectrochemistry has long been a promising avenue for the light-assisted generation of valuable substances such as chemical fuels through the use of semiconductor electrodes. Substantial progress has been made over the past five decades to identify and characterize fundamental processes relevant to fuel-forming photoelectrochemical systems.[1-5] A viable system for photoelectrochemical fuel generation has yet to surface, however, largely due to the dearth of photoelectrode materials that 1) possess desirable optical absorption characteristics, 2) can efficiently separate and transport carriers, 3) can be obtained or synthesized in a manner that is compatible with large-scale adoption and 4) are capable of producing photovoltages large enough to drive relevant electrochemical reactions.

Many of these factors have been addressed wholly or in part by the adoption of nanostructured semiconductor architectures. For instance, light-trapping effects observed in nanowire arrays have been shown to reduce the optical losses associated with reflection or transmission through a planar semiconductor, and such effects may reduce the amount of material required to fully absorb light.[6-8] Nanostructures have also proved

advantageous for materials where bulk recombination processes are limiting due to the decoupling of light absorption with carrier separation and collection.[6,9-11] Nanostructured form factors have also facilitated the development of materials that may be difficult to produce in bulk form due to lattice spacing mismatch[12-14] and have been integral in the sensitization of non-absorbing materials to achieve high optical absorption.[15,16] The high surface areas inherent to nanostructured electrodes also support a significantly higher density of electrocatalysts per geometric area than planar electrodes, which can facilitate electrochemical processes relevant to fuel generation. The development of electrode materials via chemical vapor deposition[17] or even solution-based processing[18] may also greatly reduce the processing inputs required to obtain a photoactive material.

Figure I.3 illustrates the premise that a properly designed semiconductor photoelectrode with a high-aspect-ratio morphology can decouple the processes of light absorption and minority carrier collection in a photoactive material. Losses due to carrier recombination in the bulk semiconductor can then be mitigated by collecting minority carriers at a distance less than the diffusion length, L, from where they were generated. Thus, high-aspect-ratio nanostructures can dramatically increase the performance of low-L materials, in many cases obviating the need for extensive, resource-intensive semiconductor purification. In practice, the use of high-aspect-ratio designs can translate to larger photocurrent densities for materials that perform poorly in planar systems due to poor bulk optoelectronic properties. To this end, the 'nanostructuring' approach has been applied successfully to a variety of semiconductor photoelectrode materials in an attempt to optimize their performance and fabrication requirements to design fuel-forming systems with commercial applicability. Indeed, many materials long thought impractical for solar energy conversion have exhibited promising photoelectrochemical responses upon the adoption of nanostructured form factors. A tenable system or clear set of material options that enable high efficiency solar-to-chemical energy conversion, however, has yet to be recognized.[19] A wide variety of high-aspect-ratio morphologies have been explored, including nanotubes, macroporous and mesoporous films, nanorods and nanonets, amongst others. The most ubiquitous architectures, however, feature closely-packed films of vertically oriented nanowires with radii less than 500 nm.

Accordingly, this chapter focuses on design criteria relevant to the operation of single-nanowire photoelectrodes with lengths of 100 μm and radii between 20 nm and 500 nm.

In this work, we set out to describe the typical operation of a nanowire photoelectrode operating under low level injection conditions (i.e. illumination levels where the concentration of only one charge carrier type changes appreciably) using steady-state device simulations. By these means we attempt to identify and more precisely define the limiting factors in the operation of such devices in order to aid in their experimental design, fabrication, and ultimate implementation.

B. Theory

The maximum potential that a photoelectrode can generate to drive a redox reaction generally takes the form of Equation III.1:[20]

$$V_{oc} = \frac{k_B T}{q} \ln\left(\frac{J_{ph}}{J_0} + 1\right) \approx \frac{k_B T}{q} \ln\left(\frac{J_{ph}}{J_0}\right) \qquad \text{(III.1)}$$

where V_{oc} is the open circuit voltage of the photoelectrode, k_B is Boltzmann's constant, T is temperature, q is the unsigned charge of an electron, J_{ph} is the photocurrent density and J_0 is the exchange or 'dark' current density. The magnitude of J_0 is determined by the carrier recombination processes illustrated in Figure III.1, while that of J_{ph} is determined by photogeneration rates within the semiconductor. A well-developed understanding of these recombination processes is therefore critical to simulating and interpreting the responses of the nanowire photoelectrodes investigated herein.

Figure III.1 illustrates the dominant charge carrier recombination processes in a nanowire photoelectrode in electrical contact with an electrolyte containing the redox couple A/A^-.[20] Additional loss pathways such as radiative and Auger recombination are typically negligible for indirect bandgap semiconductors like Si and GaP under low level injection, and likewise were not present at a significant level for the discrete-contact system under concentrated illumination discussed in the Results section below.[20,21] Previous experimental reports on highly doped semiconductor photoelectrodes have shown that tunneling processes such as thermally enhanced field emission and indirect, multistep tunneling are also not significant for the conditions considered herein,[22] presumably due to the relatively low density of acceptor states in solution.[23]

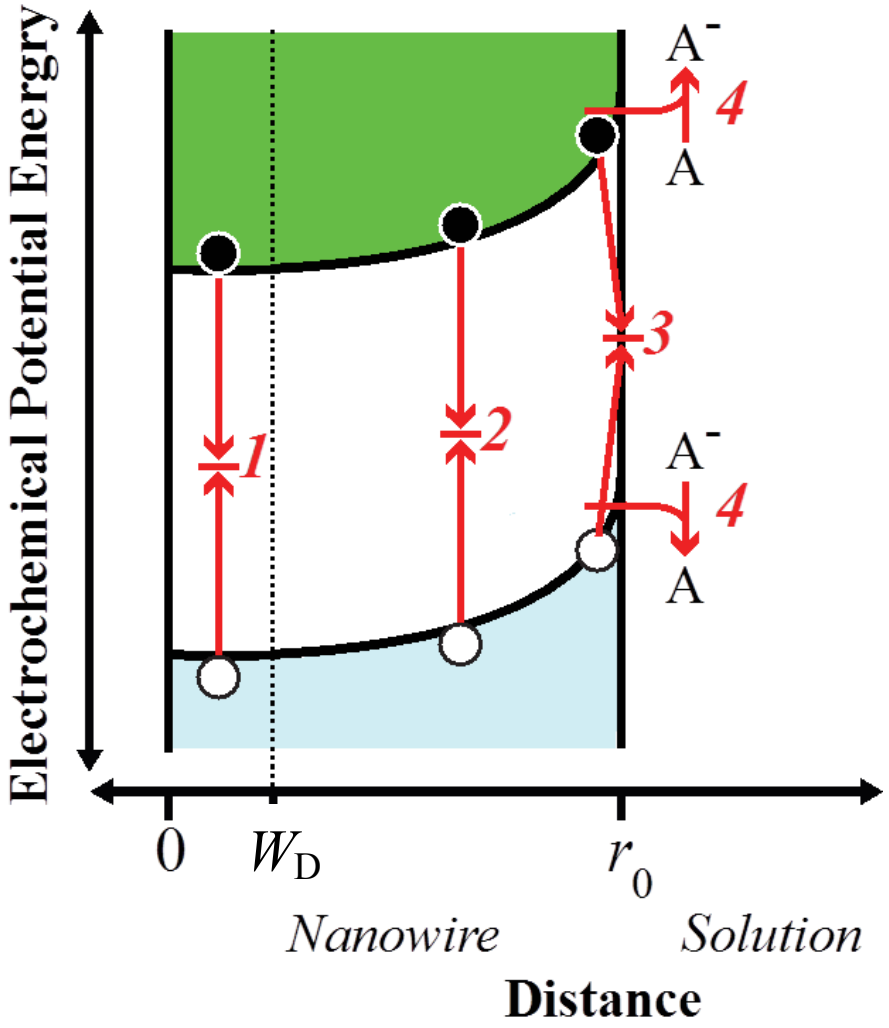

Figure III.1: Energy band diagram illustrating the four principal recombination processes in a semiconductor photoelectrode under low-level injection. Charge carrier recombination occurs (1) in the bulk, (2) in the depletion region, (3) at surface traps, and (4) through heterogeneous charge-transfer. The plane W_D represents the edge of the depletion region, r_0 is the nanowire radius and black (white) circles represent photoexcited electrons (holes).

The processes labeled 1 and 2 in Figure III.1 describe carrier recombination processes occurring in the semiconductor bulk and depletion region, respectively. For the system and conditions simulated in this report, these processes are dominated by Shockley-Read-Hall (SRH) recombination, which is typically a complex function of material- and system-dependent parameters, $R_{SRH}(n, p, n_i, p_i, \tau_n, \tau_p)$, where R_{SRH} is the SRH recombination rate, n and p are the free electron and hole densities, respectively, n_{i} and p_{i} are the respective intrinsic free electron and hole densities, and τ_{n} and τ_{p} are the respective electron and hole carrier lifetimes. For trap level energies in the middle of the band gap, the bulk time constants for SRH recombination take on the simple form

$$\tau_n = \frac{1}{\sigma_n v_{th} n_d} \qquad \text{(III.2a)}$$

$$\tau_p = \frac{1}{\sigma_p v_{th} p_d} \qquad \text{(III.2b)}$$

where n_{d} and p_{d} are the effective density of filled donor- and acceptor-like defect states, respectively, σ_{n} and σ_{p} are the effective cross sections for interaction between carriers and defects and v_{th} is the thermal carrier velocity.

Processes 3 and 4 in Figure III.1 represent parallel charge carrier recombination pathways at the semiconductor/electrolyte interface due to (3) surface recombination and (4) deleterious charge transfer to the electrolyte. Equation III.3 is an analytic expression for the 'dark' current density at a nanowire semiconductor photoelectrode when performance is limited solely by surface recombination (process 3):[20]

$$J_{sr} = qS_nS_p \frac{n_s p_s - n_i^2}{S_p\left(p_s + N_V e^{\frac{-q(E_T - E_V)}{k_B T}}\right) + S_n\left(n_s + N_C e^{\frac{-q(E_C - E_T)}{k_B T}}\right)} \qquad \text{(III.3)}$$

Here S_{n} (S_{p}) is the surface recombination velocity. The dependence of current density on applied potential is embedded in Equation III.3 via the terms n_s and p_s, which are the potential-dependent concentrations of electrons and holes at the surface. Equation III.4

gives an analogous equation for dark current density under the limiting condition of deleterious heterogeneous charge transfer at the surface:[3,24,25]

$$J_{ct} = qk_{et}[\mathrm{A}](n_s - n_{s0}) - qk_{ht}[\mathrm{A}^-](p_s - p_{s0}) \qquad \text{(III.4)}$$

Here k_{et} (k_{ht}) is the rate constant for electron (hole) transfer, n_{s0} (n_{p0}) is the surface concentration of electrons (holes) in the dark at equilibrium and [A] ([A^-]) is the concentration of acceptors (donors) in the electrolyte. The dependence of J_{ct} on applied potential in Equation III.4 is again embedded in the terms n_s and p_s. For an n-type photoelectrode, Equation III.4 indicates that higher concentrations of electrons at the surface will result in a higher J_0 that will negatively affect photoelectrode performance according to Equation III.1. Both Equations III.3 and III.4 are valid for all photoelectrode morphologies including the high-aspect-ratio nanowires investigated herein.

Conversely, the recombination pathways specified by processes *1* and *2* in Figure III.1 vary for different photoelectrode morphologies and the original expressions for recombination in a planar photoelectrode[20] are not applicable here. The analytic expressions describing charge carrier recombination in the bulk and in the depletion region of a cylindrical nanowire photoelectrode with a high aspect ratio have been derived from the flux conditions in cylindrical coordinates and are expressed in Equations III.5a and III.5b below.[19] The rate of bulk recombination in a high-aspect-ratio cylindrical n-type nanowire is expressed as a current density in Equation III.5a. Under the limiting condition $L_p >> W_D$ (the minority carrier diffusion length is much greater than the depletion width) Equation III.5a simplifies to Equation III.5b. Equation III.5 is derived in the Supporting Information of Reference 19.

$$J_{br} = \frac{qD_p p_0}{L_p}\left(\left(e^{\frac{qV}{k_B T}} - 1\right)\frac{B_1\left(\frac{W_D}{L_p}\right)}{B_0\left(\frac{W_D}{L_p}\right)}\right) \qquad \text{(III.5a)}$$

$$J_{br,cyl} = \frac{qD_p n_i^2 W_D}{4N_D L_p^2}\left(e^{\frac{qV}{k_B T}} - 1\right) \qquad \text{(III.5b)}$$

Here D_p is the hole diffusion constant, p_0 is the hole density in the dark at equilibrium, V is the applied potential and B_m is a Bessel function of order m. Charge carrier recombination in the depletion region of a high-aspect-ratio cylindrical semiconductor is given by Equation III.6a:[19]

$$J_{dr,cyl} = J_{dr,planar} + \frac{qn_i Z(r_0, W_D)}{2r_{dr,\max}\sqrt{\tau_n}\sqrt{\tau_p}} e^{\frac{qV}{2k_B T}} \qquad \text{(III.6a)}$$

$$J_{dr,cyl} = J_{dr,planar} + \frac{qn_i Z(r_0, W_D) D_p}{2r_{dr,\max} L_p^2} e^{\frac{qV}{2k_B T}} \qquad \text{(III.6b)}$$

where $Z(r_0,W_D)$ is the effective recombination area as defined by an explicit integral over W_D and r_0 and $r_{dr,max}$ is the radial position at which recombination in the depletion region is greatest. Equation III.6a is a general expression where no assumption has been made regarding electron and hole lifetimes, whereas Equation III.6b assumes SRH bulk recombination[20,21] with equal electron and hole trap capture cross sections, trap densities and carrier lifetimes. Equation III.6 is derived in the supporting information of Ref. 19.

In practice, the performance of a photoelectrode comprised of high-aspect-ratio nanowires of a given material can be susceptible to any or all of the recombination processes discussed above. Thus far, it has been difficult for experimentalists to predict *a priori* which, if any, of Equations III.3-III.6, properly describe J_0 in a particular system at every experimentally relevant condition. Quantitative insight into the controlling factors of high-aspect-ratio semiconductor nanowire photoelectrode operation is of critical value to guide experimental efforts to produce high-performance nanowire photoelectrodes. This report attempts to provide these analyses through a set of quasi-three-dimensional, finite element simulations of Si ad GaP nanowires. Such approaches have previously been used to separately model the operations of planar semiconductor photoelectrodes in

photoelectrochemical systems[26] and solid-state cylindrical *p-n* nanowire homojunctions.[11,27,28] Herein, we report modeling efforts explicitly aimed at describing the operation of high-aspect-ratio Si and GaP nanowire photoelectrochemical heterojunctions. Si and GaP are both well-characterized semiconductors with small and mid-sized bandgaps, respectively, that have been previously investigated as photoelectrode materials for artificial photosynthesis.[29] The results below detail the extent to which non-uniform dopant concentrations and nanowire shape affect deleterious heterogeneous charge transfer at the semiconductor/electrolyte interface. Effects of variation in nanowire radius, surface recombination velocity, charge carrier mobilities, and charge carrier lifetimes on photocurrent-potential responses are also presented. Finally, simulations intended to explore the possibility of nanowire photoelectrodes with a novel contacting scheme operating under high level injection conditions are discussed.

C. Methods

The steady-state characteristics of illuminated photoelectrodes were approximated by modeling a single semiconductor nanowire using the TCAD Sentaurus software package (Synopsys). Sentaurus Device utilizes the finite-element box method[30] to solve a coupled set of equations that includes Poisson's equation, Fick's law of diffusion and the continuity equations for electrons and holes. This software has been used extensively for modeling photovoltaic architectures in one, two, and three dimensions.[31-33] The three-dimensional cylindrical (and tapered cylindrical) nanowires investigated herein were modeled utilizing a two-dimensional rectangular structure in a radial coordinate system, where azimuthal symmetry about $r = 0$ was assumed in order to reduce computation resource demand. Figure III.2 shows the simulation meshing grid for portions of the simulated cross section taken from the top, middle and bottom of a nanowire, where $r = 0$ corresponds to the center of the nanowire and the pink line highlights the outer edge of (and electrical contact to) the nanowire. Mesh grid box sizes decreased as the proximity to either 1) an electrical contact or 2) the top of the nanowire decreased. This ensured that 1) electrostatic gradients could be calculated with sufficient precision to accurately model carrier transport and collection and 2) spatial resolution of short-wavelength photon absorption was sufficient to accurately model optical generation. Unless noted otherwise,

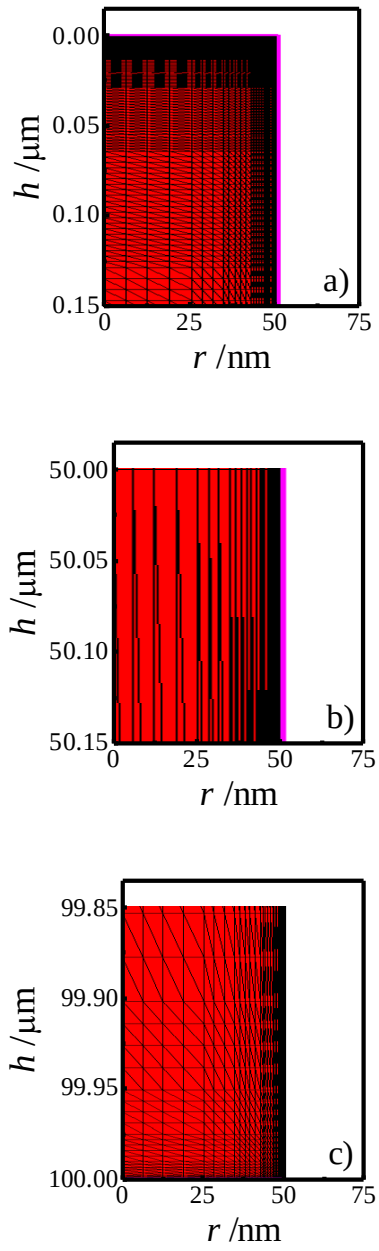

Figure III.2: Pictorial representation of the computational mesh used for nanowire simulations in TCAD Sentaurus. (a) The top portion of the nanowire structure from the top edge to a depth of 0.15 μm. (b) The middle portion of the nanowire structure from the a depth of 50 to 50.15 μm. (c) The bottom portion of the nanowire structure from the bottom edge to a height of 0.15 μm.

each simulation featured a perfect ohmic contact at the base of the nanowire (denoted as the 'back' contact) with a carrier collection velocity of $S = 10^7$ cm s^{-1}. The side and top of the nanowire comprised the 'front' contact, which featured an interfacial equilibrium barrier height, Φ_B of 1 eV for Si and 2 eV for GaP. To approximate a semiconductor/liquid contact, the front contact was uniformly in electrical contact with a single conductor with electron and hole transfer velocities (k_{et}[A] and k_{ht}[A^-], respectively) of 100 cm s^{-1} unless indicated otherwise. These velocities coincide with known rate constant values for outer-sphere redox couples (10^{-17} -10^{-19} cm^4 s^{-1})[24,34] at concentrations typical of photoelectrochemical experiments (10^{-1} to 10^1 M). No other physical aspects of the electrolyte (e.g. dielectric constant) were incorporated into the models. For simulations involving discrete ohmic-selective contacts, each contact was a thin concentric band equidistant from the other ohmic-selective contact and the nearest top/bottom boundary.

The nanowire structures reported herein featured high aspect ratios, with a length of 100 μm and a radius of 50 nm unless otherwise indicated. Tapering, where present, was achieved by decreasing the radius near the top of the structure (the end nearest the illumination source) while holding the base radius and vertical height fixed (see Figure III.3a). Bulk recombination losses were assumed to occur predominantly through SRH recombination, which was incorporated by setting values for the bulk electron and hole time constants, $\tau_n = \tau_p = \tau$. The SRH model utilized in these simulations was characterized by a single trap level located at the energy of the intrinsic Fermi level (approximately in the center of the band gap) and time constants were therefore well-described by Equations III.2a-b.

Surface defects were incorporated at the electrode interface in a manner analogous to bulk defects by setting the bulk time constant within a 5 Å semiconductor layer at the surface (t) and again constraining the defect level to the intrinsic Fermi level of the material. Surface recombination velocities could then be calculated as

$$S_n = S_p = S = \frac{t}{\tau_{surface}} \qquad \text{(III.7)}$$

The default parameter values used to describe the bulk optoelectronic properties

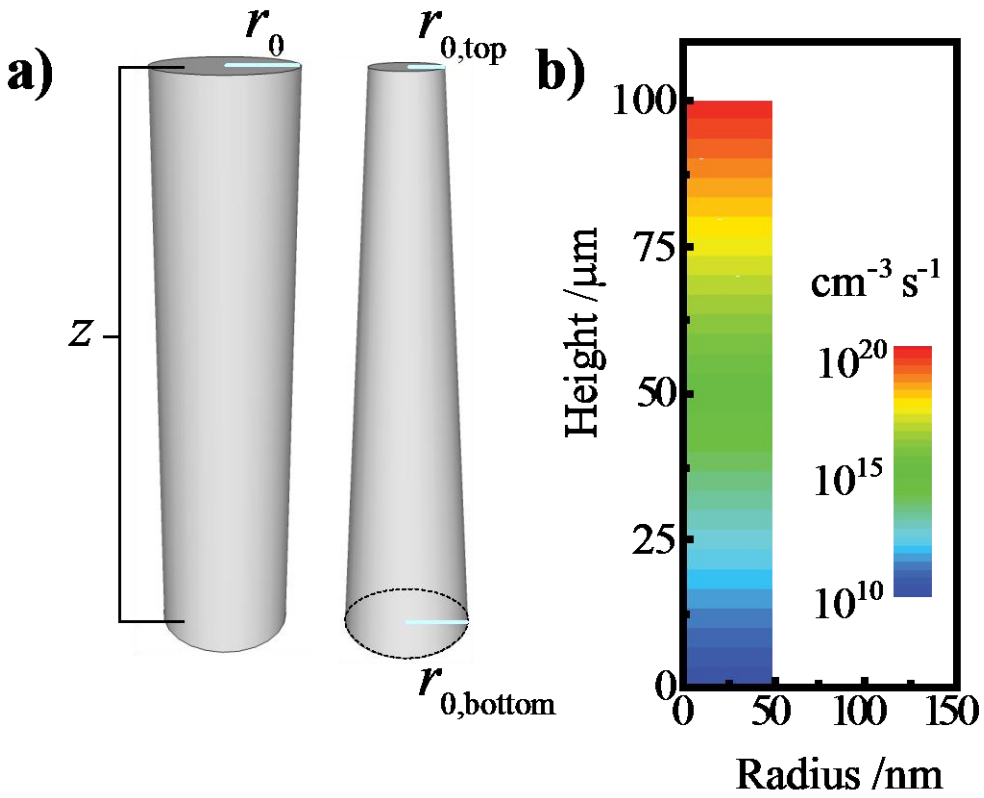

Figure III.3: (a) Depiction of the (left) cylindrical and (right) tapered cylindrical nanowire models used in this work, with r_0 indicating the effective radius. (b) The optical generation profile in a cylindrical nanowire under AM 1.5 (direct+circumsolar) illumination at normal incidence. This work utilized a simple Beer-Lambert absorption profile and did not account for reflection or diffraction from the nanowire structure.

of Si and GaP are presented in Tables III.1 and III.2, respectively along with additional variables specifying charge-transfer kinetics and electrolyte properties. Deviation from these parameters is indicated when applicable.

Unless otherwise stated, simulations utilized an AM1.5 (direct+circumsolar) spectral illumination profile with an 88 mW cm^{-2} integrated power density normally incident on the top of the nanowire. This spectrum was scaled with a uniform multiplicative factor for simulations at higher total illumination intensities. A simple Beer-Lambert absorption profile was used to generate an approximate steady-state optical carrier generation profile, with spectral absorptivity determined from published optical data for Si and GaP.[35,36] The explicit generation profile used in these simulations is shown in Figure III.3b. Reflectance and diffraction from the nanowire surface were not incorporated. Where given, quantum yield values are on a scale from 0 to 1 and represent the ratio of the collected carrier flux to the number of absorbed photons per projected area per second. Tunneling losses were found to be negligible under the conditions investigated herein, in accord with the low *S* values at the front contact of the simulated devices which reflect the relatively low density of carrier acceptor states in the contacting material.[37] Auger and radiative recombination were likewise found to be inconsequential under the operating conditions investigated, notably including the discrete contact device simulations which utilized concentrated illumination intensities.

D. Results and Discussion

i. Non-Uniform Doping Profiles

Photogenerated carrier collection efficiency has been shown to fall off dramatically at dopant concentrations that are too low to support a full depletion region within the nanowire.[7] In the absence of the strong internal electric fields within the depletion region, majority carriers are not preferentially directed away from the semiconductor interface and devices typically exhibit poor energy conversion due to high rates of surface recombination and deleterious heterogeneous charge transfer (processes *3* and *4* in Figure III.1).[7,38,39] Most nanowire synthesis techniques yield materials that are intrinsic or only lightly doped, and nanowires intended for use in photoactive

Table III.1: Default parameters for Si device simulations.

Parameter	Description	Value	Units
$q\Phi_B$	barrier height	1.0	eV
$\mathbf{E}_g$	band gap	1.16964	eV
n_i	intrinsic carrier concentration	4.6×10^{9}	cm^{-3}
ε	dielectric constant	11.7	
T	Temperature	300	K
N_{CB}	effective density of states in conduction band	2.78×10^{19}	cm^{-3}
N_{VB}	effective density of states in valence band	3.14×10^{19}	cm^{-3}
N_D	donor dopant density	1×10^{18}	cm^{-3}
τ_n	bulk electron lifetime	2.0568×10^{-6}	s
τ_p	bulk hole lifetime	2.0568×10^{-6}	s
$\tau_{n,s}$	surface electron lifetime	5×10^{-8}	s
$\tau_{p,s}$	surface hole lifetime	5×10^{-8}	s
h	nanowire height	100	um
r	nanowire radius	50	nm
μ_n	electron mobility	1417	$cm^2\ V^{-1}\ s^{-1}$
μ_p	hole mobility	470	$cm^2\ V^{-1}\ s^{-1}$
v_n	electron contact velocity	1×10^{2}	$cm\ s^{-1}$
v_p	hole contact velocity	1×10^{2}	$cm\ s^{-1}$
I_0	AM1.5 white light illumination	100	$mW\ cm^{-2}$
α	spectral absorptivity	$1.1 - 2.4 \times 10^{6}$	cm^{-1}

Table III.2: Default parameters for GaP device simulations.

Parameter	Description	Value	Units
$q\Phi_B$	barrier height	2	eV
$\mathbf{E}_g$	band gap	2.26	eV
n_i	intrinsic carrier concentration	0.66	cm^{-3}
ε	dielectric constant	10.2	
T	Temperature	300	K
N_{CB}	effective density of states in conduction band	1.78×10^{18}	cm^{-3}
N_{VB}	effective density of states in valence band	1.92×10^{19}	cm^{-3}
N_D	donor dopant density	1×10^{18}	cm^{-3}
τ_n	bulk electron lifetime	5.148×10^{-11}	s
τ_p	bulk hole lifetime	5.148×10^{-11}	s
$\tau_{n,s}$	surface electron lifetime	5×10^{-8}	s
$\tau_{p,s}$	surface hole lifetime	5×10^{-8}	s
h	nanowire height	100	um
r	nanowire radius	50	nm
μ_n	electron mobility	110	$cm^2\ V^{-1}\ s^{-1}$
μ_p	hole mobility	75	$cm^2\ V^{-1}\ s^{-1}$
v_n	electron contact velocity	1×10^2	$cm\ s^{-1}$
v_p	hole contact velocity	1×10^2	$cm\ s^{-1}$
I_0	AM1.5 white light illumination	100	$mW\ cm^{-2}$
α	spectral absorptivity	$110 - 9.8 \times 10^5$	cm^{-1}

heterojunctions must undergo further processing to increase the doping concentration to a desirable level. Post-synthesis doping is typically achieved via annealing processes that drive dopants radially into the nanowire, but it can be difficult to uniformly dope a material with such external doping techniques. Resulting wires tend to be under-doped, with lower doping concentrations at the core of the nanowire than at the surface. Such nanowires are susceptible to the same type of interfacial majority carrier recombination losses observed in lightly-doped nanowires, but the effects of non-uniform doping profiles in nanowire photoelectrodes have yet to be quantitatively assessed.

Post-synthesis doping can be achieved through means such as diffusion 'drive-in' or ion implantation,[40] both of which can result in spatial variation of dopant concentration in thin semiconductor nanowires.[40-44] Ion implantation can produce Gaussian-like spatial dopant distributions, but the specific dopant concentration-distance profile is highly dependent on the particular conditions used for implantation.[45] Drive-in diffusion doping with a constant source is in practice a simpler strategy that yields predictable dopant concentration profiles according to Equation III.8,

$$C(r,t) = C_s erfc\left(\frac{r}{2\sqrt{D_{dopant}t}}\right) \qquad \text{(III.8)}$$

where $C(r,t)$ is the dopant concentration, r is the radial dimension, t is the total time used to drive in the dopant, C_s is the surface dopant concentration, $erfc(x)$ is the complementary error function, and D_{dopant} is the temperature-dependent diffusion coefficient for a specific dopant in the semiconductor.[46] In Equation III.8, the term $2\sqrt{D_{dopant}t}$ describes an effective distance from the surface to which the dopant is able to diffuse under the employed doping conditions. Non-uniform doping occurs when temperatures and/or exposure times are below the levels necessary to satisfy $2\sqrt{D_{dopant}t} \geq r$. Figures III.4a-c illustrate the dopant concentration as a function of radial distance from the center of the nanowire according to Equation III.8 for four different values of $2\sqrt{D_{dopant}t}$ at background dopant densities of (III.5a) 1 x 10^{16} cm^{-3}, (III.5b) 1 x 10^{17} cm^{-3} and (III.5c) 3 x 10^{17} cm^{-3}. All of these background dopant levels were too low to completely suppress majority carrier recombination at the surface under 750 nm

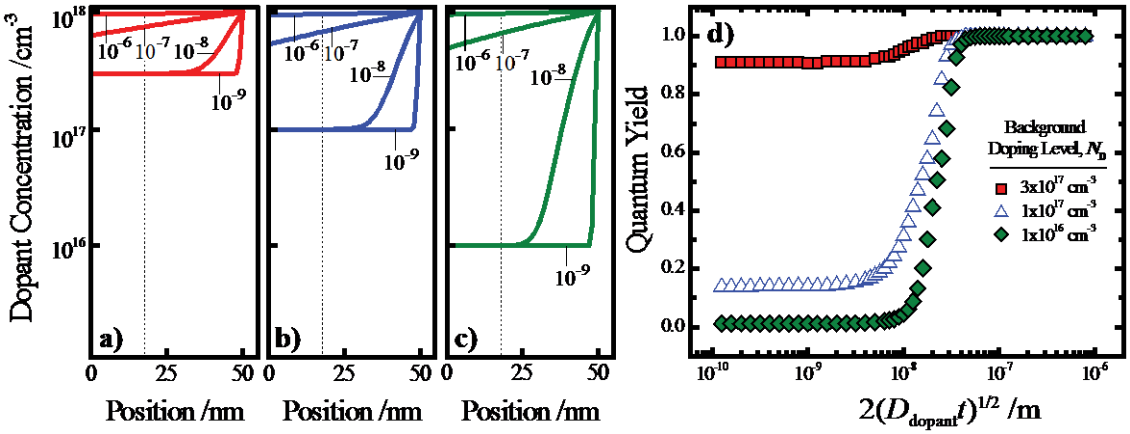

Figure III.4: (a-c) Dopant concentration versus radial distance from the center of a 50 nm radius nanowire following 'drive-in' diffusion doping to a level of 1 x 10^{18} cm^{-3}. Background dopant concentrations are (a) 3 x 10^{17} cm^{-3}, (b) 1 x 10^{17} cm^{-3}, and (c) 1 x 10^{16} cm^{-3}. Four different values of $2\sqrt{D_{dopant}t}$ are shown (see labels). (d) Simulated internal quantum yield versus the characteristic drive-in dopant diffusion length $2\sqrt{D_{dopant}t}$ at 0 V applied bias. Illumination consisted of a 1 x 10^{17} cm^{-2} s^{-1} monochromatic photon flux at λ = 750 nm.

illumination at a photon flux of 1×10^{17} cm^{-2} s^{-1}. In each profile, the surface dopant concentration was set to 1×10^{18} cm^{-3}. The inner edge of the depletion width for a 1 eV interfacial equilibrium barrier height is denoted with a vertical dotted line. Figure III.4d shows the simulated quantum yield versus $2\sqrt{D_{dopant}t}$ at zero applied bias for a cylindrical Si nanowire with r_0 = 50 nm, z = 100 μm and Φ_B = 1 eV. For values of $2\sqrt{D_{dopant}t}$ large enough to effect a uniformly high dopant density, the modeled photoelectrodes exhibited perfect quantum yields, indicating negligible majority carrier recombination losses. For the smallest values of $2\sqrt{D_{dopant}t}$, the quantum yield values were much less than unity, in agreement with results for lightly doped nanowire photoelectrodes.[7,39] For intermediate values of $2\sqrt{D_{dopant}t}$ less than 40 nm, the steepness of the dropoff in quantum yield was dependent on the background doping level. The Figure III.4d results indicate that even if the near-surface region of a thin nanowire is adequately doped, majority carrier recombination at the surface can only be adequately suppressed if the entire depletion region is sufficiently doped to sustain the internal electric field. The data in Figure III.4d can serve as a practical guide for the preparation of thin Si nanowires that are resistant to majority carrier recombination. For example, phosphorus is an n-type dopant in Si with a dopant diffusivity of 1.16×10^{-15} cm^2 s^{-1} at T = 1200 K.[46,47] This analysis indicates that a minimum 'drive-in' time of one hour is necessary to reach the minimum requisite value of $2\sqrt{D_{dopant}t}$ at this processing temperature. Shorter diffusion times, lower temperatures, or other complications in the doping process will result in materials with low or no appreciable photoactivity, irrespective of all other optoelectronic properties of the material.

ii. Tapered Nanowire Morphologies

A common observation in the preparation of nanowires longer than several μm is that their radii are not constant along their entire length, but are instead tapered at the top with respect to the base.[48-51] From previous studies[7] of high-aspect-ratio nanowire photoelectrodes, it can be inferred that nanowire sections that are too thin to support a full depletion region (given the material's dopant concentration) will allow substantial majority carrier recombination at the front contact. This effect was quantitatively

explored via simulations of ideal and tapered cylindrical Si nanowires with z = 100 μm under AM 1.5 (direct+circumsolar) insolation. The quantum yields of devices of varying morphology are shown versus applied potential in Figure III.5. The five photoelectrode architectures investigated (see Figure III.5 inset) included two thin cylindrical nanowires with r_0 =300 and 50 nm (*I* and *II*, respectively) and three tapered cylindrical nanowires with $r_{0,base}$ = 300 nm and $r_{0,top}$ = 150, 100, and 50 nm (*III*, *IV*, and *V*, respectively) with a uniform dopant concentration of 2 x 10^{16} cm^{-3}. Nanowire *I* featured a radius large enough to support a full depletion region and minimize majority carrier recombination at the surface. Accordingly, quantum yield at zero applied bias were unity. Conversely, nanowire *II* was too thin to support a full depletion region and excessive majority carrier recombination through charge transfer at the surface resulted in negligible quantum yields at zero applied bias. The three tapered nanowires *III*, *IV*, and *V* all exhibited short-circuit quantum yields of less than unity at zero applied bias. Quantum yields for nanowires *III*, *IV* and *V* were between 0.65 and 0.9, indicating significant majority-carrier losses due to deleterious charge transfer at the surface. In practice, such recombination losses will be sensitive to the precise photogeneration profile within the nanowire. Nevertheless, the data in Figure III.5 indicate that substantial losses in net photocurrent can arise from physical variation in the shape of the nanowire photoelectrode, irrespective of all other optoelectronic properties of the material.

iii. SRH Recombination Losses

For thin nanowire photoelectrodes with minimal surface defects and a full depletion region under ~1 sun illumination, the dominant recombination processes involve SRH recombination in the depletion region (i.e. the volume defined by $r = W_D$ and $r = r_0$) and the electric field-free 'bulk' (i.e. the volume defined by $r = 0$ and $r = W_D$). The most direct metric of semiconductor 'quality' as defined by SRH recombination is the minority carrier diffusion length,

$$L_p = \sqrt{\frac{k_B T}{q} \mu_p \tau_p} \qquad \text{(III.9)}$$

for an n-type material. As shown in Equations III.5 and III.6, SRH recombination losses in the depletion region versus bulk take on different functional forms with respect to L_p. For instance, Equations III.1 and III.5 predict an increase in V_{oc} of 0.12 V per decade

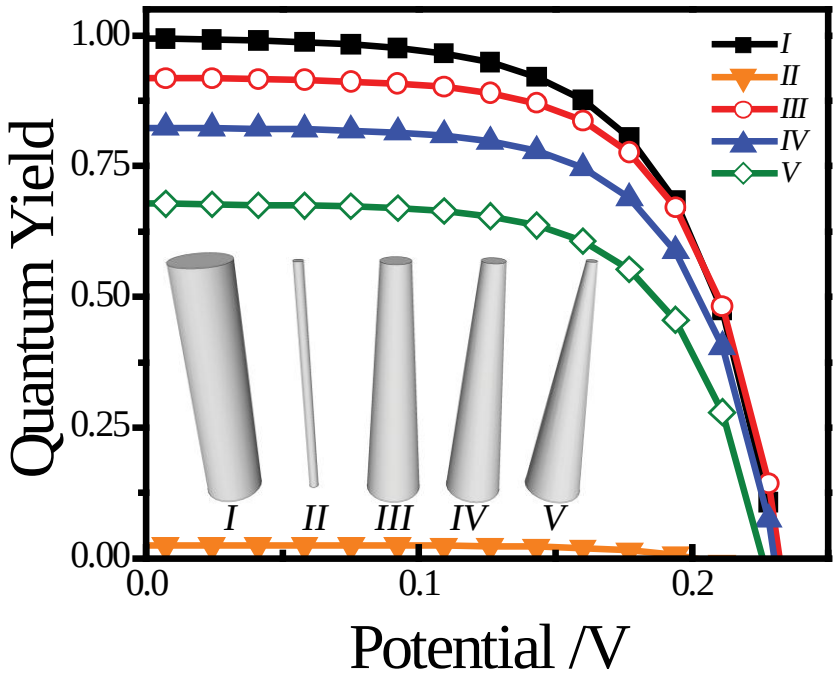

Figure III.5: Simulated quantum yield vs. potential for cylindrical and tapered nanowire photoelectrodes under AM 1.5 (direct+circumsolar) illumination. Inset: nanowire morphologies. *I:* cylinder with r_0 = 300 nm. *II:* cylinder with r_0= 50 nm. *III*-*V*: tapered cylinders with $r_{0,top}$ = 150, 115 and 50 nm, respectively and $r_{0,bottom}$ = 300 nm. All nanowires featured a uniform dopant density of 2 x 10^{16} cm^{-3} and an interfacial equilibrium barrier height of 1 eV.

increase in L_p due to bulk recombination processes, whereas Equations III.1 and III.6 predict a 0.24 V increase in V_{oc} per decade increase in L_p due to recombination in the depletion region. Since carrier diffusion length is a function of both mobility and lifetime, a series of simulations was run to determine how changes in μ_p, τ_p or both affected achievable open-circuit potentials.

Simulations were performed on cylindrical n-Si nanowire photoelectrodes with r_0 = 50 nm, z = 100 μm and Φ_B = 1 eV illuminated with AM 1.5 (direct+circumsolar) insolation. Figure III.6 summarizes the effect on the photocurrent density-potential responses of changes in μ_p and τ_p, where the value of μ_p was varied for specific values of τ_p. In these simulations, unity quantum yield corresponds to a photocurrent density of 35 mA cm^{-2}. In each plot, mobilities larger than the largest mobility value shown effected no further improvement/change in the photocurrent density-potential response. Several general points can be drawn from the data in Figure III.6. First, photoresponse behavior was not simply dictated not by the specific value for L_p, but depended instead on the interplay between μ_p and τ_p. For instance, a minority carrier diffusion length of L_p = 500 nm is shown in each plot of Figure III.6, but the photocurrent density-potential profiles are decidedly different. Second, the value of has a stronger influence on the value of V_{oc} for a thin cylindrical nanowire than μ_p. Decreasing the lifetime of the minority carrier by two orders of magnitude caused a pronounced diminution in V_{oc}. Conversely, decreasing the mobility of the minority carrier by two orders of magnitude primarily caused a decrease in photocurrent density and fill factor with minimal change in V_{oc}. Finally, a comparatively high minority carrier mobility (5 cm^2 V^{-1} s^{-1}) was required to achieve unity quantum yield at all the values of τ_p investigated in these simulations. Based on these findings, further simulations were performed to investigate the dependence of V_{oc} on L_p when μ_p was not a limiting factor. It should be noted that the threshold mobility of 5 cm^2 V^{-1} s^{-1} is well below the typical carrier mobility values for both crystalline Si and GaP, but is above that for many mid-sized bandgap metal oxides such as NiO and Fe_2O_3.[52-55]

Figures III.7a and III.7c illustrate the dependence of V_{oc} on L_p (with μ_p fixed at 470 cm^2 V^{-1} s^{-1}) for thin Si and GaP cylindrical nanowire photoelectrodes, respectively. Si and GaP nanowires featured a uniform dopant concentration of 1 x 10^{18} cm^{-3} and interfacial equilibrium barrier heights of 1 and 2 eV, respectively. For n-Si nanowire

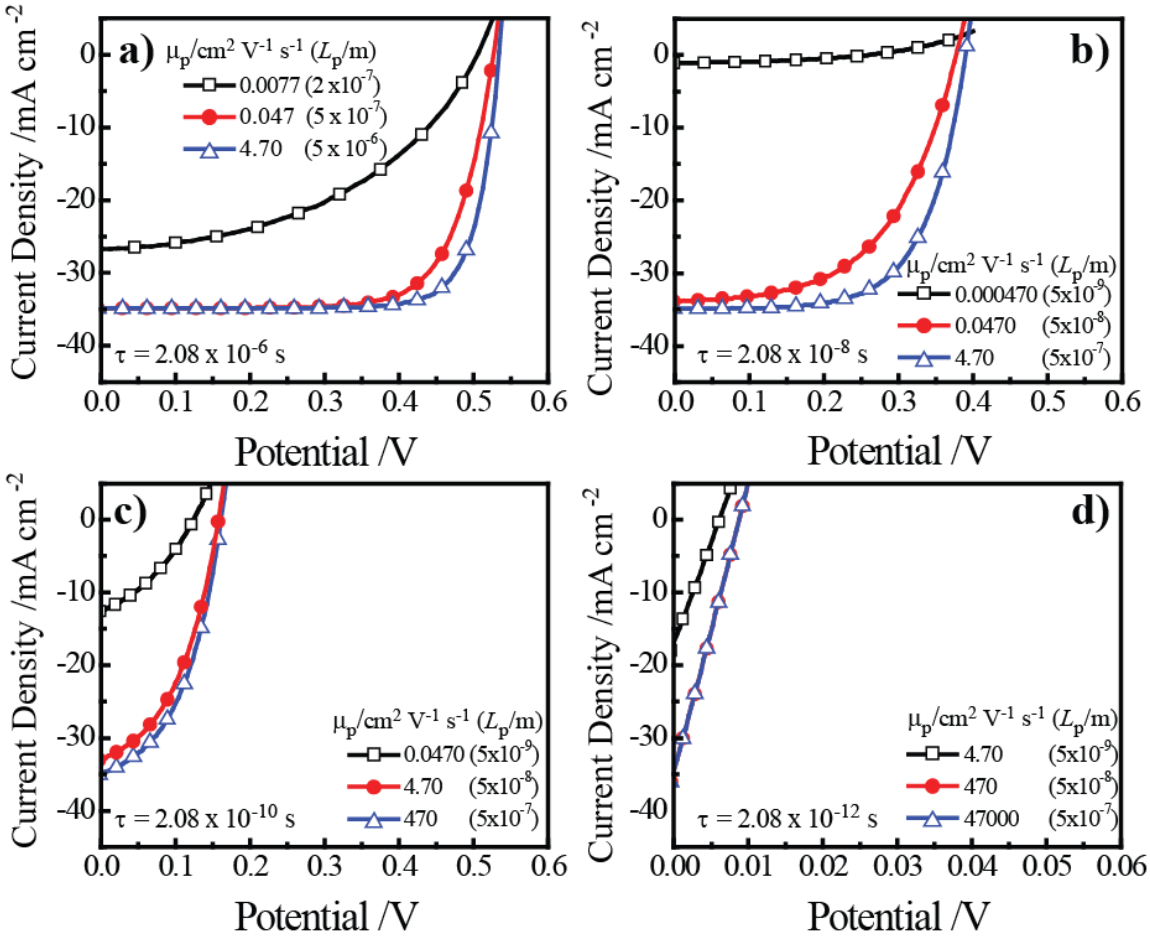

Figure III.6: Simulated current density-voltage photoresponses of a cylindrical n-Si nanowire. The nanowire featured a radius of 50 nm, a height of 100 μm and was in contact with an electrolyte resulting in an interfacial equilibrium barrier height of 1 eV. The nanowire was under AM 1.5 (direct+circumsolar) illumination. Several values of μ_p were assessed at (a) $\tau = 2.08 \times 10^{-6}$ s, (b) $\tau = 2.08 \times 10^{-8}$ s, (c) $\tau = 2.08 \times 10^{-10}$ s, and (d) $\tau = 2.08 \times 10^{-12}$ s.

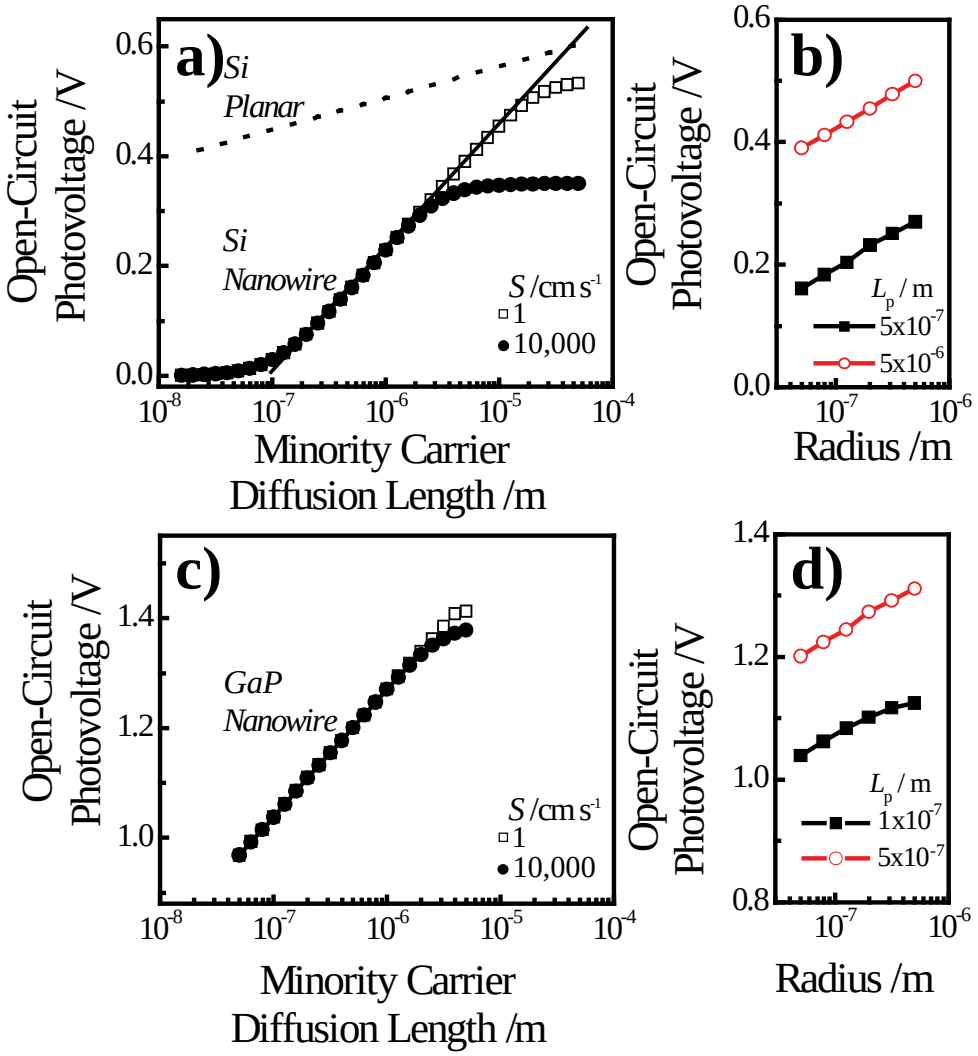

Figure III.7: Simulation results for cylindrical (a, b) n-Si and (c, d) n-GaP nanowire photoelectrodes with radii of 50 nm and heights of 100 μm under AM 1.5 (direct+circumsolar) illumination in contact with an electrolyte. Interfacial equilibrium barrier heights are (a, b) 1 eV and (c, d) 2 eV. (a) Open-circuit photovoltage of a Si nanowire versus minority carrier diffusion length simulated with at two different surface recombination velocity values. The dashed line indicates the expected dependence of a comparable planar photoelectrode operating under bulk recombination limitations. (b) Open-circuit photovoltage of a Si nanowire versus nanowire radius at two different values of minority carrier diffusion length. (c) Open-circuit photovoltage of a GaP nanowire versus minority carrier diffusion length simulated at two different values of the surface recombination velocity. (d) Open-circuit photovoltage of a GaP nanowire versus nanowire radius at two different values of the minority carrier diffusion length. In these simulations, L_p was adjusted by changing τ_p and μ_p was fixed at 470 $cm^2\ V^{-1}\ s^{-1}$.

simulations, the recorded values of V_{oc} were nominally zero and invariant to changes in L_p at values of $L_p < 100$ nm. For values of L_p greater than 100 nm, V_{oc} increased 0.229 V per decade increase in L_p. For the GaP nanowire simulations, the slope of V_{oc} versus $\log(L_p)$ was 0.232 with a minimal plateau region at large values of L_p. These slopes are noteworthy in three aspects. First, the data in Figure III.6 indicate that large photovoltages are achievable with relatively low-grade materials with moderate band gaps such as the modeled GaP, and are in accord with recent observations of the photoelectrochemical performance of high-aspect-ratio GaP photoelectrodes.[6] For a thin GaP nanowire with $r_0 = 500$ nm and $L_p = 500$ nm, an open-circuit voltage > 1.30 V is attainable under ~1 sun illumination. Second, a direct comparison of the open-circuit photovoltages attainable with planar versus thin nanowire photoelectrodes is not rigorously applicable even if the two photoelectrodes have identical optoelectronic properties. The slope values of approximately 0.24 V per decade for the nanowire simulations strongly suggest that SRH recombination in the depletion region is the limiting recombination process for both Si and GaP thin nanowires. Simulations where r_0 was varied between 50 nm and 500 nm at a constant value of L_p separately corroborated the predicted dependence of V_{oc} from Equations III.1 and III.6 when depletion region recombination dominates device performance (Figures III.7b and III.7d). For a planar n-Si photoelectrode with identical bulk and surface optoelectronic properties, the dependence of V_{oc} on L_p is **not** limited primarily by depletion region recombination. Instead, the slope of V_{oc} versus $\log(L_p)$ is 0.06 V, indicating that bulk recombination is limiting (Equation III.10; dashed line in Figure III.7a).[56]

$$V_{oc,planar} = \frac{k_B T}{q} \ln\left(\frac{J_{ph}}{J_0}\right) = \frac{k_B T}{q} \ln\left(\frac{J_{ph} q D_p n_i^2}{L_p N_D}\right) \qquad \text{(III.10)}$$

The above derivations and simulation results illustrate that the functional forms of J_0 differ significantly for high-aspect ratio nanowire versus planar electrode morphologies. Thus, the often-cited ratio of the projected to geometric surface area as justification for decreased photovoltages in high-aspect-ratio photoelectrodes is not always applicable.[6,57-59] The difference in V_{oc} observed for planar versus thin nanowire photoelectrodes is instead a consequence of the distinct spatial generation profiles within

the two architectures. Namely, in planar photoelectrodes most carriers are generated far away from the depletion region, while for thin nanowire photoelectrodes generation always occurs within or immediately adjacent to the depletion region.

For both Si and GaP nanowire simulations sets, a conversion to bulk recombination as the dominant factor controlling V_{oc} (with an expected slope of 0.12 V per decade change in L_p according to Equations III.1 and III.5) at large values of L_p was not observed. Instead, the open-circuit voltage became insensitive to L_p for large values of L_p (Figures III.7a and III.7c), indicating a switch from depletion region recombination to a surface-specific process with no functional dependence on L_p. This transition occurred at lower values of L_p for higher values of S and the discrepancy between the attainable V_{oc} values for large and small values of S were more pronounced for the n-Si nanowire than the n-GaP nanowire models (perhaps due to the larger value of Φ_B for GaP). These simulation results indicate that passivation of surface defects only results in larger open-circuit photovoltages when the bulk quality (i.e. L_p) of the nanowire is sufficiently high. In the absence of sufficiently large L_p values, passivation of surface defects is therefore predicted to have no influence on the attainable photovoltage of a thin nanowire photoelectrode. For short minority carrier diffusion lengths, additional simulations were performed to determine whether S had any effect on the expected photoresponse characteristics of thin nanowire photoelectrodes.

Figure III.8 presents three sets of photocurrent density-potential responses for models of planar n-Si, a cylindrical n-Si nanowire and a cylindrical n-GaP nanowire photoelectrode. For the two n-Si simulation sets, all optoelectronic properties are the same. For the planar n-Si photoelectrode in Figure III.8a, the shape of the photocurrent density-potential response was sensitive to the value of S with lower energy conversion efficiencies due to decreased V_{oc} for large values of S. By comparison, none of the features of the photoresponses in Figures III.8b-c showed any dependence on S. These data contradict the commonly asserted premise that the high surface area of thin nanowire photoelectrodes results in extreme sensitivity to surface defects/traps. The analysis presented here instead supports the contention that the operation of thin nanowire phototelectrodes with recombination in the depletion region as the dominant process is more sensitive to changes in bulk as compared to surface properties.

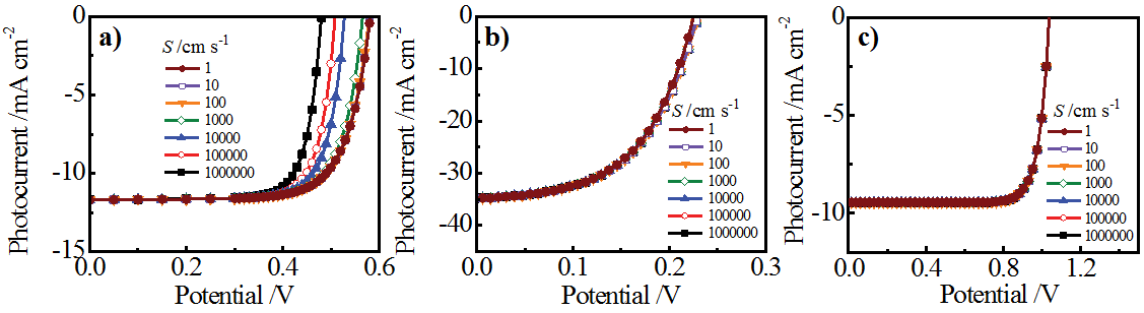

Figure III.8: Simulated current density-voltage photoresponses under AM 1.5 (direct+circumsolar) illumination. (a) A 100 μm thick planar n-Si photoelectrode, (b) an n-Si nanowire photoelectrode with a radius of 50 nm and a height of 100 μm, and (c) a n-GaP nanowire photoelectrode with a radius of 50 nm and a height of 100 μm across a range of surface recombination velocity, *S*, values.

iv. Discrete Ohmic-Selective Contacts

The preceding discussion focused exclusively on highly doped, high-aspect-ratio photoelectrodes under low-level injection (i.e. only the minority carrier concentration changed appreciably under illumination). The operation of such nanowires under high-level injection conditions (i.e. the concentration of both charge carrier types change substantially under illumination) has not yet been explored. Operation under high-level injection requires that either 1) the illumination intensity is dramatically increased versus 'normal' operation or 2) the dopant density of the nanowire is dramatically decreased. A superficial analysis indicates that both of these techniques would result in poor energy conversion performance due to 1) an intolerable level of Auger recombination or 2) lack of a sufficient electric field to efficiently separate and collect carriers.[7,60-62] Upon closer inspection, however, it is seen that these arguments hold rigorously only for doped, high-aspect-ratio nanowires contacted uniformly by a conductor that effects a large interfacial barrier height. An alternative contacting scheme featuring discrete, ohmic-selective contacts along the length of the nanowire will dramatically alter the functional form of Equations III.3 – III.6 and it is not clear *a priori* how such a system would perform. In order to assess the possible merits of high-aspect-ratio nanowire devices featuring discrete, ohmic-selective contacts, a separate set of simulations were performed that compared the performance of such a device to that of an analogous lightly-doped nanowire device with the morphology investigated above. Concentrated AM1.5 (direct+circumsolar) illumination was employed in order to achieve high-level injection and all other optoelectronic properties of the nanowires were kept constant.

Figure III.9a shows the modeling results for a lightly-doped Si nanowire photoelectrode with a uniform, conformal front contact that induces a 1 eV equilibrium barrier height. As expected from the preceding analyses, the overall quantum yields for photogenerated carriers at high-level injection for this device are exceedingly poor and fully consistent with severe majority carrier recombination losses through heterogeneous charge transfer at the surface. As a corollary, the resultant V_{oc} values are also poor even at illumination intensities 1000 times greater than AM1.5 solar insolation. Figure III.9b shows a simplified schematic for a segment of a high-aspect-ratio Si nanowire photoelectrode with discrete, ohmic-selective contact in the form of thin concentric

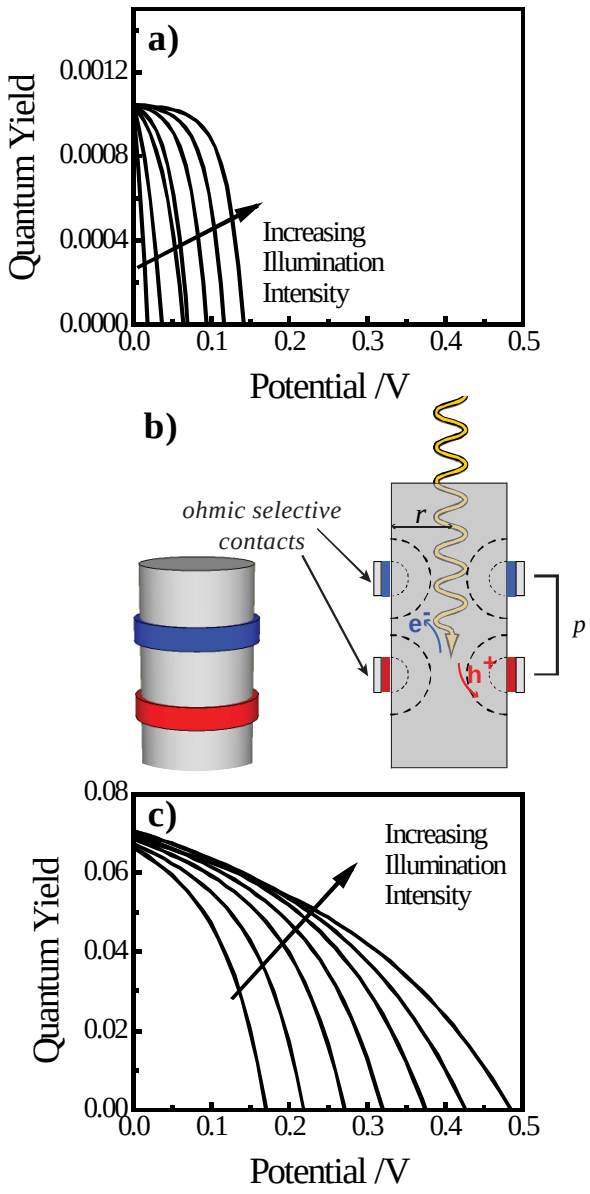

Figure III.9: Si nanowire devices with discrete, ohmic-selective contacts. (a) Simulated quantum yield versus potential responses under white light illumination at 1, 3, 10, 30, 100, 300, and 1000 times AM 1.5 (direct+circumsolar) illumination. (b) Schematic depiction of a nanowire photoelectrode with discrete, ohmic-selective contacts. (c) Simulated quantum yield versus potential responses for the same nanowire under the same illumination conditions as in (b) but with a conformal front contact with an interfacial equilibrium barrier height of 1 eV.

bands. In this structure the exposed surface between the contacts is modeled as a semiconductor/air interface subject to surface recombination at the rate set by *S*. In this scheme, the bulk of the nanowire is not depleted of carriers and thus is essentially free of any electric field (in contrast to the heterojunction model in Figure III.9a). Figure III.9c shows the modeling results of the quantum yield versus potential responses for one possible design of a discrete contact thin nanowire photoelectrode. The quantum yield versus potential responses in Figure III.9c differed significantly from those in Figure III.9a. Short-circuit quantum yields were 70 times greater than for the conventional device simulated in Figure III.9a and V_{oc} values were more than 0.15 V larger at all investigated illumination intensities. This increase in V_{oc} is in agreement with Equation III.10 and the premise that the structure in Figure III.9b (relatively devoid of strong electric fields) can support a higher built-up carrier concentration than the devices in Figure I.3. Accordingly, the net energy conversion possible with the discrete contact thin nanowire photoelectrode was approximately two orders of magnitude greater than with the conformal contact thin nanowire photoelectrode.

This preliminary analysis does not represent a thorough investigation of the discrete contact nanowire photoelectrode scheme, which follows in Chapter IV. The results shown in Figure III.9c are not expected to reflect the highest attainable collection efficiencies with this scheme. In fact, the photoresponses of planar semiconductor photoelectrodes with discrete contacts under high level injection are strongly dependent on the particular spatial arrangement of contacts and the properties of the semiconductor, and a similar dependence is expected for analogous nanowire devices.[63-67] It is noteworthy that aside from traditional group IV and III-V semiconductors, the vast majority of candidate earth-abundant semiconductors for solar energy conversion cannot be easily or precisely doped both n- and p-type. For example, doping strategies even for well-known materials like Fe_2O_3 are still active areas of research.[68-71] Precisely controlling both the morphology and electronic properties of a nanostructured semiconductor photoelectrode could be daunting for many materials and may ultimately be practical only for a select set of semiconductors. However, strategies like the use of discrete contacts, coupled with ohmic-selective contacting materials like conducting

polymers,[20,72] may be an alternative, general means for utilizing thin semiconductor nanowire materials for solar energy conversion.

E. Conclusion

This analysis focused on the operation of a single nanowire photoelectrode with greatly simplified photogeneration characteristics. Notwithstanding differences in the profiles of optical photogeneration of charge, the presented results are expected to be rigorously valid for a photoelectrode composed of a film of nanowires if all of the nanowires have equal size and electrical properties. In practice, relatively low-density nanowire arrays with heterogeneity in nanowire size and dopant levels are common. Still, in these ensemble systems, the impact of nanowire heterogeneity can be readily understood through the analyses presented here. Variation in the electronic and morphological properties of individual nanowires across a film of thin semiconductor nanowires in the manner described here will unavoidably lower the maximum attainable energy conversion efficiency of the film. To ensure that heterogeneity of nanowire structures in a film does not significantly limit the overall system energy conversion efficiency, methods to rapidly and accurately assess the doping condition in individual nanowires across large areas are vital. To date, this type of characterization in photoelectrochemical reports has not been routine.

Efficient operation of thin nanowire photoelectrodes for solar energy conversion requires precise control over both the conductive and morphological features of the nanowires. Both non-uniform dopant concentrations and tapering along the nanowire length can result in internal electric fields too small to prevent majority carriers from reaching the front contact. In the context of n-type nanowire photoelectrodes, the resultant high rate of heterogeneous electron transfer at the semiconductor/electrolyte interface partially or completely obscures the possibility of large net anodic photocurrent densities with electrodes featuring a high-aspect-ratio form factor. These results should be rigorously applicable to cathodic photocurrent densities at analogous p-type nanowire photoelectrodes as well.

For thin nanowire photoelectrodes capable of supporting a full depletion region, the presented results indicate that perhaps the most direct means of improving

photoconversion performance is to increase the minority carrier diffusion length. Although photoresponse characteristics were poor for any system featuring low carrier mobility values, extremely high carrier mobility values were likewise unnecessary to achieve high photocurrent densities, large open-circuit voltages and respectable fill factors. Thin nanowire morphologies do not appear to impose the need for the same high magnitudes of carrier mobilities as required in high-speed electronics, but neither do they overcome the reality that low carrier mobilities will still result in poor solar energy conversion properties. In practical terms, experimental efforts directed at improving the transport of charge carriers within the nanostructured semiconductor will be most effective in improving solar energy conversion for semiconductor materials with innately low carrier mobilities. Likewise, any experimental approach that can increase the minority carrier diffusion length of a material will translate to significant gains in the attainable open circuit photovoltage. The marked sensitivity of V_{oc} to L_p in thin n-type nanowire photoelectrodes arises from depletion region recombination being the limiting factor in J_0. Specifically, the notion that the minority carrier length only needs to be as large as the nanowire radius to ensure good photoconversion performance is misleading. In fact, larger increases in L_p can substantially increase the attainable photovoltage, as can increasing the radius of a thin nanowire photoelectrode. This is likely due to the ability of nanowires with larger radii and longer time constants to support higher built-up carrier concentrations. Further, from a practical standpoint, the presented analysis also quantitatively justifies the principle that mid-sized bandgap, thin nanowire photoelectrodes can feature large photovoltages (> 1 V) and appreciable photocurrent densities under solar illumination. Continued work on developing these materials for artificial photosynthetic cells do not need to focus first and foremost on passivating surface defects since depletion region and not surface recombination is the limiting factor determining J_0 in most scenarios. In fact, efforts to chemically passivate surface defects will not translate into meaningful energy conversion efficiency enhancements unless the minority carrier diffusion length is first made larger than ~1 μm.

Finally, one possible strategy to circumvent the stringent doping and sizing requirements in thin nanowire photoelectrodes is to employ discrete, ohmic-selective contacts and concentrated insolation conditions. The presented results indicate that a

lightly-doped nanowire can exhibit superior photocurrent density and photovoltage responses with thin ohmic-selective versus conformal n- and p-type contacts. Further modeling analyses that rigorously identify the benefits and limitations of this system are presented in Chapter IV. Even the cursory results presented here, however, serve as an example for new directions in the design of photoelectrodes for photoelectrochemical energy conversion.

F. References

1 Archer, M. D. & Nozik, A. J. in *Series on Photoconversion of Solar Energy* Vol. 3 (ed Mary D. Archer) (Imperial Colege Press, London, 2008).

2 Khaselev, O. & Turner, J. A. A Monolithic Photovoltaic-Photoelectrochemical Device for Hydrogen Production via Water Splitting. *Science* **280**, 425-427 (1998).

3 Morrison, S. R. & Freund, T. Chemical Role of Holes and Electrons in ZnO Photocatalysis. *Journal of Chemical Physics* **47**, 1543-1551 (1967).

4 Tan, M. X. *et al.* Principles and Applications of Semiconductor Photoelectrochemistry. *Progress in Inorganic Chemistry, Vol 41* **41**, 21-144 (1994).

5 Tributsch, H. & Gerischer, H. The Use of Semiconductor Electrodes in the Study of Photochemical Reactions. *Berichte Der Bunsen-Gesellschaft-Physical Chemistry Chemical Physics* **73**, 850-854 (1969).

6 Price, M. J. & Maldonado, S. Macroporous n-GaP in Nonaqueous Regenerative Photoelectrochemical Cells. *Journal of Physical Chemistry C* **113**, 11988-11994 (2009).

7 Hagedorn, K., Forgacs, C., Collins, S. & Maldonado, S. Design Considerations for Nanowire Heterojunctions in Solar Energy Conversion/Storage Applications. *Journal of Physical Chemistry C* **114**, 12010-12017 (2010).

8 Kelzenberg, M. D. *et al.* Enhanced Absorption and Carrier Collection in Si Wire Arrays for Photovoltaic Applications. *Nature Materials* **9**, 239-244 (2010).

9 Maiolo, J. R., Atwater, H. A. & Lewis, N. S. Macroporous Silicon as a Model for Silicon wire Array Solar Cells. *Journal of Physical Chemistry C* **112**, 6194-6201 (2008).

10 Maiolo, J. R. *et al.* High Aspect Ratio Silicon Wire Array Photoelectrochemical Cells. *Journal of the American Chemical Society* **129**, 12346-12347 (2007).

11 Kayes, B. M., Atwater, H. A. & Lewis, N. S. Comparison of the Device Physics Principles of Planar and Radial p-n Junction Nanorod Solar Cells. *Journal of Applied Physics* **97** (2005).

12 Dong, Y. J., Tian, B. Z., Kempa, T. J. & Lieber, C. M. Coaxial Group III-Nitride Nanowire Photovoltaics. *Nano Letters* **9**, 2183-2187 (2009).

13 Kuykendall, T., Ulrich, P., Aloni, S. & Yang, P. Complete Composition Tunability of InGaN Nanowires Using a Combinatorial Approach. *Nature Materials* **6**, 951-956 (2007).

14 Wang, X. D. *et al.* Growth of Uniformly Aligned ZnO Nanowire Heterojunction Arrays on GaN, AIN, and $Al_{0.5}Ga_{0.5}N$ Substrates. *Journal of the American Chemical Society* **127**, 7920-7923 (2005).
15 Leschkies, K. S. *et al.* Photosensitization of ZnO Nanowires with CdSe Quantum Dots for Photovoltaic Devices. *Nano Letters* **7**, 1793-1798 (2007).
16 Law, M., Greene, L. E., Johnson, J. C., Saykally, R. & Yang, P. Nanowire Dye-Sensitized Solar Cells. *Nature Materials* **4**, 455-459 (2005).
17 Wen, W. *et al.* Structural and Photoelectrochemical Properties of GaP Nanowires Annealed in NH3. *The Journal of Physical Chemistry C* **115**, 22652-22661 (2011).
18 Carim, A. I., Collins, S. M., Foley, J. M. & Maldonado, S. Benchtop Electrochemical Liquid–Liquid–Solid Growth of Nanostructured Crystalline Germanium. *Journal of the American Chemical Society* **133**, 13292-13295 (2011).
19 Foley, J. M., Price, M. J., Feldblyum, J. I. & Maldonado, S. Analysis of the Operation of Thin Nanowire Photoelectrodes for Solar Energy Conversion. *Energy & Environmental Science* **5**, 5203-5220 (2012).
20 Fonash, S. *Solar Cell Device Physics, 2nd Ed.*, (Academic Press, 2010).
21 Schroder, D. K. Carrier Lifetimes in Silicon. *IEEE Transactions on Electron Devices* **44**, 160-170 (1997).
22 Rosenbluth, M. L. & Lewis, N. S. Kinetic Studies of Carrier Transport and Recombination at the n-Silicon/Methanol Interface. *Journal of the American Chemical Society* **108**, 4689-4695 (1986).
23 Kumar, A., Wilisch, W. C. A. & Lewis, N. S. The Electrical Properties of Semiconductor-Metal, Semiconductor-Liquid, and Semiconductor-Polymer Contacts. *Critical Reviews in Solid State and Materials Sciences* **18**, 327-353 (1993).
24 Lewis, N. S. An Analysis of Charge Transfer Rate Constants for Semiconductor/Liquid Interfaces. *Annual Review of Physical Chemistry* **42**, 543-580 (1991).
25 Kumar, A., Santangelo, P. G. & Lewis, N. S. Electrolysis of Water at $SrTiO_3$ Photoelectrodes: Distinguishing between the Statistical and Stochastic Formalisms for Electron-Transfer Processes in Fuel-Forming Photoelectrochemical Systems. *Journal of Physical Chemistry* **96**, 834-842 (1992).
26 Anz, S. J. & Lewis, N. S. Simulations of the Steady-State Current Density vs Potential Characteristics of Semiconducting Electrodes. *Journal of Physical Chemistry B* **103**, 3908-3915 (1999).
27 LaPierre, R. R. Numerical Model of Current-Voltage Characteristics and Efficiency of GaAs Nanowire Solar Cells. *Journal of Applied Physics* **109** (2011).
28 Zervos, M. Properties of the Ubiquitous p-n Junction in Semiconductor Nanowires. *Semiconductor Science and Technology* **23**, 075016(075011-075017) (2008).
29 Finklea, H. O. *Semiconductor Electrodes*. (Elsevier, 1984).
30 Bank, R. E., Rose, D. J. & Fichtner, W. Numerical Methods for Semiconductor Device Simulation. *IEEE Electron Device Letters* **30**, 1031-1041 (1983).

31 Canovas, E. *et al.* Photoreflectance Analysis of a GaInP/GaInAs/Ge Multijunction Solar Cell. *Applied Physics Letters* **97** (2010).
32 Kapadia, R., Fan, Z. Y. & Javey, A. Design Constraints and Guidelines for CdS/CdTe Nanopillar Based Photovoltaics. *Applied Physics Letters* **96** (2010).
33 Kelzenberg, M. D. *et al.* High-Performance Si Microwire Photovoltaics. *Energy & Environmental Science* **4**, 866-871 (2011).
34 Morrison, S. R. *Electrochemistry at Semiconductor and Oxidized Metal Electrodes*. (Plenum Press, 1980).
35 Aspnes, D. E. & Studna, A. A. Dielectric Functions and Optical Parameters of Si, Ge, GaP, GaAs, InP, InAs, and InSb From 1.5 to 6.0 eV. *Physical Review B* **27**, 985-1009 (1983).
36 Lindgren, T. *et al.* Aqueous Photoelectrochemistry of Hematite Nanorod Array. *Solar Energy Materials and Solar Cells* **71**, 231-243 (2002).
37 Royea, W. J., Fajardo, A. M. & Lewis, N. S. Fermi Golden Rule Approach to Evaluating Outer-Sphere Electron-Transfer Rate Constants at Semiconductor/Liquid Interfaces. *Journal of Physical Chemistry B* **101**, 11152-11159 (1997).
38 Kelzenberg, M. D. *et al.* in *PVSC: 2008 33rd IEEE Photovoltaic Specialists Conference, Vols 1-4 IEEE Photovoltaic Specialists Conference* 144-149 (2008).
39 Yuan, G. B. *et al.* Synthesis and Photoelectrochemical Study of Vertically Aligned Silicon Nanowire Arrays. *Angewandte Chemie - International Edition* **48**, 9680-9684 (2009).
40 Schubert, E. F. *Doping in III-V Semiconductors*. (Cambridge University Press, 2005).
41 Garnett, E. C. *et al.* Dopant Profiling and Surface Analysis of Silicon Nanowires Using Capacitance-Voltage Measurements. *Nature Nanotechnology* **4**, 311-314 (2009).
42 Putnam, M. C. *et al.* Secondary Ion Mass Spectrometry of Vapor-Liquid-Solid Grown, Au-Catalyzed, Si Wires. *Nano Letters* **8**, 3109-3113 (2008).
43 Radovanovic, P. V. Nanowires: Keeping Track of Dopants. *Nature Nanotechnology* **4**, 282-283 (2009).
44 Perea, D. E. *et al.* Direct Measurement of Dopant Distribution in an Individual Vapour-Liquid-Solid Nanowire. *Nature Nanotechnology* **4**, 315-319 (2009).
45 Ronning, C., Borschel, C., Geburt, S. & Niepelt, R. Ion Beam Doping of Semiconductor Nanowires. *Materials Science & Engineering R - Reports* **70**, 30-43 (2010).
46 Prakasam, H. E., Varghese, O. K., Paulose, M., Mor, G. K. & Grimes, C. A. Synthesis and Photoelectrochemical Properties of Nanoporous Iron (III) Oxide by Potentiostatic Anodization. *Nanotechnology* **17**, 4285-4291 (2006).
47 Rangaraju, R. R., Raja, K. S., Panday, A. & Misra, M. Low-Cost Photoelectrocatalyst Based on a Nanoporous Oxide Layer of Low-Carbon Steel. *Journal of Physics D - Applied Physics* **43**, 445301 (2010).
48 Cao, L. Y. *et al.* Instability and Transport of Metal Catalyst in the Growth of Tapered Silicon Nanowires. *Nano Letters* **6**, 1852-1857 (2006).

49 Chen, X. L., Lan, Y. C., Li, J. Y., Cao, Y. G. & He, M. Radial Growth Dynamics of Nanowires. *Journal of Crystal Growth* **222**, 586-590 (2001).
50 Dick, K. A., Deppert, K., Samuelson, L. & Seifert, W. InAs Nanowires Grown by MOVPE. *Journal of Crystal Growth* **298**, 631-634 (2007).
51 Hannon, J. B., Kodambaka, S., Ross, F. M. & Tromp, R. M. The Influence of the Surface Migration of Gold on the Growth of Silicon Nanowires. *Nature* **440**, 69-71 (2006).
52 Beermann, N., Vayssieres, L., Lindquist, S. E. & Hagfeldt, A. Photoelectrochemical Studies of Oriented Nanorod Thin Films of Hematite. *Journal of the Electrochemical Society* **147**, 2456-2461 (2000).
53 Iordanova, N., Dupuis, M. & Rosso, K. M. Charge Transport in Metal Oxides: A Theoretical Study of Hematite Alpha-Fe_2O_3. *Journal of Chemical Physics* **122** (2005).
54 Roilos, M. & Nagels, P. Electrical Measurements on CoO and NiO Single Crystals. *Solid State Communications* **2**, 285-290 (1964).
55 Shimotani, H., Suzuki, H., Ueno, K., Kawasaki, M. & Iwasa, Y. P-type Field-Effect Transistor of NiO with Electric Double-Layer Gating. *Applied Physics Letters* **92**, 242107(242101-242103) (2008).
56 Yae, S., Kawamoto, Y., Tanaka, H., Fukumuro, N. & Matsuda, H. Formation of Porous Silicon by Metal Particle Enhanced Chemical Etching in HF Solution and its Application for Efficient Solar Cells. *Electrochemistry Communications* **5**, 632-636 (2003).
57 Dalchiele, E. A., Martin, F., Leinen, D., Marotti, R. E. & Ramos-Barrado, J. R. Single-Crystalline Silicon Nanowire Array-Based Photoelectrochemical Cells. *Journal of the Electrochemical Society* **156**, K77-K81 (2009).
58 Spurgeon, J. M., Atwater, H. A. & Lewis, N. S. A Comparison Between the Behavior of Nanorod Array and Planar Cd(Se, Te) Photoelectrodes. *Journal of Physical Chemistry C* **112**, 6186-6193 (2008).
59 Sankir, N. D. & Dogan, B. Investigation of Structural and Optical Properties of the CdS and CdS/PPy Nanowires. *Journal of Materials Science* **45**, 6424-6432 (2010).
60 Green, M. A. Limits on the Open-Circuit Voltage and Efficiency of Silicon Solar Cells Imposed by Intrinsic Auger Processes. *Electron Devices, IEEE Transactions on* **31**, 671-678 (1984).
61 Kerr, M. J., Cuevas, A. & Campbell, P. Limiting Efficiency of Crystalline Silicon Solar Cells Due to Coulomb-Enhanced Auger Recombination. *Progress in Photovoltaics: Research and Applications* **11**, 97-104 (2003).
62 Vossier, A., Hirsch, B. & Gordon, J. M. Is Auger Recombination the Ultimate Performance Limiter in Concentrator Solar Cells? *Applied Physics Letters* **97** (2010).
63 Swanson, R. M. Point-Contact Solar Cells: Modelling and Experiment. *Solar Cells* **17**, 85-118 (1986).
64 Allsop, N., Nurnberg, R., Lux-Steiner, M. C. & Schedel-Niedrig, T. Three-Dimensional Simulations of a Thin Film Heterojunction Solar Cell with a Point Contact/Defect Passivation Structure at the Heterointerface. *Applied Physics Letters* **95** (2009).

65 Sinton, R. A., Kwark, Y., Swirhun, S. & Swanson, R. M. Silicon Point Contact Concentrator Solar Cells. *IEEE Electron Device Letters* **6**, 405-407 (1985).
66 Sinton, R. A. & Swanson, R. M. Design Criteria for Si Point-Contact Concentrator Solar Cells. *IEEE Transactions on Electron Devices* **34**, 2116-2123 (1987).
67 Timmons, M. L., LaMorte, M. F., Chiang, P. K., Hutchby, J. A. & Delyon, T.
68 Aroutiounian, V. M. *et al.* Photoelectrochemistry of Tin-Doped Iron Oxide Electrodes. *Solar Energy* **81**, 1369-1376 (2007).
69 Cesar, I., Sivula, K., Kay, A., Zboril, R. & Graetzel, M. Influence of Feature Size, Film Thickness, and Silicon Doping on the Performance of Nanostructured Hematite Photoanodes for Solar Water Splitting. *Journal of Physical Chemistry C* **113**, 772-782 (2009).
70 Gardner, R. F. G., Tanner, D. W. & Sweett, F. Electrical Properties of Alpha Ferric Oxide 2. Ferric Oxide of High Purity *Journal of Physics and Chemistry of Solids* **24**, 1183-1196 (1963).
71 Hu, Y. S. *et al.* Pt-Doped Alpha-Fe_2O_3 Thin Films Active for Photoelectrochemical Water Splitting. *Chemistry of Materials* **20**, 3803-3805 (2008).
72 Kawakami, K., Fujii, T., Yae, S. & Nakato, Y. Improvement in Photovoltage and Stability of Porous n-Si Electrodes Coated with Platinum by Regulation of the Thickness of Nanoporous Layers. *Journal of Physical Chemistry B* **101**, 4508-4513 (1997).

CHAPTER IV

Simulation Analysis of Nanowire Solar Cells Featuring Discrete Ohmic-Selective Contacts

A. Introduction

This chapter reports on the photoresponse of single n-Si discrete-contact nanowires within nanowire solar cells modeled via the advanced finite-element software package TCAD Sentaurus (Synopsys). Specifically, the performance of discrete-contact nanowire solar cells is modeled for a variety of material properties and system configurations and is contrasted to modeled photoresponses for analogous nanowire devices featuring conformal Schottky contacts. The large open-circuit potentials, V_{oc}, short-circuit internal quantum yields, Φ_{sc}, and fill factors, *FF*, observed over a broad range of device parameters indicate that a discrete contacting scheme can offer high performance for nanowire array devices without the stringent purity requirements of planar discrete-contact solar cells.

Semiconductors featuring high-aspect-ratio morphologies with dimensions of ~10-100 nm are a promising class of materials for efficient, low-energy-input solar cells due to their excellent optical absorption properties,[1] effectiveness in overcoming short carrier diffusion lengths[2] and ability to be grown at lower processing temperatures than crystalline wafers.[3,4] Several key challenges must be addressed, however, if nanostructured solar cells are to achieve sufficient levels of performance to contribute to energy production on a meaningful scale. Nanowire solar cells such as the device featuring a conformal Schottky contact in Figure IV.1a, for example, only exhibit large photocurrents and open-circuit voltages if the nanowire donor density, N_D, and radius, r, fall within a narrow window defined by the device's barrier height and the dielectric properties of the semiconductor.[5,6] This N_D, r interdependence is problematic for many

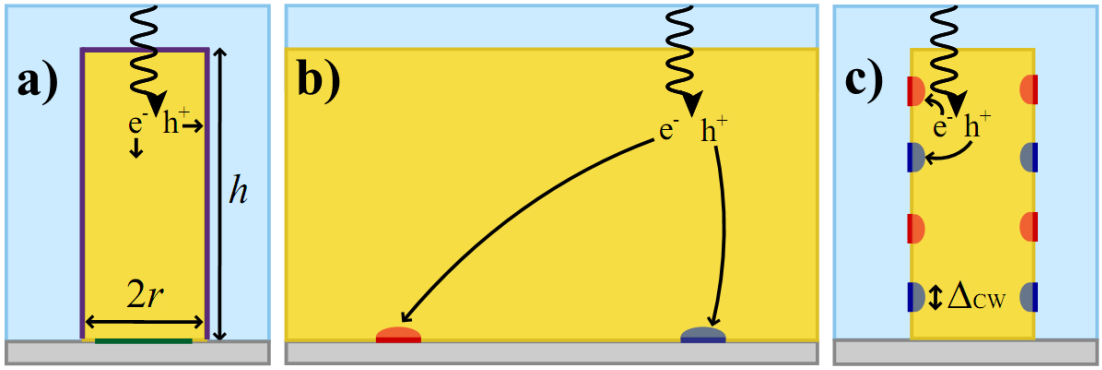

Figure IV.1: Partial cross-section schematic for (a) a typical heterojunction nanowire solar cell, (b) a planar discrete-contact solar cell, and (c) a nanowire discrete-contact solar cell. Electron-selective (hole-selective) contacts are shown in red (dark blue) and adjacent red (dark blue) regions correspond to degenerate n-type (p-type) doping. The conformal Schottky contact and back ohmic contact are shown in purple and green, respectively. Δ_{CW}, r, and h represent the contact width, nanowire height and nanowire radius, respectively. Not drawn to scale.

nanowire devices, as it is notoriously difficult to control both the n- and p-type dopant density and radius of most nanowires using scalable growth techniques.[7-13]

The strong dependence of nanowire solar cell performance on r and N_D is intrinsic to nanowire devices for which carrier separation/collection occurs primarily via drift in sizeable depletion regions within the nanowire (Figure IV.1a). In such devices, it is essential that a full depletion width 'fit' inside the nanowire to provide a sufficiently strong electric field to facilitate carrier separation/collection.[5,6] Drift-based carrier transport in a sizeable depletion region is not a prerequisite for efficient solar cell operation, however. In fact, the most efficient commercially available single-junction Si photovoltaics[14] do not feature large depletion regions for carrier separation/collection.[15-17] Planar discrete-contact solar cells typically feature a ~100 μm layer of lightly-doped or intrinsic Si with a textured front surface and a highly reflective back surface that is patterned with discrete (~100 μm^2, 50 μm center-to-center spacing) contacts made ohmic-selective toward electron or hole capture by degenerate n- or p-type doping, respectively (Figure IV.1b).[15-17] Electrons and holes photogenerated in these cells typically must diffuse up to 150 μm or more before being collected at the nearest contact. In the absence of strong electric fields to drive carriers rapidly toward contacts, carrier collection times in planar discrete-contact solar cells typically exceed 1 ms. The extreme material purity (and corresponding large energy inputs into semiconductor wafer production) necessary to realize a > 1 ms carrier lifetime in Si introduces significant challenges to the large-scale implementation of planar discrete-contact solar cells. The introduction of non-planar architectures to decrease carrier collection length in a discrete contacting scheme could, in principle, lead to a device that features the high performance of planar discrete-contact solar cells but can be constructed from lower-quality materials that can be produced with significantly reduced energy inputs.

In this chapter the finite-element software package TCAD Sentaurus (Synopsys) was used to quantitatively explore the extent to which discrete-contact *nanowire* architectures (Figure IV.1c) could (*1*) overcome the r, N_D constraints common to nanowire devices which require large depletion regions for efficient carrier separation/collection (such as those with conformal Schottky contacts), and (*2*) afford large photovoltages, high photocurrent densities and sharp fill factors while relaxing the

stringent purity requirements inherent to planar discrete-contact devices. The effects of design parameters such as the number and size of contacts and surface recombination velocity were also investigated in order to provide further insight on the design and operation of nanowire array discrete-contact solar cells.

B. Methods

The steady-state operation of single-nanowire semiconductor devices was simulated by solving for the potential, ϕ, and the carrier densities, n and p, as a function of position within each device. Potential and carrier densities were related through the coupled Poisson and carrier continuity equations, given respectively by Equations IV.1 and IV.2,[18]

$$\nabla \cdot \varepsilon_s \nabla \phi = -q\left(p - n + N_D - N_A\right) - \rho_{trap} \tag{IV.1}$$

$$\nabla \cdot \vec{J}_n = qR_{net} + q\frac{\partial n}{\partial t} \tag{IV.2a}$$

$$-\nabla \cdot \vec{J}_p = qR_{net} + q\frac{\partial p}{\partial t} \tag{IV.2b}$$

where ε_s is the semiconductor permittivity, q is the unsigned charge of an electron, N_D and N_A are the donor and accepter concentrations, ρ_{trap} is the charge density associated with traps and fixed charges, R_{net} is the net carrier recombination rate, and a cylindrical coordinate system with rotational symmetry about the center of the nanowire is assumed for all operators. The current densities $\vec{J}_n$ and $\vec{J}_p$ are given by Equation IV.3,[19]

$$\vec{J}_n = q\mu_n n\vec{E} + qD_n \nabla n \tag{IV.3a}$$

$$\vec{J}_p = q\mu_p p\vec{E} - qD_p \nabla p \tag{IV.3b}$$

where μ_n and μ_p are the electron and hole mobilities, D_n and D_p are the diffusion coefficients for electrons and holes and the sign of $\vec{J}_n$ and $\vec{J}_p$ correspond to the flow of positive charge. The first term in Equations IV.3a and IV.3b corresponds to carrier drift in response to an electric field, $\vec{E} = -\nabla\phi$, where ϕ is the electric potential. Near each contact, the electric field is proportional to the change in electric potential, $-\nabla\phi \propto -\Delta\phi\,\hat{r}$. The second term in Equations IV.3a and IV.3b describes diffusion along

a carrier concentration gradient, ∇n or ∇p. Equation IV.3a indicates that electrons diffuse toward regions with lower n and simultaneously drift toward regions at more positive potentials ($\Delta\phi > 0$). Likewise, Equation IV.3b indicates that holes diffuse toward regions with lower p and drift toward regions with negative $\Delta\phi$.

The explicit form of Equation IV.1 for the discrete-contact nanowire device pictured in Figure IV.1c is included in Appendix A. The analytic solution of the coupled set of Equations IV.1-IV.3 is not possible due to the nonuniformity in N_D and N_A along the length of each discrete-contact nanowire device. This work therefore uses the advanced multi-dimensional software package TCAD Sentaurus[18] (Synopsys) to explore the discrete-contact nanowire design using an exclusively numerical technique.

Sentaurus Device, a tool within the TCAD Sentaurus suite, served as the primary virtual semiconductor device simulator. Sentaurus Device utilized the finite-element box method[21] to simultaneously solve Equations IV.1-IV.3 subject to specified carrier recombination and generation processes throughout the device.[22-24] The nanowire device structure and simulation mesh were generated via Sentaurus Structure Editor, another tool within the TCAD suite. Finite simulation regions were defined using the automatic meshing tool snmesh. A refined mesh was incorporated near each contact (< 1 Å spacing in the radial dimension, < 5 nm spacing along the length of the nanowire for all discrete contacts) and at all material interfaces in order to better resolve carrier transport, separation and recombination processes within the device. A multi-box meshing scheme was utilized near the top of the nanowire to further improve the resolution of the carrier photogeneration profile.[20] Figure IV.2 illustrates the simulation mesh used in different portions of each nanowire device. Each three-dimensional cylindrical nanowire was modeled using only two spatial coordinates by specifying radial symmetric boundary conditions within Sentaurus Device.

Each discrete-contact nanowire simulation featured a single n-Si nanowire with between 2 and 72 contacts with alternating selectivity toward either hole or electron capture. Contacts were modeled as typically thin (20 nm), concentric bands spanning the girth of the nanowire and were made ohmic-selective either by (*1*) degenerately doping with donors (for electron collection) or accepters (for hole collection) or (*2*) specifying large asymmetries in the electron and hole collection velocities at each contact. Dopant-

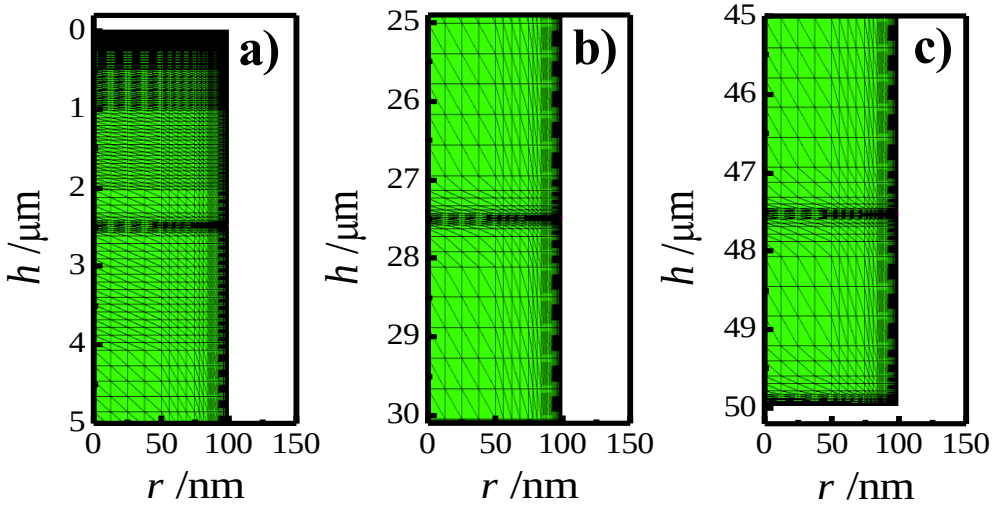

Figure IV.2: Cross-section views of the (a) top, (b) middle and (c) bottom of a single discrete contact nanowire with ten dopant-diffused, alternating hole selective and electron selective contacts along the length of the wire. The thin black lines represent mesh element boundaries. Discrete contacts are located at h = 2.5 μm, h = 27.5 μm and h = 47.5 μm. Major simulation parameters: radius = 100 nm, contact width = 20 nm, dopant density = 10^{12} cm^{-3}. Additional simulation parameters were set to default values and are given in Table B.2 in Appendix B.

diffused discrete contacts featured a complementary error function doping profile to mimic drive-in diffusion of either (electron-selective contacts) phosphorous or (hole-selective contacts) boron. Undoped discrete-contact devices featured high electron (low hole) collection velocities at electron-selective contacts and high hole (low electron) collection velocities at hole-selective contacts. Hole- and electron-selective contacts were evenly spaced along the 50 μm length of each nanowire and the electron affinity of each contact was adjusted to match that of the immediately adjacent Si. During simulated steady-state operation, the potential at electron-selective contacts was specified as 0 V and a positive bias potential was applied uniformly to all hole-selective contacts. As is discussed in detail herein, carrier transport near contact regions of each type is distinct but in both cases can support efficient carrier separation/collection. The schematic in Figure IV.3 illustrates the conduction and valence band energetics and dominant charge collection mechanisms at discrete electron-selective and hole-selective contacts for devices featuring both doped and undoped contacts. Devices featuring a single conformal Schottky contact were modeled with the side and top of the nanowire constituting a single p-type contact featuring a 1.0 V barrier height with bulk-transport-limited carrier collection velocities of 10^7 cm s^{-1} for both carrier types at each contact. A single n-type contact spanning the nanowire base was specified at a potential of 0 V for the duration of each simulation.

Each simulation accounted for radiative, Auger, and Shockley-Read-Hall (SRH) recombination processes in all device regions. As will be discussed below, Auger processes represented the limiting recombination mechanism for the single-nanowire discrete-contact devices simulated with favorable optoelectronic properties and high illumination levels herein. Shockley-Read-Hall recombination in the semiconductor bulk and at surface states was modeled with a single trap level located at the energy of the intrinsic Fermi level. Surface recombination velocity, S, was adjusted by separately tuning the SRH time constant within a thin (~ 1 lattice spacing) Si sheath enveloping the nanowire. S was calculated by dividing the sheath thickness by the SRH time constant specified for the surface layer. All other optoelectronic properties of the sheath were set equal to those in the nanowire bulk. Hole and electron lifetimes in the nanowire bulk and surface layer were set equal to each other so that $\tau_{SRH,n} = \tau_{SRH,p} = \tau_{SRH}$ and $S_n = S_p = S$.

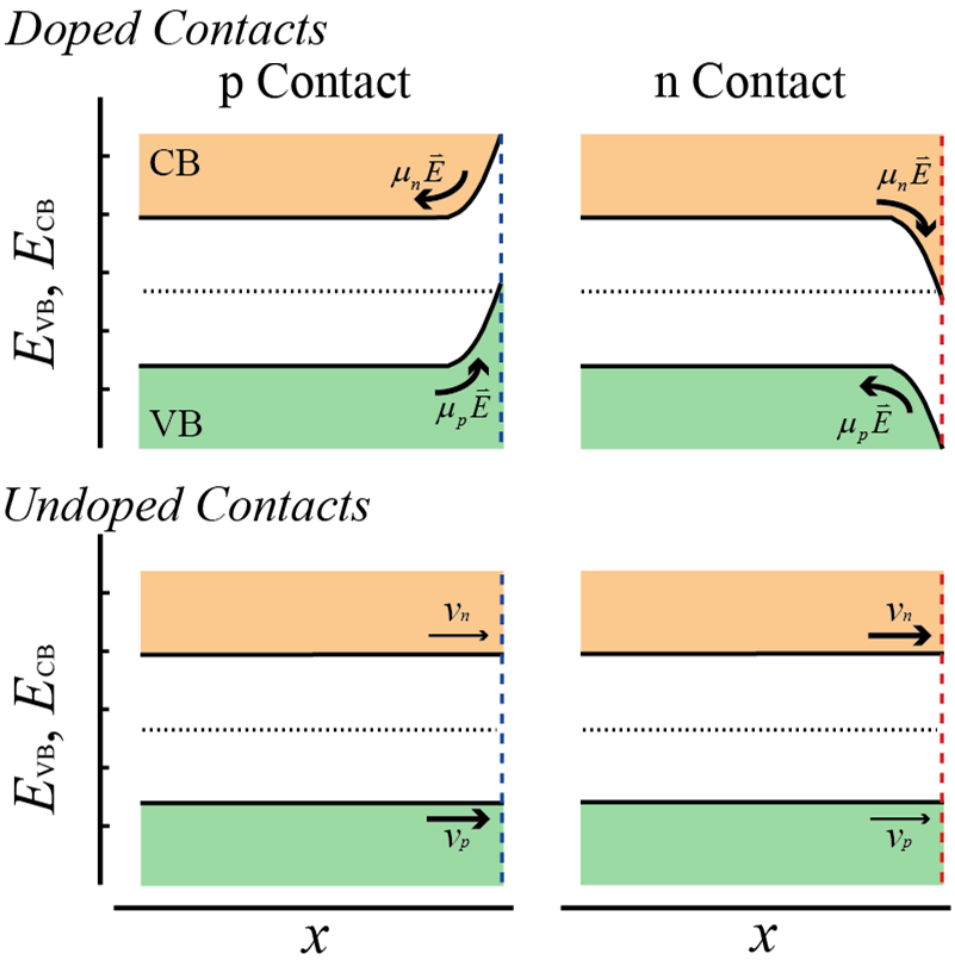

Figure IV.3: Energy band schematic for discrete-contact devices featuring doped or undoped hole- or electron-selective contacts in the dark at 0 V applied potential. The *x* parameter indicates the spatial distance from a discrete contact into the nanowire bulk and the dotted black line shows the Fermi energy. Dominant charge transfer processes are shown as bolded arrows near each contact (p- and n-type contacts denoted by dashed blue and red lines, respectively) in each band. CB = conduction band, VB = valence band.

Tunneling losses were incorporated at each contact in all device types using a WKB-based barrier tunneling approximation and a nonlocal mesh that accounted for all tunneling within 25 nm of the semiconductor/vacuum interface. Electron and hole tunneling masses were both set to $0.3m_0$ and the transmission coefficient was set to unity. Electron (hole) tunneling was not incorporated at hole-selective (electron-selective) contacts featuring asymmetric carrier collection velocities.

Unless stated otherwise, the simulation results reported here utilized a 100 x AM1.5 (Global Tilt) concentrated illumination spectrum[25] with an integrated intensity of 10 W cm^{-2} incident normal to the top of the nanowire. Optical generation was calculated via a simple Beer-Lambert absorption model based on the optical constants of Si[26] and did not include reflection of light off of the nanowire surface, which is typically low for nanowire arrays.[27,28] Internal quantum yield values, where given, are on a scale from 0 to 1 and represent the ratio of collected electrons per second to the number of absorbed photons per second. The product of short-circuit internal quantum yield, open-circuit potential and fill factor, Φ_{sc} x V_{oc} x FF, is used as a metric to gauge the overall performance of a device without accounting for specific absorption properties.

Several figures in this chapter illustrate the simulated magnitude and/or spatial distribution of carrier density, electric field or change in electric potential within a nanowire. All of these results are reported at an applied potential corresponding to the maximum power point of each device. Because a solar cell is typically poised at or near its maximum power point during operation, these conditions were considered to be the most relevant for understanding device operation. The default simulation parameters for n-Si nanowires featuring dopant-diffused discrete contacts, a single conformal Schottky contact and undoped discrete contacts are tabulated in Appendix B. Any deviation from tabulated values is stated explicitly in the text and/or figures of this chapter.

C. Results

The potential difference across a solar device is equal to the quasi-Fermi-level splitting,[19]

$$\frac{1}{q}\left(E_{F,n} - E_{F,p}\right) = \frac{k_B T}{q} \ln\left(\frac{np}{n_i^2}\right) \qquad \text{(IV.4)}$$

where $E_{F,n}$ is the electron quasi-Fermi energy, $E_{F,p}$ is the hole quasi-Fermi energy, k_B is Boltzmann's constant, T is temperature, and n_i is the intrinsic carrier density. For a given material at temperature T, Equation IV.4 indicates that the device voltage is dictated by the carrier product np, with larger np products corresponding to larger potentials across the device.

Figures IV.4a-b show the simulated internal quantum yield, Φ, versus applied potential, V, for a device featuring either ten dopant-diffused, alternating hole- and electron-selective discrete contacts or a conformal Schottky contact to a single n-Si nanowire featuring long SRH time constants (τ_{SRH} = 5 x 10^{-4} s), low surface recombination velocities (S = 10^{-4} cm s^{-1}), a radius of 200 nm and dopant densities of either 10^{12} cm^{-3} or 10^{17} cm^{-3}. When all devices were operated at potentials corresponding to their respective maximum power points, the np products for discrete-contact devices were ~ 10^{30} cm^{-6}, several orders of magnitude larger than those for the Schottky devices in Figures IV.4a and IV.4b (10^{23} cm^{-6} and 10^{26} cm^{-6}, respectively). Subsequent V_{oc} values for discrete-contact devices were > 0.3 V greater than for analogous devices featuring a conformal Schottky contact. The discrete-contact device simulated with a dopant density of 10^{12} cm^{-3} exhibited significantly higher short-circuit Φ as compared to the analogous device featuring a conformal Schottky contact. Corresponding simulated electric field strength profiles at the maximum power point of each device indicated that neither nanowire featured a significant depletion region along its length. The small open-circuit potential and exceedingly poor internal quantum yield for the device featuring a conformal Schottky contact are characteristic of a rectifying nanowire device with insufficient electric field strength to efficiently collect photogenerated charge carriers.[5] The simulated Φ versus V responses for analogous discrete-contact and Schottky contact devices are shown in Figure IV.4b for a nanowire dopant density of 10^{17} cm^{-3}. At this dopant density, the device with a conformal Schottky contact was able to support a full depletion width and strong electric fields within the nanowire. This corresponded to large increases in Φ and V_{oc} as compared to the Schottky device with N_D = 10^{12} cm^{-3}. The discrete-contact device still exhibited a 0.31 V larger V_{oc} than the Schottky device for N_D = 10^{17} cm^{-3} and did not feature strong electric fields throughout the device.

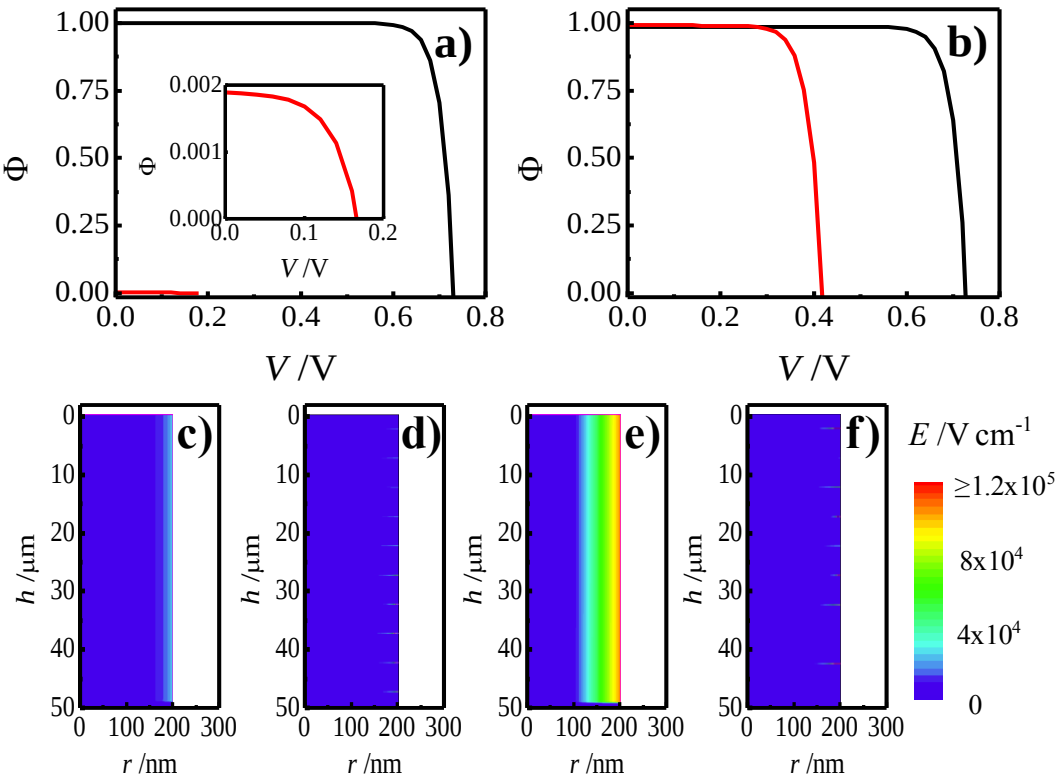

Figure IV.4: Simulated internal quantum yield versus applied potential for a single n-Si nanowire featuring either (red line) a conformal Schottky contact with a barrier height of 1.0 eV or (black line) ten alternating hole- and electron-selective discrete contacts diffused along the nanowire length. Dopant densities of (a), (c), (d) 10^{12} cm^{-3} and (b), (e), (f) 10^{17} cm^{-3} are shown. The inset in (a) details the Schottky device response. (c) – (f) Electric field as a function of the spatial coordinates *r* and *h* for (c) the Schottky device and (d) the discrete-contact device with a dopant density of 10^{12} cm^{-3} and (e) the Schottky device and (f) the discrete-contact device with a dopant density of 10^{17} cm^{-3}. Other major simulation parameters: radius = 200 nm, contact width (discrete-contact devices) = 20 nm, SRH time constant = 5 x 10^{-4} s, surface recombination velocity = 10^{-4} s, illumination = 100 x AM1.5. Additional simulation parameters were set to default values and are given in Tables B.2 and B.3 in Appendix B.

Figure IV.5 shows *n*, *p*, and the change in electric potential, $\Delta\phi$, at a radius of r = 199 nm as a function of position along the length of the discrete-contact device in Figure IV.4d. Carrier population densities were homogeneous within the bulk of the discrete-contact device, but *n* increased or decreased sharply by more than four orders of magnitude near electron- or hole-selective contacts, respectively (vice versa for *p*). A comparison of Figure IV.5a with Equation IV.3a indicates that the diffusion component of electron current flowed *away* from electron-selective contacts and *toward* hole-selective contacts, with the opposite true for hole current. Fluctuations in *n* were mirrored by those in $\Delta\phi$ along the same r = 199 nm path in Figure IV.5b, with potential changing sharply to more positive values near electron-selective contacts and to more negative values near hole-selective contacts. The drift component of electron current thus flowed *toward* electron-selective contacts and *away* from hole-selective contacts (vice versa for hole currents). The sign of the current collected at each contact indicated that drift processes dominated local carrier separation/collection at dopant-diffused contacts.

Figure IV.6 shows the simulated photoresponses of a device featuring low surface recombination velocity (10^{-4} cm s^{-1}) and ten dopant-diffused, alternating hole- and electron-selective contacts of various widths, Δ_{CW}. The Φ versus V responses for these devices show both Φ_{sc} and V_{oc} to decrease as contact width increases from 20 nm to 4.5 μm, with Figure IV.6b indicating that V_{oc} decreased monotonically by ~ 55 mV per decade increase in Δ_{CW}. The corresponding Φ_{sc} x V_{oc} x FF performance metric decreased by a factor of five as the overall contact area increased from 0.4% to 89.9% of the total nanowire surface area. The dopant density at each contact was several orders of magnitude larger than *n* and *p* values within a nanowire device operating at its maximum power point, and carrier lifetimes near contacts were subsequently decreased due to increased Auger recombination and the Scharfetter relation.[29] Figures IV.6d-g show the simulated carrier recombination rates for both Auger and Shockley-Read-Hall processes at a representative electron-selective contact either 20 nm or 500 nm wide centered at h = 7.5 μm from the top of the nanowire. Auger recombination is shown to dominate near the contact, with net (Auger + SRH) recombination rates approximately an order of magnitude larger in the near-contact region than in the nanowire bulk. Total recombination rates within each nanowire device thus increased as the degenerately

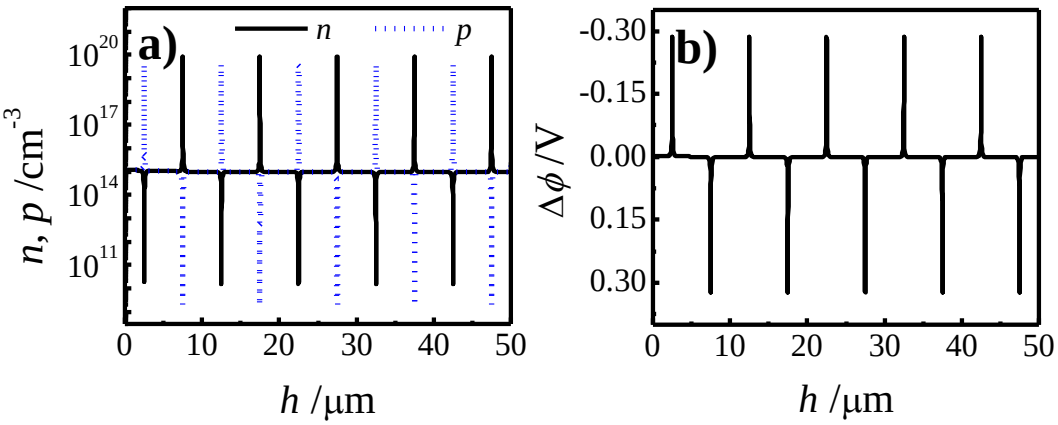

Figure IV.5: Simulated (a) n and p and (b) $\Delta\phi$ as a function of position along the length of a Si nanowire with ten dopant-diffused, alternating hole- and electron-selective contacts. Hole-selective contacts were positioned at 2.5, 12.5, 22.5, 32.5 and 42.5 μm and electron-selective contacts were positioned at 7.5, 17.5, 27.5, 37.5 and 47.5 μm. Values for n, p and $\Delta\phi$ were taken at r = 199 nm at an applied bias corresponding to the maximum power point for the device. Major simulation parameters: radius = 200 nm, contact width = 20 nm, dopant density = 10^{12} cm^{-3}, SRH time constant = 5 x 10^{-4} s, surface recombination velocity = 10^{-4} s, illumination = 100 x AM1.5. Additional simulation parameters were set to default values and are given in Table B.2 in Appendix B.

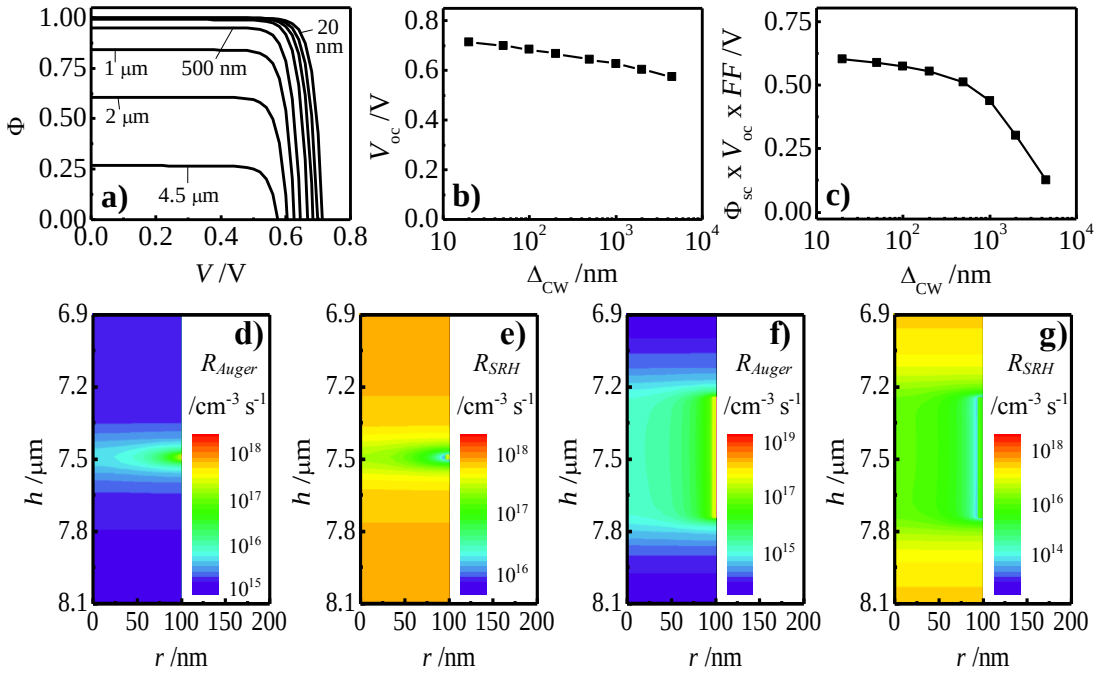

Figure IV.6: (a) Simulated internal quantum yield versus applied potential for a single-nanowire device featuring ten dopant-diffused alternating hole- and electron-selective contacts with widths ranging from 20 nm to 4.5 μm. (b)-(c) Simulated (b) V_{oc} and (c) Φ_{sc} x V_{oc} x FF as a function of contact width. (d) – (g) Auger and Shockley-Read-Hall recombination rates at an electron-selective contact as a function of r and h for Δ_{CW} = (d), (e) 20 nm or (f), (g) 500 nm. Major simulation parameters: radius = 100 nm, dopant density = 10^{12} cm^{-3}, SRH time constant = 5 x 10^{-4} s, surface recombination velocity = 10^{-4} cm s^{-1}, illumination = 100 x AM1.5. Additional simulation parameters were set to default values and are given in Table B.2 in Appendix B.

doped volume (proportional to Δ_{CW}) increased and contributed to poorer overall device performance.

Figure IV.7 shows the simulated photoresponse for a single-nanowire device featuring various Shockley-Read-Hall lifetimes, τ_{SRH}, and number of alternating hole- and electron-selective dopant-diffused contacts. The Φ versus V responses of a nanowire device with ten contacts is shown for various values of τ_{SRH} in Figure IV.7a. Φ_{sc}, V_{oc} and FF all decreased with decreasing τ_{SRH} for this device. V_{oc} and Φ_{sc} x V_{oc} x FF are shown as a function of τ_{SRH} for eight devices featuring between 2 and 72 contacts in Figures IV.7b-c. Both of these quantities increased monotonically with increasing τ_{SRH} before plateauing at an SRH time constant of approximately 1 μs for all devices. In contrast, high-performance planar devices require much higher-purity Si with τ_{SRH} values of ~ 5 ms in order to minimize bulk recombination losses. The τ_{SRH} plateau value closely matched the Auger time constant for these devices (vertical dashed line in Figures IV.7b-c), indicating that Auger recombination was the dominant carrier loss mechanism for devices simulated with $\tau_{SRH} > 10^{-6}$ s, and SRH recombination began to dominate for $\tau_{SRH} < 10^{-6}$ s. Losses in V_{oc} and Φ_{sc} x V_{oc} x FF were especially pronounced for devices simulated with fewer discrete contacts, with decreases in V_{oc} ranging from 0.099 V per decade decrease in τ_{SRH} for devices with 72 contacts to 0.125 V per decade decrease in τ_{SRH} for devices with only two contacts. The improved performance at small τ_{SRH} of devices featuring more contacts corresponded with the shorter carrier collection lengths accompanying the more closely-spaced collection regions. Carrier diffusion lengths, L, corresponding to each value of τ_{SRH} are shown on the top axes of Figures IV.7b-c. Although the performance of devices limited by SRH recombination ($\tau_{SRH} < 10^{-6}$ s) improved with the addition of more discrete contacts, V_{oc} and Φ_{sc} x V_{oc} x FF decreased with additional contacts for devices with lifetimes limited by Auger recombination ($\tau_{SRH} > 10^{-6}$ s). V_{oc} values decreased by 59 mV for every decade increase in the total contact surface area, which was comparable to the 55 mV drop/decade observed for devices simulated with increasing contact widths. Figure IV.7 thus indicates that increasing the number of discrete contacts in a device that already features sufficiently high carrier diffusion lengths can unnecessarily augment Auger recombination losses near each contact.

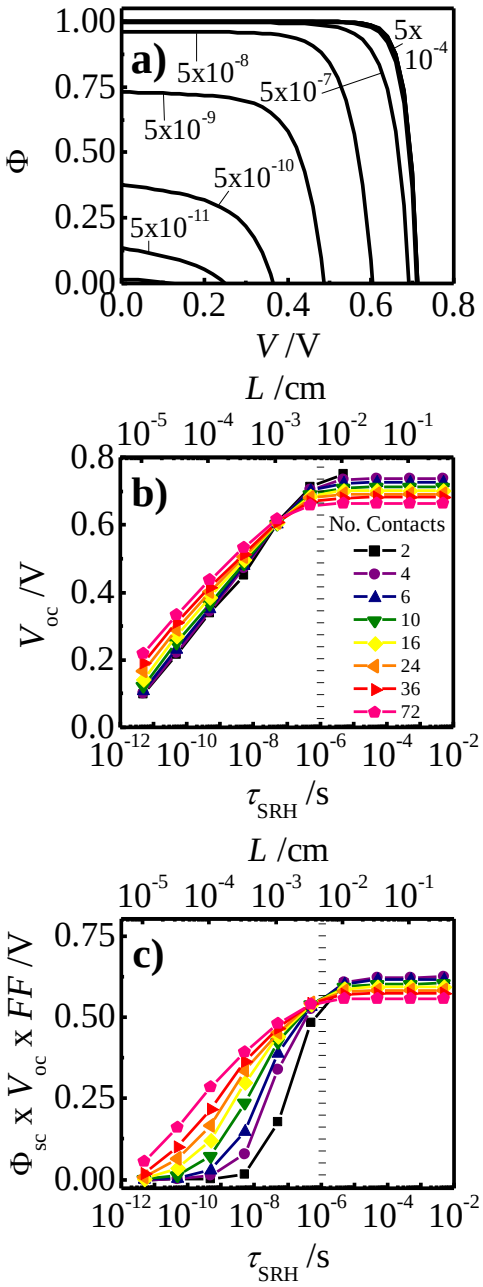

Figure IV.7: (a) Simulated internal quantum yield as a function of applied potential for a single-nanowire device with 10 dopant-diffused, alternating hole- and electron-selective contacts at various values of the Shockley-Read-Hall time constant. (b) V_{oc} and (c) Φ_{sc} x V_{oc} x *FF* as a function of τ_{SRH} for a device featuring various numbers of dopant-diffused contacts. Major simulation parameters: radius = 100 nm, contact width = 20 nm, dopant density = 10^{12} cm^{-3}, surface recombination velocity = 10^{-4} s, illumination = 100 x AM1.5. Additional simulation parameters were set to default values and are given in Table B.2 in Appendix B.

The simulated photoresponse of a single-nanowire device featuring ten dopant-diffused discrete contacts at various values of the surface recombination velocity, S, is shown in Figure IV.8. The simulated Φ versus V responses for this device indicated excellent performance for values of $S \leq 1$ cm s^{-1}, with losses in Φ_{sc}, V_{oc} and FF for values of $S \geq 1$ cm s^{-1}. In contrast, simulation results for an analogous device featuring a conformal Schottky contact with a 1.0 eV barrier height and a full depletion region (N_D = 10^{18} cm^{-3} and r = 100 nm) exhibited far less sensitivity to S (devices featuring a conformal Schottky contact and N_D = 10^{12} cm^{-3} did not exhibit appreciable Φ for any value of S and are not shown here). The device with ten discrete contacts exhibited larger Φ_{sc} x V_{oc} x FF than the Schottky device, however, for all $S \leq 200$ cm s^{-1}. Surface recombination losses were shown to be suppressed in a manner analogous to SRH recombination in the bulk by increasing the number of ohmic-selective contacts along the length of the nanowire. The nanowire device simulated with 36 discrete contacts in Figure IV.8c exhibited larger Φ_{sc} x V_{oc} x FF than the Schottky device for all $S \leq 1000$ cm s^{-1}.

The photoresponse of single-nanowire devices featuring either ten discrete contacts with alternating hole and electron selectivity or a single conformal Schottky contact with a 1.0 eV barrier height are shown in Figure IV.9 for various values of r and N_D. Figures IV.9a-b show Φ versus V for devices at a single dopant density of 10^{17} cm^{-3} at various radii. The internal quantum yield of the discrete-contact device was uniformly high for all radii and dropped slightly with decreasing radius. The Schottky device, on the other hand, exhibited large Φ only for radii $\geq$ 125 nm and uniformly smaller V_{oc} values as compared to the discrete-contact device. The V_{oc} and Φ_{sc} x V_{oc} x FF responses for both device types are shown as a function of nanowire radius for N_D = 10^{12} cm^{-3}, 10^{17} cm^{-3} and 10^{18} cm^{-3} in Figures IV.9c-d. Simulated V_{oc} increased monotonically as radii increased for both device types at all dopant densities. Open-circuit potentials of most devices were directly proportional to the log of the nanowire radius, with V_{oc} values increasing by 58 – 73 mV per decade increase in r. The Schottky device with N_D = 10^{12} cm^{-3} did not exhibit this direct proportionality, however, as photocurrent densities for these simulations plateaued at low values for r < 500 nm. As indicated in Figure IV.9b, devices featuring conformal Schottky contacts exhibited a strong N_D, r dependence, with exceedingly poor

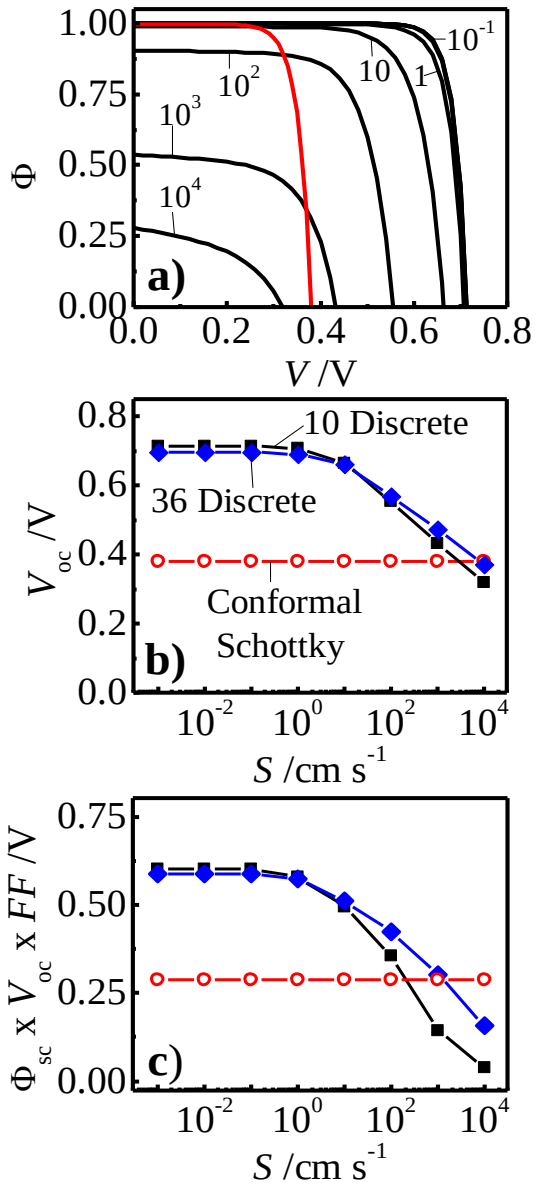

Figure IV.8: (a) Simulated internal quantum yield versus applied potential for a single-nanowire device featuring ten dopant-diffused alternating hole- and electron-selective contacts at various values of the surface recombination velocity, *S*. The red line shows the response of an analogous device featuring a conformal Schottky contact with a barrier height of 1.0 eV and $S = 10^4$ cm s^{-1}. The dopant density of the discrete-contact device was $N_D = 10^{12}$ cm^{-3} while that of the Schottky device was $N_D = 10^{18}$ cm^{-3}. (b) V_{oc} and (c) Φ_{sc} x V_{oc} x *FF* versus *S* for (solid black squares) the discrete-contact device shown in (a), (solid blue diamonds) an analogous device with 36 dopant-diffused contacts and (open red circles) the Schottky device shown in (a). Major simulation parameters: radius = 100 nm, contact width = 20 nm, SRH time constant = 5 x 10^{-4} s, illumination = 100 x AM1.5. Additional simulation parameters were set to default values and are given in Tables B.2 and B.3 in Appendix B.

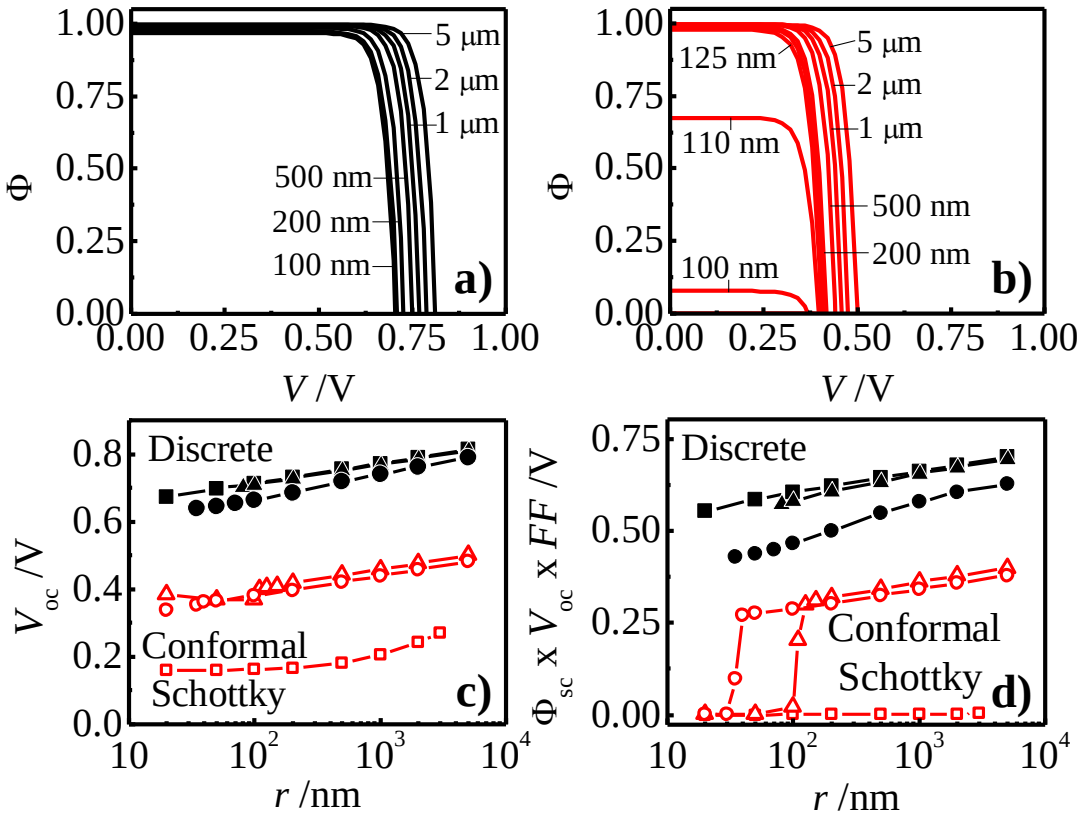

Figure IV.9: Simulated internal quantum yield versus applied potential for a single-nanowire device featuring (a) ten alternating dopant-diffused alternating hole- and electron-selective contacts or (b) a conformal Schottky contact with a barrier height of 1.0 eV shown for various nanowire radii. The dopant densities for both of these devices was $N_D = 10^{17}$ cm^{-3} (c) V_{oc} and (d) Φ_{sc} x V_{oc} x FF for a (black, closed symbols) discrete-contact or (red, open symbols) Schottky device as a function of radius for various nanowire dopant densities. Dopant density was (squares) 10^{12} cm^{-3}, (triangles) 10^{17} cm^{-3} or (circles) 10^{18} cm^{-3}. Major simulation parameters: contact width = 20 nm, SRH time constant = 5 x 10^{-4} s, surface recombination velocity = 10^{-4} cm s^{-1}, illumination = 100 x AM1.5. Additional simulation parameters were set to default values and are given in Tables B.2 and B.3 in Appendix B.

Φ_{sc} x V_{oc} x *FF* values for nanowires with radii below a particular cutoff value that increased with decreasing nanowire dopant density. The results in Figure IV.9d are in agreement with the premise that a nanowire heterojunction device must feature a sufficiently large radius to support a full depletion region for efficient carrier separation/collection.[5,6] Simulated discrete-contact devices exhibited much less sensitivity to N_D and r, with Φ_{sc} x V_{oc} x *FF* decreasing by only 20-30% as the nanowire radius decreased from 5 μm to 20 nm. Notably, the discrete-contact device performance metric was at least 60% larger than that for analogous Schottky devices for all N_D, r combinations.

Figures IV.10 – IV.11 explore the photoresponses of discrete-contact nanowire devices that did not feature localized degenerate doping at each contact. Ohmic selectivity for these devices was instead achieved by specifying (*1*) a high carrier collection velocity (v_{High} = 10^7 cm s^{-1}) for electrons at electron-selective contacts and holes at hole-selective contacts and (*2*) a 2 – 8 order of magnitude lower carrier collection velocity, v_{Low}, for electrons at hole-selective contacts and holes at electron-selective contacts (Figure IV.10a). Figure IV.10 shows the simulated photoresponse of a single-nanowire discrete-contact device of this type with ten undoped alternating electron- and hole-selective contacts with varying values of v_{Low}. Simulated Φ versus V responses for this device exhibited significant decreases in V_{oc} as v_{Low} increased, with V_{oc} decreasing 65.5 mV for every decade increase in v_{Low}. Φ_{sc} x V_{oc} x *FF* also dropped monotonically with increasing v_{Low} from a maximum value of 0.344 V. This maximum Φ_{sc} x V_{oc} x *FF* value was significantly less than the 0.603 V observed for analogous discrete-contact devices with dopant-diffused contacts, but compared favorably with both the 0.00015 V observed for an analogous Schottky contact device and the 0.287 V observed for an optimized Schottky device (N_D = 10^{18} cm^{-3}) of the same radius.

Figure IV.11 shows the simulated n, p and $\Delta\phi$ values at a radius of r = 99 nm along the length of the nanowire device with v_{Low} = 10^{-1} cm s^{-1} in Figure IV.10. Simulated n, p, and $\Delta\phi$ increased or decreased sharply near each contact in a manner similar to that observed in Figure IV.5. All responses were inverted as compared to Figure IV.5, however, with positive $\Delta\phi$ and large n near hole-selective contacts and negative $\Delta\phi$ and large p near electron-selective contacts. When compared to Equation

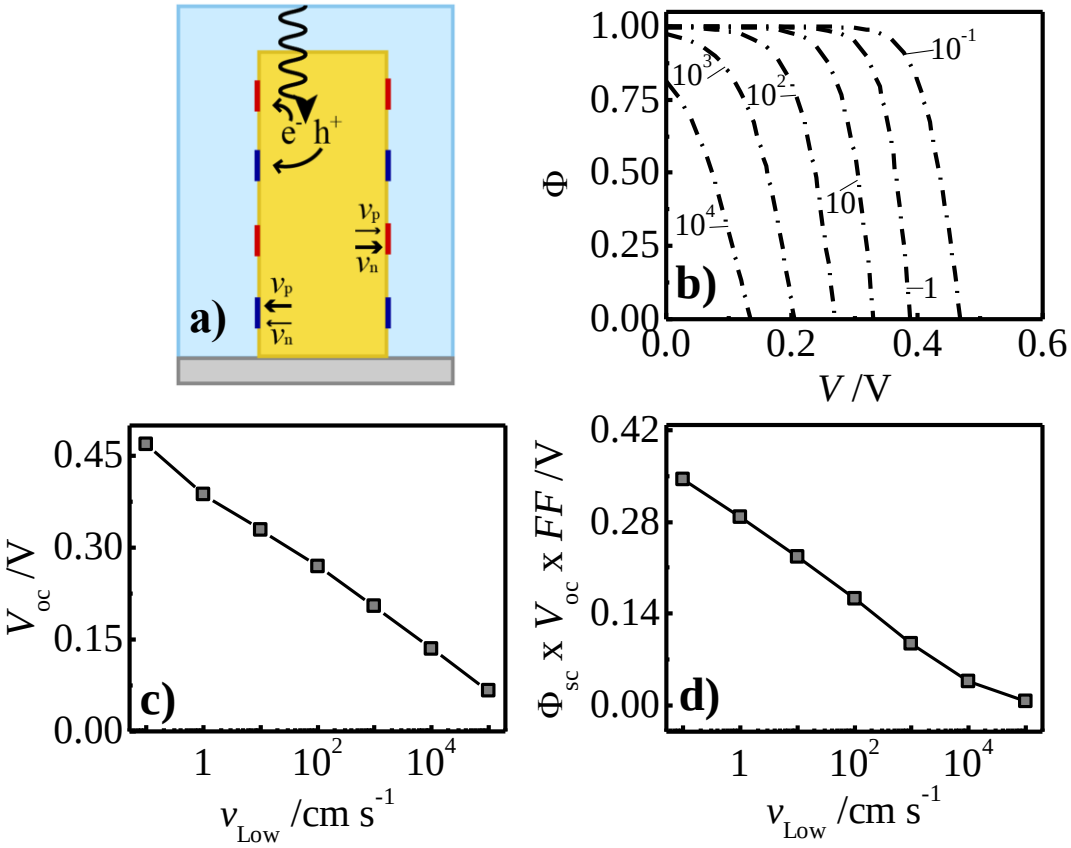

Figure IV.10: (a) Partial cross-section schematic for a nanowire device featuring undoped discrete contacts with asymmetric electron and hole collection velocities at each contact. (b) Simulated Φ versus *V* for a single-nanowire device featuring ten undoped alternating hole- and electron-selective contacts at various values of electron (hole) collection velocity at hole-selective (electron-selective) contacts, v_{Low}. Simulated (c) V_{oc} and (d) Φ_{sc} x V_{oc} x *FF* as a function of v_{Low}. Major simulation parameters: radius = 100 nm, contact width = 20 nm, dopant density = 10^{12} cm^{-3}, SRH time constant = 5 x 10^{-4} s, surface recombination velocity = 10^{-4} cm s^{-1}, electron (hole) collection velocity at electron-selective (hole-selective) contacts = 10^{7} cm s^{-1}, illumination = 100 x AM1.5. Additional simulation parameters were set to default values and are given in Table B.4 in Appendix B.

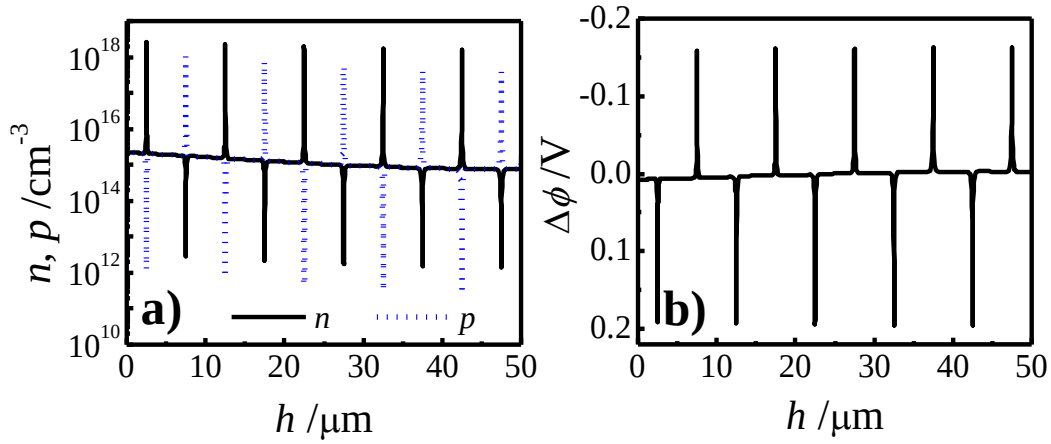

Figure IV.11: Simulated (a) n and p and (b) $\Delta\phi$ at a radius of r = 99 nm as a function of position along the length of a nanowire operating at a voltage corresponding to its maximum power point. Nanowires were simulated with ten alternating hole- and electron-selective contacts which featured electron (hole) collection velocities of 10^{7} cm s^{-1} at electron-selective (hole-selective) contacts and electron (hole) collection velocities of 10^{-1} cm s^{-1} at hole-selective (electron-selective) contacts. Hole-selective contacts were positioned at 2.5, 12.5, 22.5, 32.5 and 42.5 μm and electron-selective contacts were positioned at 7.5, 17.5, 27.5, 37.5 and 47.5 μm. Major simulation parameters: radius = 100 nm, contact width = 20 nm, dopant density = 10^{12} cm^{-3}, SRH time constant = 5 x 10^{-4} s, surface recombination velocity = 10^{-4} cm s^{-1}, illumination = 100 x AM1.5. Additional simulation parameters were set to default values and are given in Table B.4 in Appendix B.

IV.3, the Figure IV.11 results indicate that the drift component of electron current actually pushed electrons *away* from electron-selective contacts and *toward* hole-selective contacts. In contrast, the diffusion component of the electron current featured electrons diffusing *toward* the low *n* populations at electron-selective contacts and *away* from the high *n* densities at hole-selective contacts. Likewise, holes drifted away from hole-selective contacts and toward electron-selective contacts while simultaneously diffusing toward hole-selective contacts and away from electron-selective contacts. Despite the reversal in direction of the drift and diffusion components of charge carrier transport, the sign of net electron and hole currents at each contact did not change for discrete-contact devices with undoped contacts as compared to those with doped contacts. Fill factors decreased dramatically as surface recombination velocity increased (not shown), however, indicating that discrete-contact devices without dopant-diffused contacts may be more susceptible to resistance losses than devices with dopant-diffused contacts.

The simulation results shown thus far assumed a material with excellent optoelectronic properties which are varied one at a time to isolate the impact of each parameter. In practice, however, nanowires seldom feature SRH time constants of 0.5 ms, net mobilities of ~1000 $cm^2\ V^{-1}\ s^{-1}$ and carrier diffusion lengths of ~0.1 cm. Figure VI.12 shows the photoresponse of three devices with optoelectronic properties more representative of nanowires grown without extensive, energy-intensive purification (τ_{SRH} = 10 ns, $\mu_n = \mu_p$ = 1 $cm^2\ V^{-1}\ s^{-1}$, and L = 160 nm). Each device featured either 72 dopant-diffused discrete contacts, 72 undoped discrete contacts or a single conformal Schottky contact. Both discrete-contact devices far surpassed the Schottky contact device in terms of internal quantum yield, open-circuit voltage and the $\Phi_{sc} \times V_{oc} \times FF$ performance metric (Table IV.1). With a dopant density of 3 x 10^{13} cm^{-3} and radius of 100 nm, the Schottky device was not capable of supporting a sufficient depletion region to efficiently collect carriers, and its overall performance metric was on the order of 10^{-4} V. Both discrete-contact devices exhibited $\Phi_{sc} > 0.77$, indicating reasonably efficient short-circuit carrier separation/collection in both devices. The fill factor and open-circuit voltage of the device with undoped contacts were 0.350 and 0.286 V, respectively, and the resulting $\Phi_{sc} \times V_{oc} \times FF$ value was 0.083. The device with dopant-diffused discrete contacts featured

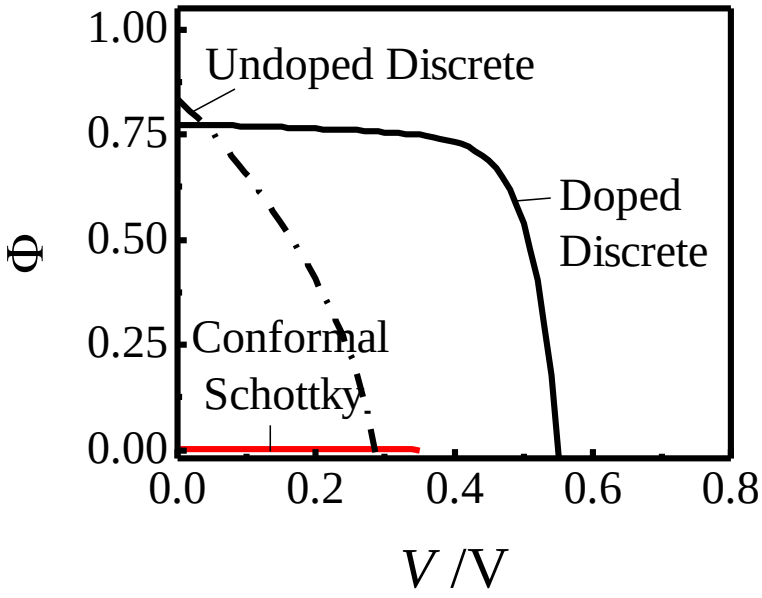

Figure IV.12: Simulated Φ versus V for a Si nanowire device with relatively poor optoelectronic properties. The response for a discrete-contact device featuring 72 alternating hole- and electron-selective dopant-diffused contacts is shown along with that for an analogous device featuring undoped discrete contacts with $v_{High} = 10^{7}$ cm s^{-1} and $v_{Low} = 10^{-1}$ cm s^{-1} and a device with a conformal Schottky contact with a barrier height of 1.0 eV. The performance metrics for all three devices are given in Table VI.1. Major simulation parameters: dopant density = 3 x 10^{13} cm^{-3}, radius = 100 nm, contact width = 20 nm, SRH time constant = 10^{-8} s, electron and hole mobility = 1 cm^{2} V^{-1} s^{-1}, surface recombination velocity = 5 cm s^{-1}, illumination = 100 x AM1.5. Additional simulation parameters were set to default values and are given in Tables B.2-B.4 in Appendix B.

Table IV.1: Φ_{sc}, V_{oc}, *FF* and Φ_{sc} x V_{oc} x *FF* for the devices simulated in Figure IV.12.

	Schottky	**Dopant-Diffused Discrete**	**Undoped Discrete**
Φ_{sc}	1.46×10^{-3}	0.774	0.833
V_{oc} /V	0.348	0.551	0.286
FF	0.649	0.725	0.350
Φ_{sc} x V_{oc} x *FF* /V	3.29×10^{-4}	0.309	0.083

an open-circuit voltage of 0.551 V and a fill factor of 0.725 for a total Φ_{sc} x V_{oc} x *FF* value of 0.309. Notably, the performance metric for this device exceeded that of an optimized Schottky device of the same radius (Figure IV.9d) despite its much poorer optoelectronic properties.

D. Discussion

The cumulative simulation data shown in Figures VI.4-VI.12 indicate that nanowire devices with discrete, ohmic-selective contacts can offer high performance even for nanowires featuring dimensions and/or optoelectronic properties that would preclude effective operation in other device types. Specifically, simulated discrete-contact devices operated with high performance even when bulk SRH time constants were three orders of magnitude lower than those typical for planar discrete-contact devices. Discrete-contact nanowire device simulations also exhibited minimal sensitivity to nanowire radius and dopant density, without the precipitous drop in performance at small radii observed for analogous Schottky devices. Efficient carrier separation/collection was observed for devices with discrete contacts made ohmic-selective by both localized degenerate doping as well as asymmetric carrier kinetics at each contact, indicating a significant degree of flexibility in the implementation of the discrete-contact design.

The discrete-contact nanowires with dopant-diffused contacts simulated herein exhibited open-circuit potentials that were several tenths of a volt larger than V_{oc} values for analogous Schottky devices and compared favorably to those for efficient planar Si photovoltaics.[14] Such large V_{oc} values are particularly promising for nanowire light-harvesting devices, which tend to suffer from relatively small open-circuit photovoltages[1,30-34] due in part to high dark exchange currents. Exchange currents are typically proportional to the surface area of a contact and are thus intrinsically large for high-surface-area nanowire devices with full conformal contacts. The discrete contacting scheme featured herein did not require that contact area increase proportionally to nanowire surface area. The lower simulated Φ_{sc} and V_{oc} for devices with larger contacts coincided with high Auger recombination rates in the degenerately doped region near each contact, and device performance improved monotonically as contact size decreased.

These results appear to be in slight contrast, however, to those reported for planar discrete-contact solar cells, which have exhibited optimal diffusion sizes for maximum device performance that did not necessarily correspond to the smallest contact size.[15] This difference is most likely an artifact of the relative scales of the two devices. The high surface area and small volume of the nanowire device led to a relatively large degenerately doped volume (more than 15% of total nanowire volume for devices simulated with Δ_{CW} = 4.5 μm) as compared to planar devices. The smallest (20 nm) contacts simulated in Figures IV.6a-d correspond to a degenerately doped volume accounting for 0.08% of the total nanowire volume. The optimal contact size for planar discrete-contact devices, on the other hand, corresponded to a volume that was < 0.02% of the total device volume. Thus, the absence of a mid-size optimal peak in the Figure IV.6b results may be due more to the range of simulated contact widths than to a difference in the operation of nanowire versus planar discrete-contact devices. Another contributing factor may be that smaller contacts also correspond to longer collection lengths. While such differences in collection lengths are ~100 nm or so in nanowire devices and are unlikely to strongly affect device performance, in planar discrete-contact devices collection lengths can increase by ~10 μm or more as the contact size decreases.

The discrete-contact nanowire design offers a clear benefit in terms of carrier collection length scales as compared to planar devices. For instance, it is well-known that high (> 28%) energy conversion efficiencies can be achieved with planar crystalline Si using planar discrete-contact designs.[15] The chief disadvantage of these devices from the perspective of commercially viable terrestrial solar energy conversion, however, are stringent bulk purity requirements that necessitate extensive, energy-intensive purification to achieve bulk time constant values > 1 ms.[15] The simulations shown in Figure IV.7 suggest that the discrete-contact design relaxes this τ_{SRH} restriction by up to three orders of magnitude. Figure IV.12 offers additional evidence that discrete contacting schemes featuring semiconductor nanowires are not limited to materials with exceptional optoelectronic properties. In fact, such schemes may also find applications in materials with a low tolerance for the concentrated illumination conditions that are typical for discrete-contact devices. Simulated photoresponses of single-nanowire discrete-contact devices under a range of illumination conditions (not shown) exhibit

increases in V_{oc} as illumination levels become more intense due to higher n and p populations under high photon fluxes. V_{oc} values are still significantly larger for discrete-contact devices as compared to analogous Schottky devices even under 1-sun illumination, however. Similar responses have been observed for planar discrete-contact devices,[15] which have exhibited > 22% efficiency under 1 sun illumination.[35]

The n, p and $\Delta\phi$ profiles shown in Figures IV.5 and IV.11 indicate that the high performance of the discrete-contact devices simulated herein was not dictated strictly by the mode of carrier transport near each contact. In fact, local separation/collection of carriers at a given contact appeared to be dominated by drift for devices featuring dopant-diffused contacts and diffusion for devices without dopant-diffused contacts. The key feature driving the high performance of these devices instead seemed to be the large n and p populations present in the nanowire during operation, which translated to large open-circuit photovoltages according to Equation IV.4. The ability to support large carrier densities is apparent in the analytical expressions that describe the operation of planar discrete-contact devices, which also leverage this aspect to achieve higher open-circuit photovoltages and energy conversion efficiencies.[16] Although the scale and geometry of nanowire discrete-contact devices complicates their analytical characterization as compared to planar devices, these same factors made them a natural fit for the finite-element, radially symmetric numerical modeling utilized in this work. One of the more notable implications of the carrier transport mechanisms present in discrete-contact devices is the broad array of operating parameters and conditions over which a high-performance device can be designed. Specifically, discrete-contact nanowire designs effectively removed constraints on nanowire radius and dopant density, in sharp contrast to the Schottky nanowire design.

One of the more severe limitations of the discrete-contact nanowire design is carrier loss due to SRH recombination at the semiconductor surface. Indeed, simulation results indicate that S must be less than ~100 cm s^{-1} for devices with dopant-diffused discrete contacts (Figure IV.8c) and less than ~4 cm s^{-1} for devices with undoped discrete contacts (not shown) to avoid excessive surface recombination losses in Si devices. Planar discrete-contact devices exhibit a similar sensitivity to S,[36] with S values < 7 cm s^{-1} typical in high-performance Si devices.[15] Significant progress has been made in the

surface passivation of semiconductor nanowires over the past two decades, however, with multiple successes in decreasing surface recombination with a variety of material-specific passivation techniques that include both core-shell structures[37,38] and chemical passivation.[39-41] Importantly, the levels of surface recombination velocity necessary for the devices simulated herein appear to be well within ranges achieved for planar devices. For example, planar crystalline Si can be manufactured with an S value of ~ 2 cm s^{-1} even with low-temperature processing techniques.[42]

The specific device design and geometry featured herein served as a useful starting point for understanding discrete-contact nanowire systems, but is not meant to exclude alternative designs and by no means represents a fully optimized system. The explicit contact geometry and contacting technique represent just two of several system aspects that may take on radically different forms in different permutations of a discrete-contact nanowire device. For instance, the concentric band contacts simulated throughout featured a convenient radial symmetry that facilitated device simulation and could potentially be achieved experimentally through top-down processing methods amenable to scalable manufacturing. In practice, however, this level of uniformity may not offer a sizeable advantage over a more random contact geometry that may require less precision and/or control in fabrication processes. In fact, the sizeable carrier losses associated with larger net contact areas in Figures IV.6 and IV.7 suggest that smaller contacts that do not span the entire circumference of a nanowire may actually improve device performance.

This report focuses on two ways to achieve ohmic-selective contacts for carrier separation/collection: either through localized degenerate doping or localized contacts that feature different carrier collection velocities. There are many ways to achieve such contacts operationally, with the field of semiconductor nanoelectronics providing a particularly rich body of research on ohmic-selective contacting techniques.[43] For instance, the dopant-diffused contacts featured herein may be achieved by introducing dopants into just a few nanowires at a time (useful for initial characterization) using advanced processing techniques,[44] adapting more conventional gas-phase dopant diffusion techniques[45,46] to generate discrete contacts, or even by the non-uniform attachment (and subsequent annealing) of dopant-containing moieties onto a nanowire array.[47] Likewise, devices made ohmic-selective through asymmetric carrier kinetics

could be achieved by introducing hole-/electron-selective conductors or electron/hole blocking layers via top-down processing methods.[48-50] Another approach not addressed in this investigation is an electrochemical design featuring a nanowire surface decorated with catalysts that favor either reduction or oxidation processes.[51] Such photoelectrochemical systems offer additional possibilities for the development of solar-to-chemical energy conversion systems utilizing discrete-contact nanowires.[5,52] In any case, the optimal configuration and ohmic-selective nature of the contacts will likely be strongly influenced by the experimental success of various fabrication techniques, which were beyond the focus of this report.

The results shown here strongly motivate an experimental investigation of discrete-contact nanowire solar devices via both single-nanowire measurements and with nanowire array cells and/or photoelectrodes. Si nanowires provide an excellent experimental platform to complement the modeling analysis presented above since they can be grown with relatively precise control over properties such as radius and dopant density[53,54] and have been rigorously characterized in their own right.[46,55-57] As mentioned above, there also exist well-defined protocol for the passivation of planar Si devices, which may offer the shortest route to high-performance nanowire devices.[42] The recent increased interest in single-nanowire device measurements has facilitated the development of advanced fabrication techniques that may prove useful in the preliminary experimental analysis of discrete-contact nanowire devices.[30,57,58] The simulations presented herein can be readily adapted to such an experimental system by utilizing TCAD Sentaurus in three dimensions to model contacts that may not possess radial symmetry.[24] Explicit generation profiles can also be incorporated into such simulations to better approximate experimental systems.[24,59,60]

E. Conclusion

The simulation results presented here indicate that nanowire discrete-contact solar devices may offer both practical and operational advantages over planar discrete-contact devices and nanowire devices featuring conformal Schottky contacts. Specifically, nanowire discrete-contact devices exhibited high internal quantum yields, open-circuit potentials and fill factors even when surface recombination velocities and Shockley-

Read-Hall recombination lifetimes were two orders of magnitude higher and three orders of magnitude lower, respectively, than for efficient planar discrete-contact devices. Discrete-contact nanowire devices also featured open-circuit potentials several tenths of a volt larger than those for analogous devices with conformal Schottky contacts and did not suffer from the drop-off in Φ and V_{oc} at low r common for Schottky nanowire devices. The simulated operation and performance of discrete-contact nanowire devices was sensitive to several interdependent features of the semiconductor material (τ_{SRH}, S, N_D), ohmic-selective contacts (Δ_{CW}, contact spacing, carrier collection velocity) and other system parameters (r, illumination intensity). High performance was observed over wide ranges of the investigated parameters, however, including for a discrete-contact nanowire device featuring relatively poor optoelectronic properties.

This work motivates a number of additional computational and experimental studies that include (*1*) a computational investigation of photoelectrochemical discrete-contact nanowire systems, (*2*) a computational assessment of the effects of charge carrier transport, separation and recombination processes at discrete contacts that do not feature radial symmetry, (*3*) the experimental design, fabrication and operation of a single-nanowire discrete-contact device with accompanying computational simulations that incorporate the explicit geometry and material parameters, and (*4*) experimental efforts to achieve ohmic-selective contacts on nanowire arrays using scalable processing techniques. Such efforts will be instrumental in the successful realization of high-efficiency devices made from low-energy-input materials that would otherwise be unsuitable for light-harvesting applications.

F. References

1 Garnett, E. & Yang, P. D. Light Trapping in Silicon Nanowire Solar Cells. *Nano Letters* **10**, 1082-1087 (2010).

2 Price, M. J. & Maldonado, S. Macroporous n-GaP in Nonaqueous Regenerative Photoelectrochemical Cells. *The Journal of Physical Chemistry C* **113**, 11988-11994 (2009).

3 Carim, A. I., Collins, S. M., Foley, J. M. & Maldonado, S. Benchtop Electrochemical Liquid–Liquid–Solid Growth of Nanostructured Crystalline Germanium. *Journal of the American Chemical Society* **133**, 13292-13295 (2011).

4 Yu, L. *et al.* Plasma-Enhanced Low Temperature Growth of Silicon Nanowires and Hierarchical Structures by Using Tin and Indium Catalysts. *Nanotechnology* **20**, 225604 (2009).
5 Foley, J. M., Price, M. J., Feldblyum, J. I. & Maldonado, S. Analysis of the Operation of Thin Nanowire Photoelectrodes for Solar Energy Conversion. *Energy & Environmental Science* **5** (2012).
6 Hagedorn, K., Forgacs, C., Collins, S. & Maldonado, S. Design Considerations for Nanowire Heterojunctions in Solar Energy Conversion/Storage Applications. *The Journal of Physical Chemistry C* **114**, 12010-12017 (2010).
7 Erwin, S. C. *et al.* Doping Semiconductor Nanocrystals. *Nature* **436**, 91-94 (2005).
8 Norris, D. J., Efros, A. L. & Erwin, S. C. Doped Nanocrystals. *Science* **319**, 1776-1779 (2008).
9 Takenaka, K., Imanaka, Y., Tamasaku, K., Ito, T. & Uchida, S. Anisotropic Optical Spectrum of Untwinned $PrBa_2Cu_3O_7$ - Persistence of the Charte-Transfer Insulating State of the CuO_2 Plane Against Hole Doping. *Physical Review B* **46**, 5833-5836 (1992).
10 Laks, D. B., Vandewalle, C. G., Neumark, G. F., Blochl, P. E. & Pantelides, S. T. Native Defects and Self-Compensation in ZnSe. *Physical Review B* **45**, 10965-10978 (1992).
11 Di Paola, A. *et al.* Preparation of Polycrystalline TiO_2 Photocatalysts Impregnated with Various Transition Metal Ions: Characterization and Photocatalytic Activity for the Degradation of 4-Nitrophenol. *The Journal of Physical Chemistry B* **106**, 637-645 (2001).
12 Persson, C., Zhao, Y.-J., Lany, S. & Zunger, A. N-Type Doping of $CuInSe_2$ and $CuGaSe_2$. *Physical Review B* **72**, 035211 (2005).
13 Wei, S. H. Overcoming the Doping Bottleneck in Semiconductors. *Computational Materials Science* **30**, 337-348 (2004).
14 Green, M. A., Emery, K., Hishikawa, Y., Warta, W. & Dunlop, E. D. Solar Cell Efficiency Tables (Version 39). *Progress in Photovoltaics: Research and Applications* **20**, 12-20 (2012).
15 Sinton, R. A. & Swanson, R. M. Design Criteria for Si Point-Contact Concentrator Solar Cells. *IEEE Transactions on Electron Devices* **34**, 2116-2123 (1987).
16 Swanson, R. M. Point-Contact Silicon Solar Cells. Report No. EPRI AP-2859, (Electric Power Research Institute, Stanford, 1983).
17 Swanson, R. M. *et al.* Point-Contact Silicon Solar Cells. *IEEE Transactions on Electron Devices* **31**, 661-664 (1984).
18 TCAD Sentaurus (Synopsys Incorporated, 2010).
19 Sze, S. M. N., Kwok K. *Physics of Semiconductor Devices*. 3rd Edition edn, (John Wiley & Sons, 2007).
20 Chitambar, M. & Maldonado, S. Simulation Analysis of Nanowire Solar Cells Featuring Discrete Ohmic-Selective Contacts. *In preparation* (2012).
21 Bank, R. E., Rose, D. J. & Fichtner, W. Numerical Methods for Semiconductor Device Simulation. *IEEE Transactions on Electron Devices* **30**, 1031-1041 (1983).

22 Canovas, E. *et al.* Photoreflectance analysis of a GaInP/GaInAs/Ge multijunction solar cell. *Applied Physics Letters* **97** (2010).
23 Kapadia, R., Fan, Z. Y. & Javey, A. Design Constraints and Guidelines for CdS/CdTe Nanopillar Based Photovoltaics. *Applied Physics Letters* **96** (2010).
24 Kelzenberg, M. D. *et al.* High-Performance Si Microwire Photovoltaics. *Energy & Environmental Science* **4**, 866-871 (2011).
25 ASTM. *Reference Solar Spectral Irradiance: Air Mass 1.5*, <http://rredc.nrel.gov/solar/spectra/am1.5/> (2012).
26 Aspnes, D. E. & Studna, A. A. Dielectric Functions and Optical Parameters of Si, Ge, GaP, GaAs, GaSb, InP, InAs, and InSb from 1.5 to 6.0 eV. *Physical Review B* **27**, 985-1009 (1983).
27 Hochbaum, A. I. & Yang, P. D. Semiconductor Nanowires for Energy Conversion. *Chemical Reviews* **110**, 527-546 (2010).
28 Zhu, J. *et al.* Optical Absorption Enhancement in Amorphous Silicon Nanowire and Nanocone Arrays. *Nano Letters* **9**, 279-282 (2009).
29 Schenk, A. *Advanced Physical Models for Silicon Device Simulation*. (Springer-Verlag/Wien, 1998).
30 Tian, B., Kempa, T. J. & Lieber, C. M. Single Nanowire Photovoltaics. *Chemical Society Reviews* **38**, 16-24 (2009).
31 Garnett, E. C. & Yang, P. Silicon Nanowire Radial p-n Junction Solar Cells. *Journal of the American Chemical Society* **130**, 9224-9225 (2008).
32 Tsakalakos, L. *et al.* Silicon Nanowire Solar Cells. *Applied Physics Letters* **91**, 233117 (2007).
33 Kempa, T. J. *et al.* Single and Tandem Axial p-i-n Nanowire Photovoltaic Devices. *Nano Letters* **8**, 3456-3460 (2008).
34 Stelzner, T. *et al.* Silicon Nanowire-Based Solar Cells. *Nanotechnology* **19**, 295203 (2008).
35 King, R. R., Sinton, R. A. & Swanson, R. M. Doped Surfaces in One Sun, Point-Contact Solar Cells. *Applied Physics Letters* **54**, 1460-1462 (1989).
36 Gruenbaum, P. E., King, R. R. & Swanson, R. M. Photoinjected Hot-Electron Damage in Silicon Point-Contact Solar Cells. *Journal of Applied Physics* **66**, 6110-6114 (1989).
37 Dan, Y. *et al.* Dramatic Reduction of Surface Recombination by in Situ Surface Passivation of Silicon Nanowires. *Nano Letters* **11**, 2527-2532 (2011).
38 Hu, S. *et al.* Thermal Stability and Surface Passivation of Ge Nanowires Coated by Epitaxial SiGe Shells. *Nano Letters* **12**, 1385-1391 (2012).
39 Hang, Q. *et al.* Role of Molecular Surface Passivation in Electrical Transport Properties of InAs Nanowires. *Nano Letters* **8**, 49-55 (2007).
40 Hanrath, T. & Korgel, B. A. Chemical Surface Passivation of Ge Nanowires. *Journal of the American Chemical Society* **126**, 15466-15472 (2004).
41 Tajik, N., Peng, Z., Kuyanov, P. & LaPierre, R. R. Sulfur Passivation and Contact Methods for GaAs Nanowire Solar Cells. *Nanotechnology* **22**, 225402 (2011).
42 Dingemans, G., van de Sanden, M. C. M. & Kessels, W. M. M. Excellent Si Surface Passivation by Low Temperature SiO_2 Using an Ultrathin Al_2O_3 Capping Film. *Physica Status Solidi (RRL) – Rapid Research Letters* **5**, 22-24 (2011).

43 Fan, H. J., Werner, P. & Zacharias, M. Semiconductor Nanowires: From Self-Organization to Patterned Growth. *Small* **2**, 700-717 (2006).
44 Shinada, T. *et al.* in *Electron Devices Meeting (IEDM), 2010 IEEE International.* 26.25.21-26.25.24.
45 Wen, W. *et al.* Structural and Photoelectrochemical Properties of GaP Nanowires Annealed in NH3. *The Journal of Physical Chemistry C* **115**, 22652-22661 (2011).
46 Chung, S. W., Yu, J. Y. & Heath, J. R. Silicon Nanowire Devices. *Applied Physics Letters* **76**, 2068-2070 (2000).
47 Ho, J. C. *et al.* Controlled Nanoscale Doping of Semiconductors via Molecular Monolayers. *Nature Materials* **7**, 62-67 (2008).
48 Hains, A. W., Liu, J., Martinson, A. B. F., Irwin, M. D. & Marks, T. J. Anode Interfacial Tuning via Electron-Blocking/Hole-Transport Layers and Indium Tin Oxide Surface Treatment in Bulk-Heterojunction Organic Photovoltaic Cells. *Advanced Functional Materials* **20**, 595-606 (2010).
49 Hains, A. W. & Marks, T. J. High-Efficiency Hole Extraction/Electron-Blocking Layer to Replace Poly(3,4-ethylenedioxythiophene): Poly(styrene sulfonate) in Bulk-Heterojunction Polymer Solar Cells. *Applied Physics Letters* **92**, 23504 (2008).
50 Hayakawa, A., Yoshikawa, O., Fujieda, T., Uehara, K. & Yoshikawa, S. High Performance Polythiophene/Fullerene Bulk-Heterojunction Solar Cell with a TiO_x Hole Blocking Layer. *Applied Physics Letters* **90**, 163517 (2007).
51 Peng, K. Q., Wang, X., Wu, X. L. & Lee, S. T. Platinum Nanoparticle Decorated Silicon Nanowires for Efficient Solar Energy Conversion. *Nano Letters* **9**, 3704-3709 (2009).
52 Lewis, N. S. & Nocera, D. G. Powering the Planet: Chemical Challenges in Solar Energy Utilization. *Proceedings of the National Academy of Sciences of the United States of America* **103**, 15729-15735 (2006).
53 Huang, J., Chiam, S. Y., Tan, H. H., Wang, S. & Chim, W. K. Fabrication of Silicon Nanowires with Precise Diameter Control Using Metal Nanodot Arrays as a Hard Mask Blocking Material in Chemical Etching. *Chemistry of Materials* **22**, 4111-4116 (2010).
54 Lu, W. & Lieber, C. M. Semiconductor Nanowires. *Journal of Physics D-Applied Physics* **39**, R387-R406 (2006).
55 Cui, Y., Duan, X. F., Hu, J. T. & Lieber, C. M. Doping and Electrical Transport in Silicon Nanowires. *Journal of Physical Chemistry B* **104**, 5213-5216 (2000).
56 Rao, C. N. R., Deepak, F. L., Gundiah, G. & Govindaraj, A. Inorganic Nanowires. *Progress in Solid State Chemistry* **31**, 5-147 (2003).
57 Kelzenberg, M. D. *et al.* Photovoltaic Measurements in Single-Nanowire Silicon Solar Cells. *Nano Letters* **8**, 710-714 (2008).
58 Tutuc, E., Appenzeller, J., Reuter, M. C. & Guha, S. Realization of a Linear Germanium Nanowire p−n Junction. *Nano Letters* **6**, 2070-2074 (2006).
59 Crocherie, A. *et al.* in *IEEE 2009 International Image Sensor Workshop* (Bergen, Norway, 2009).
60 Koelling, S. *et al.* Characteristics of Cross-Sectional Atom Probe Analysis on Semiconductor Structures. *Ultramicroscopy* **111**, 540-545 (2011).

CHAPTER V

Heterogeneous Charge Transfer at Highly Rectifying n-Si/PEDOT:PSS Heterojunctions

A. Introduction

This chapter explores charge transfer at a representative heterojunction between an organic conducting polymer and an inorganic semiconductor. The specific objective of this investigation is to present a quantitative analysis of the implications of such charge transfer features at representative highly rectifying polymer/inorganic semiconductor photovoltaic interfaces and contrast their photoresponse characteristics to analogous metal/inorganic semiconductor heterojunctions. Results indicate that the difference in charge transfer rates at these heterojunctions may enhance the operation of heterojunction solar cells.

Organic polymers are a promising class of materials for scalable light-harvesting systems due to their abundance, low cost and compatibility with inexpensive processing techniques such as casting, spraying and roll-to-roll printing.[1,2] The electrical properties of degenerately doped conducting polymers in particular, which form a subset of organic polymers, can additionally foster complementary charge transfer rates that are of interest for the development of advanced optoelectronics.

Polymer contacts to inorganic semiconductors can take on multiple configurations, in each of which the organic materials play a different role in carrier transport and transfer across an interface. In the first type of system, organic chromophores absorb light and inject photoexcited carriers into an inorganic semiconductor for further transport. In other devices, the tasks of light absorption and carrier transport are shared,[3] while in still others organic polymers take on a role analogous to that of a metal in highly rectifying Schottky-type heterojunctions.[4-6] The

latter type of system is attractive due to the broadband absorption, superior charge transport properties and resistance to degradation of relevant inorganic semiconductors. Rectifying contacts between polymers and inorganic semiconductors have exhibited electrical properties that compare favorably with metal/inorganic semiconductor contacts[4,7] and have also offered an unprecedented level of control for tuning the electrical properties of a device.[8] Organic polymers are of particular interest in solar devices due to their appreciable optical transparency when utilized as thin films, near-metallic conductivity and ability to form highly rectifying contacts that support large current densities.[9-11] The design of efficient solar energy conversion devices based on organic polymer/inorganic semiconductor heterojunctions, however, requires a proper characterization of the charge transfer processes that occur at such interfaces.

This chapter attempts to facilitate a deeper understanding charge transfer processes at inorganic semiconductor/organic polymer interfaces by contrasting the optoelectronic properties of Si/polymer and Si/metal heterojunctions. The commercially available conductive polymer blend poly(3,4-ethylenedioxythiophene) poly(styrenesulfonic acid) (PEDOT:PSS) was used as the organic contacting material due to its high conductivity, suitable optical transmittance properties, and stability under ambient conditions. Au was chosen as the contacting material for the contrasting metal/inorganic semiconductor heterojunctions. Since the work function of Au was similar to that of PEDOT:PSS (5.1 eV),[12] heterojunctions of each type featured similar barrier heights, facilitating comparison of relevant operational features.

B. Methods

Si samples were prepared from single-crystalline n-Si wafers with dopant densities of 6 x 10^{12} cm^{-3} and 1.7 x 10^{15} cm^{-3} (MEMS Engineering & Material). A Si wafer was diced into ~0.7 cm x 0.7 cm sections, immersed in a 3:1 sulfuric acid (A.C.S. Plus grade, Fisher): hydrogen peroxide (30 wt. %, Sigma Aldrich) piranha solution for 35 min at 80ºC to remove any organic residue, and triple-rinsed with purified water (> 18 MΩ cm^{-1}, Barnstead Nanopure III purifier). The samples were then etched for 30 s in concentrated HF (49% v/v, Transene), rinsed with purified water, dried under a N_2 stream, masked using inert PVC electrical insulating tape and immediately used. Polymer

contacts were formed by drop-casting a 1:1 solution of PEDOT:PSS (Clevios^{TM} P, H.C. Starck): ethylene glycol (≥ 99%, Aldrich) onto the masked Si samples and curing in an oven (Thermolyne F47925-80, Thermo Scientific) at 125°C for ~10 min. Profilometry measurements indicated that the PEDOT:PSS films were non-uniform with layer thickness that varied from 400 to 1000 nm in a typical sample. Gold contacts were formed by evaporating 10 – 35 nm Au (99.99%, Kurt J. Lesker) through a stainless steel mask onto identically prepared Si samples. Back contacts were formed by roughing the backside of the Si with a diamond scribe, etching the roughened surface for 30 s in concentrated HF, depositing a thin layer of indium gallium eutectic (99.9+%, Aldrich and 99.99%, Aldrich) onto the freshly etched surface and mounting each sample on a stainless steel chip for structural support. Electrical contact to the face of the device was made with a small amount of silver print (GC Electronics) deposited on the edge of the mask.

Room temperature current-voltage (*J*-*V*) characteristics taken in the dark were obtained using a PAR 273 potentiostat. Temperature-dependent *J*-*V* data was collected with an Eco Chemie Autolab PGSTAT302N with temperature control achieved by varying the spatial proximity of the sample to a liquid nitrogen pool or hot plate. Temperature was monitored with a type J thermocouple (Omega) and an Omega 650 thermocouple thermometer. Device performance under white light illumination from an ELH light source was characterized by recording steady-state *J*-*V* data using a CH Instruments 700 potentiostat.

Spectral quantum yields were measured under 15 Hz chopped illumination with an Oriel 150 W Xe arc lamp and a quarter-turn single-grating monochromator. The system was calibrated with a Si photodiode of known response and fluctuations in output light intensity were accounted for via a quartz beam splitter and a separate Si photodiode monitored by a Merlin 70104 lock-in amplifier (all from Newport). Electrical control and monitoring were performed by a digital PAR 273 potentiostat connected to a Stanford Instruments SR830 lock-in amplifier. Output signals from the lock-in amplifier and reference Si photodiode were read by custom-written LabVIEW software.[13] For Au devices, internal quantum yield was calculated by dividing raw external quantum yield by the modeled transmittance, T_{opt}, from air through a Au film into a Si substrate (Figure

V.1a). Reported PEDOT:PSS device quantum yield spectra were corrected for film transparency and reflectivity by dividing raw external quantum yield by the transmittance of a polymer layer on quartz as determined from a Cary 5000 spectrophotometer (Varian, adjusted for differential film thickness). The spectra was also corrected for modeled reflectivity, R_{opt}, at the polymer/Si interface (Figure V.1b). Transmittance and reflectance models were based on the Fresnel equations for thin films. Optical constants for Au and PEDOT:PSS films were determined by performing ellipsometry on representative samples (Figure V.2). The MATLAB (MathWorks) script used in this model is included in Appendix C. Capacitance-voltage measurements were made using a Schlumberger SI1286 electrochemical interface and a Schlumberger SI1250 frequency response analyzer controlled by CorrWare and ZPlot software. Frequency response was measured with a 10 mV AC signal superimposed onto a DC voltage that ranged from 0 to 1 V into reverse bias.

C. Results

Figure V.3 shows representative C^{-2}-V data for PEDOT:PSS and Au contacts to n-Si with dopant densities of both 6 x 10^{12} cm^{-3} and 1.7 x 10^{15} cm^{-3}. The capacitance measured at the heterojunctions investigated herein was described by Equation V.1,[14,15]

$$\frac{1}{C^2} = \frac{2}{qA_s^2\varepsilon_s N_D}\left(V_{bi} - \frac{k_B T}{q} - V\right) \qquad \text{(V.1)}$$

for V_{bi} the built-in potential, A_s the cross-sectional contact area, ε_s the semiconductor permittivity and V the potential applied in reverse bias. Bode slopes were found to be -1 for both Au and PEDOT:PSS devices (Figure V.3 insets), indicating that the measured impedance response could be fit with a simple parallel RC equivalent circuit to accurately gauge the interface capacitance of these devices. Dopant densities were self-consistent between Au and PEDOT:PSS contacts and also agreed with values determined from separate wafer resistivity measurements. Values for V_{bi} were nominally identical for Au and PEDOT:PSS devices and tracked dopant density over a frequency range of 0.655 to 65.5 kHz, indicating that potential drops occurred almost entirely across the Si phase. C^{-2}-V measurements provided an independent determination of barrier heights as well as depletion widths and interfacial electric fields, which were nominally identical for Au

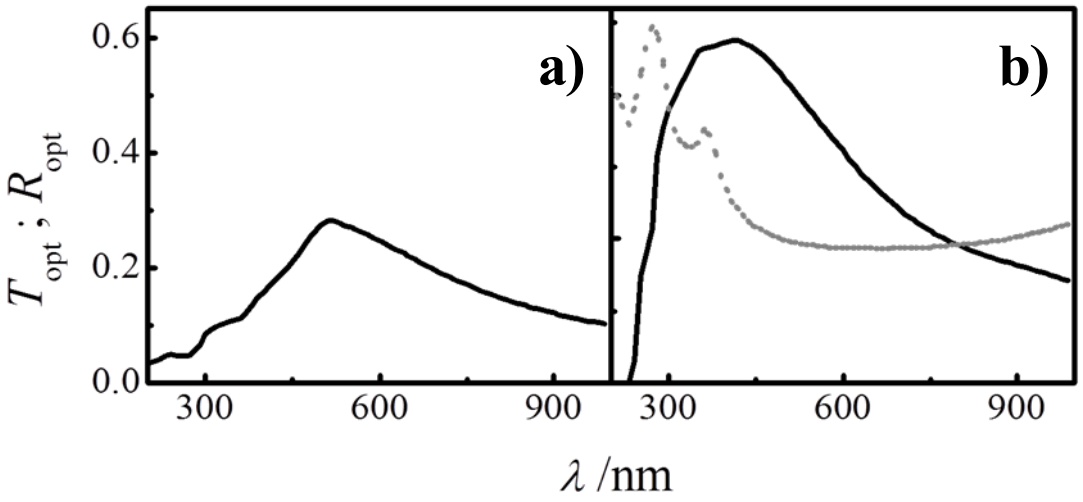

Figure V.1: Transmission (T_{opt}, solid black line) and reflectance (R_{opt}, dotted gray line) at (a) n-Si/Au and (b) n-Si/PEDOT:PSS interfaces.

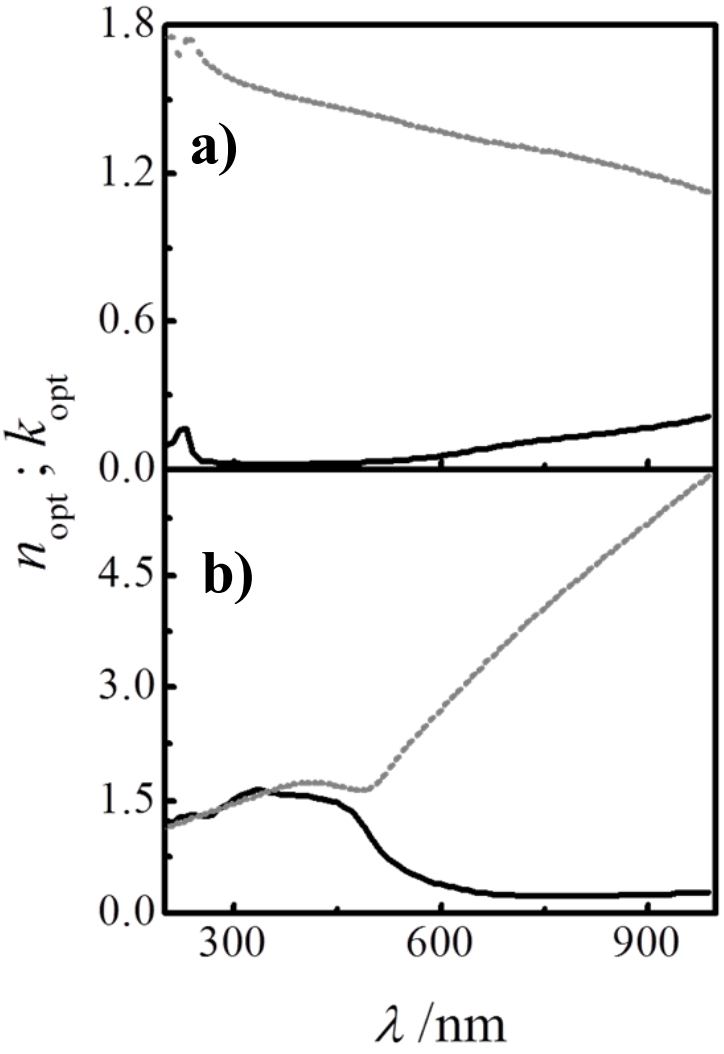

Figure V.2: Optical constants n_{opt} (solid black line) and k_{opt} (dotted gray line) for (a) PEDOT:PSS and (b) Au films with thicknesses of ~650 and ~35 nm, respectively. Values determined from ellipsometric analysis of representative samples.

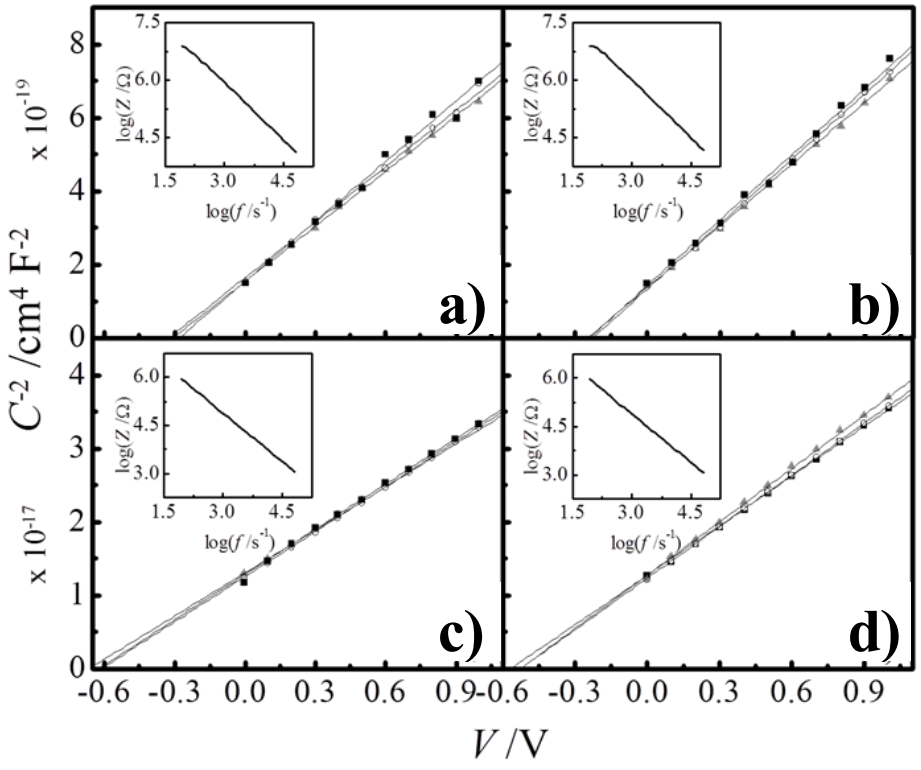

Figure V.3: Capacitance-voltage measurements for (a) PEDOT:PSS and (b) Au contacts to Si with N_D = 6 x 10^{12} cm^{-3} and (c) PEDOT:PSS and (d) Au contacts to Si with N_D = 1.5 x 10^{15} cm^{-3}. Solid squares, open circles and gray triangles correspond to 65.535 kHz, 6.554 kHz and 655.4 Hz, respectively. Insets: Bode plots at an applied potential of 0.5 V.

and PEDOT:PSS contacts to Si with dopant densities of both 6 x 10^{12} and 1.7 x 10^{15} cm^{-3}. Values for dopant density, built-in potential, depletion width, interfacial electric field and barrier height for Au and PEDOT:PSS contacts as determined from C^{-2}-V measurements are given in Table V.1.

Figure V.4 shows the dark J-V properties of representative Au and PEDOT:PSS contacts to both n- and p-type Si substrates with nominally identical dopant densities. Au and PEDOT:PSS contacts to p-Si exhibit ohmic-like responses to small applied biases, indicative of a small or zero barrier height. Au and PEDOT:PSS contacts to n-Si, however, exhibited strongly rectifying J-V responses. Current density through a rectifying heterojunction contact is described by the Bethe diode equation,[16]

$$J = J_0\left(e^{\frac{qV}{\eta k_B T}} - 1\right) \qquad \text{(V.2)}$$

where J_0 is the exchange current density and η is the so-called 'ideality' factor. Measured J_0, η and Φ_B (see below) values are listed for a number of n-Si/Au and n-Si/PEDOT:PSS contacts to Si of two different dopant densities in Table V.2. The ideality factors obtained for the n-Si/PEDOT:PSS contacts are consistent with reported values[2] and are representative of Si/organic polymer[11,17] and inorganic semiconductor/organic polymer[8-10,18-21] contacts in general.

When charge transfer across a heterojunction is limited solely by thermionic emission, the exchange current density can be approximated by Equation V.3,

$$J_0 \approx A^{**}T^2 e^{\frac{-q\Phi_B}{k_B T}} \qquad \text{(V.3)}$$

where the reduced effective Richardson constant, A^{**}, is determined solely by the electrical properties of the inorganic semiconductor and is agnostic to changes in the contacting material.[22] Current densities measured at PEDOT:PSS contacts, however, were significantly lower than those measured at Au contacts at the same applied bias. The dissimilarity of the dark J-V responses of rectifying n-Si/Au and n-Si/PEDOT:PSS contacts indicates that the electronic properties of the contacting material is not irrelevant to the operation of these two device types. Equation V.4 expresses the exchange current density for an n-type inorganic semiconductor heterojunction that is limited by both thermionic emission and carrier diffusion within the inorganic semiconductor toward a

Table V.1: Dopant density, N_D, built-in potential, V_{bi}, depletion width, W_D, interfacial electric field, E_{int}, and barrier height, Φ_B, for Au and PEDOT:PSS contacts to n-Si samples of two different dopant densities as determined from C^2-V measurements. The uncertainty reported for 'Average' values represents the standard deviation of measured values.

Contact	Device	N_D / cm^{-3}	V_{bi} / V	W_D / µm	E_{int} / V cm^{-1} x 10^3	Φ_B / V
Au	**1**	5.932 x 10^{12}	0.192	6.48	0.513	0.612
	2	5.765 x 10^{12}	0.167	6.12	0.461	0.588
	3	6.663 x 10^{12}	0.168	5.71	0.498	0.585
	4	5.747 x 10^{12}	0.266	7.74	0.620	0.687
	5	6.419 x 10^{12}	0.174	5.92	0.500	0.592
	Average	**(6.1 ± 0.4) x 10^{12}**	**0.19 ± 0.04**	**6.4 ± 0.8**	**0.52 ± 0.06**	**0.61 ± 0.04**
	6	1.552 x 10^{15}	0.538	0.669	1.53	0.8
	7	1.559 x 10^{15}	0.533	0.665	1.55	0.796
	Average	**(1.56 ± 0.01) x 10^{15}**	**0.536 ± 0.002**	**0.667 ± 0.005**	**1.54 ± 0.02**	**0.798 ± 0.002**
PEDOT:PSS	**11**	7.156 x 10^{12}	0.299	7.35	0.743	0.714
	12	6.799 x 10^{12}	0.271	7.18	0.683	0.688
	13	7.743 x 10^{12}	0.177	5.43	0.557	0.589
	14	5.217 x 10^{12}	0.418	10.2	0.769	0.842
	15	5.346 x 10^{12}	0.392	9.74	0.752	0.815
	16	7.073 x 10^{12}	0.301	7.41	0.743	0.716
	Average	**(6.6 ± 1.0) x 10^{12}**	**0.31 ± 0.09**	**20 ± 40**	**0.71 ± 0.08**	**0.73 ± .09**
	23	1.559 x 10^{15}	0.626	0.721	1.66	0.888
	24	1.465 x 10^{15}	0.652	0.758	1.65	0.916
	25	1.719 x 10^{15}	0.641	0.694	1.77	0.9
	26	1.786 x 10^{15}	0.614	0.667	1.76	0.872
	27	1.695 x 10^{15}	0.618	0.689	1.72	0.878
	Average	**(1.64 ± 0.13) x 10^{15}**	**0.630 ± 0.016**	**0.71 ± 0.04**	**1.71 ± 0.06**	**0.891 ± 0.018**

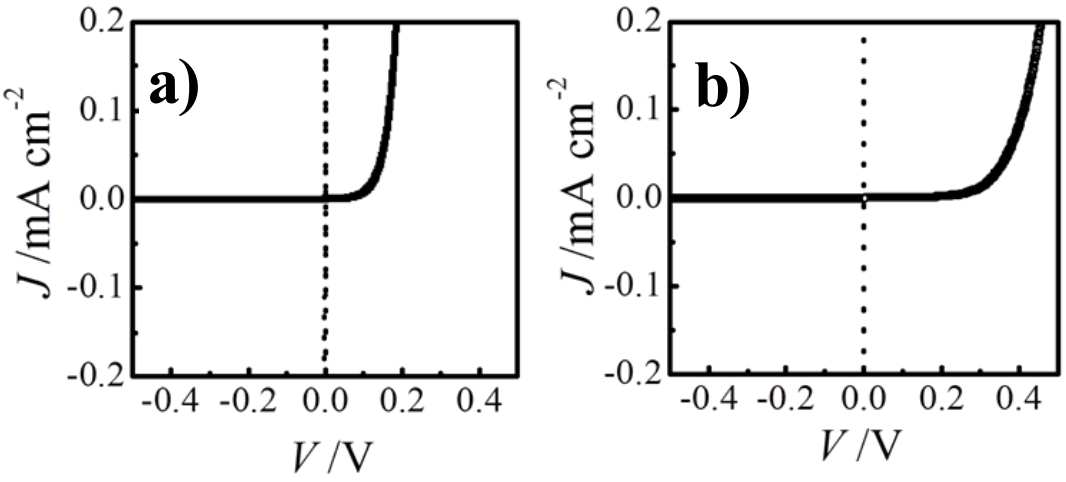

Figure V.4: Dark *J-V* curves for (a) Au and (b) PEDOT:PSS contacts to (solid line) n-type and (dotted line) p- type Si. N-type and p-type dopant densities were 1.7 x 10^{15} cm^{-3} and 5 x 10^{15} cm^{-3}, respectively.

Table V.2: Exchange current density, J_0, barrier height, Φ_B, and diode ideality factor, η, as determined from dark, room-temperature *J-V* measurements and Equations V.2 and V.4 in the text.

Contact	Device	N_D /cm^{-3}	J_0 /nA cm^{-2}	Φ_B /V	η
Au	**1**	6 x 10^{12}	43.7	0.8477	1.0352
	2		42.3	0.8485	1.0423
	3		46	0.8464	1.0395
	4		45.4	0.8467	1.0354
	5		39.9	0.85	1.0341
	Average		**43 ± 2**	**0.8479 ± 0.0015**	**1.037 ± 0.003**
	6	1.7 x 10^{15}	178	0.8004	1.0237
	7		153	0.8078	1.0188
	8		188	0.7997	1.0521
	9		182	0.7977	1.0553
	10		170	0.7993	1.0582
	Average		**175 ± 15**	**0.801 ± 0.0039**	**1.042 ± 0.019**
PEDOT:PSS	**11**	6 x 10^{12}	22.6	0.8646	1.276
	12		39.3	0.8504	1.2795
	13		42.6	0.8484	1.3073
	14		20.4	0.8672	1.201
	15		31.7	0.8559	1.2277
	16		30.5	0.8569	1.2377
	Average		**31 ± 8**	**0.857 ± 0.007**	**1.25 ± 0.04**
	17	1.7 x 10^{15}	7.74	0.892	1.5991
	18		8.85	0.8740	1.8720
	19		0.489	0.9471	1.3838
	20		3.20	0.9062	1.6257
	21		2.15	0.9130	1.6122
	22		1.19	0.9279	1.3751
	Average		**3.9 ± 3.5**	**0.91 ± 0.03**	**1.58 ± 0.18**

specific contact.[22]

$$J_0 = \frac{qN_D v_n}{1+\frac{v_n}{v_d}} e^{\frac{-q\Phi_B}{k_B T}} \qquad \text{(V.4)}$$

Here, v_n is the effective recombination velocity for electrons (majority carriers) at the heterojunction, v_d is the carrier drift velocity and the denominator in Equation V.4 approaches unity for $v_d >> v_n$. A value of v_n equal to the thermal velocity, v_{th}, is implicit in Equation V.3.

Figure V.5a shows the dark *J*-*V* responses of a representative PEDOT:PSS contact to n-Si with N_D = 1.7 x 10^{15} cm^{-3} at various temperatures. Corresponding Richardson plots for both n-Si/PEDOT:PSS and n-Si/Au devices are shown in Figure V.5b. Figure V.5b was generated by fitting the linear portion of each ln(*J*)-*V* response in Figure V.5a and extrapolating to $V = 0$ to obtain the exchange current density for the device at each temperature. The ln(*J*)-*V* and Richardson responses in Figure V.5 are both linear, indicating that device operation was not dominated by space-charge limited conduction[22] in the PEDOT:PSS film or the ionization of surface traps.[23] Richardson plots were fit to Equations V.3 and V.4 to estimate A^{**} and v_n values, respectively. N-Si/Au devices were found to have A^{**} = 130 ± 40 A cm^{-2} K^{-2} and v_n = (2.5 ± 0.9) x 10^6 cm s^{-1}. These values were close to the tabulated values for A^{**} (~110 A cm^{-2} K^{-2}) and the thermal velocity (~10^7 cm s^{-1}) in Si. N-Si/PEDOT:PSS devices, however, exhibited much lower values of both A^{**} (0.0014 ± 0.002 A cm^{-2} K^{-2}) and v_n (30 ± 50 cm s^{-1}). Despite the reduced precision of this technique to determine A^{**} and v_n for smaller values of v_n, these results strongly suggest that v_n is several orders of magnitude lower at n-Si/PEDOT:PSS versus n-Si/Au heterojunctions. Fitting parameters, reduced effective Richardson constants, barrier heights and v_n values for measurements performed on three Au and six PEDOT:PSS contacts are listed in Table V.3.

A second, independent comparison of v_n values was made via analysis of the photoresponses of n-Si/Au and n-Si/PEDOT:PSS devices. The internal quantum yield, $\Phi(\lambda)$, for a semiconductor heterojunction under illumination is sensitive to both minority and majority carrier processes and is given by Equation V.5 for an n-type inorganic semiconductor,[24]

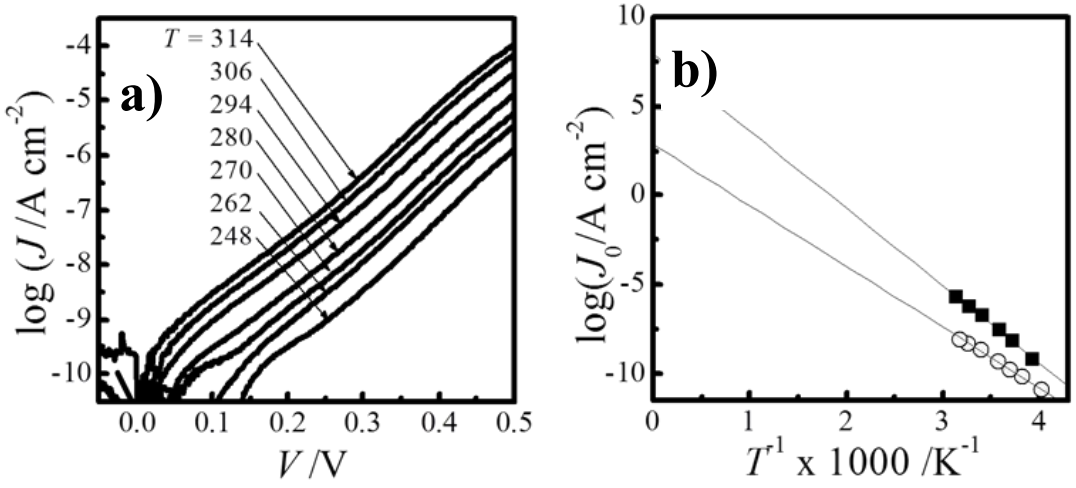

Figure V.5: (a) Log(*J*)-*V* characteristics for a representative n-Si/PEDOT:PSS device at a range of temperatures. (b) Richardson plot of representative (solid squares) Au (device 10) and (open circles) PEDOT:PSS (device 21) contacts.

Table V.3: Effective Richardson constant, A^{**}, effective recombination velocity, v_n, barrier height, Φ_B, and fit parameters for PEDOT:PSS contacts to n-Si with N_D = 1.7 x 10^{15} cm^{-3}. Values determined from temperature-dependent dark *J-V* measurements and Equations V.3 and V.4 in the text.

Contact	Device	$\log(J_0T^{-2})$-T^{-1} Fit		R^2	A^{**} /A cm^{-2} K^{-2}	Φ_B /V	v_n /cm s^{-1}
		Intercept /log(AK^{-2})	Slope /log(AK^{-2})K				
Au	**8**	1.90	-4010	0.99737	79.4	0.80	1.56 x 10^6
	9	2.21	-4080	0.9991	162.2	0.81	3.21 x 10^6
	10	2.16	-4090	0.99636	144.5	0.80	2.85 x 10^6
PEDOT:PSS	**18**	-5.14	-2287	0.99605	7.22 x 10^{-6}	0.45	0.140
	19	-2.25	-3504	0.99841	5.60 x 10^{-3}	0.70	109
	20	-4.68	-2581	0.99873	2.10 x 10^{-5}	0.51	0.408
	21	-2.92	-3171	0.99745	1.20 x 10^{-3}	0.63	23.3
	22	-4.20	2831	0.99285	6.31 x 10^{-5}	0.56	1.23

$$\Phi(\lambda) = 1 - \frac{e^{-\alpha(\lambda)W_D}}{1+\alpha(\lambda)L_p} - \frac{1}{\left(1+\frac{qE_0}{\alpha(\lambda)k_BT}\right)\left(1+\frac{v_d}{v_n}\right)} \qquad \text{(V.5)}$$

where E_0 is the electric field at the interface. The first two terms of Equation V.5 comprise the so-called Gärtner model, which accounts for bulk minority carrier recombination losses by assessing the overlap in carrier photogeneration and collection profiles using the spectral absorbance, $\alpha(\lambda)$, and minority carrier diffusion length, L_p, of the semiconductor along with the depletion width, W_D, at the junction.[13] The third term in Equation V.5 is an exact solution of the transport equation for n-type carriers in a semiconductor depletion region and accounts for competition between deleterious majority carrier charge transfer across the front contact and collection at the back contact (Figure V.6). [24] Semiconductor absorbance is generally much more pronounced at shorter wavelengths[25] (Figure V.7), and photoresponses at small λ typically correspond to processes occurring near the directly illuminated surface (here, the semiconductor immediately adjacent to the Au or PEDOT:PSS contact). The different forms of $\alpha(\lambda)$ dependence in the second and third terms of Equation V.5 thus result in an effective decoupling of majority carrier recombination processes, which manifest as decreases in $\Phi(\lambda)$ at shorter wavelengths,[26] from the minority carrier processes which cause decreases in $\Phi(\lambda)$ at longer wavelengths.

Figures V.8a-d show calculated and measured photoresponses for Au and PEDOT:PSS contacts to n-Si with N_D = 6 x 10^{12} cm^{-3}. The utilization of Si with low N_D was significant, as the decoupling of minority and majority carrier recombination processes is particularly well-illustrated for lightly doped Si substrates due to the N_D dependence of the W_D and E_0 terms in Equation V.5. Figure V.8a shows $\Phi(\lambda)$ as calculated from Equation V.5 for N_D = 6 x 10^{12} cm^{-3}, L_p = 250 μm and μ_n (used to calculate v_d) = 1500 cm^2 v^{-1} s^{-1} at various collection velocities. Majority carrier losses at the front contact were severe for large v_n and negligible for $v_n \leq 10^4$ cm s^{-1}. The internal quantum yield response of a representative n-Si/Au contact as a function of wavelength is shown in Figure V.8b. This response was in excellent agreement with Equation V.5 and a value of v_n equal to the thermal velocity of electrons in Si (10^7 cm s^{-1}). Figure V.8c shows an analogous response for an n-Si/PEDOT:PSS device along with a fit to Equation V.5

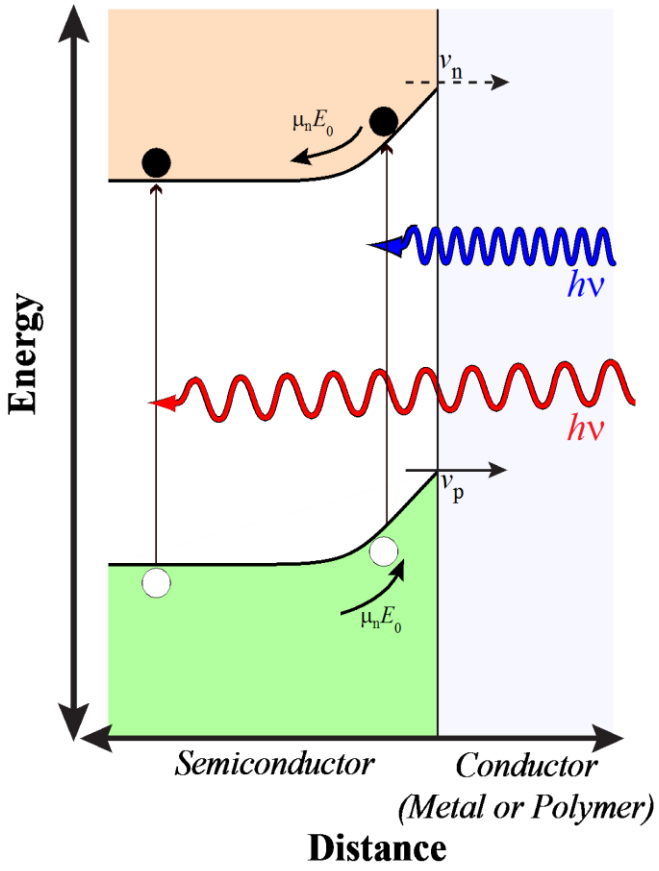

Figure V.6: Band bending diagram for an n-type semiconductor heterojunction illuminated by short- and long-wavelength light. Solid and dashed arrows indicate favorable and deleterious processes for photogenerated carrier collection, respectively.

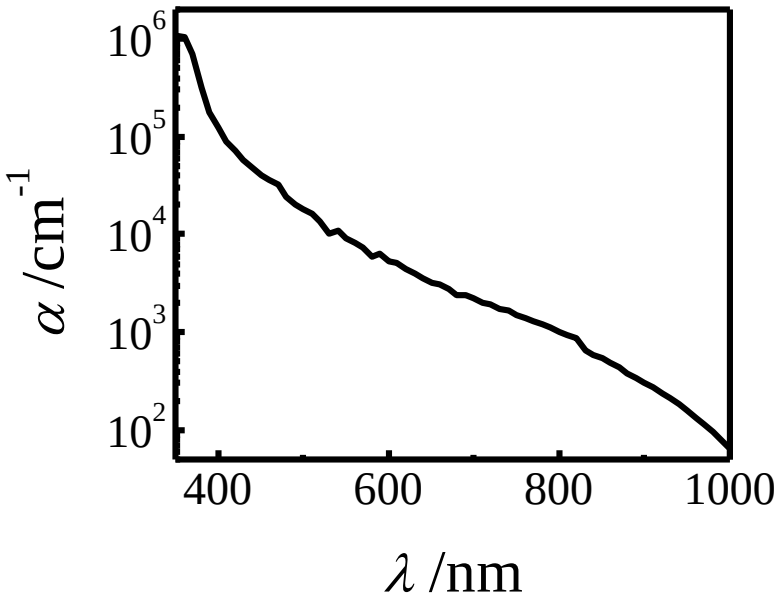

Figure V.7: Absorptivity $\alpha(\lambda)$ of Si at visible wavelengths. Adapted from Reference 30.[25]

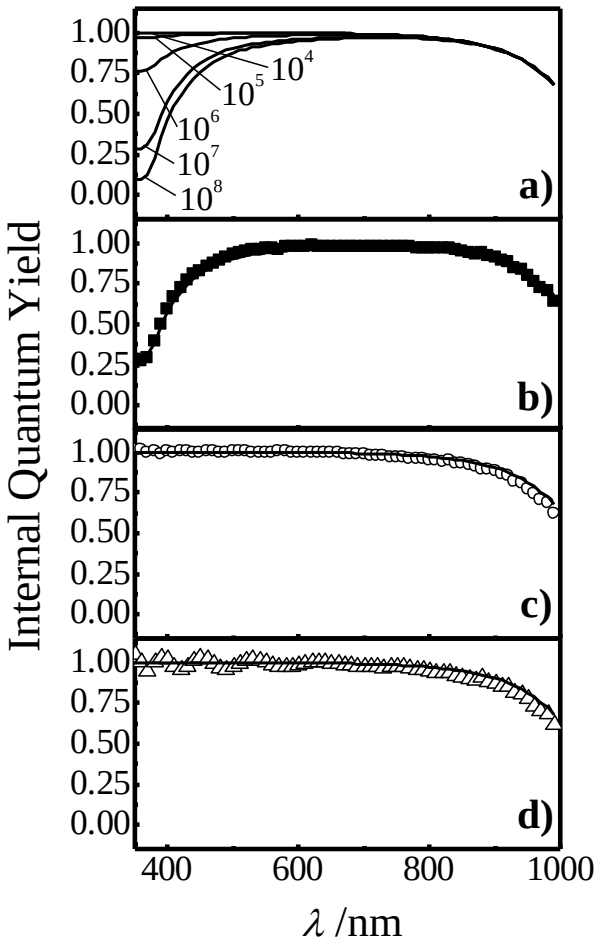

Figure V.8: (a) Internal quantum yields as calculated from Equation V.5 in the text for N_D = 6 x 10^{12} cm^{-3}, L_p = 0.025 cm, electron mobility μ_n = 1500 cm^2 V^{-1} s^{-1} and several values of v_n. (b) Measured internal quantum yield for a representative Au contact to n-Si with N_D = 6 x 10^{12} cm^{-3}. The solid line is a fit with v_n = 10^7 cm s^{-1}. (c) Measured internal quantum yield for a representative PEDOT:PSS contact to n-Si with N_D = 6 x 10^{12} cm^{-3}. The solid line is a fit with v_n = 10^4 cm s^{-1}. (d) Measured internal quantum yield for a representative PEDOT:PSS contact made with CH_3-terminated n-Si(111) with N_D = 6 x 10^{12} cm^{-3}. The solid line is a fit with v_n = 10^4 cm s^{-1}.

with $v_n = 10^4$ cm s^{-1}. Deleterious majority carrier recombination at the n-Si/PEDOT:PSS interface was negligible at short wavelengths, consistent with values of $v_n < 10^5$ cm s^{-1}. Figure V.8d shows $\Phi(\lambda)$ for a PEDOT:PSS contact to CH_3-terminated n-Si(111) prepared from the same wafer as other devices. CH_3 groups are known to passivate Si surfaces, preventing the formation of insulating oxide layers.[27] The internal quantum yield response for the CH_3-terminated Si device was in agreement with a fit to Equation V.5 with $v_n = 10^4$ cm s^{-1}. The nominally identical responses of PEDOT:PSS contacts to CH_3-terminated Si and etched Si suggest that neither type of heterojunction featured a significant interfacial oxide layer that could be responsible for the high $\Phi(\lambda)$ values measured at short wavelengths in these devices.[26] The quasi-periodic modulation in the Figure V.8d response at lower wavelengths is consistent with reflectance/transmittance fringes and was observed for several devices.[28]

Figures V.9a-V.9c depict representative *J-V* responses of PEDOT:PSS contacts to n-Si with dopant densities of 7 x 10^{13}, 1.7 x 10^{15} and 3 x 10^{16} cm^{-3} under enough ELH white light illumination to generate 10 mA cm^{-2} photocurrent densities in each device. The maximum possible open circuit voltage, V_{oc}, for a photodiode operating at the bulk recombination limit is determined from the short-circuit current density, J_{sc}, and the bulk electronic properties of the inorganic semiconductor according to Equation V.6,

$$V_{oc} = \frac{k_B T}{q} \ln\left(\frac{J_{sc} L_p N_D}{n_i^2 \mu_p k_B T} \right) \qquad \text{(V.6)}$$

where L_p is the hole diffusion length in the semiconductor, D_p is the hole diffusion coefficient and n_i the intrinsic semiconductor carrier concentration. Inorganic semiconductor/metal devices do not typically exhibit sensitivity to dopant density since the defining features of Schottky device operation (see Equations V.2 and V.3) have minimal dependence on N_D. Average n-Si/PEDOT:PSS device V_{oc} values, however, increased from 0.43 V at $N_D = 7$ x 10^{13} cm^{-3} to 0.51 V at $N_D = 1.7$ x 10^{15} cm^{-3} and 0.53 V for $N_D = 3$ x 10^{16} cm^{-3}. Figure V.9d shows V_{oc} values for Au and PEDOT:PSS contacts to n-Si with three different values of N_D plotted against the bulk-recombination-limited V_{oc} as determined from Equation V.6. N-Si/PEDOT:PSS device V_{oc} values were within 0.02 to 0.1 V of the bulk-recombination-limited V_{oc} values and were a full 0.15 to 0.3 V higher than the V_{oc} values obtained from the literature[29,30] for Au contacts to n-Si of the same

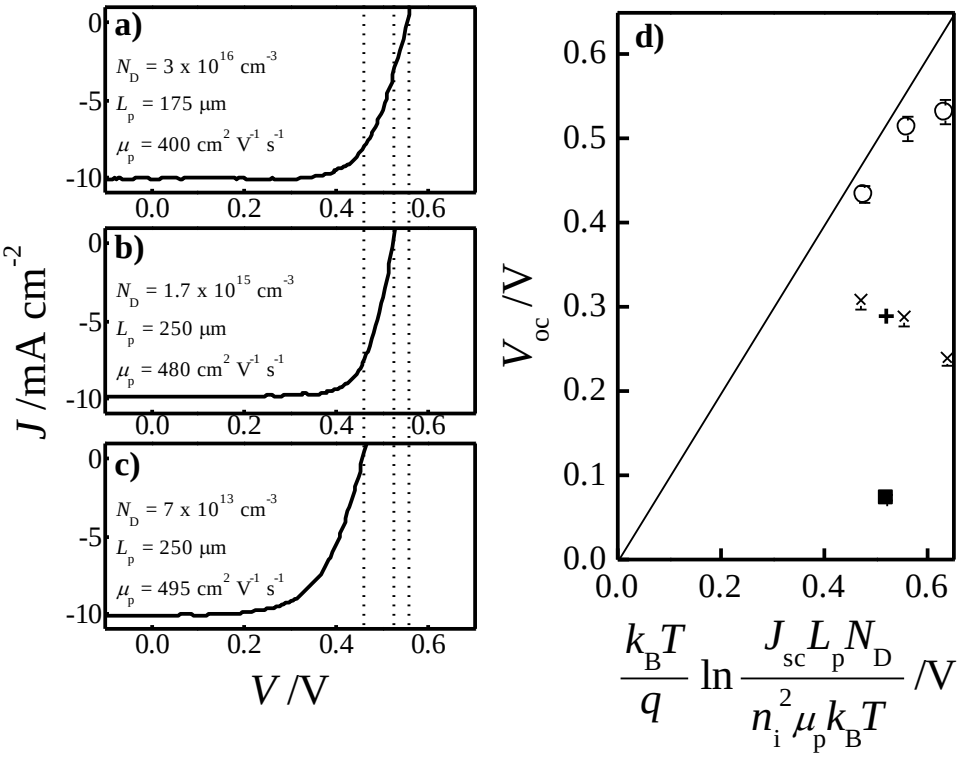

Figure V.9: Representative current density-voltage responses of PEDOT:PSS contacts to n-Si with a dopant density of (a) 7 x 10^{13}, (b) 1.7 x 10^{15} and (c) 3 x 10^{16} cm^{-3} under illumination from an ELH white light source. Dashed lines indicate V_{oc} values. (d) Measured V_{oc} values from Figures V.9a-c as a function of the maximum expected V_{oc} from Equation V.6. Responses for n-Si/Au devices from (×) Reference [36],[29] (+) Reference [39],[30] and (■) a control sample. The solid line represents the bulk-recombination-limited V_{oc} values.

dopant densities. Thus, the responses from n-Si/PEDOT:PSS contacts approached the functional form of Equation V.6, exhibiting significant sensitivity to bulk Si properties. Also shown in Figure V.9d is the V_{oc} value measured for a control n-Si/Au device that was subjected to the same processing conditions as n-Si/PEDOT:PSS devices prior to Au evaporation. That is, n-Si samples were drop-cast with a transparent aqueous solution extracted from the PEDOT:PSS solution and baked in an oven under the same conditions as PEDOT:PSS devices to determine if n-Si/PEDOT:PSS device response was affected by an interfacial insulating layer. The performance of this device was exceedingly poor, and V_{oc} values peaked at just 60 mV.

D. Discussion

Figures V.5-V.9 indicate that the majority carrier charge transfer velocity, v_n, is several orders of magnitude lower at n-Si/PEDOT:PSS versus n-Si/Au contacts. Lonergan and co-workers have previously reported similarly small J_0 values for InP/polypyrrole contacts, which they found to be inconsistent with analytical expressions such as that in Equation V.3.[31] The 'v_n' formalism used here describes these observations and highlights a direct connection of observed device responses to microscopic theories of charge transfer. The parameter v_n describes the velocity at which majority carriers cross the heterojunction interface and can be expressed as the product of the standard rate constant for majority carrier charge transfer, k_{et} (cm^4 s^{-1}), and the effective density of acceptor states in the contacting material, N_A (cm^{-3}). A diminution in k_{et}, N_A, or both thus results in smaller values of v_n. In Si/metal contacts where k_{et} and N_A are both large, interfacial charge transfer is limited by the thermal velocity of carriers within Si, $v_{th} = 10^7$ cm s^{-1}.[32] This value for v_n is implicit when the pre-exponential term in Equation V.2 includes A^{**}.[22] Multiple factors that may contribute to the smaller value of v_n observed in n-Si/PEDOT:PSS versus n-Si/Au heterojunctions are discussed below.

Interfacial oxide layers are known to impede charge transfer at heterojunctions, but the presence and/or specific operational implications of such layers are not consistent with the results shown herein. Semiclassical models for microscopic heterogeneous charge transfer have been used to interpret k_{et} for semiconductor/liquid heterojunctions.[33] However, the difficulties in determining reorganization energies in polymers,[34] in

addition to the influence of grain boundaries, complicate this type of analysis for the inorganic semiconductor/organic polymer heterojunctions shown here. Nevertheless, both the presented data and existing literature on metal-insulator-semiconductor (MIS) heterojunctions indicate that k_{et} is unlikely to be decreased at these n-Si/PEDOT:PSS contacts solely because of an interfacial oxide. For n-Si MIS devices based on native, chemical, or evaporated surface oxides, small values of V_{oc} which do not approach the limit imposed by bulk recombination processes are observed,[35] in contrast to the data shown here. Although sputtered oxides[35] and photoelectrochemical anodization[30] have been used to produce n-type MIS devices with good photoresponses, the conditions employed herein should not lead to chemically equivalent surface oxides. The small V_{oc} values obtained for control n-Si/Au devices (Figure V.9d) illustrated that an inadvertent surface oxide resulting from device fabrication is not the defining feature for good photoresponses in this system. Additionally, control n-Si/PEDOT:PSS devices made with CH_3-terminated Si(111) substrates exhibited internal quantum efficiencies consistent with $v_{n,PEDOT:PSS} << 10^7$ cm s^{-1} (Figure V.8d). Since CH_3-terminated Si(111) surfaces are strongly resistant to chemical oxidation when processed in ambient conditions and a CH_3 monolayer does not represent an appreciable tunneling barrier for electron transfer at room temperature,[27] an equivalent surface oxide that favorably affects the photoresponses of these n-Si/PEDOT:PSS heterojunctions is also unlikely.

The effective density of states at the Fermi level for PEDOT:PSS is 10^{18} cm^{-3}, several orders of magnitude lower than the equivalent density of states for Au at 10^{22} cm^{-3}.[22,36,37] The specific blend morphology of PEDOT:PSS films may contribute to the lower v_n values observed here by decreasing the electronic coupling between PEDOT and Si. In cast PEDOT:PSS films, the PSS component can form thin encapsulating shells (~ 3.5 nm thick) around the core conducting PEDOT colloids. This shell structure may contribute to the higher hole transfer versus electron transfer rates in this material.[38] Transparent conducting polymer contacts with this feature may therefore be useful as contacts to a variety of inorganic semiconductors. Recent reports that detail the excellent photoresponses of amorphous-Si/PEDOT:PSS heterojunctions[39] and PEDOT:PSS/Si nanowire composite devices[40] are consistent with this premise.

E. Conclusion

The data presented in this work cumulatively demonstrate that the majority carrier collection velocity, v_n, can be several orders of magnitude lower at n-Si/polymer versus n-Si/metal heterojunctions. Kinetic limitations at n-Si/PEDOT:PSS interfaces were shown to affect the expression for dark exchange current density. Devices with lower v_n values exhibited two properties beneficial for light-harvesting devices. First, short-wavelength light was collected with near-unity internal quantum yield due to decreased majority carrier recombination at the front contact. In contrast, corresponding internal quantum yields for Si/metal devices featuring high v_n values were 75% lower at short wavelengths. In addition to the demonstrated increase in photocurrent collection, n-Si/PEDOT:PSS devices also exhibited larger open-circuit voltages under illumination, and in fact approached bulk-recombination-limited operation. This work suggests that the distinct majority carrier transfer properties at inorganic semiconductor/conducting polymer interfaces can be highly advantageous for solar energy conversion.

F. References

1 Groenendaal, B. L., Jonas, F., Freitag, D., Pielartzik, H. & Reynolds, J. R. Poly(3,4-ethylenedioxythiophene) and its Derivatives: Past, Present, and Future. *Advanced Materials* **12**, 481-494 (2000).

2 Moller, S., Perlov, C., Jackson, W., Taussig, C. & Forrest, S. R. A Polymer/Semiconductor Write-Once Read-Many-Times Memory. *Nature* **426**, 166-169 (2003).

3 Beek, W. J. E., Wienk, M. M., Kemerink, M., Yang, X. N. & Janssen, R. A. J. Hybrid Zinc Oxide Conjugated Polymer Bulk Heterojunction Solar Cells. *Journal of Physical Chemistry B* **109**, 9505-9516 (2005).

4 Sailor, M. J., Klavetter, F. L., Grubbs, R. H. & Lewis, N. S. Electronic Properties of Junctions Between Silicon and Organic Conducting Polymers. *Nature* **346**, 155-157 (1990).

5 Wang, W. N. & Schiff, E. A. Polyaniline on Crystalline Silicon Heterojunction Solar Cells. *Applied Physics Letters* **91** (2007).

6 Price, M. J., Foley, J. M., May, R. A. & Maldonado, S. Comparison of Majority Carrier Charge Transfer Velocities at Si/Polymer and Si/Metal Photovoltaic Heterojunctions. *Applied Physics Letters* **97** (2010).

7 Heeger, A. J. Nobel Lecture: Semiconducting and Metallic Polymers: The Fourth Generation of Polymeric Materials. *Reviews of Modern Physics* **73**, 681-700 (2001).

8 Lonergan, M. C. A Tunable Diode Based on an Inorganic Semiconductor Vertical Bar Conjugated Polymer Interface. *Science* **278**, 2103-2106 (1997).

9 Frank, A. J., Glenis, S. & Nelson, A. J. Conductive Polymer Semiconductor Junction - Characterization of Poly(3-methylthiophene)-Cadmium Sulfide Based Photoelectrochemical and Photovoltaic Cells. *Journal of Physical Chemistry* **93**, 3818-3825 (1989).

10 Halliday, D. P., Gray, J. W., Adams, P. N. & Monkman, A. P. Electrical and Optical Properties of a Polymer Semiconductor Interface. *Synthetic Metals* **102**, 877-878 (1999).

11 Vermeir, I. E., Kim, N. Y. & Laibinis, P. E. Electrical Properties of Covalently Linked Silicon Polypyrrole Junctions. *Applied Physics Letters* **74**, 3860-3862 (1999).

12 Smith, S. & Forrest, S. R. A Low Switching Voltage Organic-on-Inorganic Heterojunction Memory Element Utilizing a Conductive Polymer Fuse on a Doped Silicon Substrate. *Applied Physics Letters* **84**, 5019-5021 (2004).

13 Price, M. J. & Maldonado, S. Macroporous n-GaP in Nonaqueous Regenerative Photoelectrochemical Cells. *Journal of Physical Chemistry C* **113**, 11988-11994 (2009).

14 Goodman, A. M. Metal-Semiconductor Barrier Height Measurement by Differential Capacitance Method - 1 Carrier System. *Journal of Applied Physics* **34**, 329-& (1963).

15 Xue, F. L., Su, Y. & Varahramyan, K. Modified PEDOT-PSS Conducting Polymer as S/D Electrodes for Device Performance Enhancement of P3HT TFTs. *IEEE Transactions on Electron Devices* **52**, 1982-1987 (2005).

16 Balkanski, M. W., R. F. *Semiconductor Physics and Applications*. (Oxford University Press, 2000).

17 Campos, M. *et al.* Properties of the Heterojunction Between Poly(dithienopyrrole)-Poly(vinylchloride) Composite and n-Doped Silicon. *Synthetic Metals* **75**, 61-64 (1995).

18 Lonergan, M. C., Cooney, C. T. & Myers, J. A. in *Electrical, Optical, and Magnetic Properties of Organic Solid-State Materials Iv* Vol. 488 *Materials Research Society Symposium Proceedings* (eds J. R. Reynolds *et al.*) 707-712 (1998).

19 Nakano, M. *et al.* Schottky Contact on a ZnO (0001) Single Crystal with Conducting Polymer. *Applied Physics Letters* **91** (2007).

20 Novotny, C. J., Yu, E. T. & Yu, P. K. L. InP Nanowire/Polymer Hybrid Photodiode. *Nano Letters* **8**, 775-779 (2008).

21 Sharma, B. K., Khare, N. & Ahmad, S. A ZnO/PEDOT:PSS Based Inorganic/Organic Hetrojunction. *Solid State Communications* **149**, 771-774 (2009).

22 Sze, S. M. N., Kwok K. *Physics of Semiconductor Devices*. 3 edn, (John Wiley & Sons, 2007).

23 Carbone, A., Pennetta, C. & Reggiani, L. Trapping-Detrapping Fluctuations in Organic Space-Charge Layers. *Applied Physics Letters* **95** (2009).

24 Reichman, J. Collection Efficiency of Low-Mobility Solar Cells. *Applied Physics Letters* **38**, 251-253 (1981).

25 Green, M. A. & Keevers, M. J. Optical Properties of Intrinsic Silicon at 300 K. *Progress in Photovoltaics* **3**, 189-192 (1995).

26 Kumar, A. & Lewis, N. S. Short-Wavelength Spectral Response Properties of Semiconductor Liquid Junctions. *Journal of Physical Chemistry* **94**, 6002-6009 (1990).
27 Maldonado, S. & Lewis, N. S. Behavior of Electrodeposited Cd and Pb Schottky Junctions on CH_3-Terminated n-Si(111) Surfaces. *Journal of the Electrochemical Society* **156**, H123-H128 (2009).
28 The presence of fringes may have indicated more uniform film thickness.
29 Maldonado, S., Knapp, D. & Lewis, N. S. Near-Ideal Photodiodes from Sintered Gold Nanoparticle Films on Methyl-Terminated Si(111) Surfaces. *Journal of the American Chemical Society* **130**, 3300-+ (2008).
30 Kumar, A. *et al.* Fabrication of Minority-Carrier-Limited n-Si/Insulator/Metal Diodes. *Applied Physics Letters* **56**, 1919-1921 (1990).
31 Lonergan, M. C. & Jones, F. E. Calculation of Transmission Coefficients at Nonideal Semiconductor Interfaces Characterized by a Spatial Distribution of Barrier Heights. *Journal of Chemical Physics* **115**, 433-445 (2001).
32 Jacoboni, C., Canali, C., Ottaviani, G. & Alberigi Quaranta, A. A Review of Some Charge Transport Properties of Silicon. *Solid-State Electronics* **20**, 77-89 (1977).
33 Gerischer, H. *Advances in Electrochemistry and Electrical Engineering*. Vol. 4 142-178 (Wiley, 2004).
34 Hutchison, G. R., Ratner, M. A. & Marks, T. J. Intermolecular Charge Transfer between Heterocyclic Oligomers. Effects of Heteroatom and Molecular Packing on Hopping Transport in Organic Semiconductors. *Journal of the American Chemical Society* **127**, 16866-16881 (2005).
35 Pulfrey, D. L. MIS Solar Cells: A Review. *IEEE Transactions on Electron Devices* **25**, 1308-1317 (1978).
36 Kim, E.-G. & Brédas, J.-L. Electronic Evolution of Poly(3,4-ethylenedioxythiophene) (PEDOT): From the Isolated Chain to the Pristine and Heavily Doped Crystals. *Journal of the American Chemical Society* **130**, 16880-16889 (2008).
37 The effective conduction band density of states can be estimated by $Nc = 2(2\pi m_e k_B T/h^2)^{3/2}$, where m_e is the effective electron mass.
38 Hwang, J., Amy, F. & Kahn, A. Spectroscopic Study on Sputtered PEDOT Center Dot PSS: Role of Surface PSS Layer. *Organic Electronics* **7**, 387-396 (2006).
39 Williams, E. L. *et al.* Conducting Polymer and Hydrogenated Amorphous Silicon Hybrid Solar Cells. *Applied Physics Letters* **87**, 223504-223503 (2005).
40 Shiu, S.-C., Chao, J.-J., Hung, S.-C., Yeh, C.-L. & Lin, C.-F. Morphology Dependence of Silicon Nanowire/Poly(3,4-ethylenedioxythiophene):Poly(styrenesulfonate) Heterojunction Solar Cells. *Chemistry of Materials* **22**, 3108-3113 (2010).

CHAPTER VI

Efficient Light-Stimulated Hole Injection into p-GaP Photoelectrodes Under Depletion Conditions

A. Introduction

This chapter investigates charge injection, transport and collection processes in planar dye-sensitized p-GaP photoelectrodes. The specific focus of this chapter is to characterize and theoretically model the operation of a p-GaP dye-sensitized photoelectrode that features a depletion region with sizeable internal electric fields. The culmination of this work is a novel paradigm for the deliberate design of high-performance dye-sensitized photocathodes in aqueous systems.

To be promising for efficient and scalable light-harvesting systems, a semiconductor material must meet many conditions. These requirements typically include earth abundance, limited processing needs, strong optical absorption, and suitable electronic properties to transport carriers with high internal quantum efficiency. Dye-sensitized solar cells can relax these constraints by coupling two materials—one that strongly absorbs light and another capable of transporting carriers to proper collection terminals—to perform processes that are traditionally addressed by a single semiconductor. The additional degree of freedom offered by dye-sensitized systems appears to offer an almost limitless array of material combinations that could conceivably form an efficient solar energy conversion system. To date, however, only a single system featuring one set of materials has produced responses promising enough to validate commercialization.[1-3] Specifically, the conventional design of Grätzel cells consists of five nearly immutable features: (*1*) a wide-bandgap metal oxide (TiO_2) electrode, (*2*) panchromatic (typically Ru-based) dyes that overcome the minimal sunlight absorbance by metal oxides such as TiO_2, (*3*) charge injection of photoexcited *electrons* from an excited chromophore into an n-type semiconductor immersed in a nonaqueous solution

(Figure VI.1a), (*4*) sunlight to *electricity* (rather than chemical fuel) conversion, and (*5*) ultra-small semiconductor nanoparticles that provide a large surface area for dye loading but are too small to support appreciable internal electric fields.[4]

The constraints listed above have been useful in developing and optimizing the ubiquitous Grätzel cell, and energy conversion efficiencies for this device type have exceeded 12%.[5] Little appreciable progress has been made over the past two decades, however, in extending the principle of dye sensitization to alternative systems that may offer advantages in terms of efficiency, stability or energy storage solutions.

Perhaps the most restrictive feature of the traditional paradigm for dye-sensitized devices is the requirement that semiconductor electrodes be comprised of nanoparticles too small to support sizeable internal electric fields. While the high surface area of nanoparticle electrodes allows for the adsorption of large quantities of dye to absorb incident light, the lack of a depletion region within the semiconductor means that carrier transport is limited to relatively slow diffusion processes rather than carrier drift, which can be rapid and efficient when strong electric fields are present. This diffusion requirement places severe electrochemical demands on the system, which must feature both fast carrier injection rates and relatively slow kinetics for deleterious recombination processes.

Comparatively few efforts have focused on understanding and utilizing sensitized hole injection processes in their own right. Several reports have recently detailed sensitized p-type nanoparticle film photocathodes for solar-to-electrical energy conversion.[6-19] Many of these efforts, however, use dye-sensitized photocathodes simply as a means to boost the activity of conventional dye-sensitized photoanodes. This report describes the operation of planar dye-sensitized p-type phosphide photoelectrodes in aqueous electrolytes (Figure VI.1b). Such photocathodes are interesting for both fundamental and practical reasons. First, the valence band energetics of phosphide-based semiconductors favor sensitized hole injection as compared to the valence band of most metal oxides[20,21] (Figure VI.1b), facilitating the measurement of sensitized hole injection from a variety of dyes. Second, sensitized photocathodes in water are naturally suited for solar to *chemical* energy conversion and storage since the regeneration of the reduced dye

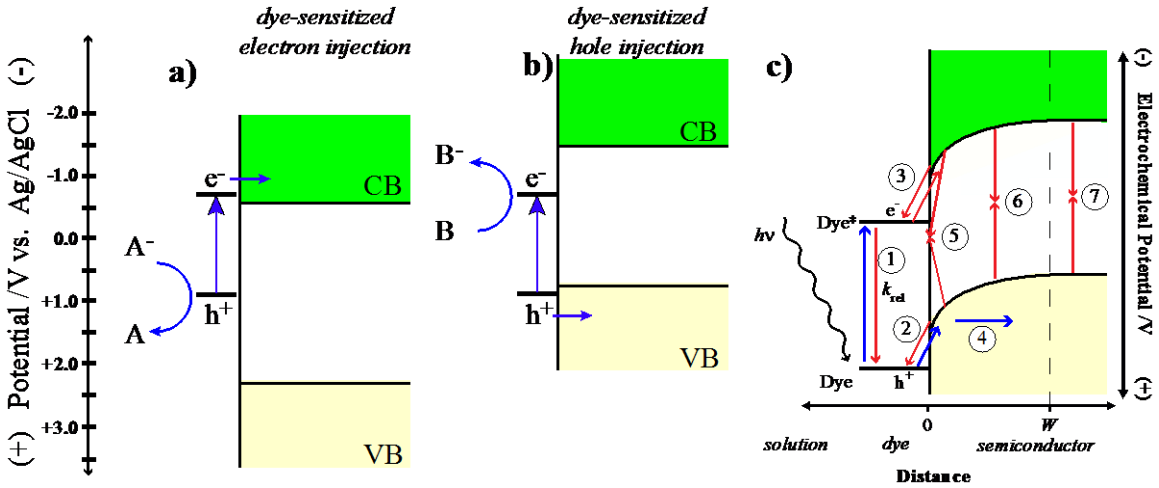

Figure VI.1: Depiction of dye sensitization at semiconductor photoelectrodes. (a) Dye-sensitized electron injection from a photoexcited chromophore at the surface of a metal oxide semiconductor. (b) Dye-sensitized hole injection from a photoexcited chromophore at the surface of a phosphide semiconductor. (c) Dye-sensitized hole injection from a photoexcited chromophore at the surface of a phosphide semiconductor under depletion conditions. The constituent processes that (blue) favor and (red) limit the magnitude of the net sensitized photocurrent are indicated. These processes are (1) optical excitation/relaxation of the dye, (2) hole transfer between the dye and semiconductor, (3) electron transfer between the dye and semiconductor (negligible in this system), (4) electric-field-induced transport within the semiconductor, (5) charge recombination at surface states at the semiconductor interface, (6) charge recombination in the depletion region, and (7) charge recombination in the bulk of the semiconductor.

molecules (following hole injection) can be coupled with reductive transformations in solution (Figure VI.1b). The development of such sensitized photocathodes requires a thorough understanding of all rate-impacting processes. Figure VI.1c shows the various charge carrier transport, transfer and recombination processes that can affect the operation of the p-type dye-sensitized photocathodes investigated in this chapter.

Our initial efforts focused on gallium phosphide (GaP) photoelectrodes, which have several properties advantageous for study. First, GaP can be prepared/obtained with well-defined bulk optoelectronic properties (e.g. mobility and dopant density) that are favorable for efficient light-harvesting systems. Second, as will be described in detail herein, dye-sensitized p-GaP can support substantial levels of light-stimulated hole injection. In contrast to previous reports of dye-sensitized p-CuSCN,[15,18] p-NiO,[7,9,10,12,14,19,22] and p-CuO,[17] this report details high internal quantum yields attainable with p-GaP photoelectrodes specifically operating under depletion conditions (i.e. featuring a large internal electric field).[23] Additionally, the response characteristics of planar p-GaP photoelectrodes operating under depletion conditions can be readily modeled and understood using finite-difference simulations, offering the opportunity for detailed analyses.[24] Finally, as a midsized bandgap semiconductor, GaP can absorb light at wavelengths shorter than 550 nm, relaxing the required panchromaticity of a sensitizer for complete visible light absorbance.

Presented in this chapter are data for single-crystalline p-GaP(100) photoelectrodes operated under potentiostatic control and sensitized by a set of triphenylmethane dyes in aqueous solution. Specifically, data are presented for two xanthene triarylmethane dyes (rose bengal (*RB*) and rhodamine B (*Rh B*)), two triaminotriphenylmethane dyes (crystal violet (*CV*) and ethyl violet (*EV*)), and two diaminotriphenylmethane dyes (fast green fcf (*FG*) and brilliant green (*BG*)). We report and assess the observed steady-state photoelectrochemical responses with these dyes, highlighting the unusually high internal quantum yields (> 0.1) observed at p-GaP photoelectrodes without prior optimization in the form of surface passivation or dye engineering. Through comparison of experimental results to those generated from a finite-difference model, we conclude that the promising photoelectrochemical responses for these dye-sensitized systems are due to the presence of an internal electric field within

the depletion layer at the p-GaP photoelectrode surface. A version of the Analysis of Microelectronic and Photonic Structures (AMPS) code previously used to study solid-state photovoltaics[25,26] was modified specifically for this work. The experimental system investigated herein was modeled with wxAMPS[26] to explicitly identify how experimentally controllable features such as surface trap density, charge transfer rate, and the bulk optoelectronic properties of the semiconductor photoelectrode impacted the attainable net quantum yields for sensitized charge injection at steady state. Finally, aspects relevant to designing efficient phosphide-based dye-sensitized cells are discussed.

B. Methods

i. Chemicals and Materials

Rhodamine B (95%), ethyl violet (≥ 80%), crystal violet (≥ 90%), fast green (≥ 85%), rose bengal (95%), brilliant green (98%), copper(II) phthalocyanine-3,4′,4″,4‴-tetrasulfonic acid tetrasodium salt (85%), nickel(II) phthalocyanine-tetrasulfonic acid, tetrasodium salt (~50%), methyl viologen dichloride (98%), ammonium sulfide (20%, aqueous solution) and potassium chloride (≥ 99%) were used as received from Sigma Aldrich. Zinc(II) phthalocyanine tetrasulfonic acid dye was obtained and used as received from Frontier Scientific. Concentrated HCl(aq) and 40% v/v NH_4F(aq) were obtained from Fisher Scientific and Transene, respectively. H_2O was purified (>18 MΩ cm) with a Barnstead Nanopure III purifier and used throughout. N_2(g) and O_2(g) were obtained from Metro Welding. GaP photoelectrodes were prepared from a 400 μm thick, single-crystalline, single-side polished p-type GaP(100) wafer doped with Zn at 1.1 x 10^{18} cm^{-3} and featuring a hole mobility μ_{net} = 70 cm^2 V^{-1} s^{-1}. GaP wafer types were obtained and used as received from ITME.

ii. Electrodes and Photoelectrochemical Cell

GaP wafers were diced into 0.5 cm x 0.5 cm sections and ohmic contacts were prepared by etching the back side for 30 s with concentrated NH_4F, rinsing with distilled H_2O, soldering a thin, even film of an In-Zn amalgam onto the etched surface and annealing for 10 min at 400°C. Electrodes were then prepared by using silver print (GC Electronics) to attach the GaP section to a copper wire coil threaded through a glass tube and sealing with inert epoxy (Hysol C). Unless otherwise indicated, electrodes were

etched for 30 s in 12.1 M HCl(aq), rinsed with H_2O, dried under N_2(g) and immediately used. Photoelectrochemical measurements were made in an airtight quartz cell with an optically flat bottom. A platinum counter electrode and Ag/AgCl reference electrode were used. For all photoelectrochemical measurements, the distance between the optical window and GaP photoelectrode face was nominally 1 mm. 1 M KCl was used as the background electrolyte unless noted otherwise. For measurements with adsorbed rose bengal, p-GaP(100) electrodes were first etched, rinsed, dried, and then soaked in ammonium sulfide solution for 6 h. The pH of the ammonium sulfide solution was set to 7 through addition of HCl(aq) aliquots.[27] This treatment resulted in surface-bound ammonium moieties. Electrodes were then immersed in aqueous solutions containing rose bengal for 30 min followed by an immersion in purified water for 1 h to remove weakly physisorbed dye before undergoing further photoelectrochemical analyses.

iii. Optical and Photoelectrochemical Measurements

All measurements were performed at room temperature (23 ± 3°C). Transmittance measurements were obtained with a Varian Cary 5000 Ultraviolet-Visible-Near-Infrared (UV-Vis-NIR) spectrometer. Absorptance (i.e. the fraction of total light absorbed) values are reported rather than absorption values where noted. All photoelectrochemical measurements were performed in a three-electrode cell under potentiostatic control (Princeton Applied Research 267A), facilitating analysis of the specific operation of the dye-sensitized photocathode. The net photocurrent collected per incident light flux is reported here as an external quantum yield on a scale from 0 to 1. Internal quantum yield, also given on a scale from 0 to 1, represents the net carrier flux collected per absorbed light flux. Wavelength-dependent external quantum yield measurements were taken with a setup described previously.[28] Illumination intensities ranged from ~0.1 – 1.0 mW cm^{-2}. External quantum yield measurements were corrected for solution transmittance using the Beer-Lambert relation and dye absorption spectra as measured with a Cary 5000 UV-Vis-NIR spectrometer. Internal quantum yield values were calculated by dividing the measured external quantum yield values by the fraction of incident light absorbed by a monolayer of dye. Monolayer absorbance was estimated via the Beer-Lambert relation, with the extinction coefficient determined from transmittance measurements of dilute dye solutions. The density of an idealized close-packed dye monolayer was estimated using

the areal footprint of the dye oriented parallel to the surface plane. Current-potential characteristics were measured either under monochromatic illumination from a 150 W Xe arc lamp and an Oriel quarter-turn single-grating monochromator (both Newport) or with a 500 mW green LED laser. The latter source type was used specifically for intensity dependence measurements.

iv. Impedance Measurements

Impedance measurements were made using a Schlumberger SI1286 electrochemical interface and a Schlumberger SI1250 frequency response analyzer modulated by CorrWare and ZPlot software. Frequency response was measured with a 10 mV AC signal superimposed onto a DC voltage that ranged from 0 to 1 V into reverse bias. Electrodes were etched in 12.1 M HCl (Fisher), rinsed with purified water (>18 MΩ cm, Barnstead Nanopure III purifier) and immediately used. Measurements were made in the dark in an electrochemical cell (as described in the text for optical measurements) with 1 M KCl as the electrolyte and a constant stream of N_2 bubbling into the solution

v. Steady-State Model of Dye-Sensitized Charge Injection

The net efficiency for charge injection between a photoexcited dye and a p-type semiconductor under depletion conditions (Figure VI.1c) is controlled primarily by features intrinsic to the semiconductor (hole mobility, band energetics, charge carrier lifetimes and populations), the dye (excited state lifetime, ground and excited state redox potentials), and the interface (rate of heterogeneous charge transfer). To determine the explicit dependence and interplay of the features described in Figure VI.1c on net sensitized charge injection at steady state, a custom-designed variant of AMPS (wxAMPS) was used. wxAMPS is a software package for modeling planar semiconductor heterojunctions in one dimension that utilizes the finite-difference method to determine the concentration of charge carriers throughout the system as a function of position and applied potential according to Equations VI.1 and VI.2.

$$-\frac{\delta}{\delta x}\left(\varepsilon_r(x)\frac{\delta\phi(x)}{\delta x}\right)=q\rho \qquad \text{(VI.1)}$$

$$\frac{\delta J_n}{\delta x} = -qG(x) + qR(x) \qquad \text{(VI.2a)}$$

$$\frac{\delta J_p}{\delta x} = qG(x) - qR(x) \qquad \text{(VI.2b)}$$

where ϕ is the local electric potential, q is the unsigned charge of an electron, ε_r is the relative permittivity, ρ is the summed (free, ionized impurity, and trapped) charge density, J_n is the electron current density, J_p is the hole current density, $G(x)$ is the optical generation rate of carriers at x, and $R(x)$ is the total charge carrier recombination rate at x. Equation VI.1 is Poisson's equation relating charge carrier populations and the electric potential in one dimension.[24] Equations VI.2a,b are the current continuity equations for electrons and holes, respectively.[24] The key revision made to the version of AMPS used in this work is a reformulation of the boundary conditions at the material interfaces. Charge transfer rates between GaP and a dye layer were expressed in the general framework used for semiconductor electrochemistry and the principle of detailed balance.[29,30] Equations VI.3a and VI.3b describe the electron and hole current densities at the interface between the adsorbed dye and GaP,

$$-J_n = qk_{et}^0 e^{-\frac{((E_{LUMO,Dye} - E_{CB,GaP}) - \lambda)^2}{4k_B T\lambda}} N_{CB,GaP}[dye]_0 \left(\frac{[dye^*]}{[dye]_0} - \frac{n_{s,GaP}}{n_{s0,GaP}} \right) \qquad \text{(VI.3a)}$$

$$J_p = qk_{ht}^0 e^{-\frac{((E_{VB,GaP} - E_{HOMO,Dye}) + \lambda)^2}{4k_B T\lambda}} N_{VB,GaP}[dye]_0 \left(\frac{[dye^*]}{[dye]_0} - \frac{p_{s,GaP}}{p_{s0,GaP}} \right) \qquad \text{(VI.3b)}$$

where $[dye]_0$ and $[dye^*]$ are the ground and excited state dye concentrations, respectively, $E_{CB,GaP}$ and $E_{VB,GaP}$ are the energies of the GaP conduction and valence bands, $E_{LUMO,Dye}$ and $E_{HOMO,Dye}$ are the dye LUMO and HOMO energies, $N_{CB,GaP}$ and $N_{VB,GaP}$ are the densities of state in the GaP conduction and valence bands, respectively, $n_{s0,GaP}$ and $p_{s0,GaP}$ are the electron and hole surface densities in the dark at equilibrium, and $n_{s,GaP}$ and $p_{s,GaP}$ are the electron and hole surface densities. Notably, in Equation VI.3 the electron

and hole charge transfer rate constants (k_{et}^0 and k_{ht}^0, respectively) and concentrations refer to adsorbed dyes. Although the basic design of this version of AMPS allows the input of heterogeneous rate constants with the more familiar units of cm^4 s^{-1} for charge transfer to an acceptor in solution,[29] the model used herein has been designed so that this rate constant translates directly to that of an *adsorbed* dye with units of cm^3 s^{-1} through division of the input rate constant by the dye layer thickness. The products of this modified rate constant and the effective densities of states (k_{ht}^0 x $N_{VB,GaP}$ and k_{et}^0 x $N_{CB,GaP}$, respectively) have units of s^{-1} and are commensurate with the charge injection rates from an adsorbed dye. Accordingly, direct comparison to published reports of experimentally measured charge injection rates from spectroscopic quenching measurements can be made. Monolayers of adsorbed dye were approximated by defining a 5 Å dielectric layer at the GaP surface with the optical, electrical, and electrochemical properties appropriate for a generic organic dye. A description of all the default input parameters, including mesh size, spacing used for discretization and recombination velocities at the front and back contacts, is given in Tables VI.1 and VI.2.

C. Results

i. Impedance Measurements

Figure VI.2a shows a representative C^{-2}-V response of a p-GaP electrode in deaerated 1 M KCl taken at frequencies raging an order of magnitude. The capacitance measured at a p-type electrode is dependent on bulk semiconductor electronic properties as well as the depletion conditions at the interface according to Equation VI.4,

$$\frac{1}{C^2} = \frac{2}{qA_s^2\varepsilon_s N_A}\left(V_{bi} - \frac{k_B T}{q} - V\right) \qquad \text{(VI.4)}$$

where C is capacitance, A_s is electrode surface area, ε_s is semiconductor permittivity, N_A is acceptor concentration, V_{bi} is the built-in potential, k_B is Boltzmann's constant, T is temperature and V is applied potential. Impedance measurements with freshly etched electrodes yielded an apparent flatband potential of (E intercept in Figure VI.2a) +0.98 ± 0.16 V vs. Ag/AgCl, indicating an approximate value for the potential of the valence band edge, $E_{VB,GaP}$, of +1.02 ± 0.19 V vs. Ag/AgCl. Since the open-circuit rest potential

Table VI.1: Default ambient input parameters for wxAMPS simulations. Any deviations from the values listed below are stated explicitly in the figures and/or text.

Symbol	Description	Value	Units
T	temperature	300	K
ξ	illumination @ 625 nm	3	W m^{-2}
$\Phi_{B,Top}$	CB position at interface measured from $E_{F,p}$	1.05	eV
$\Phi_{B,Bottom}$	CB position in bulk measured from $E_{F,p}$	2.186	eV
$S_{n0,Top}$	velocity at which electrons approach the top interface	1 x 10^3	cm s^{-1}
$S_{n0,Bottom}$	velocity at which electrons approach the bottom interface	1 x 10^7	cm s^{-1}
$S_{p0,Top}$	velocity at which holes approach the top interface	1 x 10^3	cm s^{-1}
$S_{p0,Bottom}$	velocity at which holes approach the bottom interface	1 x 10^7	cm s^{-1}
V_{bias}	bias potential	0 - 2	V
ΔV_{bias}	bias potential step size	0.02	V

Table VI.2: Material input parameters for wxAMPS simulations.[a] Any deviations from the values listed below are stated explicitly in the figures and/or text.

$\Delta E_{D,defect}$	$E_{D,defect}$	$N_{D,defect}$[b]	N_A	N_D	μ_p	μ_n	N_v	N_c	χ_e	E_g	ε_r	D
donor-like defect energy level deviation	donor-like defect energy level w.r.t. VB	donor-like defect concentration	acceptor concentration	donor concentration	hole mobility	electron mobility	density of states of valence band	density of states of conduction band	electron affinity	band gap	relative dielectric permittivity	layer thickness
± 0.05	0.99	5×10^{14}	0	0	1×10^{-2}	1×10^{-2}	1×10^{19}	1×10^{19}	3.81	1.98	6	5×10^{-4}
± 0.05	0.89	5×10^{17}	1.1×10^{18}	0	1×10^{2}	1×10^{2}	1.9×10^{19}	1.8×10^{19}	2.93	2.26	11.1	5×10^{-4}
0	0	0	1.1×10^{18}	0	1×10^{2}	1×10^{2}	1.9×10^{19}	1.8×10^{19}	2.93	2.26	11.1	0.0995
0	0	0	1.1×10^{18}	0	1×10^{2}	1×10^{2}	1.9×10^{19}	1.8×10^{19}	2.93	2.26	11.1	0.9
0	0	0	1.1×10^{18}	0	1×10^{2}	1×10^{2}	1.9×10^{19}	1.8×10^{19}	2.93	2.26	11.1	9
0	0	0	1.1×10^{18}	0	1×10^{2}	1×10^{2}	1.9×10^{19}	1.8×10^{19}	2.93	2.26	11.1	90
0	0	0	1.1×10^{18}	0	1×10^{2}	1×10^{2}	1.9×10^{19}	1.8×10^{19}	2.93	2.26	11.1	300
eV	eV	cm^{-3}	cm^{-3}	cm^{-3}	$cm^2 V^{-1} s^{-1}$	$cm^2 V^{-1} s^{-1}$	cm^{-3}	cm^{-3}	eV	eV		µm

Symbol	Λ	k_{ht}	k_{et}	Δd_{bulk}	Δd_{edge}	$\sigma_{A,p}$	$\sigma_{A,n}$	$\Delta E_{A,defect}$	$E_{A,defect}$	$N_{A,defect}$ [b]	$\sigma_{D,p}$	$\sigma_{D,n}$
Description	reorganization energy	interfacial hole transfer rate	interfacial electron transfer rate	1D mesh spacing in segment bulk	1D mesh spacing near segment boundaries	acceptor-like defect h^+ capture cross section	acceptor-like defect e^- capture cross section	acceptor-like defect energy level deviation	acceptor-like defect energy level w.r.t. VB	acceptor-like defect concentration	donor-like defect h^+ capture cross section	donor-like defect e^- capture cross section
Dye Bulk	0.5	1×10^{-12}	1×10^{-12}	0.025	5×10^{-3}	1×10^{-15}	1×10^{-15}	± 0.05	0.99	5×10^{14}	1×10^{-15}	1×10^{-15}
GaP Surface	N/A	N/A	N/A	5×10^{-3}	1×10^{-3}	1×10^{-15}	1×10^{-15}	± 0.05	1.13	5×10^{17}	1×10^{-15}	1×10^{-15}
GaP Layer 2	N/A	N/A	N/A	2.5	0.5	1×10^{-15}	1×10^{-15}	± 0.05	1.13	5×10^{18}	0	0
GaP Layer 3	N/A	N/A	N/A	20	1	1×10^{-15}	1×10^{-15}	± 0.05	1.13	5×10^{18}	0	0
GaP Layer 4	N/A	N/A	N/A	100	10	1×10^{-15}	1×10^{-15}	± 0.05	1.13	5×10^{18}	0	0
GaP Layer 5	N/A	N/A	N/A	1000	100	1×10^{-15}	1×10^{-15}	± 0.05	1.13	5×10^{18}	0	0
GaP Layer 6	N/A	N/A	N/A	3000	300	1×10^{-15}	1×10^{-15}	± 0.05	1.13	5×10^{18}	0	0
Units	eV	$cm^4 s^{-1}$	$cm^4 s^{-1}$	nm	nm	cm^{-2}	cm^{-2}	eV	eV	cm^{-3}	cm^{-2}	cm^{-2}

[a]No band tails were addressed in these simulations
[b]Gaussian energetic distribution

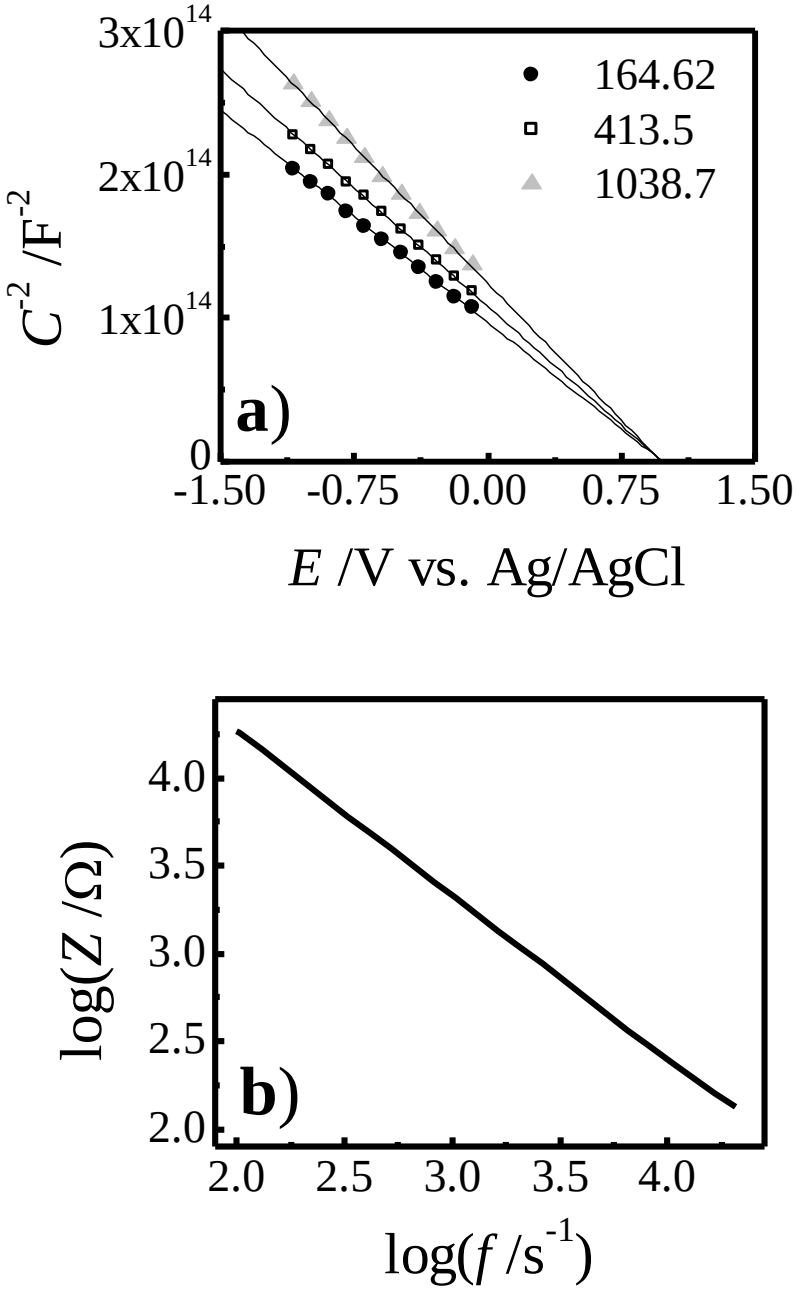

Figure VI.2: (a) Representative capacitance-voltage data for a p-GaP(100) electrode in N_2-saturated 1 M KCl taken in the dark. (b) Corresponding Bode plot with a slope of -0.933 at an applied potential of -0.5 V vs. Ag/AgCl.

of these electrodes was typically ~ 0 V vs. Ag/AgCl, these p-GaP electrodes were under strong depletion conditions and supported internal electric field strengths, $|\vec{E}|$, of ~ 8.5 x 10^5 V cm^{-1}.[31] Figure VI.2b shows a Bode plot measured at -0.5 V vs. Ag/AgCl corresponding to the data in Figure VI.2a. The Bode slope was approximately -0.93, indicating that the majority of the potential drop occurred across the semiconductor phase. The flatband potential, barrier height and GaP valence band level inferred from capacitive measurements changed by several tenths of a volt for electrodes that were allowed to age in solution for prolonged periods of time. Accordingly, all subsequent measurements were performed immediately after immersion into the test solution. Results from measurements made with and without dye in the cell were statistically indistinguishable.

ii. Sensitization of p-GaP with Dyes Dissolved in Aqueous Solutions

Figure VI.3 illustrates the observed photoelectrochemical responses for p-GaP(100) photoelectrodes biased at -0.6 V vs. Ag/AgCl while immersed in deaerated 1 M KCl(aq) containing various organic sensitizers at a concentration of 5 μM. Each dye solution elicited a photocurrent response with a wavelength dependence that followed the absorptance profile of the respective dye. The peak molar extinction coefficients for these dyes range from 10^7 to 10^8 mol^{-1} cm^{-2} for wavelengths between 500 to 700 nm. For each presented dye solution, measurable photocurrent was obtained at sub-bandgap wavelengths, i.e. at wavelengths corresponding to energies smaller than the bandgap energy of 2.26 eV (549 nm) for GaP. Under the employed conditions, the magnitudes of the external quantum yields for all six dyes at this concentration ranged from 0.001 to 0.002. Replacing the p-GaP photoelectrodes with a metal electrode in these electrolytes did not produce any detectable net photocurrents. The total light transmitted through the dye solution is indicated in black in Figure VI.3. Correction of the experimentally measured external quantum yields for optical losses incurred by light absorption from the dye solution through the ~1 mm path length between the cell window and electrode surface (Figure VI.4) did not substantially change the profiles shown in Figure VI.3. Hence, at 5 μM, the observed photoelectrochemical responses qualitatively indicated the innate spectral profile for sensitization by each dye. Notably, for each plot in Figures VI.3 and VI.4, the wavelength corresponding to the maximum sub-bandgap external

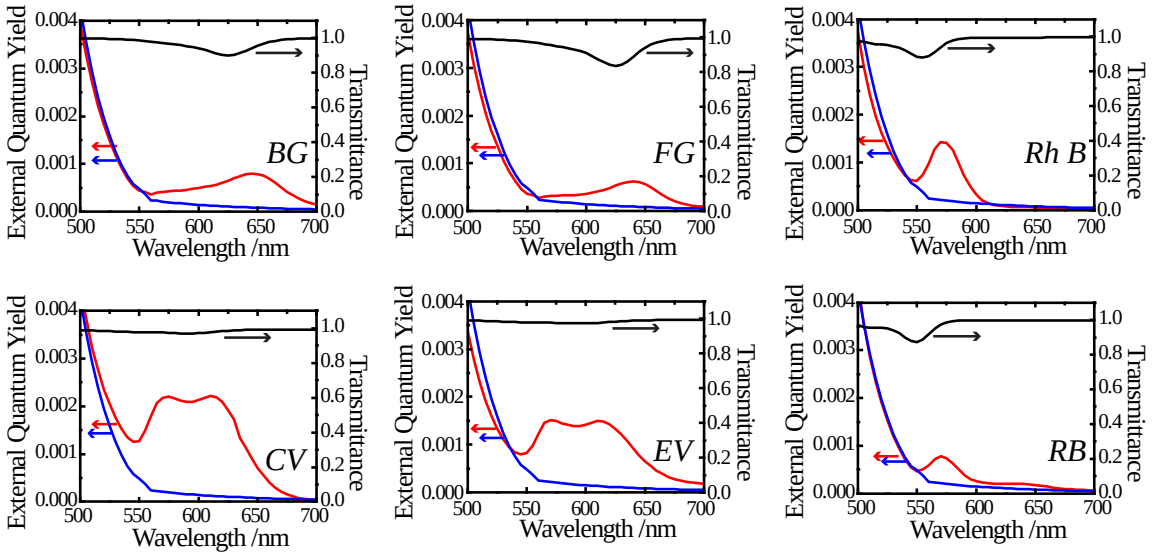

Figure VI.3: Measured wavelength dependence for net internal quantum yield of p-GaP(100) electrodes. Electrodes were poised at -0.6 V vs. Ag/AgCl while immersed either in (blue) only deaerated 1 M KCl(aq) or (red) deaerated 1 M KCl(aq) containing 5 μM dissolved dye; *BG* = brilliant green, *FG* = fast green fcf, *Rh B* = rhodamine B, *CV* = crystal violet, *EV* = ethyl violet, *RB* = rose bengal. The transmitted light through the ~1 mm spacing between the electrode face and optical window is indicated in black (right-hand y-axes).

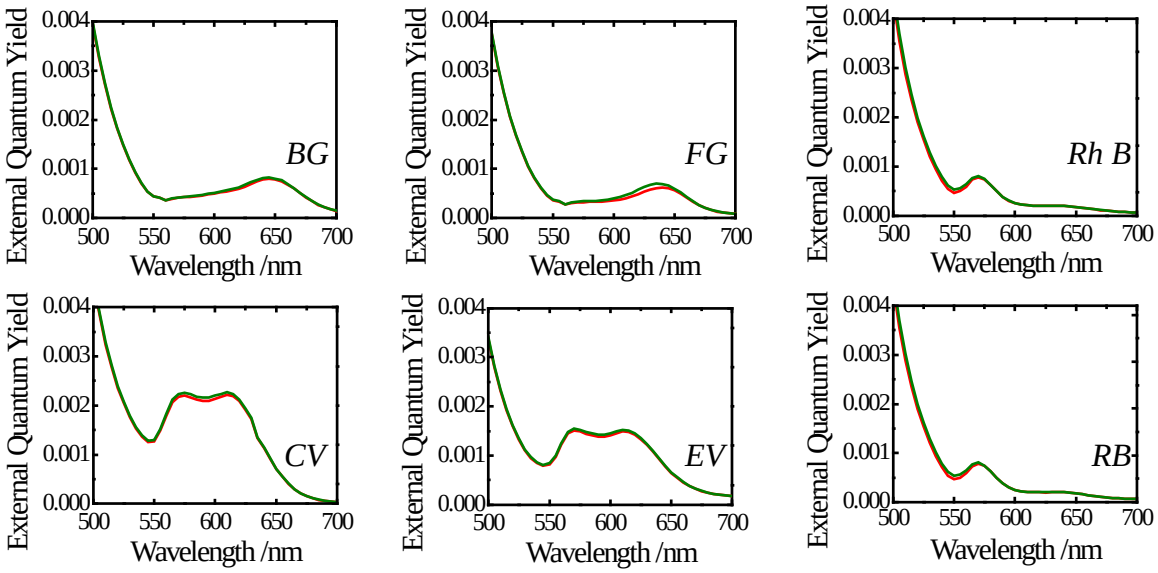

Figure VI.4: External spectral quantum yield for hole injection from various dyes into p-GaP(100). Electrodes were immersed in a solution of 1 M KCl(aq) and 5 μM dye at an applied bias of -0.6 V vs. Ag/AgCl. Responses were either (red line) not corrected or (green line) corrected for solution transmittance. Illumination intensities were approximately 0.1 – 1.0 mW cm^{-2}. *BG* = brilliant green; *FG* = fast green fcf; *Rh B* = rhodamine B; *CV* = crystal violet; *EV* = ethyl violet; *RB* = rose bengal.

quantum yield was offset from the wavelength of maximum absorbance of the dissolved dye (Table VI.3), consistent with the notion that sensitization occurred specifically through *adsorbed* dye at the photoelectrode surface.[15,32-35] Sensitized photocurrents at sub-bandgap wavelengths were not observed for all investigated dyes. Specifically, Figure VI.5 illustrates that sensitization was not detected in electrolytes containing dissolved metal phthalocyanine tetrasulfonic acid with standard potentials for oxidation that were more negative that $E_{VB,GaP}$.[36]

For every dye shown in Figures VI.3 and VI.4, the measured sensitized photocurrents were a function of the concentration of dissolved dye in solution. Figure VI.6 shows a representative plot highlighting the observed dependence of the external quantum yield of rhodamine b at 570 nm (i.e. wavelength of maximum sensitization) on the dissolved concentration of rhodamine b. At low (< 50 μM) concentrations, the sensitized photocurrent markedly increased with increasing concentration of rhodamine b, consistent with the premise that higher adsorbed dye concentrations were promoted by higher solution concentrations. At a concentration of approximately 50 μM, the measured photocurrents reached a maximum value and then decreased with further increase in concentration. At the highest concentrations, the total light loss by absorption of dye dissolved in bulk solution was appreciable (transmittance ≤ 0.1). Optical correction of the transmittance losses at the highest concentrations was difficult due to a strong dependence on the absolute distance between the cell window and p-GaP surface and was not incorporated into Figure VI.6. For every dye listed in Table VI.3, Figure VI.7 shows additional photoelectrochemical responses for p-GaP(100) photoelectrodes biased at -0.6 V vs. Ag/AgCl while immersed in deaerated 1 M KCl(aq) with dye concentrations of 50 μM. Each dye elicited a sub-bandgap photoresponse that qualitatively followed those shown in Figures VI.3 and VI.4, except convoluted more strongly with light absorption from the bulk solution. This effect contributed to slight shifts in the wavelengths corresponding to the maximum photocurrents.

The internal quantum yield-potential profiles for p-GaP(100) electrodes in the six triarylmethane dyes solutions featured in Figures VI.3, VI.4 and VI.7 are presented in Figure VI.8. Each plot represents typical photoresponses obtained with monochromatic illumination (nominal power density of 0.3 mW cm^{-2}) at a wavelength corresponding to

Table VI.3: Dye absorbance and sensitization properties.

	Dye	Absorbance Peak[a] /nm	Sensitization Peak[b] /nm
BG	brilliant green	625	645
FG	fast green fcf	624	640
Rh B	rhodamine B	555	570
CV	crystal violet	590	610
EV	ethyl violet	595	610
RB	rose bengal	549	570

[a]Measured at 7.5 μM in water

[b]Maximum quantum yield at sub-bandgap wavelengths measured at 5 μM in 0.1 M KCl(aq) with p-GaP poised at E = -0.6 V vs. Ag/AgCl

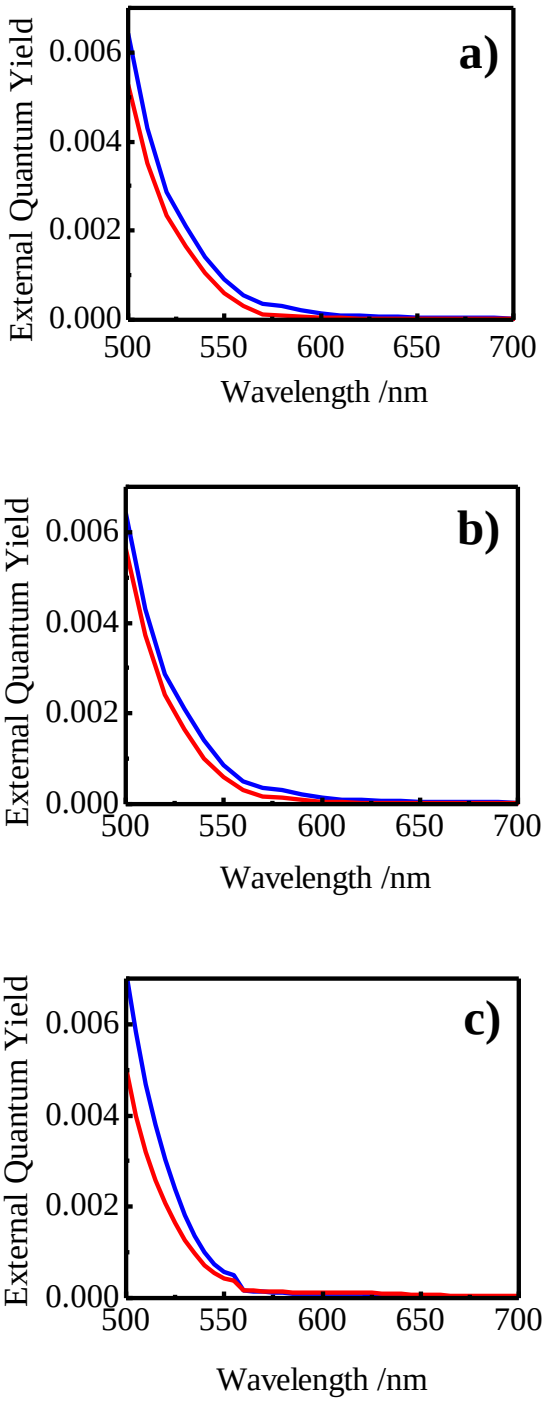

Figure VI.5: External spectral quantum yield for hole injection from three phthalocyanine dyes. (a) Cu(II) phthalocyanine-3,4',4'',4'''-tetrasulfonic acid, tetrasodium salt, (b) Ni(II) phthalocyanine tetrasulfonic acid, tetrasodium salt and (c) Zn(II) phthalocyanine tetrasulfonic acid into p-GaP(100). Electrode was immersed in a solution containing (blue line) only 1 M KCl and (red line) 1 M KCl(aq) and 50 µM dye and a bias of -0.6 V vs. Ag/AgCl was applied. Illumination intensities were approximately 0.1 – 1.0 mW cm^{-2}.

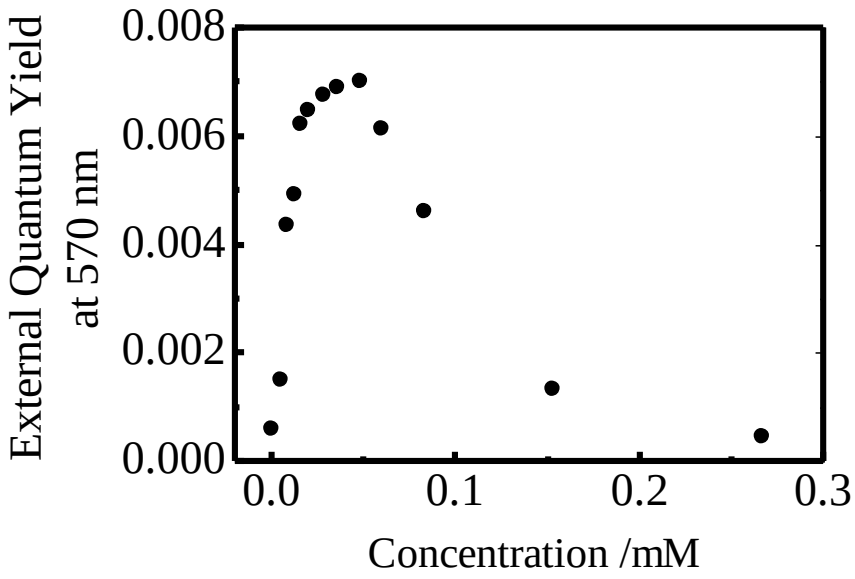

Figure VI.6: Observed dependence of the as-measured external quantum yields for a p-GaP(100) electrode recorded at 570 nm as a function of the concentration of rhodamine b. The electrode was poised at -0.6 V vs. Ag/AgCl and immersed in a 1 M KCl(aq) electrolyte containing dissolved dye.

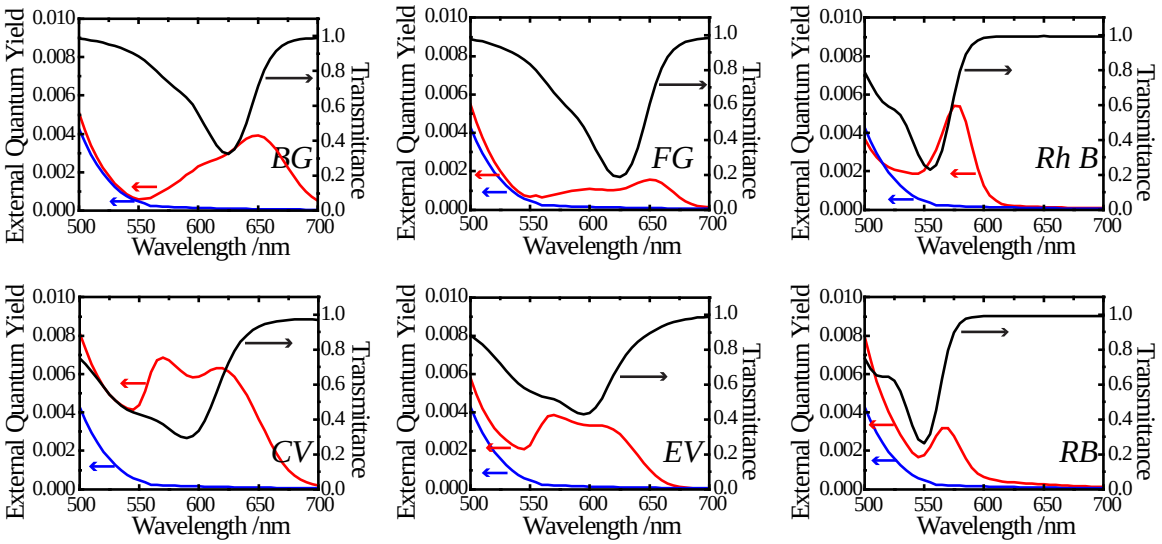

Figure VI.7: External spectral quantum yield for hole injection from various dyes into p-GaP(100). Electrodes were immersed in a solution of (blue line) only 1 M KCl(aq) and (red line) 1 M KCl(aq) and 50 μM dye at an applied bias of -0.6 V vs. Ag/AgCl. Responses were not corrected for solution transmittance. The black line shows the optical transmittance through 1 mm of dye solution. Illumination intensities were approximately 0.1 – 1.0 mW cm^{-2}. *BG* = brilliant green; *FG* = fast green fcf; *Rh B* = rhodamine B; *CV* = crystal violet; *EV* = ethyl violet; *RB* = rose bengal.

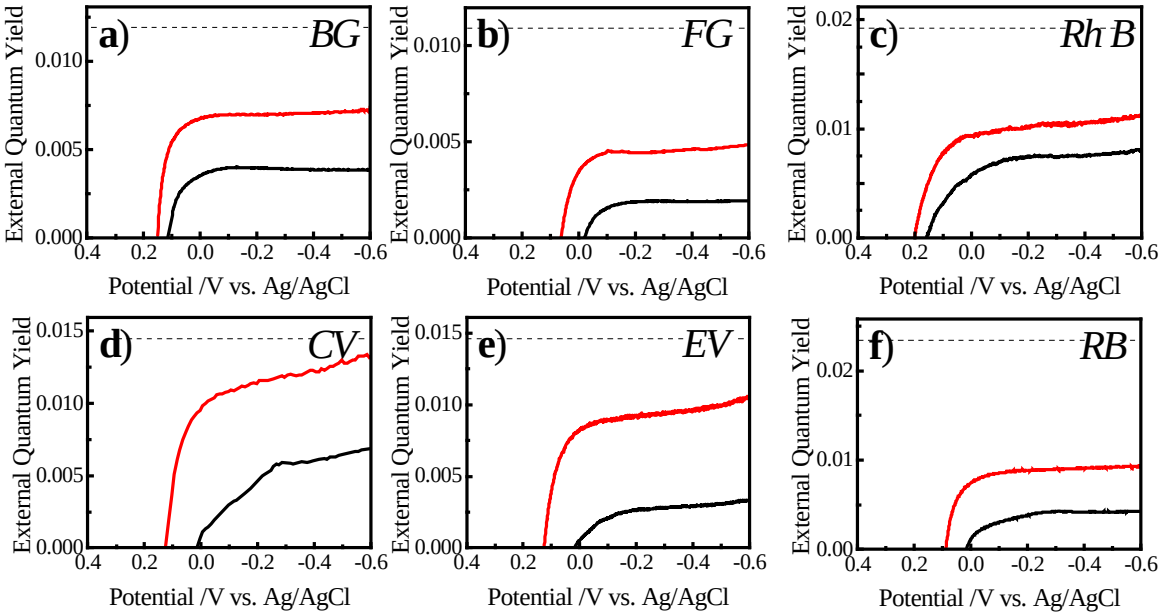

Figure VI.8: Measured potential dependence for external quantum yield of p-GaP(100) electrodes. Electrodes were under monochromatic illumination and were immersed in aerated or deaerated 1 M KCl(aq) containing 50 μM dissolved dye; *BG* = brilliant green, *FG* = fast green fcf, *Rh B* = rhodamine B, *CV* = crystal violet, *EV* = ethyl violet, *RB* = rose bengal. Red and black lines indicate measurements obtained in electrolytes that were sparged with O_2(g) and N_2(g), respectively. Each measurement was done at a wavelength that corresponded to the maximum external quantum yield in Figure VI.3. The dashed line near the top indicates the response for an ideal monolayer coverage of each dye operating with unity internal quantum yield.

the maximum photocurrent response in 50 μM dye solution. The dashed line at the top of each plot corresponds to the expected quantum yield from a close-packed monolayer of adsorbed dye that injects photogenerated holes with a unity internal quantum yield, accounting for light transmission losses through the bulk solution as shown in Figure VI.9. For each plot in Figure VI.8, two photoelectrochemical responses are shown that illustrate the behaviors observed in aerated and deaerated solutions, respectively. Several features were uniformly observed for all six dyes. First, all measured responses yielded external quantum yield values at -0.6 V vs. Ag/AgCl that were at least 10% of the predicted value for a close-packed monolayer operating with unity internal quantum yield. These features implied that the *internal* quantum yields for sensitized hole injection in all of these systems were ≥ 0.1. Second, sensitized photocurrents measured in aerated solutions were uniformly larger at every potential than sensitized photocurrents measured in deaerated solutions. The degree of difference between internal quantum yield-potential responses recorded in aerated and deaerated solutions varied across all six dyes but seemed consistent within each subset of xanthene, triaminotriphenylmethane, and diaminotriphenylmethane dyes. No photoelectrochemical response recorded in aerated solutions exceeded the expected limit for a close-packed monolayer operating with unity internal quantum yield, although the responses for the triaminotriphenylmethane dyes (crystal violet and ethyl violet) implied internal quantum yields > 0.5. Third, the profiles of the photoelectrochemical responses recorded in aerated solutions were more rectangular, i.e. attained the plateau photocurrent value at potentials closer to the rest potential. For the triaminodiphenylmethane dyes, the photoresponses did not reach a true plateau photocurrent value within the potential range of interest.

The effect of a dissolved redox mediator on measured photoresponses was further investigated by replacing O_2 with the outer-sphere redox couple methyl viologen ($MV^{2+/+}$) at a concentration of 10 mM. The addition of $MV^{2+/+}$ increased both the attainable photocurrents and open-circuit rest potentials under illumination for all dyes relative to responses measured in deaerated solutions without a dissolved mediator. However, the responses remained uniformly lower than the responses obtained in aerated solutions. While singlet oxygen ($O_2(^1\Delta)$) has been previously observed to interact with certain dye-sensitized systems in a manner that mimics hole injection,[37] the augmented

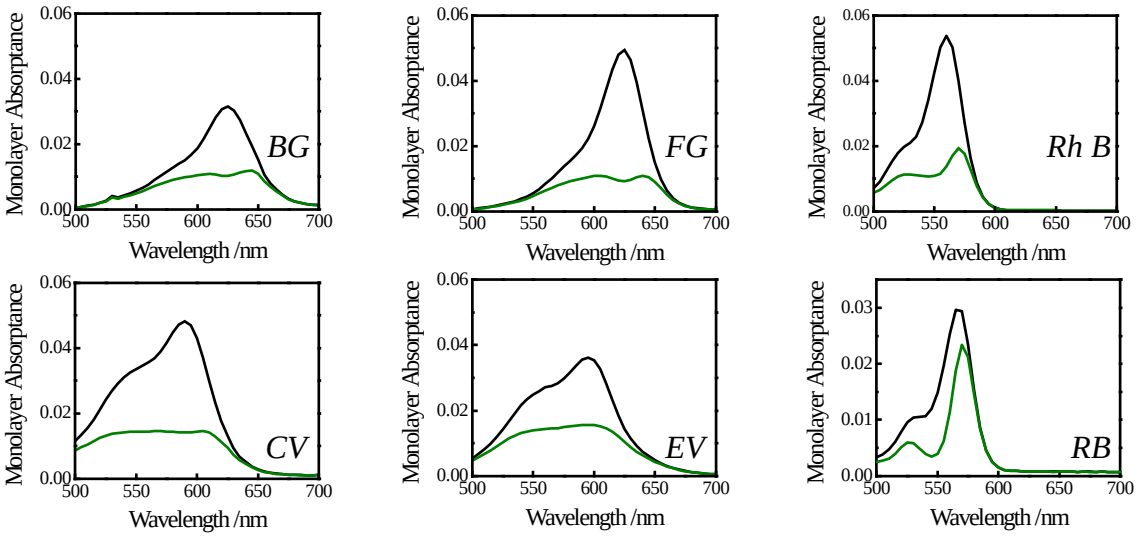

Figure VI.9: Predicted spectral absorptance for a single pass of light through a monolayer of dye. Absorptance was either (black lines) not corrected for optical filtering through solution or (green lines) divided by the optical transmittance through 1 mm of a solution containing 50 μM dissolved dye. The maxima of the green curves defined the dashed line in Figure VI.8. *BG* = brilliant green; *FG* = fast green fcf; *Rh B* = rhodamine B; *CV* = crystal violet; *EV* = ethyl violet; *RB* = rose bengal.

photoresponses in the presence of O_2 observed here were inconsistent with hole injection from $O_2(^1\Delta)$ rather than from the photoexcited dye for several reasons. First, although all of the investigated triphenylmethane dyes yielded comparable sensitization levels, the capacity of each triphenylmethane dye to generate $O_2(^1\Delta)$ varies considerably. For example, the xanthene triarylmethane dyes are known to be efficient sensitizers for $O_2(^1\Delta)$ generation,[38,39] whereas the two triaminotriphenylmethane dyes do not produce $O_2(^1\Delta)$ readily under illumination.[40,41] Second, photoresponses were not observed to be strongly affected upon the addition of $O_2(^1\Delta)$ quenchers to solution. Figure VI.10 shows photoelectrochemical measurements with ethyl violet performed before, during, and after injection of a large excess of N_3^- and histidine. N_3^- and histidine are strong 'physical' and 'chemical' quenchers, respectively, of $O_2(^1\Delta)$ in solution. Appreciable suppression of the sensitized photocurrent measured with ethyl violet was not observed immediately after the addition of either 2 mM N_3^- or 2 mM histidine to solution. Note that the addition of histamine results in a modest time-delayed decrease in observed photocurrents as well as higher 'dark' currents, but no precipitous drop in observed photocurrents. These results indicate that histidine adhered to the GaP surface, displacing some adsorbed dye and causing a slight decrease in photocurrents. The lack of any measurable photocurrent in systems featuring Zn(II) phthalocyanine tetrasulfonic acid dye is another indication that the photocurrents observed for the six triarylmethane dyes were not attributable to $O_2(^1\Delta)$ sensitization. Zn(II) phthalocyanine tetrasulfonate is known to be an efficient sensitizer for generating $O_2(^1\Delta)$ under illumination in aqueous solution, but the amount of $O_2(^1\Delta)$ presumably present in solution did not translate into any meaningful level of hole collection for the system investigated herein.[42] Finally, the peak wavelengths for sensitization were redshifted relative to the absorbance band of each dye dissolved in solution, consistent with the premise that dye specifically at the p-GaP interface was the primary sensitizing species rather than $O_2(^1\Delta)$ generated in bulk solution.

iii. Sensitization of p-GaP by an Adsorbed Dye

The six dyes featured in Figures VI.3 and VI.8 did not possess functional groups suitable for deliberate binding to etched GaP(100) interfaces. Accordingly, emersion of p-GaP(100) photoelectrodes from the dye solutions used in Figure VI.8 did not produce consistent dye loadings that persisted after re-immersion into 1 M KCl(aq). However,

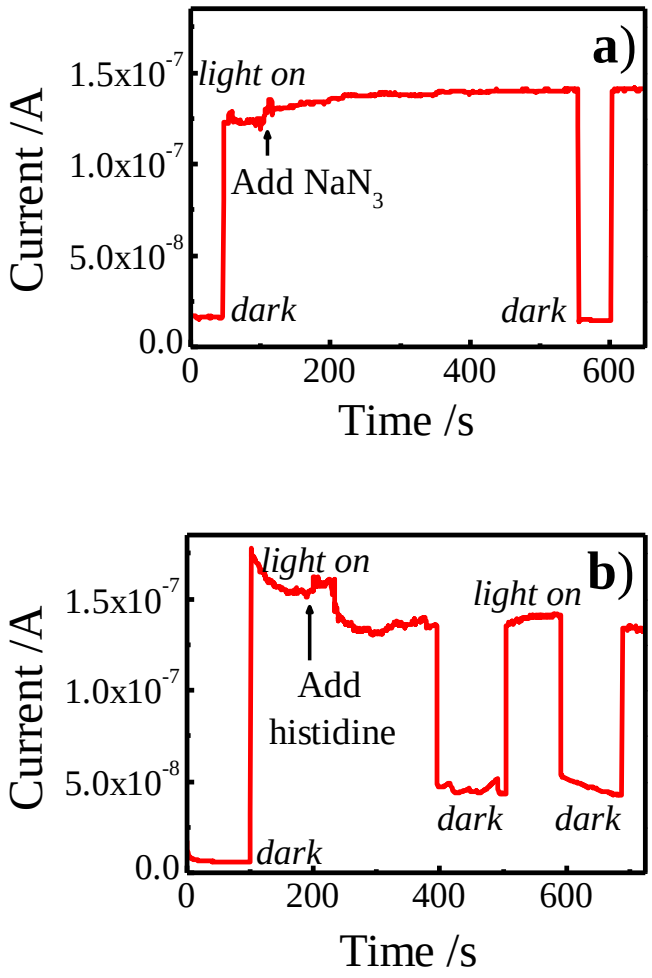

Figure VI.10: Dye-sensitized current from a p-GaP(100) electrode immersed in a solution of 50 μM ethyl violet and 1 M KCl over time. The $O_2(^1\Delta)$ quenchers (a) N_3^- (in the form of NaN_3) and (b) histidine were added to the solution at concentrations of 2 mM at the points indicated in the figures.

prior treatment of p-GaP(100) surfaces with $(NH_4)_2S$(aq) did facilitate the persistent adsorption of rose bengal. Following treatment with $(NH_4)_2S$(aq), immersion of GaP(100) surfaces in aqueous solutions with 6 mM M rose bengal for 30 min resulted in an appreciable amount of adsorbed dye. Figure VI.9 highlights the absorptance at sub-bandgap wavelengths measured for a GaP(100) substrate treated in this way. Figure VI.11a shows the wavelength-dependent external quantum yield responses recorded for p-GaP(100) photoelectrodes that were first treated with $(NH_4)_2S$(aq), soaked in aqueous solutions of various concentrations of rose bengal for 30 min, and then transferred to a deaerated solution of 1 M KCl(aq). The magnitude of the photoresponse at wavelengths > 550 nm strongly tracked the concentration of dye in solution during the soaking (adsorptive) step, increasing after soaks in more concentrated solutions. Figure VI.11b shows a plot of the measured external quantum yield at 570 nm as a function of the concentration of rose bengal during the soaking (adsorptive) step. The line in Figure VI.11b is a fit of the data to a simple Langmuir adsorption model with a binding constant of 2.8×10^4 M^{-1}. Figure VI.11c highlights representative photoelectrochemical responses obtained with monochromatic illumination at 570 nm and a p-GaP(100) electrode in deaerated 1 M KCl that was first soaked in 6 mM rose bengal solution for 30 min. In the absence of illumination, p-GaP(100) electrodes showed no appreciable cathodic currents in the investigated potential range. Photoresponses obtained under illumination in deaerated solutions featured a decidedly non-rectangular internal quantum yield-potential profile. The plateau photocurrent at -0.6 V vs. Ag/AgCl, in conjunction with the measured absorptance of the adsorbed rose bengal in Figure VI.12, corresponded to an internal quantum yield of 0.17. Photoresponses obtained under illumination in deaerated solutions with 10 mM methyl viologen yielded a modestly higher plateau photocurrent value at an applied potential of -0.6 V vs. Ag/AgCl. However, the addition of methyl viologen dichloride more significantly changed two other aspects of the overall internal quantum yield-potential profiles. First, the rest potential under illumination was shifted approximately +0.1 V. Second, the photocurrent-potential profile was significantly more 'rectangular,' i.e. the plateau photocurrent was obtained at potentials closer to the open-circuit rest potential. P-type GaP(100) photoelectrodes with deliberately adsorbed rose bengal in solutions containing methyl viologen all showed good response characteristics

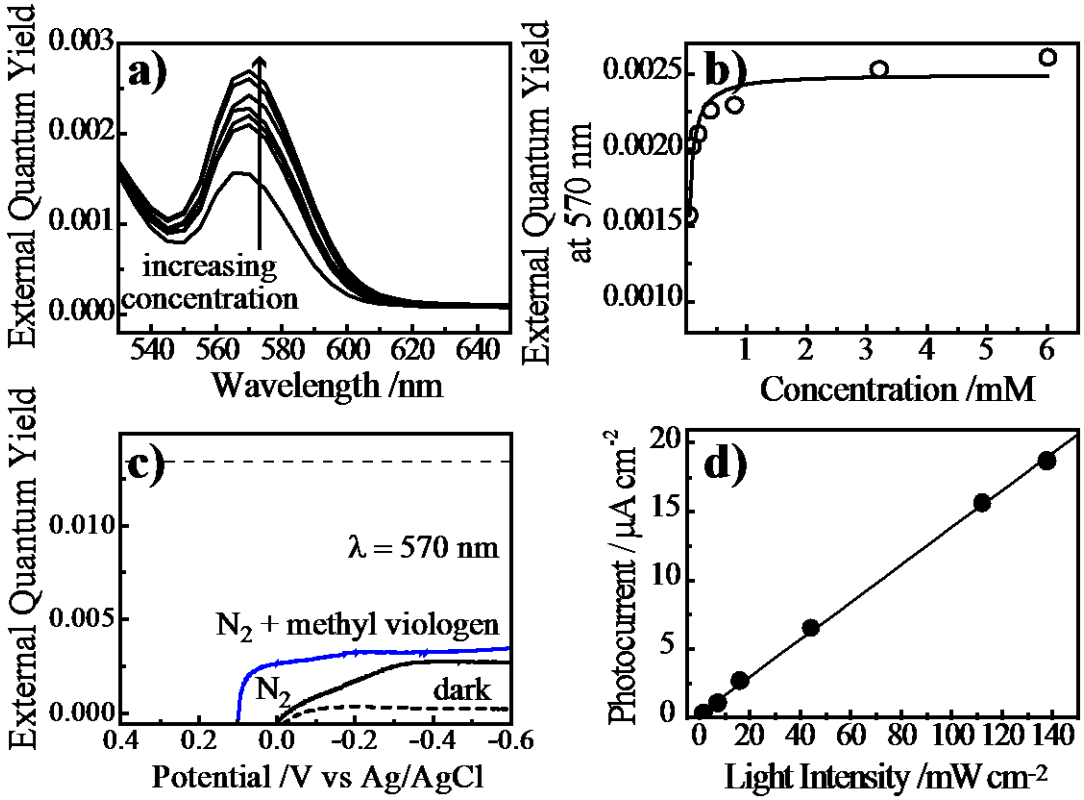

Figure VI.11: (a) Measured external quantum yield at sub-bandgap wavelengths for a p-GaP(100) photoelectrode immersed in deaerated 1 M KCl(aq). The electrode was previously treated with $(NH_4)_2S$(aq) as described in the text and soaked in aqueous solutions containing concentrations of dissolved rose bengal ranging from 0.05 mM to 6 mM for 30 min. (b) Dependence of the measured external quantum yield at 570 nm as a function of the concentration of rose bengal in the solution used for dye adsorption. The line indicates a fit to a Langmuir adsorption model with an adsorption constant of 2.8 x 10^4 M^{-1}. (c) Measured potential dependence of p-GaP(100) sensitized with adsorbed rose bengal via a 30 minute soak in a 6 mM solution while (black dashed line) in the dark or (solid lines) illuminated with 570 nm light at 0.34 mW cm^{-2}. The black solid line indicates observed response in deaerated solution with no methyl viologen dichloride. The blue solid line shows the measured response after addition of 10 mM methyl viologen dichloride. The dashed line indicates the expected external quantum yield if sensitization occurred with unity internal quantum yield for the given loading of adsorbed dye. (d) Measured dependence of the photocurrent density obtained with a p-GaP(100) electrode sensitized by adsorbed rose bengal on monochromatic light intensity.

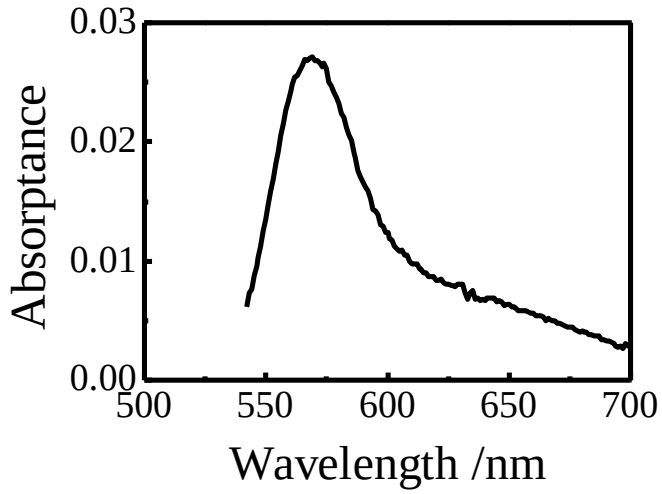

Figure VI.12: Measured spectral absorptance for a p-GaP(100) surface that was treated with $(NH_4)_2S$(aq) and then soaked in a 6 mM solution of rose bengal for 30 min. Data adapted from transmittance measurements through the treated double-side polished p-GaP(100) wafer.

at higher photon fluxes. Figure VI.11d shows that the plateau photocurrent at -0.6 V vs. Ag/AgCl was linearly dependent on the illumination intensity from 1.6-140 mW cm^{-2}.

iv. Finite-Difference Modeling of Sensitized p-GaP Steady-State Photoresponses

Modeling studies were performed to isolate the contributions from specific carrier transport processes to the observed steady-state photoelectrochemical responses of sensitized p-GaP(100). Specifically, these simulations were employed to interpret the high internal quantum yields observed in this work and to determine quantitatively the interplay between the carrier processes described in Figure VI.1c. Accordingly, simulations were performed using system parameters that approximated the experimental conditions present in this work (Tables VI.1 and VI.2). The simulation results in Figures VI.13-VI.15 describe the sensitized photoresponse of a p-GaP photoelectrode under the same depletion conditions as for the data in Figures VI.3, VI.4, VI.7 and VI.11. Since this modeling approach only considered one spatial dimension, all simulations corresponded to systems featuring a perfect monolayer of dye at the p-GaP surface. The simulation results in Figures VI.13-VI.15 model the responses of a sensitized p-GaP photoelectrode illuminated with 625 nm light at 0.3 mW cm^{-2} as a function of changes in several system variables. In these plots, the ratio of the net collected carrier flux and the total light flux absorbed by the dye film represents the internal quantum yield of the sensitized system.

Figure VI.13 shows a set of simulation results that specifically describe the influence of process (*4*) in Figure VI.1c, i.e. the drift-based removal of majority carriers from the interface following charge injection, with the parameters for the other processes held constant. Figure VI.13a shows the dependence of the internal quantum yield on applied potential for values of charge carrier mobility, μ, spanning eight orders of magnitude in p-GaP with dopant density $N_A = 10^{17}$ cm^{-3}. At this dopant density, simulation results indicated that μ values $\geq 10^{-4}$ cm^2 V^{-1} s^{-1} were sufficient to sustain the maximum net photocurrent at an applied bias of -0.6 V vs. Ag/AgCl. Charge carrier mobility values less than 10^{-4} cm^2 V^{-1} s^{-1} resulted in a steep drop in overall energy conversion at this value of N_A, effected both by decreased photocurrents and a loss of rectangularity in the internal quantum yield-potential profile. Figure VI.13b summarizes these data for several values of N_A. For $N_A = 10^{17}$ cm^{-3}, the internal quantum yield at -0.6 V vs. Ag/AgCl dropped precipitously to zero at a mobility value of 10^{-6} cm^2 V^{-1} s^{-1}.

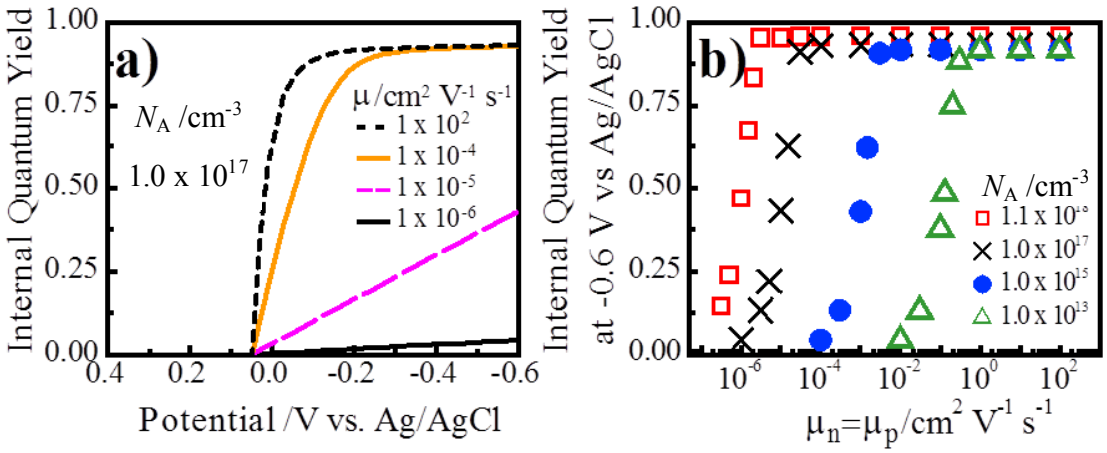

Figure VI.13: (a) Modeling results for the potential dependence of the internal quantum yield for sensitized hole injection as a function of charge carrier mobility within p-GaP at N_A = 1.0 x 10^{17} cm^{-3}. (b) The internal quantum yield for hole injection modeled at -0.6 V vs. Ag/AgCl as a function of charge carrier mobility at four different dopant densities: 1.1 x 10^{18} cm^{-3} (red open squares), 1.0 x 10^{17} cm^{-3} (black ×), 1.0 x 10^{15} cm^{-3} (blue filled circles) and 1.0 x 10^{12} cm^{-3} (green open triangles). Major simulation parameters: k_{inj} = 3.8 x 10^{14} s^{-1}; $N_{t,surface}$ = 5 x 10^{10} cm^{-2}.

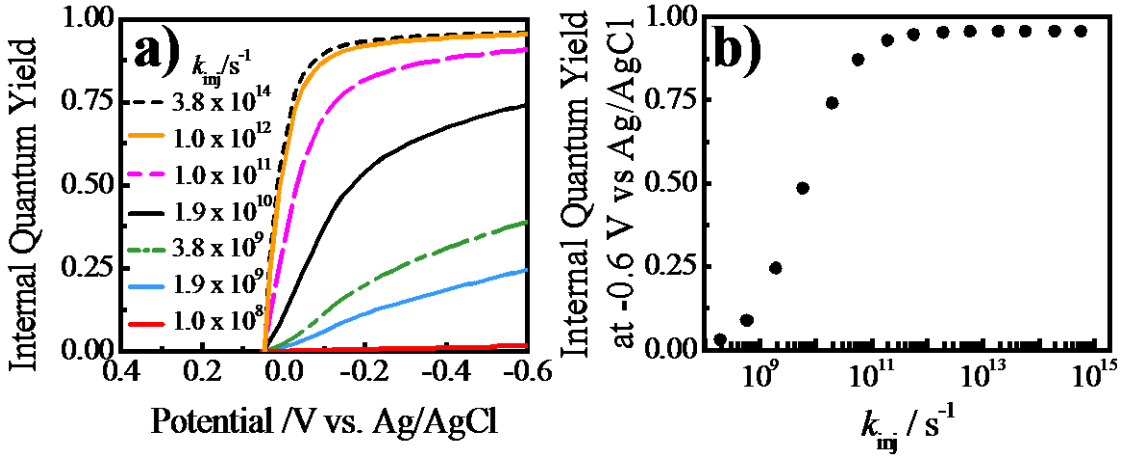

Figure VI.14: (a) Modeling results for the potential dependence of the internal quantum yield for sensitized hole injection for various values of the interfacial charge transfer rate, k_{ht}, for GaP electrodes with $N_{t,surface} = 10^{10}$ cm^{-2}. (b) The internal quantum yield for hole injection at -0.6 V vs. Ag/AgCl as a function of k_{ht}. Major simulation parameters: N_A = 1.1 x 10^{18} cm^{-3}; $\mu_n = \mu_p = 100$ cm^2 V^{-1} s^{-1}; $N_{t,surface}$ = 5 x 10^{10} cm^{-2}.

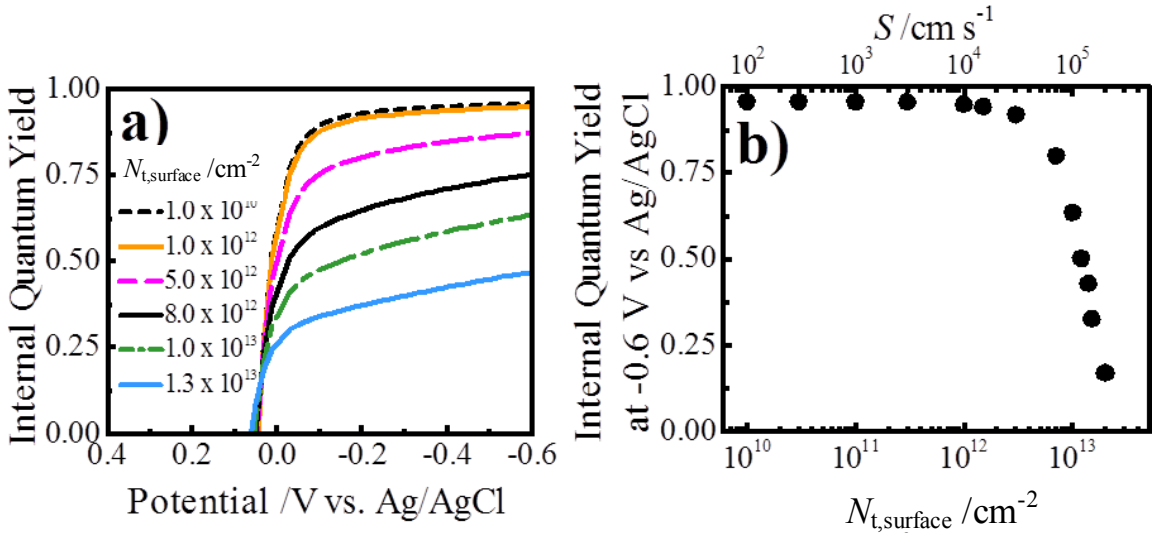

Figure VI.15: (a) Modeling results for the potential dependence of the internal quantum yield for sensitized hole injection at various GaP surface trap densities. (b) The modeled internal quantum yield for hole injection at -0.6 V vs. Ag/AgCl as a function of surface trap density. The corresponding values for surface recombination velocity are also shown. Major simulation parameters: N_A = 1.1 x 10^{18} cm^{-3}; $\mu_n = \mu_p$ = 100 cm^2 V^{-1} s^{-1}; k_{inj} = 3.8 x 10^{14} s^{-1}.

Simulations with other dopant density values exhibited similar behavior, with the falloff in high vs. low internal quantum yield occurring at larger charge carrier mobility values for lower values of N_A. For a dopant density of 1.1 x 10^{18} cm^{-3}, the simulations indicated a threshold charge carrier mobility value of 10^{-6} cm^2 V^{-1} s^{-1}. For a dopant density of 1.0 x 10^{13} cm^{-3}, charge carrier mobilities $\geq 10^0$ cm^2 V^{-1} s^{-1} were required to obtain high net internal quantum yields. In total, the data in Figure VI.13 indicated that the dopant level (1.1 x 10^{18} cm^{-3}) and mobility properties (70 cm^2 V^{-1} s^{-1}) of the p-GaP(100) materials used in this work were sufficient to afford high internal quantum yields.

Figure VI.14 presents a series of simulations that detail the effect of changes in process (*2*) in Figure VI.1c, i.e. the heterogeneous charge transfer of holes between the adsorbed dye and the p-GaP valence band, with the parameters for the other relevant processes held constant. Figure VI.14a shows a set of internal quantum yield-potential responses that feature values of k_{inj} that span five orders of magnitude. For simulations with hole transfer occurring at frequencies greater than 10^{12} s^{-1}, the model predicted high internal quantum yields for sensitization and rectangular internal quantum yield-potential profiles. For simulations with hole transfer frequencies slower than 10^{12} s^{-1}, the model indicated pronounced changes in the photoelectrochemical response. Although the rest potential under illumination was not predicted to change appreciably, the attainable photocurrent at -0.6 V vs. Ag/AgCl and sharpness of the internal quantum yield-potential profile decreased gradually as the timescales for hole transfer increased. Figure VI.14b shows that the model predicted a drop of the internal quantum yield to ~0 when k_{inj} was 10^8 s^{-1}. Conversely, these simulations indicated a minimum value of 10^{12} s^{-1} for k_{inj} to ensure that process (*2*) in Figure VI.1c was not the rate-limiting factor in the sensitization process.

Figure VI.15 shows a series of simulations that illustrate the effect of changes to process (*5*) in Figure VI.1c, i.e. Shockley-Read-Hall charge recombination at surface states at the semiconductor/dye interface. In Figure VI.15a, the internal quantum yield-potential responses are shown at several values of the surface trap density, $N_{t,surface}$. For Shockley-Read-Hall recombination, $N_{t,surface}$ is proportional to the total surface recombination velocity, *S*, through Equation VI.5,

$$S = \sigma \, v_T N_{t,surface} \qquad \text{(VI.5)}$$

where σ is the effective surface trap cross section (~10^{-15} cm^{-2}) and v_T is the thermal velocity (10^7 cm s^{-1}) of carriers in GaP. $N_{t,surface}$ values from 10^{10} to 10^{14} cm^{-2} for these simulations corresponded to S values between 10^2 and 10^6 cm s^{-1}. Assuming a nominal surface atom density of 10^{15} cm^{-2}, this range of $N_{t,surface}$ values corresponded to surfaces with as few as one trap per 100,000 surface atoms and as many as one trap per 10 surface atoms. The results in Figure VI.15a show no appreciable change in the sensitized internal quantum yield-potential response $N_{t,surface}$ values between 10^{10} and 10^{12} cm^{-2} ($10^2 \leq S \leq 10^4$ cm s^{-1}), implying that surface recombination is not rate-limiting for defect densities on the order of one trap per 1000+ surface atoms. For higher surface trap densities, the internal quantum yield-potential profile became slightly less square and did not plateau at more negative potentials. The principal effect, however, was a strong attenuation of the maximum attainable internal quantum yield. Figure VI.15b details this point more explicitly. The internal quantum yield at -0.6 V vs. Ag/AgCl estimated from these simulations dropped sharply for $N_{t,surface} > 2 \times 10^{12}$ cm^{-2}. The model results indicated attainable quantum yields of < 0.1 for defect densities worse than one trap per 100 surface atoms ($N_{t,surface} > 10^{13}$ cm^{-2}).

D. Discussion

The experimental and simulation results presented herein indicate that p-GaP electrodes in aqueous electrolyte support sensitized hole injection from a variety of common triphenylmethane dyes. Furthermore, p-GaP photoelectrodes under depletion conditions supported sensitization with high internal quantum yields in otherwise non-optimized systems. These data collectively provide insight on new strategies for designing high-efficiency sensitized photoelectrodes.

i. Sensitized Hole Injection

Several results from the photoelectrochemical measurements in 1 M KCl(aq) performed with sensitizers either dissolved in solution or adsorbed onto the p-GaP surface implicate sensitized hole injection from adsorbed excited chromophores into the valence band of GaP. First, in both measurement types, the general spectral profile of the measured cathodic external quantum yields followed the absorptance profile of each dissolved dye, indicating that sub-bandgap photocurrents arose specifically due to the photoexcited dye. In all cases, the wavelength for maximum absorptance was redshifted

from the wavelength of maximum sensitization. Irrespective of whether the dye was purposely tethered to the electrode surface or partitioned from solution onto the electrode surface (i.e. physisorbed), a redshift in the sensitized spectrum is a hallmark of sensitized injection from photoexcited chromophores specifically at a semiconductor electrode interface[15,33-35] and suggests that a sensitization process occurred at the semiconductor electrode/electrolyte interface. Second, sensitized cathodic currents were only measured in experiments featuring dyes with excited states that had enough oxidizing strength to abstract an electron from (i.e. inject a hole into) p-GaP(100). Specifically, the triphenylmethane dyes have standard potentials for oxidation equal to or more positive than $E_{VB,GaP}$.[43-46] In contrast, assuming redox properties similar to Zn phthalocyanine, the first oxidation process for Zn phthalocyanine tetrasulfonate is at a significantly more negative potential[36] (~+0.76 V vs. SCE) than for this set of triphenylmethane dyes. These observations are consistent with the general sensitization scheme described in Figure VI.1b and further indicate that the cathodic photocurrents do not arise purely from reduction of photogenerated species dissolved in solution. In addition, the observed photoelectrochemical responses were inconsistent specifically with the reduction of $O_2(^1\Delta)$ generated from photoexcited dye. Notably, hole injection from $O_2(^1\Delta)$ (generated via energy transfer from a dissolved photoexcited chromophore) into p-type semiconductors in acetonitrile has been noted previously. Grätzel and Frei reported photoreduction of $O_2(^1\Delta)$ in acetonitrile with dissolved methylene blue after irradiation with visible light and raised the possibility that the primary source of cathodic photocurrent at sub-bandgap wavelengths in other systems was hole injection from photogenerated singlet oxygen, $O_2(^1\Delta)$.[37] However, the observed invariance of cathodic photocurrents measured here in the presence of known, potent $O_2(^1\Delta)$ quenchers and the lack of sensitized photocurrents specifically in experiments containing Zn phthalocyanine tetrasulfonate directly counters this premise. A similar increase in hole injection levels in the presence of O_2 has been reported for cyanine dyes adsorbed onto CuSCN and was attributed to O_2 accepting electrons from depleted chromophores.[15] Although the specific sensitivity of the observed sensitized photoresponses towards dissolved, reducible species in solution like MV^{2+} and O_2 was not elucidated here, these cumulative observables strongly support the notion that sensitized hole injection from photoexcited

triphenylmethane dyes at the p-GaP(100) surface was the primary process responsible for the measured photocurrent.

ii. Influence of an Internal Electric Field on Net Photocurrent Yield

A notable finding from this report is the measurement of uniformly high (> 0.1) internal quantum yields for hole injection from all investigated triphenylmethane dyes into p-GaP(100) in aqueous electrolytes. These systems possessed several features that could preclude efficient charge injection. First, the dyes were not bonded to the surface of GaP through well-defined covalent bonds. Even for purposely adsorbed rose bengal using GaP surfaces pretreated with $(NH_4)_2S$, there was no deliberate attempt to strongly couple the dye and p-GaP electronically. Second, all measurements were performed in an aqueous electrolyte where suppressed sensitization levels are common.[47] Third, no measures were taken to preserve the electronic integrity of p-GaP(100) surfaces. As is common with most III-V semiconductors, the native oxide on p-GaP that forms quickly in ambient conditions is known to have an exorbitantly high density of surface traps ($N_t \geq 10^5$).[48,49] The cumulative effect of these three separate aspects could be expected to severely limit the measurable level of sensitized photocurrents. Clearly, the results shown here indicate that a separate feature(s) mitigated these three possible problems.

The combined experimental and modeling results implicate the internal electric field within the p-GaP(100) photoelectrodes in this study as a primary factor for why high internal quantum yields were observed. As observed here, freshly etched, non-degenerately doped p-GaP(100) in this electrolyte in the dark possesses nominally a 1 V potential drop in the near-surface region. The resultant electric field within the near-surface region of GaP directs holes at the interface away from the surface towards the bulk (Figure VI.1c) at a drift velocity, v_d,

$$\vec{v}_d = \mu_p \vec{E} \qquad \text{(VI.6)}$$

The results shown here specifically suggest that large values of v_d in sensitized photoelectrodes are sufficient to offset sub-optimal conditions such as poor (ill-defined) dye connectivity to the surface and a high density of surface trap states. To be clear, these data do not suggest that sensitized photoelectrodes cannot operate with high efficiency for charge injection in the absence of an appreciable internal electric field. The prevalence and success of the system pioneered by O'Regan and Grätzel clearly shows

that high net charge injection yields are possible at semiconductor photoelectrodes with little or no internal electric fields. However, it is possible that the inability to support large internal electric fields has mitigated alternative means to achieve high energy conversion efficiencies in systems suitable for large-scale implementation. In the conventional sensitized photoanodes pioneered by O'Reagan and Grätzel, a high net collection efficiency was obtained only with a specific set of semiconductor, dye, and redox couple components that collectively featured fortuitously slow deleterious chemical/electrochemical rates.[50,51] In essence, that system leveraged only chemical/molecular aspects to achieve high net collection efficiencies. Enormous efforts over the past two decades have been directed at modifying one or many of the chemical components, with little overall gains or improvement.[4] In fact, only recently have sensitized systems with substantially different dyes, semiconductor morphologies and redox couples been able to match effectively the efficiency of the original systems described by O'Regan and Grätzel in 1991.[5,52-59]

As described in Figure VI.1c, a sensitized photoelectrode that possesses a large internal electric field (i.e. operates under depletion conditions) can also utilize rapid carrier drift to suppress deleterious processes. Specifically, a sufficiently large value of v_d limits the availability of holes at the photoelectrode interface to participate in deleterious chemical/electrochemical processes. The successful competition of carrier drift processes with undesirable electrochemical reactions at semiconductor photoelectrodes under strong depletion conditions underpins the field of non-sensitized regenerative photoelectrochemistry.[60] Sweeping majority carriers away from semiconductor electrode interfaces through carrier drift in the depletion region has been exploited to produce non-sensitized semiconductor/liquid heterojunctions with solar energy conversion properties that match or exceed conventional solid state semiconductor photovoltaics.[61] In the context of dye-sensitized systems, the value and utility of internal electric fields has been less clearly defined.

Recently, a modeling report concluded that internal electric fields within nanostructured TiO_2 photoelectrodes would not substantially augment their performance as sensitized photoanodes in the standard cell design.[62] The findings reported here do not contradict that work. Instead, the modeling results and the apparent high internal quantum

yields measured experimentally in this work indicate that carrier drift within a semiconductor electrode can ameliorate the operation of sensitized systems in systems with 'suboptimal' rates for relevant *chemical* processes. Several other groups have postulated this beneficial feature of sensitized semiconductor electrodes operating under depletion conditions. Most notably, Spitler et. al. utilized a model based on an Onsager treatment to describe the influence of electric fields in the depletion region on carrier transport.[63,64] Separately, Parkinson et. al.[65] and Honda et. al.[66,67] have independently reported data that show low sensitized photocurrents at either undoped or lightly doped planar semiconductor photoelectrodes that cannot support large internal electric fields. The modeling performed with the wxAMPS code in this work directly describes this phenomenon and indicates that high net sensitization yields are achievable when the semiconductor electrode supports an appreciable electric field and charge carrier mobilities are above a threshold value, consistent with both the results reported herein and previous reports.

Numerous modeling approaches have been used to describe the operation of dye-sensitized 'Grätzel' cells.[68-74] The majority of these models were not intended to describe a semiconductor photoelectrode under depletion conditions and many do not provide direct physical or chemical insight into the kinetic properties of the system. The salient feature of the wxAMPS code used in this work is that rather than using an approach based on an equivalent circuit modeling[70,71,73] or one that assumes only transport limitations,[68,69,72,75] a direct, quantitative description of the interrelation of several system parameters is possible for a planar photoelectrode sensitized by a dye layer. The approach taken here with wxAMPS could be further improved to address sub-monolayer dye loadings, image charges,[63] and possible Frumkin corrections[76] for heterogeneous rate constants. The latter point has been previously shown to be small for semiconductor electrodes under depletion conditions as compared to metal electrodes, where the primary potential drop is across the double layer in solution and can sometimes affect the rate of charge transfer by more than an order of magnitude.[76] Irrespective, the interpretation of the data shown here is that, if bulk optoelectronic properties such as dopant density and charge carrier mobility are sufficiently large to minimize deleterious 'back' charge transfer processes (Figure VI.1c), efficient sensitization does not require ultra-fast (10^{-15}

s) timescales for hole transfer and/or semiconductor surfaces that are rigorously free of surface trap states (< 10^{10} cm^{-2}) to function. Instead, semiconductor photoelectrodes operating under strong depletion conditions should have a high tolerance towards both slow interfacial charge transfer rates with an adsorbed chromophore and high populations of trap states. More detailed studies are needed to further describe the generality of these 'tolerances.' Nevertheless, these simulation results are in line with the empirical observations for sensitized p-GaP(100).

iii. Design Strategies for Achieving Large External Quantum Yields from Sensitized Photocathodes in Water

These data on planar, macro-scale p-GaP electrodes provide useful insight on design criteria for sensitized photocathodes with high external quantum yields and, correspondingly, the capacity for efficient solar energy conversion/storage. One obvious requisite feature is a higher total optical absorptance by the sensitizer film. A planar photoelectrode coated by a sensitizer monolayer with an absorptivity of 10^8 mol^{-1} cm^2 can have an absorptance value of ~0.01, representing the upper limit for the external net quantum yield for charge injection if the internal net quantum yield is unity. For lightly doped semiconductors with poor electronic properties in 'non-optimized' cells (e.g. no I_3^-/I^-, tert-butyl pyridine, N3 dye, etc.), low internal quantum yields require a significant (>1000) increase in total surface area to support enough dye to achieve high external quantum yields.[4] In contrast, for a sensitized semiconductor under depletion conditions operating with unity internal quantum yield, electrodes with an order of magnitude smaller surface area would likewise achieve comparably high external quantum efficiencies. A p-GaP electrode that has just two orders of magnitude greater surface area than a planar electrode is still capable of supporting large internal electric fields[77] and could in principle support high external quantum yields. Ultra-small semiconductor nanoparticles (<50 nm) provide ample surface areas but cannot typically support large internal electric fields.[77] However, alternative photoelectrode form factors with high aspect ratios can satisfy both criteria. Although sensitized nanowires/nanotubes in the conventional cell design popularized by O'Regan and Grätzel have been explored,[78-80] sensitized high-aspect-ratio p-GaP photoelectrodes have yet to be explored in the context of the work presented here. Previously, we have demonstrated that doped thin nanowire

arrays[81] and macroporous films[28] with large aspect ratios (>10^2) that support appreciable internal electric fields can function as promising photoelectrodes for conversion of supra-bandgap illumination with high quantum yields. An additional advantage of high-aspect-ratio GaP architectures is their excellent light scattering properties at sub-bandgap wavelengths,[82] an aspect that could be used to further increase the effective light absorptance of a sensitizer coating.

A second feature required in sensitized photocathodes with high external quantum yields for hole injection is a different/improved surface chemistry relative to the native surface of p-GaP(100). Three separate deficiencies in the surface chemistry of GaP must be addressed. First, the native interface of GaP is prone to chemical attack and degradation.[83] Second, the native surface of GaP has a high density of electronic defects.[48,49] Third, the typical binding mode strategies for dyes on metal oxides like TiO_2 are not appropriate for the native surface of GaP. Unlike for indium phosphide (InP),[84] neither native nor thermal oxides are tenable surfaces for GaP in optoelectronic applications. Recent results from our group suggest a possible wet chemical surface modification strategy to circumvent these issues. Deliberate alkylation of GaP interfaces using nucleophilic (Grignard) reagents has been shown as a viable strategy for introducing organic groups that substantially impede chemical degradation of the surfaces of GaP and related III-V materials.[85] Further, the same alkylation chemistry has been shown to lower substantially trap densities at GaAs interfaces.[86] Additional work is needed to determine to what extent surface traps can be reduced at GaP surfaces. However, the simulation results in this work suggest that only a modest decrease in surface trap density to a level of 10^{12} traps cm^{-2} (approximately 1 trap per 1000 surface atoms) would effect a meaningful gain in the internal quantum yield. This benchmark is significant because significantly lower densities of surface traps are presently unattainable for most semiconductor materials but are not necessary for dye-sensitized applications under depletion conditions equivalent to those shown here. Further work is also needed to demonstrate whether functional groups that simultaneously passivate electronic defects (i.e. don't involve binding through surface oxides) as well as introduce secondary chemical handles for binding sensitizers are possible. The attachment scheme used here with ammonium sulfide provided a means to make measurements with

persistently adsorbed sensitizer. However, a binding strategy that used deliberate chemical bonding rather than mostly charge affinity has more potential for long-term stability. The experimental data shown here for adsorbed rose bengal and the simulation results for k_{inj} demonstrate that sensitization can occur without strong electronic coupling, potentially widening the useful bonding motifs that can be used to tether a sensitizer to the electrode surface.

A final comment can be made regarding two additional aspects in the design of sensitized photocathodes. Many of the desirable features identified here (band edge energetics, capacity to be doped p-type, large charge carrier mobilities) are not specific to GaP. P-type InP has long been recognized as a potential photocathode material in water.[87,88] However, many other binary and ternary phosphides with the same or related crystal structures (zincblende and chalcopyrite, respectively) also share many of these desirable properties without including rare-earth elements like In.[89] Related phosphides like BP and $ZnGeP_2$ have been prepared with high-aspect-ratio form factors.[90,91] Separately, this work did not focus on identifying particular dye-redox mediator combinations. Sensitizer/redox mediator combinations that can be used for a fuel-forming reaction like H^+(aq) reduction to H_2 would enable such sensitized photocathodes to be used for generating chemical fuels rather than solely electricity. A recent report that describes dissolved H_2 generation in water by cobalt complexes sensitized with rhodamine B suggests such systems may be possible.[92]

E. Conclusion

The cumulative experimental and modeling results shown here illustrate an alternative design strategy for constructing dye-sensitized photoelectrochemical systems that differ in composition, configuration, and function from existing convention in the arena of dye sensitized solar cells. Specifically, the present report shows that sensitized hole injection from photoexcited dyes is readily observed at p-type GaP photoelectrodes. Further, when operating under depletion conditions, p-GaP photoelectrodes support sensitization with high internal quantum yields in aqueous electrolytes. Electrochemical measurements and finite-difference simulations using a modified version of the wxAMPS program showed that these high internal quantum yield values were most likely afforded

by the internal electric fields present in the depletion region in GaP. These fields effectively swept injected holes away from the interface and minimized their participation in deleterious pathways that would otherwise limit their net collection yield. The results of these simulations defined effective benchmark values in dopant density, charge carrier mobilities, injection rate constants, and surface trap densities for attaining high net internal quantum yields for hole collection. Operating dye-sensitized systems under depletion conditions therefore embodies a revision to the general sensitized photoelectrode design strategies and potentially adds new flexibility in using sensitized photoelectrochemistry for direct solar energy storage in chemical bonds.

F. References

1 Elliott, C. M. Dye-Sensitized Solar Cells: Out with Both Baby and Bathwater. *Nature Chemistry* **3**, 188-189 (2011).

2 Hardin, B. E., Snaith, H. J. & McGehee, M. D. The Renaissance of Dye-Sensitized Solar Cells. *Nature Photonics* **6**, 162-169 (2012).

3 Gratzel, M. Photoelectrochemical Cells. *Nature* **414**, 338-344 (2001).

4 Hamann, T. W., Jensen, R. A., Martinson, A. B. F., Van Ryswyk, H. & Hupp, J. T. Advancing Beyond Current Generation Dye-Sensitized Solar Cells. *Energy and Environmental Science* **1**, 66-78 (2008).

5 Yella, A. *et al.* Porphyrin-Sensitized Solar Cells with Cobalt (II/III)-Based Redox Electrolyte Exceed 12 Percent Efficiency. *Science* **334**, 629-634 (2011).

6 Bandara, J. & Yasomanee, J. P. P-Type Oxide Semiconductors as Hole Collectors in Dye-Sensitized Solid-State Solar Cells. *Semiconductor Science and Technology* **22**, 20-24 (2007).

7 Borgstrom, M. *et al.* Sensitized Hole Injection of Phosphorus Porphyrin Into NiO: Toward New Photovoltaic Devices. *Journal of Physical Chemistry B* **109**, 22928-22934 (2005).

8 Fernando, A. N., Kitagawa, A., Suzuki, M., Takahashi, K. & Komura, T. A Sharp Photocurrent Enhancement in Photoelectrochemical Cells with a Photocathode Sensitized by Dye Films of Rhodamine-C-18 and Methylviolet-C-18 Prepared by Langmuir-Blodgett Techniques. *Japanese Journal of Applied Physics* **34**, 6100-6105 (1995).

9 Gibson, E. A. *et al.* A p-Type NiO-Based Dye-Sensitized Solar Cell with an Open-Circuit Voltage of 0.35 V. *Angewandte Chemie-International Edition* **48**, 4402-4405 (2009).

10 He, J. J., Lindstrom, H., Hagfeldt, A. & Lindquist, S. E. Dye-Sensitized Nanostructured p-Type Nickel Oxide Film as a Photocathode for a Solar Cell. *Journal of Physical Chemistry B* **103**, 8940-8943 (1999).

11 He, J. J., Lindstrom, H., Hagfeldt, A. & Lindquist, S. E. Dye-Sensitized Nanostructured Tandem Cell-First Demonstrated Cell with a Dye-Sensitized Photocathode. *Solar Energy Materials and Solar Cells* **62**, 265-273 (2000).

12 Li, L. *et al.* Double-Layered NiO Photocathodes for p-Type DSSCs with Record IPCE. *Advanced Materials* **22**, 1759-1762 (2010).
13 Morandeira, A., Boschloo, G., Hagfeldt, A. & Hammarstrom, L. Photoinduced Ultrafast Dynamics of Coumarin 343 Sensitized p-Type-Nanostructured NiO Films. *Journal of Physical Chemistry B* **109**, 19403-19410 (2005).
14 Nakasa, A. *et al.* A High Voltage Dye-Sensitized Solar Cell Using a Nanoporous NiO Photocathode. *Chemistry Letters* **34**, 500-501 (2005).
15 Oregan, B. & Schwartz, D. T. Efficient Photo-Hole Injection from Adsorbed Cyanine Dyes into Electrodeposited Copper(I) Thiocyanate Thin Films. *Chemistry of Materials* **7**, 1349-1354 (1995).
16 Qin, P. *et al.* Synthesis and Mechanistic Studies of Organic Chromophores with Different Energy Levels for p-Type Dye-Sensitized Solar Cells. *Journal of Physical Chemistry C* **114**, 4738-4748 (2010).
17 Sumikura, S., Mori, S., Shimizu, S., Usami, H. & Suzuki, E. Photoelectrochemical Characteristics of Cells with Dyed and Undyed Nanoporous p-Type Semiconductor CuO Electrodes. *Journal of Photochemistry and Photobiology A-Chemistry* **194**, 143-147 (2008).
18 Tennakone, K. *et al.* Dye Sensitization of Cuprous Thiocyanate Photocathode in Aqueous KCNS. *Journal of the Electrochemical Society* **131**, 1574-1577 (1984).
19 Zhang, X. L. *et al.* Enhanced Open-Circuit Voltage of p-Type DSC with Highly Crystalline NiO Nanoparticles. *Chemical Communications* **47**, 4808-4810 (2011).
20 Gerischer, H. in *Solar Energy Conversion: Solid-State Physics Aspects* Vol. 31 (ed B. O. Seraphin) 115-172 (Springer Berlin, 1979).
21 McDaniel, A. M., Tseng, H. W., Damrauer, N. H. & Shores, M. P. Synthesis and Solution Phase Characterization of Strongly Photooxidizing Heteroleptic Cr(III) Tris-Dipyridyl Complexes. *Inorganic Chemistry* **49**, 7981-7991 (2010).
22 Mori, S. *et al.* Charge-Transfer Processes in Dye-Sensitized NiO Solar Cells. *Journal of Physical Chemistry C* **112**, 16134-16139 (2008).
23 Memming, R. & Tributsch, H. Electrochemical Investigations on Spectral Sensitization of Gallium Phosphide Electrodes. *Journal of Physical Chemistry* **75**, 562-& (1971).
24 Fonash, S. J. *et al. A Manual for AMPS-1D for Windows 95/NT*. (The Pennsylvania State University, 1997).
25 McElheny, P. J., Chatterjie, P. & Fonash, S. J. Collection Efficiency of a-Si:H Schottky Barriers: a Computer Study of the Sensitivity to Material and Device Parameters. *Journal of Applied Physics* **69**, 7674-7688 (1991).
26 Liu, Y., Sun, Y. & Rockett, A. A New Simulation Software of Solar Cells-wxAMPS. *Solar Energy Materials and Solar Cells* **98**, 124-128 (2012).
27 Yuan, Z. L. *et al.* Investigation of Neutralization $(NH_4)_2S$ Solution Passivation of GaAs(100) Surfaces. *Applied Physics Letters* **71**, 3081-3083 (1997).
28 Price, M. J. & Maldonado, S. Macroporous n-GaP in Nonaqueous Regenerative Photoelectrochemical Cells. *Journal of Physical Chemistry C* **113**, 11988-11994 (2009).
29 Lewis, N. S. An Analysis of Charge-Transfer Rate Constants for Semiconductor Liquid Interfaces. *Annual Review of Physical Chemistry* **42**, 543-580 (1991).

30 Salvador, P. Semiconductor Photoelectrochemistry: A Kinetic and Thermodynamic Analysis in the Light of Equilibrium and Nonequilibrium Models. *Journal of Physical Chemistry B* **105**, 6128-6141 (2001).
31 Hagedorn, K., Forgacs, C., Collins, S. M. & Maldonado, S. Design Considerations for Nanowire Heterojunctions in Solar Energy Conversion/Storage Applications. *Journal of Physical Chemistry C* **114**, 12010-12017 (2010).
32 McRae, E. G. Theory of Solvent Effects on Molecular Electronic Spectra-Frequency Shifts. *Journal of Physical Chemistry* **61**, 562-572 (1957).
33 Moser, J. & Gratzel, M. Photosensitized Electron Injection in Colloidal Semiconductors. *Journal of the American Chemical Society* **106**, 6557-6564 (1984).
34 Lendvay, E. Photoluminescence of Adsorbed Dyes. *Journal of Physical Chemistry* **69**, 738-744 (1965).
35 Spitler, M. & Calvin, M. Adsorption and Oxidation of Rhodamine B at ZnO Electrodes. *Journal of Chemical Physics* **67**, 5193-5200 (1977).
36 Leznoff, C. C. & Lever, A. B. P. Vol. 3 (VCH Publishers, New York, 1993).
37 Gratzel, M. & Frei, H. Evidence for Hole Injection From $O_2(^1\Delta)$ Into p-Si. *Journal of Physical Chemistry* **93**, 7038-7041 (1989).
38 DeRosa, M. C. & Crutchley, R. J. Photosensitized Singlet Oxygen and Its Applications. *Coordination Chemistry Reviews* **233-234**, 351-371 (2002).
39 Redmond, R. W. & Gamlin, J. N. A Compilation of Singlet Oxygen Yields from Biologically Relevant Molecules. *Photochemistry and Photobiology* **70**, 391-475 (1999).
40 Reszka, K., Cruz, F. S. & Docampo, R. Photosensitization by the Trypanocidal Agent Crystal Violet. Type I versus Type II Reactions. *Chemical-Biological Interactions* **58**, 161-172 (1986).
41 Duxbury, D. F. The Photochemistry and Photophysics of Triphenylmethane Dyes in Solid and Liquid Media. *Chemical Reviews* **93**, 381-433 (1993).
42 Spikes, J. D., Van Lier, J. E. & Bommer, J. C. A Comparison of the Photoproperties of Zinc Phthalocyanine and Zinc Napthalocyanine Tetrasulfonates: Model Sensitzers for the Photodynamic Therapy of Tumors. *Journal of Photochemistry and Photobiology A* **91**, 193-198 (1995).
43 Austin, J. M., Harrison, I. R. & Quickenden, T. I. Electrochemical and Photoelectrochemical Properties of Rhodamine B. *Journal of Physical Chemistry* **90**, 1839-1843 (1986).
44 Mori, S. *et al.* Charge-Transfer Processes in Dye-Sensitized NiO Solar Cells. *J. Phys. Chem. C* **112**, 16134-16139 (2008).
45 Linden, S. M. & Neckers, D. C. Bleaching Studies of Rose Bengal Onium Salts. *Journal of the American Chemical Society* **110**, 1257-1260 (1988).
46 Adams, R. N. & Galus, Z. The Anodic Oxidation of Triphenylmethane Dyes. *Journal of the American Chemical Society* **86**, 1666-1671 (1964).
47 Law, C. H. *et al.* Water-Based Electrolytes for Dye-Sensitized Solar Cells. *Advanced Materials* **22**, 4505-4509 (2010).
48 Gershenzon, M. & Mikulyak, R. M. Radiative Pair Recombination and Surface Recombination in GaP Photoluminescence. *Applied Physics Letters* **8**, 245-247 (1966).

49 Stringfellow, G. B. Effect of Surface Treatment on Surface Recombination Velocity and Diode Leakage Current in GaP. *Journal of Vacuum Science & Technology* **13**, 908-913 (1976).

50 Boschloo, G. & Hagfeldt, A. Characteristics of the Iodide/Triiodide Redox Mediator in Dye-Sensitized Solar Cells. *Accounts of Chemical Research* **42**, 1819-1826 (2009).

51 Oregan, B. & Gratzel, M. A Low-Cost, High-Efficiency Solar Cell Based on Dye-Sensitized Colloidal TiO_2 Films. *Nature* **353**, 737-740 (1991).

52 Zeng, W. *et al.* Efficient Dye-Sensitized Solar Cells with an Organic Photosensitizer Featuring Orderly Conjugated Ethylenedioxythiophene and Dithienosilole Blocks. *Chemistry of Materials* **22**, 1915-1925 (2010).

53 Planells, M. *et al.* Energy Levels, Charge Injection, Charge Recombination and Dye Regeneration Dynamics for Donor-Acceptor Pi-Conjugated Organic Dyes in Mesoscopic TiO_2 Sensitized Solar Cells. *Energy & Environmental Science* **4**, 1820-1829 (2011).

54 Nusbaumer, H., Zakeeruddin, S. M., Moser, J. E. & Gratzel, M. An Alternative Efficient Redox Couple for the Dye-Sensitized Solar Cell System. *Chemistry-A European Journal* **9**, 3756-3763 (2003).

55 Li, R., Liu, J., Cai, N., Zhang, M. & Wang, P. Synchronously Reduced Surface States, Charge Recombination, and Light Absorption Length for High-Performance Organic Dye-Sensitized Solar Cells. *The Journal of Physical Chemistry B* **114**, 4461-4464 (2010).

56 Ghadiri, E., Taghavinia, N., Zakeeruddin, S. M., Gratzel, M. & Moser, J. E. Enhanced Electron Collection Efficiency in Dye-Sensitized Solar Cells Based on Nanostructured TiO2 Hollow Fibers. *Nano Letters* **10**, 1632-1638 (2010).

57 Daeneke, T. *et al.* High-Efficiency Dye-Sensitized Solar Cells with Ferrocene-Based Electrolytes. *Nature Chemistry* **3**, 211-215 (2011).

58 Bai, Y. *et al.* High-Efficiency Organic Dye-Sensitized Mesoscopic Solar Cells with a Copper Redox Shuttle. *Chemical Communications* **47**, 4376-4378 (2011).

59 Bessho, T., Zakeeruddin, S. M., Yeh, C. Y., Diau, E. W. G. & Gratzel, M. Highly Efficient Mesoscopic Dye-Sensitized Solar Cells Based on Donor-Acceptor-Substituted Porphyrins. *Angewandte Chemie-International Edition* **49**, 6646-6649 (2010).

60 Tan, M. X. *et al.* Principles and Applications of Semiconductor Photoelectrochemistry. *Progress in Inorganic Chemistry* **41**, 21-144 (1994).

61 Gibbons, J. F., Cogan, G. W., Gronet, C. M. & Lewis, N. S. A 14% Efficient Nonaqueous Semiconductor /Liquid Junction Solar Cell. *Applied Physics Letters* **45**, 1095-1097 (1984).

62 Hill, J. J., Banks, N., Haller, K., Orazem, M. E. & Ziegler, K. J. An Interfacial and Bulk Charge Transport Model for Dye-Sensitized Solar Cells Based on Photoanodes Consisting of Core-Shell Nanowire Arrays. *Journal of the American Chemical Society* **133**, 18663-18672 (2011).

63 Spitler, M. T. One-Dimensional Onsager Model for Dye Sensitized Charge Injection into Semiconductors. *Journal of Electroanalytical Chemistry* **228**, 69-76 (1987).

64 Parkinson, B. A. & Spitler, M. Recent Advances in High Quantum Yield Dye Sensitization of Semiconductor Electrodes. *Electrochimica Acta* **37**, 943-948 (1992).
65 Fillinger, A., Soltz, D. & Parkinson, B. A. Dye Sensitization of Natural Anatase Crystals with a Ruthenium-Based Dye. *Journal of the American Chemical Society* **149**, A1146-A1156 (2002).
66 Nakao, M., Itoh, K. & Honda, K. Optimization of the Donor Density of a Semiconductor Electrode for Enhancement of the Quantum Yield of the Dye-Sensitized Photocurrent. *Journal of Physical Chemistry* **88**, 4906-4907 (1984).
67 Nakao, M., Itoh, K., Watanabe, K. & Honda, K. Mechanism of Electrochemical Dye Sensitization: Effects of Semiconductor Doping Level and Reducing Agent on the Photocurrent Quantum Yield. *Berichte der Bunsen-Gesellschaft fuer Physikalische Chemie* **89**, 134-138 (1985).
68 Barnes, P. R. F., Anderson, A. Y., Durrant, J. R. & O'Regan, B. C. Simulation and Measurement of Complete Dye Sensitised Solar Cells: Including the Influence of Trapping, Electrolyte, Oxidised Dyes and Light Intensity on Steady State and Transient Device Behaviour. *Physical Chemistry Chemical Physics* **13**, 5798-5816 (2011).
69 Gonzalez-Vazquez, J. P., Anta, J. A. & Bisquert, J. Determination of the Electron Diffusion Length in Dye-Sensitized Solar Cells by Random Walk Simulation: Compensation Effects and Voltage Dependence. *Journal of Physical Chemistry C* **114**, 8552-8558 (2010).
70 Han, L. Y., Koide, N., Chiba, Y. & Mitate, T. Modeling of an Equivalent Circuit for Dye-Sensitized Solar Cells. *Applied Physics Letters* **84**, 2433-2435 (2004).
71 Han, L. Y., Koide, N., Chiba, Y., Islam, A. & Mitate, T. Modeling of an Equivalent Circuit for Dye-Sensitized Solar Cells: Improvement of Efficiency of Dye-Sensitized Solar Cells by Reducing Internal Resistance. *Comptes Rendus Chimie* **9**, 645-651 (2006).
72 Lee, J. J., Coia, G. M. & Lewis, N. S. Current Density Versus Potential Characteristics of Dye-Sensitized Nanostructured Semiconductor Photoelectrodes. 2. Simulations. *Journal of Physical Chemistry B* **108**, 5282-5293 (2004).
73 Murayama, M. & Mori, T. Evaluation of Treatment Effects for High-Performance Dye-Sensitized Solar Cells Using Equivalent Circuit Analysis. *Thin Solid Films* **509**, 123-126 (2006).
74 Penny, M., Farrell, T. & Will, G. A Mathematical Model for the Anodic Half Cell of a Dye-Sensitised Solar Cell. *Solar Energy Materials and Solar Cells* **92**, 24-37 (2008).
75 Sodergren, S., Hagfeldt, A., Olsson, J. & Lindquist, S. E. Theoretical Models for the Action Spectrum and the Current-Voltage Characteristics of Microporous Semiconductor Films in Photoelectrochemical Cells. *Journal of Physical Chemistry* **98**, 5552-5556 (1994).
76 Royea, W. J., Kruger, O. & Lewis, N. S. Frumkin Corrections for Heterogeneous Rate Constants at Semiconducting Electrodes. *Journal of Electroanalytical Chemistry* **438**, 191-197 (1997).

77 Foley, J. M., Price, M. J., Feldblyum, J. I. & Maldonado, S. Analysis of the Operation of Thin Nanowire Photoelectrodes for Solar Energy Conversion. *Energy & Environmental Science* **5**, 5203-5220 (2012).
78 Law, M., Greene, L. E., Johnson, J. C., Saykally, R. & Yang, P. D. Nanowire Dye-Sensitized Solar Cells. *Nature Materials* **4**, 455-459 (2005).
79 Baxter, J. B. & Aydil, E. S. Nanowire-Based Dye-Sensitized Solar Cells. *Applied Physics Letters* **86** (2005).
80 Tan, B. & Wu, Y. Y. Dye-Sensitized Solar Cells Based on Anatase TiO_2 Nanoparticle/Nanowire Composites. *Journal of Physical Chemistry B* **110**, 15932-15938 (2006).
81 Wen, W. *et al.* Structural and Photoelectrochemical Properties of GaP Nanowires Annealed in NH(3). *Journal of Physical Chemistry C* **115**, 22652-22661 (2011).
82 Schuurmans, F. J. P., Megens, M., Vanmaekelbergh, D. & Lagendijk, A. Light Scattering near the Localization Transition in Macroporous GaP Networks. *Physical Review Letters* **83**, 2183-2186 (1999).
83 Khaselev, O. & Turner, J. A. Electrochemical Stability of p-$GaInP_2$ in Aqueous Electrolytes toward Photoelectrochemical Water Splitting. *Journal of the Electrochemical Society* **145**, 3335-3339 (1998).
84 Lewerenz, H. J., Aspnes, D. E., Miller, B., Malm, D. L. & Heller, A. Semiconductor Interface Characterization in Photoelectrochemical Solar Cells: the p-InP(111)A Face. *Journal of the American Chemical Society* **104**, 3325-3329 (1981).
85 Mukherjee, J., Peczonczyk, S. & Maldonado, S. Wet Chemical Functionalization of III-V Semiconductor Surfaces: Alkylation of Gallium Phosphide Using a Grignard Reaction Sequence. *Langmuir* **26**, 10890-10896 (2010).
86 Peczonczyk, S. L., Mukherjee, J., Carim, A. I. & Maldonado, S. Wet Chemical Functionalization of III-V Semiconductor Surfaces: Alkylation of Gallium Arsenide and Gallium Nitride by a Grignard Reaction Sequence. *Langmuir* **28**, 4672–4682 (2012).
87 Heller, A., Miller, B. & Thiel, F. A. 11.5% Solar Conversion Efficiency in the Photocathodically Protected p-InP V^{3+}-V^{2+} HCl-C Semiconductor Liquid Junction Cell. *Applied Physics Letters* **38**, 282-284 (1981).
88 Aharon-Shalom, E. & Heller, A. Efficient p-InP(Rh-H alloy) and p-InP(Re-H alloy) Hydrogen Evolving Photocathodes. *Journal of the Electrochemical Society* **129**, 2865-2866 (1982).
89 Berger, L. I. *Semiconductor Materials*. (CRC Press, Inc., 1997).
90 Schroten, E., Goossens, A. & Schoonman, J. Synthesis of Nanometer-Scale Boron Phosphide Whiskers by Vapor-Liquid-Solid Chemical Vapor Deposition. *Journal of Applied Physics* **79**, 4465-4467 (1996).
91 Collins, S. M., Hankett, J. M., Carim, A. I. & Maldonado, S. Preparation of $ZnGeP_2$ Nanowire Films. *Journal of Materials Chemistry* **22**, 6613-6622 (2012).
92 McCormick, T. M. *et al.* Reductive Side of Water Splitting in Artificial Photosynthesis: New Homogeneous Photosystems of Great Activity and Mechanistic Insight. *Journal of the American Chemical Society* **132**, 15480-15483 (2010).

APPENDIX A

Explicit Form of Poisson Equation in Discrete-Contact Nanowires

Poisson's equation for the electric potential, ϕ, within a dielectric is given by Equation A.1,

$$\nabla \cdot \varepsilon_s \nabla \phi = -q\left(p - n + N_D - N_A\right) - \rho_{trap} \qquad \text{(A.1)}$$

where ε_s is the semiconductor permittivity, q is the unsigned charge of an electron, p and n are the respective hole and electron densities, N_D and N_A are the respective donor and accepter dopant densities and ρ_{trap} is the density of trap states. All of the above parameters can vary nontrivially with spatial position within the dielectric, making an analytical description of Equation A.1 difficult or impossible. Equation A.1 can be simplified for select dielectric properties and operating conditions, however, by assuming that (*1*) permittivity is constant throughout the dielectric, (*2*) the device is not under illumination and intrinsic carrier densities are << $|N_D\text{-}N_A|$, and (*3*) trap density is negligible. Applying (*1*)-(*3*) to Equation A.1 yields Equation A.2,

$$\nabla^2 \phi = -\frac{q\left(N_D - N_A\right)}{\varepsilon_s} \qquad \text{(A.2)}$$

For a nanowire device with radial symmetry, Equation A.2 can be written as Equation A.3,

$$\frac{1}{\rho}\frac{\partial}{\partial \rho}\left(\rho \frac{\partial \phi}{\partial \rho}\right) + \frac{\partial^2 \phi}{\partial z^2} = -\frac{q\left(N_D - N_A\right)}{\varepsilon_s} \qquad \text{(A.3)}$$

where ρ is the radial coordinate and z represents the position along the length of the nanowire. For an n-type semiconductor with discrete contacts diffused at various intervals along the length of the nanowire (Chapter IV), Equation A.3 becomes

$$\frac{1}{\rho}\frac{\partial}{\partial\rho}\left(\rho\frac{\partial\phi(\rho,z)}{\partial\rho}\right)+\frac{\partial^2\phi(\rho,z)}{\partial z^2}=$$

$$-\frac{q}{\varepsilon_s}\left(N_{D0}+erfc\left(\frac{r-\rho}{\rho_0}\right)\left[N_{D,\max}\sum_i\left(\Theta\left(z_i-\frac{\Delta_{CW}}{2}\right)-\Theta\left(z_i+\frac{\Delta_{CW}}{2}\right)\right)+N_{A,\max}\sum_j\left(\Theta\left(z_j-\frac{\Delta_{CW}}{2}\right)-\Theta\left(z_j+\frac{\Delta_{CW}}{2}\right)\right)\right]\right)$$

(A.4)

where N_{D0} is the dopant density of the bulk nanowire, r is the nanowire radius, ρ_0 is the characteristic contact dopant diffusion depth, $N_{D,max}$ and $N_{A,max}$ are the maximum contact dopant densities, Δ_{CW} is the contact width, the sums over i and j are for n-type contacts and p-type contacts, respectively, z_i and z_j represent the position of the center of each respective n-type and p-type contact, Θ denotes the Heaviside step function and a complementary error function profile is assumed for the degenerately doped contacts. Equation A.4 is not separable, and numerical solutions are used in Chapter IV to solve for the electrostatic potential and carrier densities within the nanowire.

APPENDIX B

Parameters for Chapter IV Simulations

The tables in this appendix give the default simulation parameters for the single-nanowire simulations featuring (Table B.1) dopant-diffused discrete contacts, (Table B.2) a single conformal Schottky contact, or (Table B.3) undoped discrete contacts. Any deviation from these parameters is detailed in the text and figure captions of Chapter IV.

The Auger recombination rate, R_{Auger}, calculated by Sentaurus Device is given by Equation B.1,

$$R_{Auger} = \left(C_n n + C_p p\right)\left(np - n_i^2\right) \qquad \text{(B.1)}$$

where n and p are the electron and hole carrier densities, respectively, n_{i} is the effective intrinsic carrier density and C_{n} and C_{p} are the temperature-dependent Auger coefficients[4]

$$C_n = \left(A_n + B_n \frac{T}{T_0} + M_n \left(\frac{T}{T_0}\right)^2\right)\left(1 + H_n e^{\frac{-n}{N_{0,n}}}\right) \qquad \text{(B.2a)}$$

$$C_p = \left(A_p + B_p \frac{T}{T_0} + M_p \left(\frac{T}{T_0}\right)^2\right)\left(1 + H_p e^{\frac{-p}{N_{0,p}}}\right) \qquad \text{(B.2b)}$$

A_{x}, B_{x}, M_{x} and H_{x} are fit parameters given for Si in Table B.1,[4] T_0 is a baseline temperature equal to 300 K and N_0 is the characteristic carrier density. The exponential factor in Equations B.2a-b accounts for the sensitivity of Auger recombination to carrier injection levels and is required to accurately incorporate Auger effects under the concentrated illumination conditions investigated in this work.

Table B1: Si Auger coefficients for Equations B.1 and B.2. Adapted from [4].[4]

C_n Parameters			C_p Parameters		
A_n	6.7×10^{-32}	$cm^6\ s^{-1}$	A_p	7.2×10^{-32}	$cm^6\ s^{-1}$
B_n	2.45×10^{-31}	$cm^6\ s^{-1}$	B_p	4.5×10^{-33}	$cm^6\ s^{-1}$
M_n	-2.22×10^{-32}	$cm^6\ s^{-1}$	M_p	2.63×10^{-32}	$cm^6\ s^{-1}$
H_n	3.46667		H_p	8.25688	
$N_{0,n}$	1×10^{18}		$N_{0,p}$	1×10^{18}	

Table B.2: Default parameters for Si nanowire featuring dopant-diffused discrete contacts.

Parameter	Description	Value	Units
E_g	Bandgap	1.16964	eV
N_{CB}	effective density of states in conduction band	2.78×10^{19}	cm^{-3}
N_{VB}	effective density of states in valence band	3.14×10^{19}	cm^{-3}
n_i	intrinsic carrier concentration	4.6×10^{9}	cm^{-3}
ε_{Si}	Si dielectric constant	11.7	ε_0
R	radiative recombination constant	4.73×10^{-15}	$cm^3\ s^{-1}$
N_D	donor dopant density	1×10^{12}	cm^{-3}
$\tau_{SRH,n}$	SRH electron lifetime	5×10^{-4}	s
$\tau_{SRH,p}$	SRH hole lifetime	5×10^{-4}	s
S_n	surface recombination velocity for electrons	1×10^{-4}	$cm\ s^{-1}$
S_p	surface recombination velocity for holes	1×10^{-4}	$cm\ s^{-1}$
μ_n	electron mobility	1417	$cm^2\ V^{-1}\ s^{-1}$
μ_p	hole mobility	470	$cm^2\ V^{-1}\ s^{-1}$
$v_{n,\,n}$	electron collection velocity at n-type contacts	1×10^{7}	$cm\ s^{-1}$
$v_{n,\,p}$	electron collection velocity at p-type contacts	1×10^{7}	$cm\ s^{-1}$
$v_{p,\,n}$	hole collection velocity at n-type contacts	1×10^{7}	$cm\ s^{-1}$
$v_{p,\,p}$	hole collection velocity at p-type contacts	1×10^{7}	$cm\ s^{-1}$
$m_{T,e,n}$	electron tunneling mass at n-type contacts	0.3	m_0
$m_{T,h,p}$	electron tunneling mass at p-type contacts	0.3	m_0
$m_{T,e,n}$	hole tunneling mass at n-type contacts	0.3	m_0
$m_{T,h,p}$	hole tunneling mass at p-type contacts	0.3	m_0
g	tunneling fit parameter, all instances	1.0	
$\varphi_{W,n}$	work function at n-type contacts	4.05	eV
$\varphi_{W,p}$	work function at p-type contacts	5.04	eV
$N_{As,p}$	As dopant density at p contacts	1×10^{20}	cm^{-3}
$N_{B,n}$	B dopant density at n contacts	1×10^{20}	cm^{-3}
Φ_B	barrier height	N/A	eV
h	nanowire height	50	μm
r	nanowire radius	100	nm
	number of n-type contacts	5	
	number of p-type contacts	5	
Δ_{CW}	contact width	20	nm
T	Temperature	300	K
I_0	AM1.5 illumination	100	AM1.5
ΔV	applied bias step size	0.02	V

Table B.3: Default parameters for a Si nanowire featuring a single Schottky contact.

Parameter	Description	Value	Units
E_g	Bandgap	1.16964	eV
N_{CB}	effective density of states in conduction band	2.78×10^{19}	cm^{-3}
N_{VB}	effective density of states in valence band	3.14×10^{19}	cm^{-3}
n_i	intrinsic carrier concentration	4.6×10^{9}	cm^{-3}
ε_{Si}	Si dielectric constant	11.7	ε_0
R	radiative recombination constant	4.73×10^{-15}	$cm^3\ s^{-1}$
N_D	donor dopant density	1×10^{12}	cm^{-3}
$\tau_{SRH,n}$	SRH electron lifetime	5×10^{-4}	s
$\tau_{SRH,p}$	SRH hole lifetime	5×10^{-4}	s
S_n	surface recombination velocity for electrons	1×10^{-4}	$cm\ s^{-1}$
S_p	surface recombination velocity for holes	1×10^{-4}	$cm\ s^{-1}$
μ_n	electron mobility	1417	$cm^2\ V^{-1}\ s^{-1}$
μ_p	hole mobility	470	$cm^2\ V^{-1}\ s^{-1}$
$v_{n,\,n}$	electron collection velocity at n-type contacts	1×10^{7}	$cm\ s^{-1}$
$v_{n,\,p}$	electron collection velocity at p-type contacts	1×10^{7}	$cm\ s^{-1}$
$v_{p,\,n}$	hole collection velocity at n-type contacts	1×10^{7}	$cm\ s^{-1}$
$v_{p,\,p}$	hole collection velocity at p-type contacts	1×10^{7}	$cm\ s^{-1}$
$m_{T,e,n}$	electron tunneling mass at n-type contacts	0.3	m_0
$m_{T,h,p}$	electron tunneling mass at p-type contacts	0.3	m_0
$m_{T,e,n}$	hole tunneling mass at n-type contacts	0.3	m_0
$m_{T,h,p}$	hole tunneling mass at p-type contacts	0.3	m_0
g	tunneling fit parameter, all instances	1.0	
$\varphi_{W,n}$	work function at n-type contacts	4.05	eV
$\varphi_{W,p}$	work function at p-type contacts	5.04	eV
$N_{As,p}$	As dopant density at p contacts	N/A	cm^{-3}
$N_{B,n}$	B dopant density at n contacts	N/A	cm^{-3}
Φ_B	barrier height	1.0	eV
h	nanowire height	50	μm
r	nanowire radius	100	nm
	number of n-type contacts	1	
	number of p-type contacts	1	
Δ_{CW}	contact width	N/A	nm
T	Temperature	300	K
I_0	AM1.5 illumination	100	AM1.5
ΔV	applied bias step size	0.01	V

Table B.4: Default parameters for Si nanowire featuring undoped discrete contacts.

Parameter	Description	Value	Units
E_g	Bandgap	1.16964	eV
N_{CB}	effective density of states in conduction band	2.78×10^{19}	cm^{-3}
N_{VB}	effective density of states in valence band	3.14×10^{19}	cm^{-3}
n_i	intrinsic carrier concentration	4.6×10^{9}	cm^{-3}
ε_{Si}	Si dielectric constant	11.7	ε_0
R	radiative recombination constant	4.73×10^{-15}	$cm^3\ s^{-1}$
N_D	donor dopant density	1×10^{12}	cm^{-3}
$\tau_{SRH,n}$	SRH electron lifetime	5×10^{-4}	s
$\tau_{SRH,p}$	SRH hole lifetime	5×10^{-4}	s
S_n	surface recombination velocity for electrons	1×10^{-4}	$cm\ s^{-1}$
S_p	surface recombination velocity for holes	1×10^{-4}	$cm\ s^{-1}$
μ_n	electron mobility	1417	$cm^2\ V^{-1}\ s^{-1}$
μ_p	hole mobility	470	$cm^2\ V^{-1}\ s^{-1}$
$v_{n,\,n}$	electron collection velocity at n-type contacts	1×10^{7}	$cm\ s^{-1}$
$v_{n,\,p}$	electron collection velocity at p-type contacts	1×10^{-3}	$cm\ s^{-1}$
$v_{p,\,n}$	hole collection velocity at n-type contacts	1×10^{-3}	$cm\ s^{-1}$
$v_{p,\,p}$	hole collection velocity at p-type contacts	1×10^{7}	$cm\ s^{-1}$
$m_{T,e,n}$	electron tunneling mass at n-type contacts	0.3	m_0
$m_{T,h,p}$	electron tunneling mass at p-type contacts	N/A	m_0
$m_{T,e,n}$	hole tunneling mass at n-type contacts	N/A	m_0
$m_{T,h,p}$	hole tunneling mass at p-type contacts	0.3	m_0
g	tunneling fit parameter, all instances	1.0	
$\varphi_{W,n}$	work function at n-type contacts	4.46	eV
$\varphi_{W,p}$	work function at p-type contacts	4.46	eV
$N_{As,p}$	As dopant density at p contacts	0	cm^{-3}
$N_{B,n}$	B dopant density at n contacts	0	cm^{-3}
Φ_B	barrier height	N/A	eV
h	nanowire height	50	μm
r	nanowire radius	100	nm
	number of n-type contacts	5	
	number of p-type contacts	5	
Δ_{CW}	contact width	20	nm
T	Temperature	300	K
I_0	AM1.5 illumination	100	AM1.5
ΔV	applied bias step size	0.02	V

APPENDIX C

MATLAB Script for Modeling Thin Film Transmittance

The following Matlab script was based on equations presented in the book *Optical Properties of Thin Solid Films* by T. S. Heavans.[1]

```
clear

columns=<integer>;  %Number of wavelength increments
d=<float>;  %Film thickness in cm
wave=10^-7*dlmread('<Wavelength Array','\t',[0,0,columns,0]);  %/cm
AlphaData=dlmread('<Alpha Array>','\t',[0,0,columns,0]);  %/cm-1
alpha=AlphaData(:,1);  %/cm-1

%Optical constants
n2=dlmread('<n Array>','\t',[0,0,columns,0]); %n, single-crystalline Si
k2=dlmread('<k Array>','\t',[0,0,columns,0]); %k, single-crystalline Si
n1=dlmread('<n Array>','\t',[0,1,columns,1]); %n, Au or PEDOT:PSS film
k1=dlmread('<k Array>','\t',[0,1,columns,1]); %k, Au or PEDOT:PSS film
n0=dlmread('<n Array>','\t',[0,0,columns,0]); %n, vacuum
k0=zeros(columns+1,1);                         %k, vacuum

phase=2.*pi.*n1.*d./wave;  %Phase shift through film

%Transmittance equations from Heavens reference
t1=2*(n0+i*k0)./(n0+i*k0+n1+i*k1);
t2=2*(n1+i*k1)./(n1+i*k1+n2+i*k2);
r1=(n0+i*k0-n1-i*k1)./(n0+i*k0+n1+i*k1);
r2=(n1+i*k1-n2-i*k2)./(n1+i*k1+n2+i*k2);

tE=t1.*t2.*exp(1i*phase-alpha*d/2)./(1+r1.*r2.*exp(2*1i*phase-alpha*d));

%Complex conjugates of the above terms
t1cc=2*(n0-i*k0)./(n0-i*k0+n1-i*k1);
t2cc=2*(n1-i*k1)./(n1-i*k1+n2-i*k2);
r1cc=(n0-i*k0-n1+i*k1)./(n0-i*k0+n1-i*k1);
r2cc=(n1-i*k1-n2+i*k2)./(n1-i*k1+n2-i*k2);

tEcc=t1cc.*t2cc.*exp(-1i*phase-alpha*d/2)./(1+r1cc.*r2cc.*exp(-2*1i*phase-
alpha*d));

%Transmittance
T=real(n2.*tE.*tEcc);
```

References:

1 Heavans, O. S. Optical Properties of Thin Solid Films (General Publishing, 1991).